



**HAL**  
open science

# Development of a falling-film desorber combining vapor generation and purification for ammonia-water absorption chiller (Modeling and Experiments)

Mathilde Wirtz

► **To cite this version:**

Mathilde Wirtz. Development of a falling-film desorber combining vapor generation and purification for ammonia-water absorption chiller (Modeling and Experiments). Chemical and Process Engineering. Université Savoie Mont Blanc, 2022. English. NNT : 2022CHAMA009 . tel-03889787

**HAL Id: tel-03889787**

**<https://theses.hal.science/tel-03889787>**

Submitted on 8 Dec 2022

**HAL** is a multi-disciplinary open access archive for the deposit and dissemination of scientific research documents, whether they are published or not. The documents may come from teaching and research institutions in France or abroad, or from public or private research centers.

L'archive ouverte pluridisciplinaire **HAL**, est destinée au dépôt et à la diffusion de documents scientifiques de niveau recherche, publiés ou non, émanant des établissements d'enseignement et de recherche français ou étrangers, des laboratoires publics ou privés.

## THÈSE

Pour obtenir le grade de

### DOCTEUR DE L'UNIVERSITÉ SAVOIE MONT BLANC

Spécialité : **Énergétique et Génie des Procédés**

Arrêté ministériel : 25 Mai 2016

Présentée par

**Mathilde WIRTZ**

Thèse dirigée par **Benoit STUTZ**

préparée au sein du

**Laboratoire des Technologies Thermodynamiques et Solaires (CEA Liten)**  
Et du **Laboratoire LOCIE UMR CNRS 5271**

dans l'École Doctorale SIE

### **Development of a falling-film desorber combining vapor generation and purification for ammonia-water absorption chiller (Modeling and Experiments)**

Développement d'un désorbeur à film tombant combinant la génération et la purification de vapeur pour une machine à absorption ammoniac-eau (Modélisation et Expériences)

Thèse soutenue publiquement le « **Judi 24 Février 2022** »,  
Devant le jury composé de :

**M. Alberto CORONAS SALCEDO**

Professeur, Universitat Rovira i Virgili, Rapporteur

**M. Jocelyn BONJOUR**

Professeur, INSA de Lyon, CETHIL, Rapporteur

**Mme Nathalie MAZET**

Directrice de recherche, PROMES, Examinatrice et Présidente

**M. Michel PONS**

Directeur de Recherche émérite, LIMSI, Examineur

**M. Benoit STUTZ**

Professeur, Université Savoie Mont Blanc, LOCIE, Directeur de thèse

**M. Hai Trieu PHAN**

Docteur-ingénieur, CEA-Liten, L2TS, Encadrant

**M. François BOUDÉHENN**

Ingénieur, CEA-Liten, LSET, Encadrant



# Remerciements

*Mon premier remerciement va à mon directeur de thèse Benoit Stutz. Merci pour ta force morale et ton soutien, pour ta bonne humeur et ta pédagogie, pour nos réunions de travail qui m'ont toujours boostée et tes nombreux conseils, et bien sûr pour ton immense investissement dans la réussite de cette thèse, je suis chanceuse d'avoir travaillé à tes côtés.*

*À mon encadrant Hai Trieu Phan, pour ton suivi attentif, tes idées, tes conseils avisés, ta disponibilité et ta contribution à ma formation durant trois belles années de travail commun.*

*À mon encadrant François Boudéhenn, pour nos discussions qui m'ont fait grandir, pour ton support et tes encouragements, et pour être resté présent à mes côtés pour me guider dans la réalisation de ce doctorat.*

*À Bertrand Chandez, technicien hors-pair et roi du montage de machine abso, merci pour ton formidable travail technique, pour les bons moments partagés au travail et en dehors, et de t'être occupé de moi et ma patte cassée ;).*

*À Fabien Bruyat, maître incontesté des mesures et de leurs incertitudes, merci pour ton investissement sur la partie expérimentale, pour les heures passées à parler de nombreux sujets dans la halle et ailleurs. Merci pour ton partage de culture, ton amitié et pour les randos !*

*À Nathalie Dupassieux, cheffe de labo prévenante envers les doctorants, pour ton suivi, tes conseils et ton soutien.*

*À Angela Disdier ma co-bureau, pour nos journées communes au labo et toutes les discussions que nous avons eues.*

*À Hélène Desmales, pour nos longues conversations, tes conseils, ton expérience et ta franchise. À Simone Braccio, mon compagnon de thèse, pour le travail conjoint, le soutien mutuel et les bons moments que nous avons partagé, hâte de te voir réussir à ton tour ! À Fabio Aste, Florent Lefrançois, Romain Joubert, et toute l'équipe abso et technique, pour votre bonne humeur, votre motivation dans les projets et les moments joyeux où l'on a pu trinquer (et les chants dans la halle...).*

*À Nolwenn LePierrès pour ton suivi en comité de thèse, les conseils et perspectives de travail donnés et ta confiance pour les TP. À Nicolas Cellier, pour ta nouvelle approche mathématique de mon modèle numérique. À David Cloet, pour les nombreux essais d'impression 3D. À Fred Vidal, pour ton aide sur les problématiques de mécanique du générateur.*

*À Nadine, pour notre année de thèse ensemble, à Yann, Thibaut et Jaume pour nos longues discussions et votre support final. À Estelle, à Françoise, aux Nicolas, à Cédric, Valery, Jean-François, Quentin, à tout le labo L2TS du CEA à l'INES et à Grenoble, et à tous les collègues de PUMA 3 pour avoir partagé mon quotidien au travail et de bons moments de convivialité, et pour avoir suivi mes recherches. Au labo LOCIE pour votre accueil, pour les quelques rassemblements toujours agréables durant ces trois années, et aux enseignants qui m'ont confié leurs classes. Merci à tous les doctorants, postdoctorants, enseignants, ingénieurs, techniciens, étudiants et formateurs avec qui j'ai partagé un bout de chemin et qui ont contribué à ma formation et à mon gain en compétences et en expérience.*

*À Alberto Coronas pour votre suivi en comité de thèse, votre intérêt pour mon travail, et pour avoir rapporté mon manuscrit et fait partie du jury. À Jocelyn Bonjour, pour votre travail de rapporteur et les échanges intéressants que nous avons eus lors de la soutenance. À Michel Pons, pour votre minutieuse lecture du manuscrit et vos précieuses recommandations. À Nathalie Mazet, pour avoir présidé le jury, et apporté un regard extérieur sur mon travail.*

-----

*À mes amis Gtiens : Maxime, pour nos échanges quotidiens et ce lien spécial qui nous uni, et les chatons Guillaume et Maiwenn, pour toutes nos escapades en Rhône-Alpes et ces moments magiques vécus ensemble qui vont me manquer ; Tony, pour nos longues discussions profondes et nos partages d'expérience ; Gauthier, Paul et Vivian ; pour tous nos délires et nos souvenirs mémorables, parce qu'on forme un groupe absolument fantastique et qu'on sera toujours une deuxième famille ; merci de partager mes émotions et chaque étape de ma vie.*

*À Baptiste, présent depuis longtemps, merci pour nos aventures bien ressourçantes loin du quotidien, et pour ta personnalité qui font de toi un ami inestimable.*

*À mes « bad hombres », Amin, Hasan, Parul, Jackson et Taini, rencontrés pendant ma thèse, avec qui j'ai partagé d'incroyables moments de fête, et surtout les succès, les doutes, et tous les moments forts qui rythment le doctorat.*

*Et à tous mes autres amis, qui me soutiennent depuis le début de mes études universitaires ou même avant, et avec qui je partage des instants précieux.*

*À mes frangins qui m'ont accompagnée tout au long de mon parcours, merci pour notre merveilleux passé commun, on vivra le futur ensemble parce qu'on est la meilleure fratrie dont on puisse rêver : À mon grand frère Rémi, pour tes avis, ton oreille attentive et pour tous les moments géniaux passés à Grenoble et Chambéry, et à Océane, pour ta bonne humeur et ton accueil chaleureux. À mon petit frère Julien avec qui je partage la fibre de la recherche, pour nos instants de rires et de complicité, et à Léa, les deux prochains doc c'est vous ! À mon petit frère Bastien, mon compagnon de confinement et de code, pour les heures partagées dans les Ardennes sur nos travaux respectifs, nos discussions, nos fous rires et le soutien qu'on s'est donné.*

*Enfin, à mes parents Marinette et Ludovic, qui m'ont toujours soutenue et encouragée tout au long de mes études, et ont toujours tout fait pour que l'on soit heureux et épanouis dans notre vie. Spécialement à toi Maman, tant la reconnaissance et la gratitude que j'ai envers toi sont infinies car tu as été, tu es, et tu seras toujours le meilleur des soutiens dont on puisse rêver.*



# Table of contents

<b>Abstract</b> .....	<b>8</b>
<b>Résumé</b> .....	<b>9</b>
<b>Lay Summary</b> .....	<b>11</b>
<b>List of Figures</b> .....	<b>12</b>
<b>List of Tables</b> .....	<b>15</b>
<b>Nomenclature</b> .....	<b>16</b>
<b>Part I. Introduction</b> .....	<b>19</b>
<b>Part II. State of the art</b> .....	<b>33</b>
<b>I. Absorption chiller operation and performance</b> .....	<b>35</b>
I.1. Absorption chiller operation.....	35
I.2. Absorption chiller performance.....	37
I.2.1. Main coefficients of performance.....	37
I.3. Working fluids review and selection.....	39
I.3.1. General working-fluid review.....	39
I.3.2. Working-fluid selection.....	39
I.3.3. Ammonia–water pair properties.....	40
I.4. Studies of absorption chillers.....	40
<b>II. Review of generator and rectifier technologies</b> .....	<b>42</b>
II.1. Generation and purification of refrigerant vapor.....	42
II.2. Classification of heat exchanger technologies and vapor generation processes.....	42
II.2.1. Classification of heat exchangers.....	42
II.2.2. Direct or indirect-coupled systems.....	43
II.2.3. Vapor generation process: pool boiling.....	43
II.2.4. Vapor generation process: falling-film.....	44
II.3. Heat exchanger technologies used for vapor generation and purification.....	45
II.3.1. Plate heat exchangers.....	45
II.3.2. Microchannel exchanger.....	47
II.3.3. A tubular exchanger: the distillation column.....	48
II.3.3.1. Tray columns.....	48
II.3.3.2. Packed columns.....	48
II.3.3.3. Flooded columns.....	49
II.3.4. Rectifier.....	49
II.3.5. Combined technologies: vapor generation and purification in the same component.....	50
II.3.5.1. Distillation columns.....	50
II.3.5.2. Micro-scale systems.....	51
II.3.6. Concept versatility.....	52
II.3.7. Combined generator studied.....	52
II.4. Distribution system.....	53
II.5. Synthesis of the generator and rectifier systems presented.....	55
<b>III. Dynamics of transfers inside the falling film</b> .....	<b>57</b>
III.1. Physical properties of the falling film.....	57
III.2. Flow on a vertical plate.....	57
III.2.1. Film thickness.....	57
III.2.2. Shear stress at the solution–vapor interface.....	58
III.2.3. Surface tension.....	59
III.2.4. Head losses.....	60
III.2.5. Flooding.....	60
III.3. Heat and mass transfer at the solution–vapor interface of an ammonia–water solution falling film.....	62
III.3.1. Characteristic numbers.....	62
III.3.2. Heat and mass transfer inside a falling film.....	63
III.3.3. Falling-film boiling.....	64
III.3.4. Notion of dry-out of the plate.....	65
III.3.5. Heat and mass transfer during the pool boiling of ammonia–water solution.....	65
II.3.5.1. Pool boiling mechanisms.....	66
II.3.5.2. Review of some boiling models.....	66
<b>IV. Synthesis</b> .....	<b>68</b>
<b>V. References</b> .....	<b>70</b>

<b>Part III. Design and performance predictions.....</b>	<b>75</b>
<b>Chapter I. Design of a new falling-film and plate combined generator.....</b>	<b>77</b>
1. Introduction.....	80
2. Numerical model.....	81
2.1. Boiling appearance.....	84
3. Model validation.....	85
4. Numerical results in nominal case.....	87
4.1. Co-current and counter-current cases.....	87
4.1. Combined generator concept.....	89
5. Parametric studies.....	90
5.1. Impact of the inlet conditions.....	90
5.1.1 Impact of the inlet temperature and the ammonia concentration of the solution.....	92
5.1.2 Impact of the heat transfer fluid temperature.....	93
5.1.3 Impact of the heat transfer fluid flowrate.....	94
5.2. Impact of design parameters.....	95
5.3. Study of energy costs.....	96
6. Conclusion.....	97
7. References.....	98
<b>Chapter II. Evaluation of the NH<sub>3</sub>-H<sub>2</sub>O absorption chiller performance equipped with the combined generator.....</b>	<b>101</b>
1. Introduction.....	104
2. Absorption chiller.....	104
2.1. Absorption chiller model.....	104
2.2. Validation of the model on experimental values.....	106
3. Development of the correlations for the novel falling-film combined generator.....	107
3.1. Combined generator concept.....	107
3.2. Definition of effectiveness characterizing the combined generator.....	108
3.2.1 Mass, thermal and species effectiveness.....	108
3.2.2 Equilibrium factor $R_{eq}$ .....	109
3.2.3 Application to the 5-kW absorption machine.....	109
3.3. Characterization of the effectiveness.....	110
4. Performances of the absorption chiller equipped with the combined generator.....	113
4.1. Performance comparison.....	113
4.2. Impact of the rectification at the combined generator outlet.....	114
4.3. Impact of the inlet HTF temperature.....	114
4.4. Impact of the inlet solution temperature.....	115
4.5. Impact of the equilibrium factor of the combined generator.....	116
4.6. Impact of the inlet solution mass flowrate.....	117
5. Conclusion.....	118
6. References.....	119
<b>Part IV. Experimental characterization and model validation.....</b>	<b>121</b>
<b>Chapter III. Experimental characterization of the NH<sub>3</sub>-H<sub>2</sub>O absorption chiller equipped with the combined generator.....</b>	<b>123</b>
1. Introduction.....	126
2. Integration of the combined generator in an NH <sub>3</sub> -H <sub>2</sub> O absorption chiller of 5-kW cooling capacity.....	126
2.1. The NH <sub>3</sub> -H <sub>2</sub> O absorption chiller.....	126
2.2. Implementation of the combined generator.....	128
2.2.1 The heated plates.....	128
2.2.2 Distribution-rectification system.....	129
2.2.3 Combined generator operation.....	130
2.3. Measurements.....	131
3. Experimental comparison of the absorption chiller performance, equipped with the combined generator and with the generator-separators-rectifier assembly.....	132
4. Parametric analysis.....	134
4.1. Mass flowrate of the heat transfer fluid.....	134
4.2. Nominal operating conditions.....	135
4.3. Impact of the solution subcooling on the absorption chiller performance.....	135
4.4. Experimental performance of the absorption chiller.....	137
5. Design of experiments.....	138
5.1. Description of the design of experiments.....	138
5.2. Doehlert model and polynomial coefficients determination.....	138
5.3. Model prediction.....	139
5.4. Validation of the design of experiments.....	140
6. Parametric analysis of the combined generator.....	140

6.1. Adapted NTU method.....	140
6.2. Performance of the combined generator .....	142
7. Parametric analysis of the absorption chiller performance.....	143
7.1. Performance of the machine.....	143
7.2. Application case .....	144
8. Conclusion.....	146
9. References.....	147
<b>Chapter IV. Improvement of the modeling tools dedicated to the design of generators .....</b>	<b>149</b>
1. Introduction.....	152
2. Experimental setup: the single-stage ammonia–water absorption chiller.....	152
2.1. The flooded generator.....	152
2.2. Inlet absorption chiller operating parameters- Flooded generator .....	152
3. Numerical model.....	153
3.1. Heat transfer model.....	153
3.2. Application to the nominal case .....	157
3.3. Pressure drop model.....	159
3.4. Application to the nominal case .....	160
4. Comparison between measurements and simulations.....	161
5. Unflooded combined generator model.....	162
5.1. Falling-film model and combined generator integration in the absorption chiller .....	162
5.2. Inlet absorption chiller operating parameters–Unflooded combined generator .....	162
5.3. Comparison between measurements and simulations for the unflooded combined generator.....	163
5.4. Introduction of wettability in the model.....	164
5.5. New comparison between measurements and simulations .....	165
6. Partly flooded combined generator model.....	166
6.1. Boiling heat transfer model.....	166
6.2. Inlet absorption chiller operating parameters–Partly flooded combined generator .....	167
6.3. Partly flooded combined generator nominal case .....	167
6.4. Comparison between measurements and simulations for the partly flooded combined generator.....	169
7. Comparison of performance between the flooded generator and the combined generator for its two operating modes .....	170
7.1. Inlet operating conditions of the generators.....	170
7.2. Impact of the inlet HTF temperature.....	171
7.3. Impact of the inlet solution mass flowrate .....	172
7.4. Impact of the inlet solution superheat.....	173
7.5. Impact of the generators performances on the absorption chiller performance.....	174
8. Conclusion.....	175
9. References.....	177
<b>Part V. Discussion, conclusions, perspectives .....</b>	<b>179</b>
Reminder of the challenge .....	180
Specificity of the approach .....	180
Improved overview.....	182
Perspectives and expansion .....	182
<b>Part VI. Appendix.....</b>	<b>185</b>
Appendix 6.1. Uncertainties .....	187
Appendix 6.2. Liquid and vapor head losses .....	190
Appendix 6.3. Design of experiments .....	201
Appendix 6.4. Scientific production.....	204

# Abstract

The need to meet the growing demand for cooling capacity, as well as to favor the use of fatal heat as a source of energy are among the main challenges of the energy transition. Absorption machines can be used to address these two problems, by producing cold for the industry or air-conditioning of buildings, by recovering heat, coming from abundant and low costs sources such as the sun and the heat networks. Among the existing working-pair, ammonia water has interesting physical properties, in addition to having a very low environmental impact. One of the constraints for better performance of an  $\text{NH}_3\text{-H}_2\text{O}$  absorption machine is the purity of the ammonia vapor generated, which must be high. However, the small volatility gap between ammonia and water induces the presence of traces of water in ammonia vapor.

The work carried out in this thesis presents the development of a new combined generator, combining the generation and the rectification of ammonia vapor in a falling-film and plate exchanger, and the impact of its implementation on the performances of a small capacity  $\text{NH}_3\text{-H}_2\text{O}$  absorption chiller designed for refreshment.

First of all, a numerical model is developed, allowing simulating the desorption and absorption processes, as well as the coupled heat and mass transfer operating within the falling-film, in co-current or counter-current configuration. Adiabatic plates are placed above the heated plates, allowing increasing the fraction of ammonia in the vapor generated. The impact of the input variables and the geometry of the plates is studied, in order to determine the ideal input conditions, and the most compact geometry, allowing generating the purest ammonia vapor possible at lower energy costs. Then, the combined generator, characterized by new correlations establishing its mass, thermal and species effectiveness, is implemented in an  $\text{NH}_3\text{-H}_2\text{O}$  absorption chiller model to study its impact on the machine's performance. The influence of the input parameters of the combined generator is analyzed. The new combined generator is then experimentally designed and implemented in a single-effect  $\text{NH}_3\text{-H}_2\text{O}$  absorption chiller of 5 kW cold capacity. Parametric studies are carried out on the operating conditions of the machine, (in particular through a design of experiments), which allows characterizing its operation including the new combined generator, and defining the operating limits and optimums in terms of coefficient of performance and cooling capacity. Finally, according to the operating conditions of the absorption chiller, a comparative analysis of the combined generator performance is carried out between modeling and experiments. Two modes of operation are studied: with falling-film only, or with the third bottom flooded and seat of boiling phenomena. A boiler (formerly implemented in the machine) is also modelled and its numerical performance is compared to the measurements. The comparison of the performance and effectiveness of the three generator models showed that the combined falling-film combined generator produces purer ammonia vapor for a better cycle performance.

Keywords:  $\text{NH}_3\text{-H}_2\text{O}$  absorption chiller; Combined generator; Modeling and Experiments

# Résumé

La nécessité de répondre à la demande de production de froid croissante, ainsi que de privilégier la valorisation de chaleur fatale comme source d'énergie, comptent parmi les nombreux enjeux de la transition énergétique. Les machines à absorption permettent de répondre à ces deux problématiques, en produisant du froid pour l'industrie ou la climatisation des bâtiments, par récupération de chaleur, venant de sources abondantes et à faibles coûts, telles que le soleil et les réseaux de chaleur. Parmi les fluides de travail existants, le couple  $\text{NH}_3\text{-H}_2\text{O}$  présente des propriétés physiques intéressantes, en plus d'avoir un très faible impact environnemental. L'une des contraintes pour de meilleures performances d'une machine à absorption  $\text{NH}_3\text{-H}_2\text{O}$  est la pureté de la vapeur générée, qui doit être élevée. Or, le faible écart de volatilité entre l'ammoniac et l'eau induit la présence de traces d'eau dans la vapeur d'ammoniac.

Le travail mené dans cette thèse présente le développement d'un nouveau générateur combiné, associant la génération et la rectification de la vapeur d'ammoniac dans un échangeur à plaques et films tombants, ainsi que l'impact de son implémentation sur les performances d'une machine à absorption  $\text{NH}_3\text{-H}_2\text{O}$  conçue pour le rafraîchissement.

Tout d'abord, un modèle numérique est développé, permettant de simuler les processus de désorption et d'absorption, ainsi que les transferts couplés de masse et de chaleur s'opérant au sein des films tombants, en configuration à co-courant ou contre-courant. Des plaques adiabatiques sont implantées au-dessus des plaques chauffées, permettant d'augmenter la fraction d'ammoniac de la vapeur produite. L'impact des variables d'entrée et de la géométrie des plaques est étudié, afin de déterminer les conditions d'entrée idéales, et la géométrie la plus compacte, permettant de générer une vapeur d'ammoniac pure, et à moindre coût énergétique. Puis, le générateur combiné, caractérisé par de nouvelles corrélations établissant ses efficacités de masse, thermique et d'espèces, est implémenté dans un modèle de machine à absorption  $\text{NH}_3\text{-H}_2\text{O}$  afin d'étudier son impact sur les performances de la machine. L'influence des paramètres d'entrée du générateur combiné est analysée. Ensuite, le nouveau générateur combiné est conçu expérimentalement, puis implanté dans une machine à absorption  $\text{NH}_3\text{-H}_2\text{O}$  simple effet, d'une capacité de 5 kW froid. Des études paramétriques sont menées sur les conditions opératoires de la machine, (notamment à travers un plan d'expérience), ce qui a permis de caractériser son fonctionnement incluant le nouveau générateur combiné, puis, de définir les optimums de fonctionnement en termes de coefficient de performance et de production de froid et les limites de fonctionnement. Finalement, une analyse comparative des performances du générateur combiné est menée, entre modélisation et mesures, en fonction des conditions de fonctionnement de la machine à absorption  $\text{NH}_3\text{-H}_2\text{O}$ . Deux modes de fonctionnement sont étudiés : avec des films tombants uniquement, ou avec la partie basse noyée, siège de phénomènes d'ébullition. Un générateur bouilleur (anciennement implanté dans la machine), est également modélisé et ses performances numériques sont comparées aux mesures. Une comparaison des performances et des efficacités des trois modèles de générateur a permis de démontrer que le générateur combiné à films tombants produit une vapeur plus pure, pour de meilleures performances du cycle.

Mots-clés : Machine à absorption  $\text{NH}_3\text{-H}_2\text{O}$  ; Générateur combiné ; Modélisation et Expériences



## Lay summary

Due to global warming, the buildings air-conditioning needs are growing steadily. A tripling of the demand is expected worldwide by 2050, which would lead to a sharp increase in electricity consumption, particularly in hot countries. An alternative solution to traditional vapor compression machines, which consume electricity, is to produce cold by using abundant and low-cost heat sources such as industrial waste heat, urban heating networks or solar thermal energy by means of tri-thermal machines. Indeed, these machines, coupling a motor cycle to a heat pump cycle, are characterized by significantly lower electrical consumption than mechanical compression technology.

Among the tri-thermal machines, the absorption chillers are particularly well adapted for this type of use. They use working fluid pairs that are mostly natural and environment-friendly. This work takes part into the general framework of improving the performance and the compactness of ammonia–water absorption machines in order to make them more attractive on air-conditioning market. It focuses more particularly on the generator component, often considered as non-limiting in terms of performance, and aims specifically to integrate in the same component, called the combined generator, the vapor generation and purification functions.

This innovative component was developed, designed, patented and experimentally tested in an absorption machine. A numerical model describing the heat and mass transfer occurring within the component was developed, in order to allow its dimensioning, to characterize its performance and to evaluate its impact on the machine operation.

## Résumé vulgarisé

En raison du réchauffement climatique, les besoins en rafraîchissement des bâtiments croissent rapidement. Un triplement de la demande est attendu au niveau mondial d'ici 2050 ; ce qui entraînerait une forte hausse de la consommation d'électricité, en particulier dans les pays chauds. Une solution alternative aux machines à compression de vapeur classiques, consommatrices d'électricité, consiste à produire du froid en valorisant des sources de chaleur abondantes et à faibles coûts telles que la chaleur fatale industrielle, les réseaux de chaleur urbains ou encore le solaire thermique au moyen de machines tri-thermes. En effet, ces machines couplant un cycle moteur à un cycle de pompe à chaleur, sont caractérisées par des consommations électriques sensiblement plus faibles que celles de leurs homologues à compression mécanique.

Les machines à absorption sont, parmi les machines tri-thermes, particulièrement bien adaptées pour ce type d'utilisation. Elles mettent en œuvre des couples de fluides pour la plupart naturels et non-nocifs pour l'environnement. Ces travaux s'intègrent dans le cadre général de l'amélioration de la performance et de la compacité des machines à absorption ammoniac-eau en vue de les rendre plus attractives sur le marché de la climatisation. Ils portent plus particulièrement sur le composant générateur, souvent considéré comme non limitant en terme de performance, et visent notamment à intégrer dans un même composant, appelé générateur combiné, des fonctions de génération et de purification de la vapeur.

Ce composant innovant a été développé, conçu, breveté et testé expérimentalement dans une machine à absorption. Un modèle numérique décrivant les transferts de masse et de chaleur se produisant au sein du composant a été développé, afin de permettre son dimensionnement, de caractériser ses performances et d'évaluer son impact sur le fonctionnement de la machine.

# List of figures

## Part I. Introduction

<b>Figure 1.1.</b> Primary energy for heating and cooling in the EU, 2012 (SHC annual report 2018).....	21
<b>Figure 1.2.</b> Global solar thermal capacity in operation and annual energy yields 2000–2017 (Weiss and SpörkDür 2018).....	22
<b>Figure 1.3.</b> Market share of solar-driven sorption chillers, DEC, desiccant and evaporative cooling–2009 (Stryi–Hipp 2016) .....	22
<b>Figure 1.4.</b> Cold energy mix market in France, 2018 (www.fedene.fr 2019).....	22
<b>Figure 1.5.</b> Technology roadmap for solar heating and cooling, share of solar cooling by 2050–IEA–2012 (Stryi–Hipp 2016) .....	23
<b>Figure 1.6.</b> Technology roadmap for solar heating and cooling, Market Potential by 2050–International Energy Agency–2012 (Stryi–Hipp 2016) .....	23

## Part II. State of the art

<b>Figure 2.1.</b> Schematic representation of the two Rankine thermodynamic cycles with external energy sources .....	35
<b>Figure 2.2.</b> Schematic view of a single-stage absorption chiller.....	36
<b>Figure 2.3.</b> Compression and absorption refrigeration machines (Balmer 2011).....	37
<b>Figure 2.4.</b> COP <sub>el</sub> depending on refrigerating power for over 600 single-effect absorption machines references (CEA database) .....	37
<b>Figure 2.5.</b> COP <sub>th</sub> depending on COP <sub>Carnot</sub> for single-effect absorption machines references (CEA database) .....	38
<b>Figure 2.6.</b> Number of publications related to absorption chiller per year according to Scopus website (2021).....	41
<b>Figure 2.7.</b> Number of publications related to “Absorption chiller” and “absorber” or “desorber”, Scopus website (2021) .....	41
<b>Figure 2.8.</b> Classification of some heat exchangers (Kuznetsov 2018).....	43
<b>Figure 2.9.</b> Heater geometry influence on boiling process (Kenning, thermopedia.com, 2019) .....	44
<b>Figure 2.10.</b> Saturated and subcooled liquid boiling methods (Kenning, thermopedia.com, 2019) .....	44
<b>Figure 2.11.</b> Schema of falling-film inside the generator: co-current configuration .....	45
<b>Figure 2.12.</b> Gasketed chevron plates exchanger (Abou Elmaaty et al. 2017) .....	46
<b>Figure 2.13.</b> Heat exchangers with asterisk and corrugated surfaces (Durmus et al. 2009) .....	46
<b>Figure 2.14.</b> Example of a branched tray design (Keinath et al. 2019) .....	48
<b>Figure 2.15.</b> Flooded column design (Staedter and Garimella 2018a) .....	49
<b>Figure 2.16.</b> Various types of top distributor (Koch–Glitsch 2009) .....	53
<b>Figure 2.17.</b> Different types of flow manifolds: (a) dividing, (b) combining, (c) U-manifold, (d) Z-manifold (Hassan et al. 2014).....	54
<b>Figure 2.18.</b> Baffle position and construction in the header (Wen et al. 2006).....	54
<b>Figure 2.19.</b> Double-header configuration (Jiao et al. 2003) .....	55
<b>Figure 2.20.</b> Flow inlet configurations (Kim and Byun 2013).....	55
<b>Figure 2.21.</b> Flow profile along a vertical plate, under the gravity effect.....	57
<b>Figure 2.22.</b> Schematic profile of the vapor flow between two plates.....	59
<b>Figure 2.23.</b> Temperature profile during desorption phenomenon in a falling-film .....	63
<b>Figure 2.24.</b> Falling-film boiling representation by (Cerza and Semas 1985) .....	64

## Part III. Design and performance predictions

### Chapter I

<b>Figure 3.1.</b> Schematic view of the combined generator with its main inputs and outputs, its dimensions, and the heat and mass transfers involved.....	80
<b>Figure 3.2.</b> Schematic view of the heated part of the combined generator with the three fluid flows and the heat and mass transfers occurring in each segment.....	83
<b>Figure 3.3.</b> Numerical calculation scheme .....	84
<b>Figure 3.4.</b> Range of active cavity radius and superheat of the wall as a function of the position in the combined generator .....	85
<b>Figure 3.5.</b> Comparison of absorber internal power and vapor mass flow absorbed .....	86
<b>Figure 3.6.</b> Temperatures profile along the generator.....	87
<b>Figure 3.7.</b> Profile of ammonia concentrations along the generator.....	88
<b>Figure 3.8.</b> Profile of temperatures and ammonia concentrations along the combined generator for nominal case.....	89

<b>Figure 3.9.</b> Evolution of the ammonia vapor concentration at the exit as a function of the combined generator mass effectiveness for various inlet conditions (ammonia concentration and temperature of the solution).....	92
<b>Figure 3.10.</b> Evolution of energy costs as a function of the inlet values of both the ammonia concentration and temperature of the solution.....	93
<b>Figure 3.11.</b> Evolution of ammonia vapor concentration and energy cost as a function of HTF inlet temperature.....	93
<b>Figure 3.12.</b> Evolution of ammonia vapor concentration and energy cost as a function of HTF mass flowrate.....	94
<b>Figure 3.13.</b> Evolution of ammonia vapor concentration and energy costs as a function of the combined generator mass effectiveness for various geometrical configurations.....	95
<b>Figure 3.14.</b> Evolution of the cold power production per kW of heat supplied in the combined generator according to the plate.....	96

## Chapter II

<b>Figure 4.1.</b> Schematic model of the absorption machine.....	105
<b>Figure 4.2.</b> COP and cooling capacity as a function of the inlet absorber HTF temperature.....	106
<b>Figure 4.3.</b> COP and cooling capacity as a function of the inlet generator HTF temperature.....	107
<b>Figure 4.4.</b> Combined generator geometry and heat and mass transfer involved.....	108
<b>Figure 4.5.</b> Effectiveness evolutions as a function of the Jakob number.....	111
<b>Figure 4.6.</b> Comparison of the effectiveness predicted by the correlations and the modeling.....	112
<b>Figure 4.7.</b> Error rate between the effectiveness calculated with the correlations and the modeling, distribution for the number of values in each range.....	112
<b>Figure 4.8.</b> Comparison of the absorption chiller COP and of the refrigerant ammonia concentration at the inlet of the condenser for the machine equipped with the combined generator vs. the machine equipped with the flooded generator and rectifier.....	113
<b>Figure 4.9.</b> Refrigerant mass flowrate and concentration, COP and cooling capacity as a function of the rectifier effectiveness.....	114
<b>Figure 4.10.</b> COP, cooling capacity, and effectiveness evolution as a function of the HTF temperature at inlet of the combined generator.....	115
<b>Figure 4.11.</b> COP, cooling capacity, and effectiveness evolution as a function of the solution superheating at the inlet of the combined generator.....	116
<b>Figure 4.12.</b> COP, cooling capacity, and effectiveness evolution as a function of the equilibrium factor.....	116
<b>Figure 4.13.</b> COP, cooling capacity, and effectiveness evolution as a function of the solution mass flowrate at the combined generator inlet.....	117

## *Part IV. Experimental characterization and model validation*

### Chapter III

<b>Figure 5.1.</b> Single-stage $\text{NH}_3\text{-H}_2\text{O}$ absorption chiller implemented in the CEA laboratory.....	127
<b>Figure 5.2.</b> The single-stage $\text{NH}_3\text{-H}_2\text{O}$ absorption chiller and the external hydraulic modules.....	127
<b>Figure 5.3.</b> Interior of the combined generator before integrating the distribution-rectification system.....	128
<b>Figure 5.4.</b> Distribution-rectification system (patent EP 3 885 673 A1).....	129
<b>Figure 5.5.</b> Combined generator (patent EP 3 885 672 A1) and fluids circulation.....	130
<b>Figure 5.6.</b> PID of the $\text{NH}_3\text{-H}_2\text{O}$ absorption chiller.....	131
<b>Figure 5.7.</b> COP and cooling capacity evolution as a function of the inlet temperatures of the external circuits and of the inlet solution mass flowrate, for the absorption chiller equipped with the former assembly and equipped with the combined generator.....	133
<b>Figure 5.8.</b> Evolution of COP and cooling capacity as a function of the inlet HTF mass flowrate for both configurations of combined generator.....	134
<b>Figure 5.9.</b> COP, cooling capacity, vapor concentration, and mass flowrate as a function of the saturation temperature gap at the inlet of the combined generator.....	136
<b>Figure 5.10.</b> COP and cooling capacity measured as a function of the inlet HTF temperature and of the solution mass flowrate at the inlet of the combined generator, for unflooded and partly flooded configurations.....	137
<b>Figure 5.11.</b> Heat supplied calculated through the DOE as a function of the measurements.....	139
<b>Figure 5.12.</b> Comparison of the heat supplied interpolated and measured.....	140
<b>Figure 5.13.</b> Comparison of the effectiveness predicted by the adapted NTU method correlations and the modeling.....	141
<b>Figure 5.14.</b> Comparison of mass and thermal effectiveness determined experimentally, with the values estimated using the second-order polynomial resulting from the adapted Doehlert design of experiment (DOE), and from the adapted Nusselt approach (NTU), in regard to the impact of the equilibrium factor and of the Jakob number.....	142
<b>Figure 5.15.</b> COP and cooling capacity as a function of the Carnot-COP for various solution mass flowrates.....	143
<b>Figure 5.16.</b> Number of operating hours required for each cooling capacity event of the absorption chiller, cumulative energetic gains, and % of total energy saved for the two comparisons made.....	145

## Chapter IV

<b>Figure 6.1.</b> Numerical calculation scheme .....	156
<b>Figure 6.2.</b> Macroscopic and microscopic contributions, heat transfer coefficient, and quality vs. position .....	157
<b>Figure 6.3.</b> Temperature, ammonia concentration, and mass flowrate profile in the flooded generator.....	158
<b>Figure 6.4.</b> Pressure gradient and pressure profile along the flooded generator plates for the nominal case.....	160
<b>Figure 6.5.</b> Numerical results vs. measurements for the flooded generator.....	161
<b>Figure 6.6.</b> Comparison between measurements and simulations for the combined generator operating in unflooded mode. .....	163
<b>Figure 6.7.</b> Schemes of completely wetted and partly wetted surfaces of the grooved plates .....	164
<b>Figure 6.8.</b> Percentage of the wetted area for the adiabatic and heated plates of the combined generator.....	164
<b>Figure 6.9.</b> Numerical results vs. measurements for the unflooded combined generator, with reduced wettability .....	165
<b>Figure 6.10.</b> Temperature, mass flowrate, and ammonia concentration profile along the combined generator in partly flooded operating mode .....	168
<b>Figure 6.11.</b> Numerical results vs. measurements for the partly flooded combined generator, with plate wettability reduced .....	169
<b>Figure 6.12.</b> Mass, thermal, and species effectiveness vs. inlet HTF temperature evolution for the three generators.....	171
<b>Figure 6.13.</b> Mass, thermal, and species effectiveness vs. inlet solution mass flowrate evolution for the three generators .....	172
<b>Figure 6.14.</b> Mass, thermal, and species effectiveness vs. inlet solution superheat evolution for the three generators ....	173
<b>Figure 6.15.</b> Mass and thermal effectiveness and effectiveness ratio vs. inlet HTF temperature and inlet solution mass flowrate evolution for the unflooded combined generator and the flooded generator .....	174

# List of tables

## *Part II. State of the art*

<b>Table 2.1.</b> Advantages and drawbacks of $\text{NH}_3\text{-H}_2\text{O}$ and $\text{H}_2\text{O-LiBr}$ pairs as compared to other refrigerant fluids .....	39
<b>Table 2.2.</b> Thermo-physical properties of ammonia and water .....	40
<b>Table 2.3.</b> Advantages and drawbacks of $\text{NH}_3\text{-H}_2\text{O}$ vs. $\text{H}_2\text{O-LiBr}$ absorption systems.....	40
<b>Table 2.4.</b> Advantages of direct and indirect-coupled systems .....	43
<b>Table 2.5.</b> Main parameters affecting PHE behavior .....	47

## *Part III. Design and performance predictions*

### Chapter I

<b>Table 3.1.</b> Geometrical data of the absorber studied by (Triché 2016).....	85
<b>Table 3.2.</b> Operating conditions of the absorber studied by (Triché 2016) .....	86
<b>Table 3.3.</b> Dimensions of the generator.....	87
<b>Table 3.4.</b> Initial operating conditions in the generator.....	87
<b>Table 3.5.</b> Comparison of the performances of co- and counter-current vapor flow configurations.....	88
<b>Table 3.6.</b> Combined generator geometrical parameters.....	95

### Chapter II

<b>Table 4.1.</b> Constant values for the mass, thermal, and species effectiveness correlations .....	111
<b>Table 4.2.</b> Operating inlet conditions of the absorption chiller .....	113

## *Part IV. Experimental characterization and model validation*

### Chapter III

<b>Table 5.1.</b> Range of values of parameters measured and uncertainties .....	131
<b>Table 5.2.</b> Inlet nominal operating conditions and ranges of operating conditions of the absorption chiller .....	132
<b>Table 5.3.</b> Nominal operating parameters of the absorption chiller .....	135
<b>Table 5.4.</b> Range of values for the inlet variables of the DOE.....	138
<b>Table 5.5.</b> Confidence ranges of each parameter evaluated .....	139
<b>Table 5.6.</b> Constant values for the mass and thermal effectiveness correlations.....	141

### Chapter IV

<b>Table 6.1.</b> Nominal conditions and ranges of operating conditions for the tests run with the flooded generator of (Triché 2016).....	153
<b>Table 6.2.</b> Nominal operating conditions and operating ranges of the $\text{NH}_3\text{-H}_2\text{O}$ absorption machine used to characterize the combined generator operating in unflooded mode.....	162
<b>Table 6.3.</b> Relative accuracy of the model in predicting the output of the combined generator with a confidence level of 90%.....	166
<b>Table 6.4.</b> Nominal operating conditions and operating ranges of the $\text{NH}_3\text{-H}_2\text{O}$ absorption machine used to characterize the combined generator operating in partly flooded mode.....	167
<b>Table 6.5.</b> Nominal inlet operating conditions of the three generators.....	170

# Nomenclature

<i>Variables – Latin letters</i>		
$A$	Cross sectional area	$[m^2]$
$C_p$	Heat capacity	$[J.kg^{-1}K^{-1}]$
$D$	Mass diffusivity	$[m^2.s^{-1}]$
$dA_i$	Elementary exchange surface	$[m^2]$
$d_e$	Equivalent diameter	$[m]$
$D_h$	Hydraulic diameter	$[m]$
$dM$	Elementary mass flowrate transferred	$[kg.s^{-1}]$
$dz$	Partial height	$[m]$
$e$	Space been two plates	$[m]$
$E$	Reduction heat transfer coefficient	$[-]$
$F$	Enhancement factor	$[-]$
$f$	Friction factor	$[-]$
$g$	Gravitational acceleration	$[m.s^{-2}]$
$H$	Enthalpy	$[J.kg^{-1}]$
$h$	Heat transfer coefficient	$[W.m^{-2}.K^{-1}]$
$j$	Superficial velocity	$[m.s^{-1}]$
$k$	Mass transfer coefficient	$[m.s^{-1}]$
$k_p$	Thermal conductivity of stainless steel	$[W.m^{-1}.K^{-1}]$
$L$	Length of the plate	$[m]$
$L_{sp}$	Specific length	$[m]$
$L_v$	Latent heat of vaporization	$[kJ.kg^{-1}]$
$\dot{m}$	Mass flowrate	$[kg.s^{-1}]$
$\dot{m}'$	Linear mass flowrate	$[kg.m^{-2}.s^{-1}]$
$\dot{m}''$	Mass flowrate density	$[kg.m^{-2}.s^{-1}]$
$n$	Number of plates	$[-]$
$N$	Number of experiments	$[-]$
$P$	Pressure	$[bar]$
$P_{er}$	Perimeter	$[m]$
$\Delta P$	Overall pressure drop / head losses	$[bar]$
$Q$	Heat	$[J]$
$\dot{Q}$	Heat rate	$[W]$
$\dot{Q}''$	Heat flux	$[W.m^{-2}]$
$Q_v$	Volume mass flowrate	$[m^3.s^{-1}]$
$r^*$	Equilibrium bubble radius	$[m]$
$R_{eq}$	Equilibrium factor	$[-]$
$S$	Supression factor	$[-]$
$S_{ect}$	Section	$[m^2]$
$S_{exch}$	Exchange surface	$[m^2]$
$T$	Temperature	$[K]$
$\Delta T$	Temperature difference	$[^{\circ}C]$
$\Delta T_F$	Dew and boiling temperature gap	$[K]$
$\Delta T_{id}$	Ideal wall superheat	$[K]$
$\Delta T_{w.sat}$	Wall superheat temperature	$[K]$
$th$	Thickness of the plates	$[m]$
$U$	Overall thermal transfer coefficient	$[W.m^{-2}.K^{-1}]$
$v$	Velocity	$[m.s^{-1}]$
$v_n$	Number of variables	$[-]$
$w$	Width of the plate/duct	$[m]$
$X$	Mixture quality	$[-]$
$X_{ll} X_{tt}$	Lockhart–Martinelli parameter	$[-]$
$X_m$	Martinelli parameter	$[-]$
$x$	Liquid ammonia concentration	$[-]$
$\tilde{x}$	Liquid molar ammonia concentration	$[-]$
$y$	Vapor ammonia concentration	$[-]$
$z$	Mass flow fraction	$[-]$

<b>Variables – Greek letters</b>			
$\alpha$	Void fraction		[ - ]
$\delta$	Thickness of the film		[m]
$\varepsilon$	Effectiveness		[ - ]
$\mu$	Dynamic viscosity		[kg.m <sup>-1</sup> .s <sup>-1</sup> ]
$\nu$	Kinematic viscosity		[m <sup>2</sup> .s <sup>-1</sup> ]
$\rho$	Density		[kg.m <sup>-3</sup> ]
$\sigma$	Surface tension		[kg.s <sup>-2</sup> ]
$\lambda$	Thermal conductivity		[W.m <sup>-1</sup> .K <sup>-1</sup> ]
$\lambda_p$	Head losses coefficient		[ - ]
$\theta$	Contact angle		[ ° ]
$\tau$	Shearing stress		[kg.s <sup>-2</sup> ]
$\Phi$	Two-phase multiplier		[ - ]
<b>Acronyms</b>			
<i>AC</i>	Absorption Chiller	<i>ER</i>	Effectiveness ratio
<i>AHR</i>	Adiabatic/Heated Ratio	<i>FG</i>	Flooded Generator
<i>AR</i>	Aspect Ratio	<i>FGS</i>	Flooded Generator System
<i>CEG</i>	Cumulative Energetic gains	<i>HTF</i>	Heat Transfer Fluid
<i>CG</i>	Combined generator	<i>NTU</i>	Number of Transfer Units
<i>COP</i>	Thermal Coefficient Of Performance	<i>PF</i>	Partly Flooded configuration
<i>COP<sub>Carnot</sub></i>	Carnot coefficient of performance	<i>PHE</i>	Plate Heat Exchanger
<i>COP<sub>el</sub></i>	Electrical coefficient of performance	<i>TES</i>	Total Energy Saved
<i>DOE</i>	Design Of Experiments	<i>UF</i>	Unflooded configuration
<b>Non-dimensional numbers</b>			
<i>Bo</i>	Bond number	<i>Re</i>	Reynolds number
<i>Fr</i>	Froude number	<i>Sc</i>	Schmidt number
<i>Ja</i>	Jakob number	<i>Sh</i>	Sherwood number
<i>Nu</i>	Nusselt number	<i>We</i>	Weber number
<i>Pr</i>	Prandtl number		
<b>Indices</b>			
<i>1</i>	Initial state	<i>mass</i>	Mass
<i>2</i>	State after transfers	<i>max</i>	Maximum
<i>2ph</i>	Two phases	<i>medium</i>	Heat rejection source (absorber)
<i>abs</i>	Absorption/absorber	<i>mic</i>	Microscopic contribution
<i>ad</i>	Adiabatic	<i>min</i>	Minimum
<i>amb</i>	Ambient	<i>mix</i>	Mixture
<i>C</i>	Heat transfer fluid	<i>nb</i>	Nucleate boiling
<i>crit</i>	Critical	<i>NH<sub>3</sub></i>	Ammonia
<i>cold</i>	Chilling source (evaporator)	<i>num</i>	Numerical
<i>cond</i>	Condenser	<i>ONB</i>	Onset of boiling
<i>eco</i>	Economizer	<i>out</i>	Outlet
<i>eq</i>	Equilibrium	<i>parti</i>	Partial
<i>ev</i>	Evaporator	<i>PS</i>	Poor solution
<i>exp</i>	Experimental	<i>rect</i>	Rectifier
<i>ext</i>	External	<i>RS</i>	Rich solution
<i>gen</i>	(Combined) generator	<i>sat</i>	Saturation
<i>H<sub>2</sub>O</i>	Water	<i>sen</i>	Sensible
<i>hot</i>	Heating source (generator)	<i>sp</i>	Species
<i>i</i>	Interface	<i>sub</i>	Sub-cooler
<i>id</i>	Ideal	<i>th</i>	Thermal
<i>in</i>	Inlet	<i>tot</i>	Total
<i>int</i>	Internal	<i>V / vap</i>	Vapor
<i>L</i>	Liquid / solution side	<i>V0</i>	Vapor only
<i>L0</i>	Liquid only	<i>w</i>	Wall
<i>mac</i>	Macroscopic contribution	<i>wett</i>	Wetting



# Part I: Introduction

*The first part of this manuscript is dedicated to the general introduction of the current PhD work. The global market of cooling capacity for air-conditioning is addressed, including data from reference studies. The technology of the absorption chiller investigated in this work, and more specifically the component that generates refrigerant vapor are introduced. Some studies focusing on the generator and conducted before this work are presented, along with their advances and limitations. Then, the rationale behind this study is described, and work that will follow as the next step is introduced.*



The main challenges in producing cold for air-conditioning are to reduce electricity consumption, heat emissions, and greenhouse gas emissions.

The reduction of fossil energy consumption is a crucial global objective for the coming years, in order to limit the effects of global warming. According to the *Communication "An EU Strategy on Heating and Cooling"* (2016), half of the energy consumed within the European Union is used for heating and cooling needs (i.e., approximately 546 Mtoe in 2012), and much of it is wasted. Overall, 45% of this energy is used in the residential sector, 37% in industry, and 18% in services. As shown in Figure 1.1, only one quarter of this energy that is used for heating and cooling is produced via low-carbon fuels. Buildings account for over 40% of the world's total primary energy use, which corresponds to 24% of greenhouse gas emissions. Making buildings more energy efficient by using a larger part of renewable energy is therefore a key issue (SHC annual report 2018).

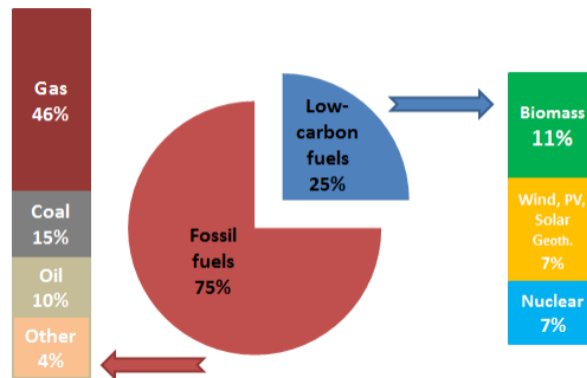


**Figure 1.1.** Primary energy for heating and cooling in the EU, 2012 (SHC annual report 2018).

For more than 15 years, the demand for air-conditioning has been increasing to offer more comfort during summer periods, and particularly during heat waves. Most of the air-cooling systems use vapor-compression thermodynamic cycles with mechanical compressors. The development of these systems has led to a significant increase in electricity consumption during summer, as well as an increase in outdoor temperature through the heat emissions they cause. The use of this technology is in fact a paradox: the higher the number of air conditioners installed in cities and the greater the heat generated in urban areas, the higher the outside temperature becomes. This rise in temperature results in a reduced chiller performance and an increase in air-conditioning demand. According to the IEA, without major efficiency improvements in cooling equipment, the electricity demand for cooling in buildings could more than triple by 2050.

One of the solutions to the problems related to air-conditioning development in urban zones could be the use of absorption refrigeration machines fed by waste heat or thermal solar energy via district heating during summer periods. The electrical consumption of these machines is significantly lower than that of conventional compression machines. Most of them use fluids with zero global warming potential. The thermal waste they cause can be stored in the ground through geothermal boreholes to be reused in winter. A feature of solar energy for cooling is the match in the time between solar radiation (supply) and demand. Expensive electricity during peak times can therefore be saved. Furthermore, solar thermal energy is outstanding for its ability to store solar heat and to shift it for cooling demand in the evenings and nights, while also keeping the remaining energy for morning cooling (Weiss and Spörk-Dür 2018).

The cumulated solar thermal capacity in operation by the end of 2017 for 95% of the solar thermal market worldwide was 472 GWth, almost 8 times more than the capacity in operation in 2000. The corresponding annual solar thermal energy yield in 2017 amounted to 388 TWh, which correlates to savings of 41.7 million tons of oil and 134.7 million tons of CO<sub>2</sub> (Weiss and Spörk-Dür 2018).

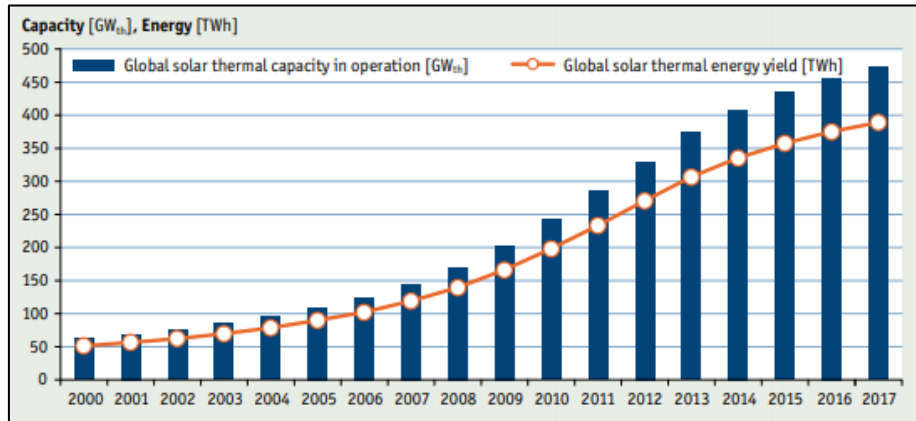


Figure 1.2. Global solar thermal capacity in operation and annual energy yields 2000-2017 (Weiss and Spörk-Dür 2018).

By the end of 2015, an estimated 1,350 solar cooling systems were installed worldwide (Weiss and Spörk-Dür 2018). Most of the solar cooling systems (84% in 2009) are sorption machines, among which the majority are absorption machines, chosen for their higher thermal performances (Stryi-Hipp 2016). Figure 1.3 shows the different sorts of cooling systems available. Most of them are used for refrigeration and air-conditioning, but also for heat production or for fatal heat recovery.

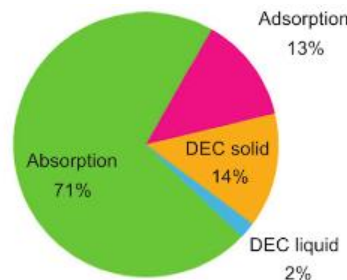


Figure 1.3. Market share of solar-driven sorption chillers, DEC, desiccant and evaporative cooling-2009 (Stryi-Hipp 2016).

In France, the mix market of cooling systems is shared as shown in Figure 1.4. However, today, air-conditioning and solar heating technologies are at a level of technological maturity that would correspond to a more developmental and demonstration stage. Several small and medium-sized companies are working on solutions to reduce the relatively high system costs, the space requirements, and the complexity of solar thermal-based cooling, especially for small-capacity (as domestic) systems (Weiss and Spörk-Dür 2018).

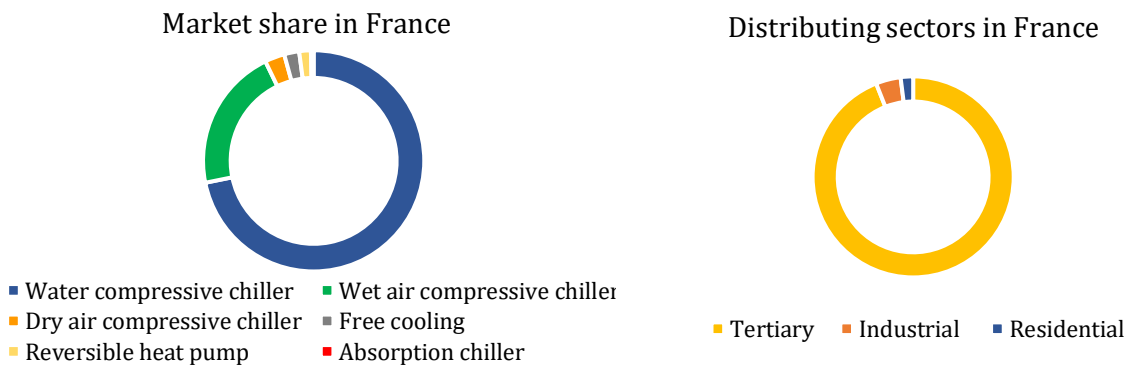
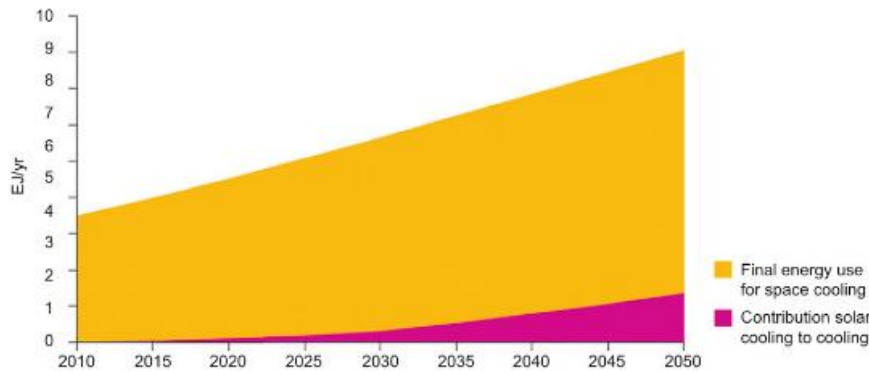


Figure 1.4. Cold energy mix market in France, 2018 (www.fedene.fr 2019).

The current sharp increase in air-conditioning requirements during summer periods translates to a very important developmental potential for the solar cooling market. The market potential for solar cooling by 2050 is estimated at approximately 417 TWh/a, which could be nearly 17% of the total energy use for cooling (Stryi-Hipp 2016). The global solar energy industry is expected to reach \$422 billion by 2022 from \$86 billion in 2015, growing nearly 24.2% between 2016 and 2022 (www.alliedmarketresearch.com 2019).



**Figure 1.5.** Technology roadmap for solar heating and cooling, share of solar cooling by 2050-IEA-2012 (Stryi-Hipp 2016).

By 2050 a worldwide capacity of 5 kWth per capita of solar thermal energy systems installed and a significant reduction in energy consumption to be achieved by using passive solar energy and daylighting are expected. The vision of the SHC (Solar Heating and Cooling program) is that 50% of low-temperature heating and cooling demands will be sustained by solar thermal energy (SHC annual report 2018).

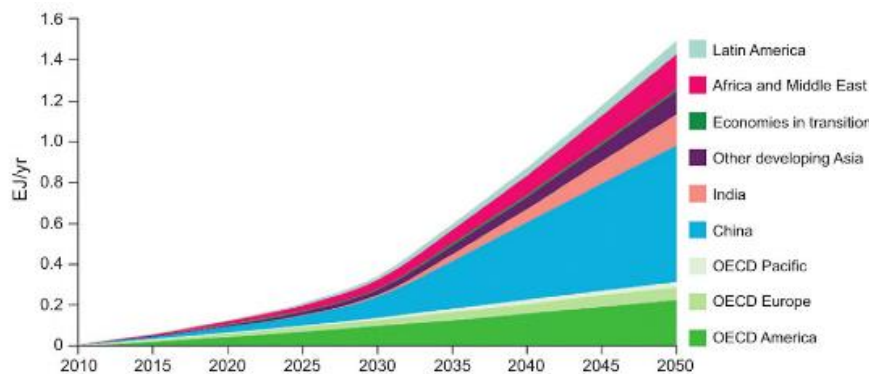


**Figure 1.6.** Technology roadmap for solar heating and cooling, Market Potential by 2050 International Energy Agency-2012 (Stryi-Hipp 2016).

Europe’s manufacturers report a rising demand for solar thermal cooling, and specifically for the niche market of sorption chillers (www.alliedmarketresearch.com 2019). This growth is attributed to many factors: Absorption machines differ from mechanical compression machines in their ability to compress the working fluid using absorption-desorption mechanisms that have low electricity consumption. The electrical demand for air-conditioning in a building can be cut by more than 80% compared with conventional HVAC equipment (Weiss and Spörk-Dür 2018; www.alliedmarketresearch.com 2019). Moreover, they are silent, adaptable, have an ease of integration into various industrial processes, and can reach a good performance coefficient when recovering fatal heat. According to (Stryi-Hipp 2016; Dincer and Rosen 2013), the costs for production and maintenance are moderate and they offer a long service life. These systems also have the ability to heat or cool on demand throughout the year.

Boosted by the new and renewed policies and initiatives at the local, state, and federal level, and by the need to reduce environmental pollution, sorption chillers will likely grow in the market of heating and cooling energy in the coming years (www.alliedmarketresearch.com 2019; DELOITTE 2019). For example, in Europe, their application is already promoted by the European F-gas regulation (Weiss and Spörk-Dür 2018).

Currently, 98% of absorption machines around the world function with  $\text{H}_2\text{O}$ -LiBr and only 2% with  $\text{NH}_3$ - $\text{H}_2\text{O}$ . Among these machines, 87% are located in Asia (mainly in Japan, China, and India), 11% are in North America, and only 2% in Europe.

The ammonia-water absorption machine was firstly developed by the French scientist Ferdinand Carré in 1858. His machine was used to manufacture ice for sale was presented at the World Exhibition in London in 1862. After a period of strong expansion, the interest in absorption machines declined because of the introduction and boost of vapor-compression technologies, which were more competitive thanks to low electricity prices (DELOITTE 2019; [www.europeana.eu](http://www.europeana.eu) 2019) and greater performance. Today, the interest in developing absorption machines is growing once again, since they offer an ecological replacement solution to the conventional compression systems and enable the recovery of industrial thermal waste.

Many studies of absorption machines were carried out during the last century. The authors investigated not only the performance of the system, but also its components and the different physical phenomena that occur in it. Special attention was paid to the absorbers that proved to be a critical component of the absorption machine, while few studies focused on generators. In the case of ammonia-water machines, the small volatility difference between the refrigerant and the absorbent leads to the presence of water traces in the vapor produced at the generator. This water affects the cycle performance and can even make it inoperative if the machine is aimed to negative refrigeration. The inability of the generator to deliver pure ammonia vapor is usually addressed by a rectifier placed at its outlet. Liquid separators are also required if flooded generators are used (Triché 2016). The implementation of such components affects the compactness and the performance of the machines. The development of a compact ammonia generator with sufficiently low water emission to avoid the use of a rectifier is an important key step in the development of compact and efficient machines.

A review of the literature on generators for ammonia-water machines was conducted at the beginning of the thesis, listing the main studies that were preliminary to this work.

(Fernandez-Seara et al. 2002) developed a differential mathematical model based on heat and mass transfer, and mass and energy balance equations, to simulate the distillation process in a packed column used as a rectifier in an ammonia-water absorption chiller. The column was composed of a rectifying section, supplied by a liquid reflux from the condenser, on top of a stripping section directly supplied by the solution. The ammonia vapor produced by the generator enters at the bottom and rises through the column, in counter-flow from the solution with which it interacts, increasing its concentration toward the top. The authors highlighted that a net molar flux is transferred at the interface, and that the liquid mass transfer resistance is negligible, while the vapor mass transfer coefficient has the most significant effect on the ammonia vapor concentration. At fixed geometric parameters and operating conditions, the optimal length of the rectifier section has to be much longer than the stripping section. Although this model is detailed, it described only the vapor purification process, and the concept was not tested in an absorption chiller.

(Fernandez-Seara and Sieres 2006) conducted a practical study on a single-stage ammonia-water absorption system with complete condensation by reflux, in order to highlight the crucial importance of the ammonia purification process in achieving an efficient and reliable system. It included a distillation column, composed of a rectifying section on the top over the column feed point, an adiabatic stripping section just below the feed point, and a heated generator section at the bottom. A model simulating the absorption chiller behavior made it possible to study the separation efficiency of the distillation column (based on Murphree efficiency) and the impact of the system operating conditions. The authors showed that for a distillation column, higher efficiencies in the stripping and rectifying sections result in higher ammonia vapor concentration, higher coefficient of performance (COP) of the system, higher pressures, and higher solution concentrations. The use of a stripping section had more effect on the system COP than the use of a rectifying section, which had more effect on the vapor concentration. In applications of low evaporation temperature, a purification process was required (otherwise, the COP would be too low, and the system operation would not be possible). However, in applications of high evaporation temperature, ammonia purification was not critical, but recommended, especially if the absorber temperature was high.

(Taboas et al. 2010) led an experimental study of a vertical brazed plate heat flooded generator for an ammonia–water absorption chiller supplied by solar energy or waste heat, at a low-temperature source. The machine operates with a [7–15bar] pressure range and a [0.42–0.62] ammonia concentration range. The mean vapor quality varies between 0.0 and 0.22, the heat flux varies from 20 to 50 kW.m<sup>-2</sup>, and the mass flow from 70 to 140 kg.m<sup>-2</sup>.s<sup>-1</sup>. This study determined the impact of these parameters on the saturated flow boiling heat transfer and on the associated frictional pressure drop of the ammonia–water solution. The boiling heat transfer coefficient depends on the mass flux. However, at high vapor qualities, the heat flux, the ammonia concentration, and the pressure influences are negligible. The pressure drop increases with the mass flux and with the vapor quality. This study helped understanding many parameters influences on each other in a plate heat generator. However, it was limited to the ammonia vapor generation and it did not relate to the purification.

(Determan and Garimella 2011) conducted an experimental and analytical study relating to the heat and mass transfer occurring in a microchannel ammonia–water generator designed for a small-capacity heat pump. This resulted in the conception of a highly compact component (178 mm, 178 mm, 0.508 m), with a heat load of 17.5 kW and a heat transfer coefficient varying between 388 and 617 W.m<sup>-2</sup>.K<sup>-1</sup>. This component was made of microchannel tubes placed in multiple square arrays, where the ammonia–water solution flows downward while the generated vapor, rising counter-current, is cooled by the solution and exits at a high ammonia concentration. Furthermore, the developed model simulated the heat and mass transfer of a crossflow well-mixed falling film over horizontal tubes and predicted the temperature, concentration, and mass flowrate profiles in the exchanger. This study followed previous work on the same component operating in absorber mode, showing the versatility of the concept. Although this concept proved to work, the transfers were limited by the wetted area ratio, which was between 25% and 69% of the tube arrays.

(Delahanty et al. 2015) developed two compact heat and mass exchangers, used as desorbers in a small-capacity ammonia–water absorption chiller. The exchangers included a desorber section, where the ammonia vapor generated rises counter-current from the solution flowing downward. The heat was supplied through a vertical microchannel array, the heat transfer fluid (HTF) flowing in counter-current mode compared to the solution. They also included an analyzer section in the middle of the component, where the solution is spread on the desorber section. A cooled rectifier section is placed over the analyzer section and condensates part of the vapor emitted by the generator. In the first concept, a falling-film configuration over vertical columns was developed. In the second one, the solution fell in a series of branched trays, where the pool boiling process prevails. A model simulating heat and mass transfer was developed, presenting the temperature and concentration profiles along the exchanger. This concept took advantage of the high heat transfer coefficients, allowing for a reduction in the component size and the production of a high-quality ammonia vapor, which induces lower rectification loads and lower operation costs. These concepts showed a definite advance in the development of compact desorption systems for small-capacity machines, through the ability of including the rectifier and the generator in a single component, and a scalability to fit various applications. However, the rectifier part needs to be cooled, which affects the cycle performance, and the design of the exchanger is quite complex.

(Keinath et al. 2015) carried out an experimental study with a 3.5-kW desorber for space-conditioning systems. The desorber consisted in a branched tray, designed as an array of alternating plates including microscale features enclosed between cover plates. An adiabatic analyzer and a solution-cooled rectifier were also integrated in the same component. A parametric analysis was made of the wide ranges of inlet operating conditions. The results showed that the vapor mass flowrate generated increases with the increase in the HTF temperature, in the mass flowrate, as well as with the increase in the solution mass flowrate. As compared to the desorber of (Determan and Garimella 2011), construction costs were reduced and implementation potential was improved. Limits of vapor generation were found at the highest HTF temperature (190°C), with flow instabilities due to flooding. Again, the component developed was compact, combining generation and purification of the vapor; however, the work focused on a microchannel falling-film concept.

(Staedter and Garimella 2018) developed a compact standalone 7-kW cooling capacity, residential-scale ammonia–water absorption chiller, composed of two monolithic blocks integrating microscale heat and

mass plate exchangers. They also developed segmented models for each component, in order to select the size depending on the thermodynamic properties simulated. The number of channels helped to specify the overall cross-sectional area for the fluid flow. The vapor generation unit includes a desorber, an analyzer, and a rectifier part. Its design is based on the previous work of (Delahanty et al. 2015) and was enlarged to obtain higher vapor generation rates (size: 400 mm x 250 mm x 130 mm). This study highlighted the ability to build highly compact systems as absorption chillers, with plate heat and mass exchangers. The whole system provided a COP of 0.44, close to the initially designed capacity. The gap between predicted COP and measured COP could be explained by the non-optimal operation of the desorber-analyzer-rectifier block. Thus, further development of this component is needed, to reduce its size and weight and to improve the global system COP.

The use of a separate generator and rectifier increases the volume of the ammonia-water absorption chiller as well as the investment and operation costs of the machine. Various designs of generator-rectifier assembly able to produce a sufficient quantity of high-quality ammonia vapor for ammonia-water absorption chillers are proposed in the literature. Efficient systems such as distillation columns exist but are not very compact. Others, such as plate exchangers, are characterized by high compactness but their performance is currently limited in terms of ammonia vapor quality and in the impact on the machine COP and cooling capacity. Furthermore, the combination of generator-rectifier sections in one unique compact falling-film and plate heat exchanger has not been studied to date.

The objective of this work is to develop a new compact combined generator involving production and purification of ammonia vapor designed for an  $\text{NH}_3\text{-H}_2\text{O}$  absorption chiller. The falling-film and plate heat exchanger technology is chosen in view of its potential. Indeed, falling film makes it possible, on one hand, to increase the density of exchange surface per unit of volume, and on the other hand, to combine the rectification process within the same component. To limit the water content in the ammonia vapor generated, the counter-flow falling-film configuration is preferred. Therefore, at the top part of the generator, which is not warmed, the vapor emitted in the low part comes into contact with the solution film and is partially reabsorbed.

The development of this combined generator design requires the use of an adapted numerical model, able to simulate the heat and mass transfer occurring in the solution-vapor counter-current flow configuration.

Various heat and mass transfer modeling along falling film exists in the literature.

(Goel and Goswami 2005) investigated numerically the coupled heat and mass transfer processes occurring in a counter-current ammonia-water falling-film absorber. They found that the liquid mass transfer resistance controls the absorption process, while the liquid heat transfer resistance is negligible. A parametric analysis underlined that the absorption rate increases with the solution and coolant inlet temperature decrease and with the coolant mass flowrate increase. This model enabled a precise prediction of the behavior of a counter-current falling-film absorber, by detailing the thermophysical phenomenon; however, the process of desorption was not investigated.

In the framework of her PhD thesis, (Triché 2016) led an analytical and experimental study on the heat and mass transfer occurring in the absorber of a small-capacity ammonia-water absorption chiller. She developed a model detailing the interactions between the solution and the vapor inside a falling-film and plate absorber, in the co-current flow configuration. The model enabled the prediction of the absorber performance, such as the absorption efficiency, and the power supplied. The absorber was built and was integrated into a 5-kW cold capacity absorption chiller, and its impact on the global machine performance (COP and cooling capacity) for various operating conditions was studied. This work underlined that understanding the absorption and desorption processes is crucial for the improvement of the absorption chiller performance.

As mentioned above, the wetted area ratio is a key point of falling-film exchangers. Indeed, the distribution and the wetting properties of the liquid film over the surface of the plate are crucial for efficient heat and mass transfer. (Lu et al. 2017) studied experimentally the wetting behavior of a falling film on a vertical flat plate. They found that the minimum wetting rate for full surface coverage was the same for two different

liquid distributors. The influence of the physical properties of water and water-glycerol mixtures on the minimum wetting rate and on the mean film thickness was investigated. The authors showed that the minimum wetting rate decreases when the falling-film regime tends to be wavy, and that the viscosity of the solution has a significant effect on the falling-film behavior. An equation predicting the mean film thickness and including the characteristic length was established. This study helped in understanding the behavior of a falling film on a vertical plate; however, it did not present the case of an ammonia–water solution. Moreover, this work did not take into account the influence of thermal exchanges.

Current falling-film models simulate the coupled heat and mass transfer of solution–vapor co-current flow configurations. However, these models do not take into account the wettability problems and the potential development of boiling. Therefore, one of the objectives of this thesis is to develop a model able to simulate heat and mass transfer of solution–vapor counter-current flow configurations, capable of taking into account different phenomena limiting the performances of the falling-film exchangers.

This PhD work was considered a continuity of the studies within the framework of the project Carnot Energy of the Future TRICYCLE (collaboration between CEA and LOCIE\*). Based on the technological choices made for developments realized during the last 7 years in the CEA-INES, a focus on the vapor generation in an absorption chiller using ammonia–water as a working fluid was chosen for this study.

The manuscript is divided into five parts.

*Part I* introduces the PhD work in its context and defines the main objectives.

*Part II* presents the state of the art in absorption machines, generator and rectifier technologies, distribution systems, and physical phenomena involved in an ammonia–water plate heat exchanger. Then, the approach of this work is presented, comprising two parts.

*Part III* concerns the design of the combined generator, the assessment of its performance, as well as that of the absorption machine for which it was designed.

The objective of the first chapter is to simulate the performance of a combined generator designed to be integrated in an NH<sub>3</sub>–H<sub>2</sub>O absorption chiller. The absorption and desorption phenomena occurring inside a falling-film and plate heat exchanger are studied. This modeling went through the development of the heat and mass transfer correlations, of the equilibrium equations at the solution–vapor interface, as well as of the mass, thermal, and species balances. Co-current and counter-current configurations are simulated and compared. Finally, the impact of the inlet variables and the impact of the geometry of the combined generator on its own performance are investigated, in order to determine the appropriate inlet conditions and a compact design that will enable the production of high-quality ammonia vapor at low cost. To this end, a parametric analysis is performed on the many inlet variables and on the plate geometry and number (Wirtz et al. 2022a).

The purpose of the second chapter is to characterize numerically the impact of the combined generator on the performance of an NH<sub>3</sub>–H<sub>2</sub>O absorption chiller dedicated to air-conditioning. A numerical model of an NH<sub>3</sub>–H<sub>2</sub>O absorption chiller is first developed in order to determine its performance, in particular the thermal COP and cooling capacity. The modeling is validated using experimental data. Then, the unique combined generator developed in *Chapter I* numerically replaces the flooded generator-separators-rectifier assembly initially implemented in the machine. The combined generator performance is taken into account by considering the mass, thermal, and species effectiveness, which allow us to determine the outlet values. Finally, the impact of the integration of the combined generator on the absorption chiller performance is investigated. The influence of the operating conditions, such as the temperatures and the mass flowrates of both the solution and HTF, on the absorption chiller performance is analyzed (Wirtz et al. 2022b).

*Part IV* presents the experimental characterization of the performance of the combined generator and of the machine in which it was integrated.

The third chapter aims to characterize experimentally the combined generator and its impact on the performance of the  $\text{NH}_3\text{-H}_2\text{O}$  absorption chiller for two different operating modes: partly flooded and unflooded. First, the impact of the HTF mass flowrate and solution subcooling at the combined generator inlet on the COP and cooling capacity of the absorption chiller is examined. Two parametric studies are conducted, with the combined generator partly flooded and unflooded. Then, the impact of the heating, chilling, and heat rejection source temperatures, as well as the impact of the solution mass flowrate, on the performance of the absorption chiller is studied through a design of experiments. Two correlation forms are used to describe the combined generator performance. Moreover, the performance of the machine equipped with the initial generator-separators-rectifier assembly and equipped with the combined generator is compared thanks to the Carnot-COP approach. The influence of the solution mass flowrate on the COP and cooling capacity is investigated. Finally, a case study is carried out on a tertiary building to compare the performance of the different machine configurations and the associated energy gains. The required cooling capacity is determined for the operating periods, and the solution mass flowrate and heating temperature influences are investigated (Wirtz et al. 2022c). The design and operation of the combined generator and of its distribution-rectification system are detailed in the patents (Wirtz et al. 2021a, 2021b).

The purpose of the fourth chapter is to provide a comparative analysis of the performance of a flooded generator and of the combined generator operating with two modes, as a function of the operating conditions of the  $\text{NH}_3\text{-H}_2\text{O}$  absorption chiller in which they are integrated. A numerical model simulating the nucleate and convective boiling mechanisms occurring in a plate heat exchanger is developed. This took into account the establishment of heat and mass transfer correlations from the literature, as well as mass, thermal, and energy balances. The model is validated using the experimental data. The pressure drop and the heat transfer contributions along the plates are examined (Wirtz et al. 2022d). Then, the combined generator model presented in *Chapter I* is compared with the experimental results. New physical phenomena are taken into account to improve its predictability such as the impact of the wettability of the plates and the boiling occurrence (Wirtz et al. 2022e). Finally, the impact of the inlet operating parameters of the generators on their own performances is investigated in order to define the operating conditions of the machine allowing them to operate in an optimal way. To this end, the mass, thermal, and species effectiveness of each generator is analyzed.

*Part V* presents the conclusion and the perspectives of this work.

## References

- [www.alliedmarketresearch.com/solar-energy-market](http://www.alliedmarketresearch.com/solar-energy-market) (2019)
- [www.europeana.eu](http://www.europeana.eu) (2019), Biography of F. Carré
- [www.fedene.fr](http://www.fedene.fr) (2019)
- Communication from the Commission to the European Parliament, the Council, the European Economic and Social Committee and the Committee of the Regions, (February 2016), “An EU Strategy on Heating and Cooling”
- Determan M.D., Garimella S., (2011), “Ammonia–water desorption heat and mass transfer in microchannel devices”, *International Journal of Refrigeration* 34, 1197–1208
- Fernandez–Seara J., Sieres J., Vazquez M., (2002), “Simultaneous heat and mass transfer of a packed distillation column for ammonia–water absorption refrigeration system”, *International Journal of Thermal Sciences* 41, 927–935
- Delahanty J.C., Garimella S., Garrabrant M., (2015), “Design of compact microscale geometries for ammonia–water desorption”, *Science and Technology for the Built Environment* 21, 365–374
- DELOITTE (2019), Renewable energy industry review
- Dincer I., Rosen M.A., (2013), “Exergy, energy, environment and sustainable development”, Second edition Elsevier
- Fernandez–Seara J., Sieres J., (2006), “The importance of the ammonia purification process in ammonia–water absorption systems”, *Energy Conversion and Management* 47, 1975–1987
- Goel N., Goswami Y., (2005), “Analysis of a counter-current vapor flow absorber”, *International Journal of Heat and Mass Transfer* 48, 1283–1292
- International Energy Agency Report, (2018), “The Future of Cooling, Opportunities for energy-efficient air conditioning”, *OECD/IEA*
- Keinath C.M., Hoysall D., Delahanty J.C., Determan M.D., Garimella S., (2015), “Experimental assessment of a compact branched tray generator for ammonia–water desorption”, *Science and Technology for the Built Environment* 21, 348–356
- Lu Y., Stehmann F., Yuan S., Scholl S., (2017), “Falling-film on a vertical plate–Influence of liquid distribution and fluid properties on wetting behavior”, *Applied Thermal Engineering* 123, 1386–1395
- Solar Heating and Cooling Technology Collaboration Programme, (March 2018), *Annual Report 2017*, SHC
- Staedter M.A., Garimella S., (2018), “Development of a micro-scale heat exchanger based, residential capacity ammonia–water absorption chiller”, *International Journal of Refrigeration* 89, 93–103
- Stryi–Hipp G., (2016), “Renewable Heating and Cooling Technologies and Applications”, *Woodhead publishing series in energy number 89*
- Taboas F., Vallès M., Bourouis M., Coronas A., (2010), “Flow boiling heat transfer of ammonia/water mixture in a plate heat exchanger”, *International Journal of Refrigeration* 33, 695–705
- Triché D., (2016), “Étude numérique et expérimentale des transferts couplés de masse et de chaleur dans l’absorbeur d’une machine à absorption ammoniac-eau”, *Université de Grenoble Alpes*
- Weiss W., Spörk–Dür M., (2018 Edition), “Solar Heat Worldwide–Global Market Development and Trends in 2017, Detailed market figures 2016”
- Wirtz M., Boudéhenn F., Phan H.T., Stutz B., (2021a), “Générateur comprenant une fonction de rectification, une machine à absorption comprenant ledit générateur et un procédé de production de vapeur de fluide frigorigène par ledit générateur”, *European patent EP 3 885 672 A1*

- Wirtz M., Chandez B., Phan H.T., Stutz B., (2021b), “Dispositif de rectification comprenant un rectifieur et un dispositif de distribution, et machine à absorption comprenant ledit dispositif de rectification”, *European patent EP 3 885 673 A1*
- Wirtz M., Stutz B., Phan H.T., Boudéhenn F., (2022a), “Numerical modeling of falling-film plate generator and rectifier designed for NH<sub>3</sub>-H<sub>2</sub>O absorption machine”, *Heat and Mass Transfer* 58, 431-446
- Wirtz M., Stutz B., Phan H.T., Boudehenn F., (Submission process 2022b) “Numerical studies of an NH<sub>3</sub>-H<sub>2</sub>O absorption chiller containing a novel falling-film desorber, characterization through its efficiencies”, *Applied Thermal Engineering*
- Wirtz M., Stutz B., Phan H.T., Boudéhenn F., (Submission process 2022c) “Experimental study of the impact of a combined generator behavior on NH<sub>3</sub>-H<sub>2</sub>O absorption chiller performances”, *International Journal of Refrigeration*
- Wirtz M., Stutz B., Phan H.T., Boudéhenn F., (Submission process 2022d) “Characterization and modeling of a flooded generator for small capacity NH<sub>3</sub>-H<sub>2</sub>O absorption chillers.”, *Heat and Mass Transfer*
- Wirtz M., Stutz B., Phan H.T., Boudéhenn F., (Submission process 2022e) “Behavior and performances of a combined generator with two operating modes integrated in an NH<sub>3</sub>-H<sub>2</sub>O absorption chiller (numerical model and experiments)”, *International Journal of Heat and Mass Transfer*





## Part II: State of the art

*The second part of this manuscript is dedicated to the state of the art of absorption chillers, and focuses particularly on the vapor generation and purification components. First, the description of an absorption chiller, with its main components, its operation, its performance evaluation, and the choice of the working pair is presented. In the second section, the review focuses on the vapor generation and purification components. Their roles are investigated through the review of various technologies and models developed in the literature. Then, the main role of the fluid distribution in the generator is introduced through the analysis of various distribution systems. Finally, the last section of the state of the art introduces the physical processes occurring in the falling film of the generator, in particular the heat and mass transfer involved and the dynamics of the flows, including the main correlations from the literature.*



## I. Absorption chiller operation and performance

Absorption and desorption processes describe the ability of a liquid (the sorbent) to catch or release vapor (the refrigerant) whose composition differs from that of the liquid. Under certain conditions, liquid and vapor can be at equilibrium. Absorption and desorption involve exothermic and endothermic reactions that modify the thermodynamic equilibrium and the diffusion processes within the liquid and the vapor phases.

### I.1. Absorption chiller operation

An absorption chiller is the combination of two Rankine cycles. It uses a pair of fluids of different volatility: an absorbent (the fluid with the lowest volatility) and a refrigerant (with the highest volatility). These fluids can be in liquid or vapor phase depending on the pressure, temperature, and concentration. At the evaporator level, the liquid refrigerant extracts heat from a cold source to evaporate. This corresponds to the cooling capacity. At the condenser level, heat is released by the refrigerant vapor to condensate. The working pair interacts through the absorption and desorption processes. The working cycle involves a thermochemical compression driven by a heat source (as waste heat, solar thermal energy etc.). The electricity supply required is located at the level of the solution pump. The electricity consumption is very low compared to that of a classic compression system operating in similar conditions (Triché 2016).

Schemes of the general principle of a single-stage absorption chiller are presented in Figure 2.1 and in Figure 2.2.

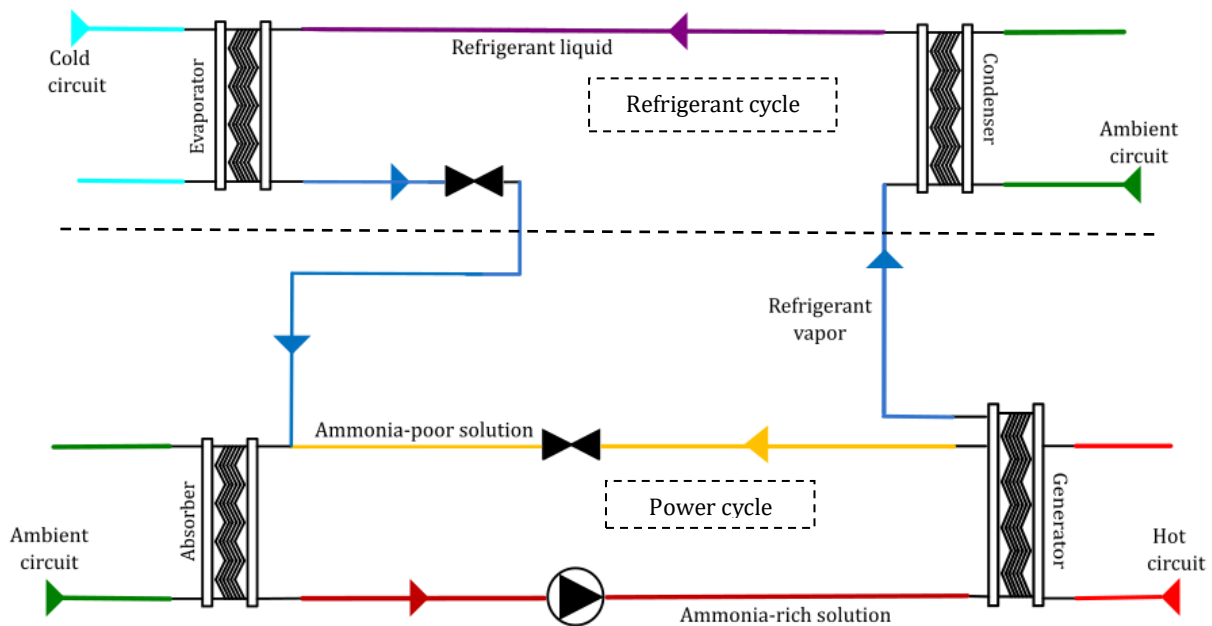


**Figure 2.1.** Schematic representation of the two Rankine thermodynamic cycles with external energy sources.

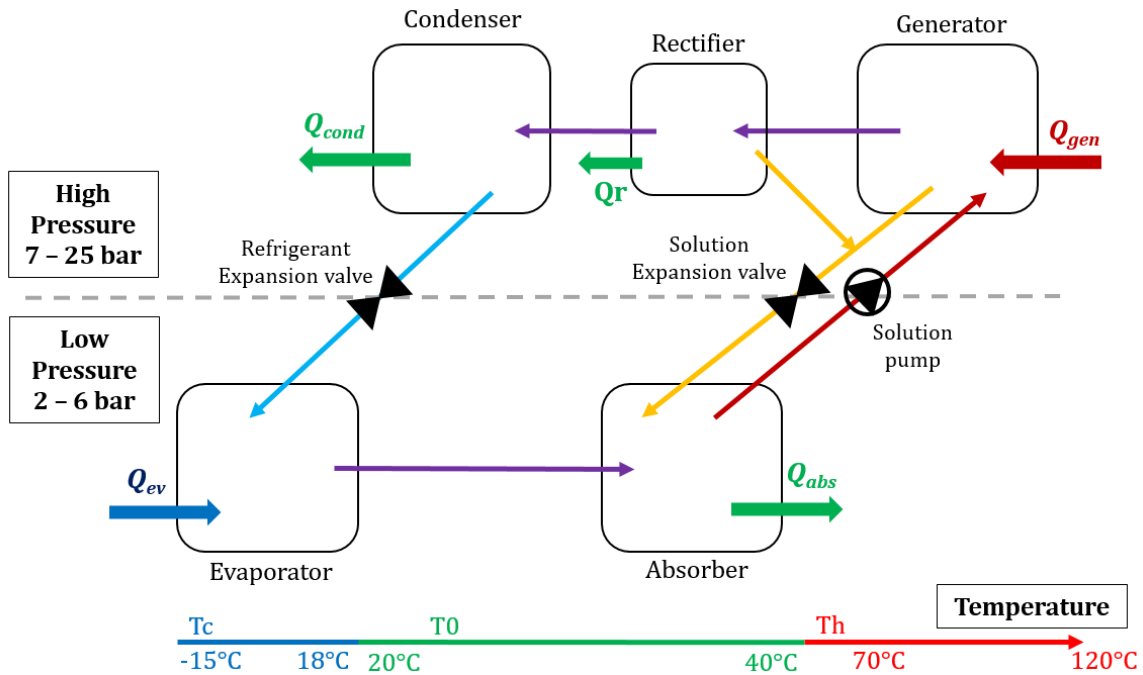


Figure 2.2. Schematic view of a single-stage absorption chiller.

Four main components make up the absorption chiller: the absorber, the generator, the evaporator, and the condenser.

- ✦ **Evaporator:** The liquid-phase refrigerant enters in the evaporator. A cold heat transfer fluid (HTF) flows into an external circuit through the evaporator. The refrigerant takes the heat from the cold source to be evaporated: This is the cooling capacity of the absorption machine ( $Q_{ev}$ ). After evaporation, the refrigerant circulates to the absorber. The evaporator is at the low-pressure level of the system.
- ✦ **Absorber:** The poor solution composed of the sorbent and a low concentration of the refrigerant (yellow parts in Figures 2.1 and 2.2), enters the absorber. The poor solution absorbs the refrigerant vapor coming from the evaporator, and becomes a rich solution, close to the refrigerant saturated condition. This rich solution flows to the generator. The absorption process occurs at the low-pressure level, and releases an amount of heat ( $Q_{abs}$ ) to the ambient air or to an external cooling circuit.
- ✦ **Generator:** An HTF flowing through the generator heats the rich solution coming from the absorber (red parts in Figure 2.1 and 2.2). Thanks to this heat, the rich solution desorbs the refrigerant vapor, and the resultant poor solution flows back to the absorber. The desorption process takes place at the high-pressure level, and requires a quantity of heat ( $Q_{gen}$ ). The refrigerant vapor produced circulates to the condenser.
- ✦ **Condenser:** The refrigerant vapor coming from the generator is cooled by the ambient air or by an external fluid to be condensed and become liquid. The liquid refrigerant passes through an expansion valve to decrease the pressure before entering the evaporator. The condenser is at the high-pressure level and releases a quantity of heat ( $Q_{cond}$ ).

In order to allow the refrigerant fluid, the poor solution, and the rich solution to flow from one component, which works at a high pressure, to another at low pressure and conversely, two expansion valves and a pump are needed in the system. They can also be used as regulation components of the machine. Some other components can be added in order to enhance the performance of the absorption chiller.

- ✦ **Rectifier:** For ammonia–water absorption machines, the use of a rectifier enables the elimination of some of the absorbent (water) vapor traces remaining in the refrigerant (ammonia) vapor at the outlet of the generator. Indeed, pure refrigerant vapor is needed for a better performance of the system. The use of the rectifier will be detailed in *Sect. II*.
- ✦ **Sub-cooler:** Located between the evaporator and the condenser, this component cools the refrigerant leaving the condenser, using the cooler vapor exiting the evaporator. At the same time, it pre-heats the vapor entering the absorber (Herold et al. 2016). It allows the quantity of liquid residue at the evaporator outlet to be decreased.

- ✦ *Internal heat exchanger*: Located between the absorber and the generator, the internal heat exchanger allows the rich solution that flows to the generator to be pre-heated, thanks to the heat of the poor solution returning to the absorber. This saves some energy needed to pre-heat the rich solution before desorption.

## I.2. Absorption chiller performance

### I.2.1. Main coefficients of performance

The absorption chiller produces cold, thanks to a heat supply at the generator level. The only need for external electrical work is to run the solution pump between the generator and the absorber.

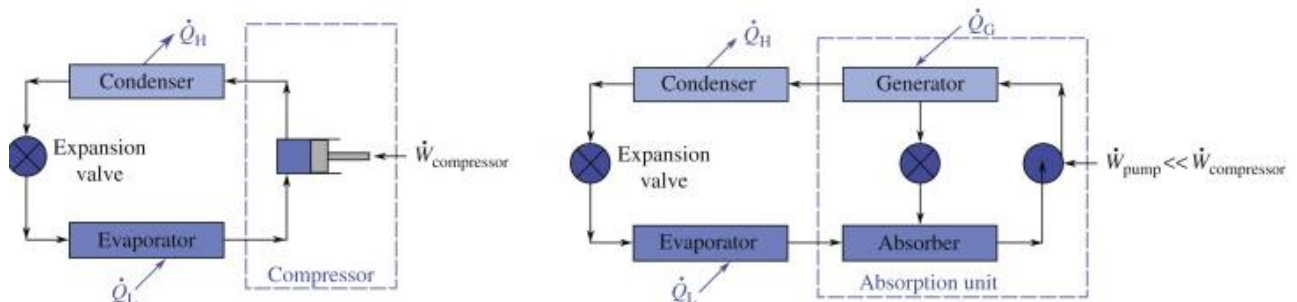


**Figure 2.3.** Compression and absorption refrigeration machines (Balmer 2011).

The thermal coefficient of performance (COP) quantifies the conversion efficiency of the energy consumed by the chiller in cold at the evaporator. For an absorption chiller, it is defined as:

$$COP = \frac{\text{Cooling capacity at the evaporator outlet}}{\text{Input heat rate at the generator} + \text{input power at the pump}} \quad (2.1)$$

The electrical COP makes it possible to quantify the conversion efficiency of the electrical energy consumed by the absorption chiller.

$$COP_{el} = \frac{\text{Refrigerating power produced}}{\text{Electrical power consumed}} = \frac{\text{Cooling capacity at the evaporator outlet}}{\text{Input power at the pump}} \quad (2.2)$$

Figure 2.4 presents the electrical COP of many single-stage absorption chillers as a function of their cooling power. According to the CEA internal database, which integrates around 600 single-effect machines references, it appears that the ratio quickly surpasses 100, which means that these machines produce 100 times more refrigeration power than what they consume in electrical power.

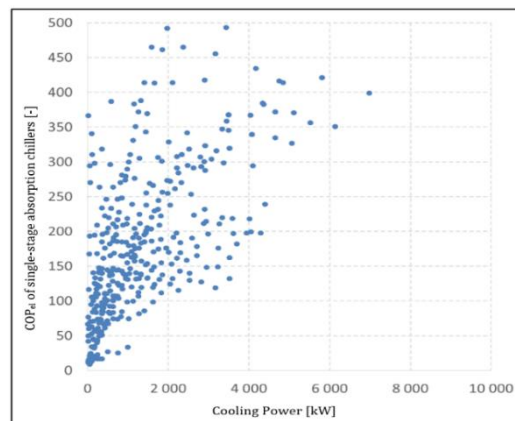


**Figure 2.4.**  $COP_{el}$  depending on refrigerating power for over 600 single-effect absorption machines references (CEA database).

According to manufacturers, most of the time, the thermal COP of a single-stage absorption chiller is between 0.6 and 0.7, but it depends on the temperature of the external sources. The variations in this temperature are highlighted by the Carnot-COP, which can also characterize the absorption chiller performance, by quantifying the performance degradation due to the system irreversibility.

The  $COP_{carnot}$  represents the ideal performance of a machine, i.e., a system that works without irreversibility. The system studied here works with three main sources, each one at a specific temperature, which exchange thermal power with one another. Neglecting the work at the pump, the first principle of thermodynamics allows us to write:

$$Q_{cold} + Q_{medium} + Q_{hot} = 0 \quad (2.3)$$

Assuming that the system is completely reversible and the heat exchanges are at the constant temperature of the three main sources, the second principle of thermodynamics can be written as:

$$\frac{Q_{cold}}{T_{cold}} + \frac{Q_{int}}{T_{medium}} + \frac{Q_{hot}}{T_{hot}} = 0 \quad (2.4)$$

Then,

$$COP_{Carnot} = \frac{T_{hot} - T_{medium}}{T_{medium} - T_{cold}} \cdot \frac{T_{cold}}{T_{hot}} \quad (2.5)$$

This coefficient can be considered as the combination of two yields: the COP of a refrigerating Carnot machine, which produces cold at  $T_{cold}$  and releases heat at  $T_{medium}$ , combined with the COP of a Carnot motor that works between  $T_{medium}$  and  $T_{hot}$ . Therefore, it is noted that  $COP_{carnot}$  increases when  $T_{cold}$  increases, when  $T_{hot}$  increases, and when  $T_{medium}$  decreases.

Figure 2.5 presents the evolution of the  $COP$  as a function of the  $COP_{Carnot}$  for various known CEA machines. The  $COP$  values given by constructors [0.6–0.7] are almost the maximal possible values. Their nominal zone of functioning is only between 3 and 5 of  $COP_{Carnot}$ . The seasonal average values are lower than the prescribed values. The external temperatures also influence the cooling power of an absorption chiller.

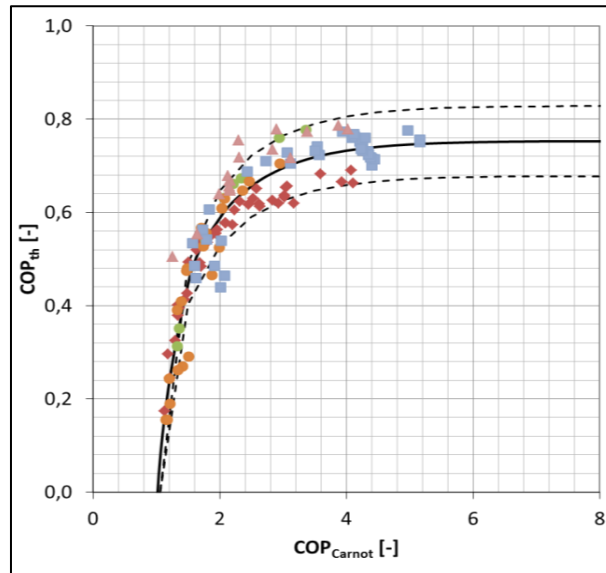


**Figure 2.5.**  $COP_{th}$  depending on  $COP_{Carnot}$  for single-effect absorption machines references (CEA database).

The impact of the external-source temperatures and the various factors that lead to irreversibility accentuate the importance of a suitable design, allowing the absorption chiller to operate in the best conditions. The performance of the generator can also be predicted, for example, with the mass efficiency.

### I.3. Working fluids review and selection

#### I.3.1. General working-fluid review

For an absorption machine, the choice of the working-fluid pair is crucial, since all the operating parameter ranges and the system performance depend on their chemical and thermodynamic properties.

The main selection criteria are the following (Triché 2016; Srihirin et al. 2011; Sun et al. 2012):

- ✦ The working fluids should be miscible within the operating temperature and pressure range of the cycle;
- ✦ The gap between the pure refrigerant and the mixture boiling point has to be the widest possible, then the refrigerant can vaporize alone;
- ✦ The latent heat of vaporization of the refrigerant has to be high, then the work supplied to the cycle for its operation is lower;
- ✦ Favorable properties in terms of heat and mass transfer: viscosity, thermal conductivity, and diffusion coefficient;
- ✦ The fluids are preferred to be non-corrosive, non-toxic, environmentally clean, and low-cost.

According to (Marcriss et al. 1988), around 40 refrigerant fluids and about 200 absorbent fluids can be coupled. Many of them work with  $\text{NH}_3$ ,  $\text{H}_2\text{O}$ ,  $\text{LiBr}$ , halogenated hydrocarbon, and some alcohol derivatives. (Sun et al. 2012) made a review of many mixtures and compiled their operating ranges and specificities. The most commonly used working-fluid pairs are  $\text{NH}_3\text{-H}_2\text{O}$  and  $\text{H}_2\text{O-LiBr}$ . Their main advantages and drawbacks as compared to other refrigerant fluids are presented in Table 2.1 (Triché 2016; Srihirin et al. 2011; Sun et al. 2012).

Advantages	Drawbacks
Low viscosity High refrigerant-absorbent affinity Not noxious for the ozone layer	Corrosion High volatility

**Table 2.1.** Advantages and drawbacks of  $\text{NH}_3\text{-H}_2\text{O}$  and  $\text{H}_2\text{O-LiBr}$  pairs as compared to other refrigerant fluids.

Two main advantages of the  $\text{H}_2\text{O-LiBr}$  pair are that  $\text{LiBr}$  is a non-volatile absorbent, and the heat of vaporization of water is high,  $2265 \text{ kJ.kg}^{-1}$  at boiling point (1.013 bar;  $100^\circ\text{C}$ ). This pair has a high COP and is currently the most widely used on the absorption machines market. Nevertheless, the refrigerant ( $\text{H}_2\text{O}$ ) freezes at  $0^\circ\text{C}$ , which limits the use of the machine in a narrow temperature range, and makes negative cooling capacity impossible.  $\text{LiBr}$  is also a corrosive component, and is more expensive than  $\text{NH}_3$ . Furthermore, it has limitations in operating in hot environment ( $> 35^\circ\text{C}$ ) due to crystallization.

The  $\text{NH}_3\text{-H}_2\text{O}$  pair can be used for low temperature applications, since the refrigerant ( $\text{NH}_3$ ) freezes at  $-77.7^\circ\text{C}$  and its heat of vaporization is high,  $1369 \text{ kJ.kg}^{-1}$  at boiling point (1.013 bar;  $-33.3^\circ\text{C}$ ). However,  $\text{NH}_3$  is also a toxic and corrosive component, and a major limitation is the high volatility of this pair, due to the low gap in vapor pressure between the two components (Triché 2016; Herold et al. 2016; Kherris 2008).

#### I.3.2. Working-fluid selection

In the continuity of the development strategy in CEA, the  $\text{NH}_3\text{-H}_2\text{O}$  pair is chosen for its physical properties, its temperatures operating range (negative refrigeration and hot ambiance), as well as its high-pressure range operation. An  $\text{NH}_3\text{-H}_2\text{O}$  absorption chiller prototype is already implemented in the laboratory and one of the goals of this PhD work is to investigate the desorption processes happening inside the generator and their impacts on the global chiller performance, using the ammonia-water working-fluid pair (Triché 2016).

### I.4.3. Ammonia–water pair properties

As shown by (Lima et al. 2021) and reported in Table 2.2, the ammonia–water pair can be used for a large range of temperatures and pressures.

Properties	Water	Ammonia
Freezing point	0 °C	-77.7 °C
Boiling point	100°C	-33.35 °C
Temperature operating range	-60°C / +377°C	
Pressure range	[0–400] bar	

**Table 2.2.** Thermo-physical properties of ammonia and water.

NH<sub>3</sub>–H<sub>2</sub>O absorption chillers are of particular interest for refrigerating areas with a high heat rate. Their advantages and drawbacks as compared to the H<sub>2</sub>O–LiBr pair are listed in Table 2.3 (Triché 2016; Srikhirin et al. 2011; Sun et al. 2012).

Advantages	Drawbacks
No solid phase possible	Toxicity
Attractive compactness	High volatility
Favorable functioning pressure	Rectification needed
Low cost	

**Table 2.3.** Advantages and drawbacks of NH<sub>3</sub>–H<sub>2</sub>O vs. H<sub>2</sub>O–LiBr absorption systems.

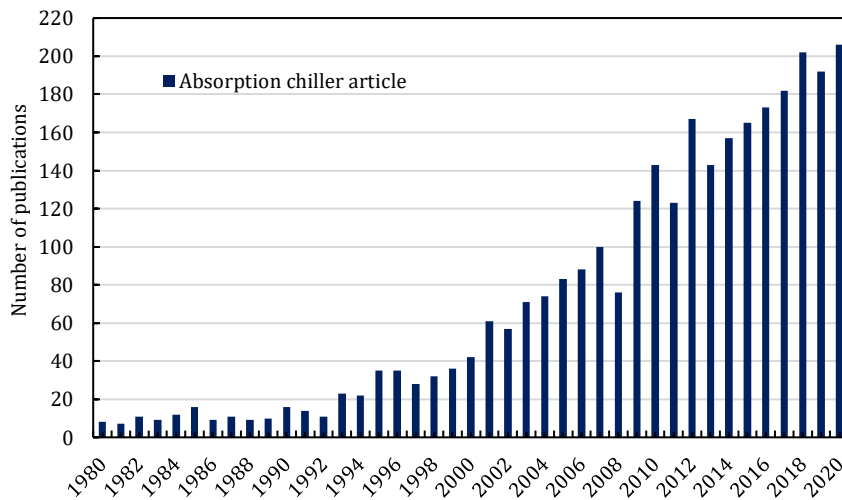
The thermodynamic cycle of NH<sub>3</sub>–H<sub>2</sub>O systems can work at high pressures, which is favorable to the optimization of the internal heat and mass transfer, the reduction in fluid quantity, the limitation of pressure drops, and to a compact design of the machine.

The main default of this working-fluid pair lies in the low gap of volatility between the absorbent fluid and the coolant. Indeed, a small part of water can be generated with the ammonia vapor. In order to purify the refrigerant, a rectifier has to be used at the outlet of the generator, to eliminate the tracks of water in ammonia vapor. Other features of ammonia are its corrosiveness, which limits the choice of compatible material, and its toxicity, which means that the absorption chiller must respect environmental regulations such as *Standard NF-EN 378-1* (AFNOR 2016).

### I.4. Studies of absorption chillers

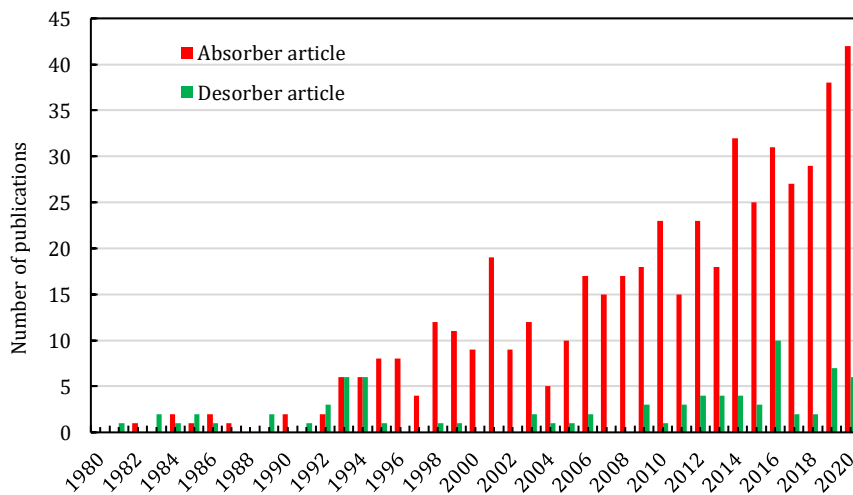
In the first section, the operation of an absorption chiller with its main components was detailed, and the choice of the working-fluid pair was explained. To investigate the performance of the absorption chiller, two main components are focused on: the absorber and the generator. Concerning the absorber, many publications in the literature have studied the different types of technology and performance, as well as the impact of various parameters such as mass flowrate, temperature, and pressure on the absorption chiller operation, as for the falling-film absorber developed in the CEA Laboratory by (Triché 2016).

Figure 2.6 shows the number of publications on the topic “absorption chillers” over the past 40 years.



**Figure 2.6.** Number of publications related to absorption chiller per year according to Scopus website (2021).

Figure 2.7 shows the number of these publications dealing with the topic of “absorber” and “desorber”.



**Figure 2.7.** Number of publications related to “Absorption chiller” and “absorber” or “desorber”, Scopus website (2021).

The study of the desorption process in an absorption chiller remains a relatively new topic that needs further investigations. Each year over the past 20 years, only 0–6% of publications on absorption chillers were related to the desorption process, or directly to the desorber component. However, according to (Mittermaier and Ziegler 2015) the desorber is the more restrictive component in an absorption cycle. For example, the pressure in the condenser and desorber is directly linked to the efficiency of vapor generation, as it is influenced by the water content in the refrigerant vapor.

The objective of the present work is to investigate the impact of the “desorber” component in an NH<sub>3</sub>-H<sub>2</sub>O absorption chiller, through its operation and performance.

## II. Review of generator and rectifier technologies

In an  $\text{NH}_3\text{-H}_2\text{O}$  absorption chiller, the generator is the component where the process of ammonia desorption from the aqueous solution occurs. Most of the time its only role is to generate the refrigerant vapor, yet it can also include a section where the purification of the vapor occurs. The roles and utility of the generation and rectification parts are described in *Sect. II.1*. Together with the absorber, the desorber has proved to be a crucial component of an absorption chiller, owing to the impact of its performance on the performance of the absorption system as a whole and to its size and cost. A better understanding of the physical phenomena occurring in the desorber is necessary for an improvement of the absorption chiller performance and for gains in compactness and costs. A state of the art of the existing technologies of desorbers, rectifiers, and combined components is detailed in the following paragraphs. Both experimental and numerical works are investigated, through the functioning, specificities, geometries, and operating ranges of the components.

### II.1. Generation and purification of refrigerant vapor

The desorber takes part in the refrigerant cycle, it works at high pressure and involves the working-fluid pair, i.e., ammonia for the refrigerant and water for the absorbent in the context of this work. The mixed solution of water with a high ammonia concentration, called the “rich solution”, comes from the absorber and is heated by the HTF of the external hot source circuit. The rich solution generates ammonia vapor, via the desorption process, thus its ammonia concentration decreases and the exiting solution, called the “poor solution” goes back to the absorber. The ammonia vapor produced from the rich solution contains a few traces of water that must be eliminated for a higher-quality vapor and thus improvement of the absorption chiller performance. This purification is the purpose of the rectifier.

The rectifier is located at the outlet of the desorber, and its role is to purify the ammonia vapor, i.e., to remove as much water as possible from the vapor before it goes to the condenser. This refrigerant purification is a key issue of the  $\text{NH}_3\text{-H}_2\text{O}$  absorption system performance. Indeed, the less the water contained in refrigerant vapor, the more efficient the system. According to (Fernandez-Seara and Sieres 2006), the purity of ammonia determines the evaporation and absorption pressure for the evaporation temperature design. Indeed, the temperature glide necessary to complete a total refrigerant evaporation is strongly dependent on the water content in the vapor. If the evaporation process is not complete, an accumulation of water will occur in the evaporator, and the system operation is altered (decrease in cold power production, decrease in COP, etc.). There are various processes of rectification available, depending on the absorption system configuration.

The desorption phenomenon is led by the heat and mass transfer occurring in the ammonia–water liquid mixture and in the vapor phase. The main issue encountered is related to the narrow gap between the ammonia and the water volatilities and evaporating pressures, which lead to water release in the ammonia vapor generated. Thus, various parameters of the desorber and of the rectifier need to be meticulously studied, especially the geometry, because the desorption phenomenon is strongly dependent on the interior design of the desorber. Different technologies of desorbers, rectifiers, and components combining both functions are detailed in the following parts.

### II.2. Classification of heat exchanger technologies and vapor generation processes

#### II.2.1. Classification of heat exchangers

The process of desorption occurs thanks to a heat supply. Therefore, a desorber is a heat exchanger. In the literature, many heat exchanger technologies are described and their characteristics are highlighted. Figure 2.8 presents some technologies of heat exchangers that can be used to design a desorber.

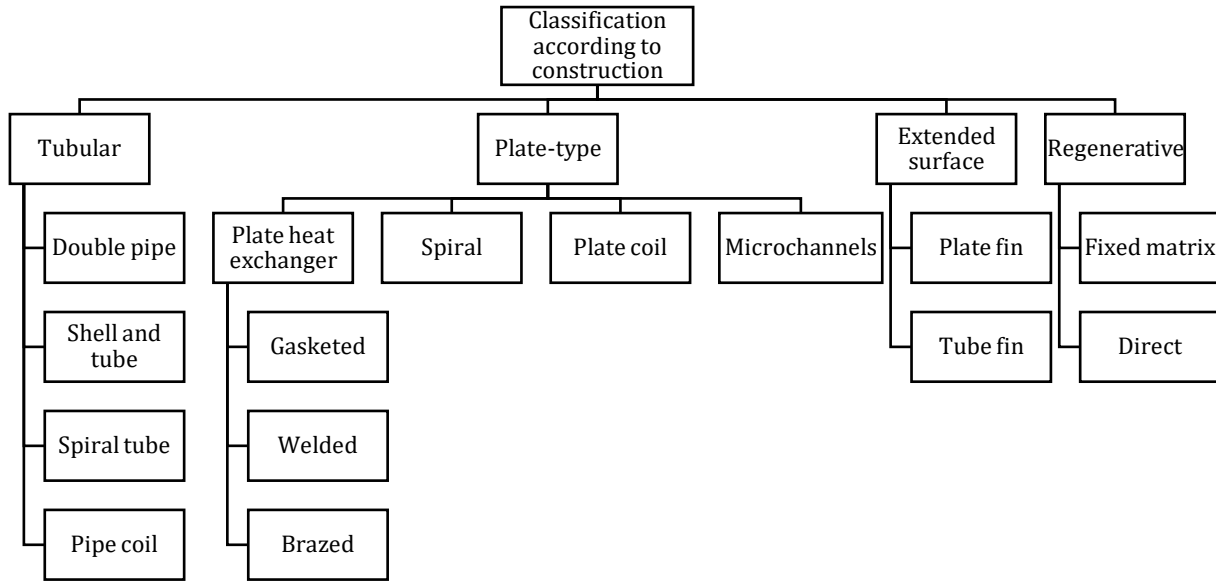


Figure 2.8. Classification of some heat exchangers (Kuznetsov 2018).

### II.2.2. Direct or indirect-coupled systems

The heat exchanger exploited as a desorber is supplied by a hot source, in order to bring to the solution the heat needed for the vapor desorption. The exchanger can be “direct-coupled”, the desorber is directly coupled to the heat source, avoiding an intermediate fluid-circuit exchanger, or “indirect-coupled”, the desorber is coupled with a primary heat exchanger that is itself coupled to the heat source (Staedter and Garimella 2018a). The main advantages of direct or indirect-coupled systems are presented in Table 2.4.

Direct-coupled	Indirect-coupled
<ul style="list-style-type: none"> <li>✦ Overall system size and weight are lower because there is no heat source fluid circuit and linked components</li> <li>✦ Less exergy destruction due to less heat transfer process</li> <li>✦ Shell and tube construction is more suitable to direct-coupled design</li> </ul>	<ul style="list-style-type: none"> <li>✦ Desorber size is significantly reduced because less working-fluid is needed</li> <li>✦ Control over the system is large, particularly over working-fluid temperatures for thermodynamic optimization</li> <li>✦ The separate primary heat exchanger facilitates management of fouling</li> <li>✦ The heat source can be of different sorts, while in direct-coupled design it is limited to hot gas source;</li> <li>✦ The heat source can be centralized and its temperature adapted</li> </ul>

Table 2.4. Advantages of direct and indirect-coupled systems.

In the following study, only indirect-coupled systems are presented, the hot source is an HTF provided by an external circuit.

### II.2.3. Vapor generation process: pool boiling

The process of pool boiling occurs in stagnant liquid solution, in which a heat source is immersed, often a hot fluid separated from the boiling liquid by a thin superheated metal wall. The boiling process induces the liquid motion and vapor generation. There is no forced liquid flow in the pool, but the confinement of the liquid and the close spacing of wall heaters drive the conditions close to forced convective boiling.

According to (Khir et al. 2005a; Spindler 2010; Shakir R. and S. 1987), boiling desorption is the most common method of desorption. (Taboas et al. 2007) presented a bibliographic review of the literature on nucleate pool boiling in  $\text{NH}_3\text{-H}_2\text{O}$  absorption chillers. Pool boiling methods can be classified depending on the physical conditions, the geometry of the heated wall, and the heating method. Figure 2.9 shows some of the heating geometry used.

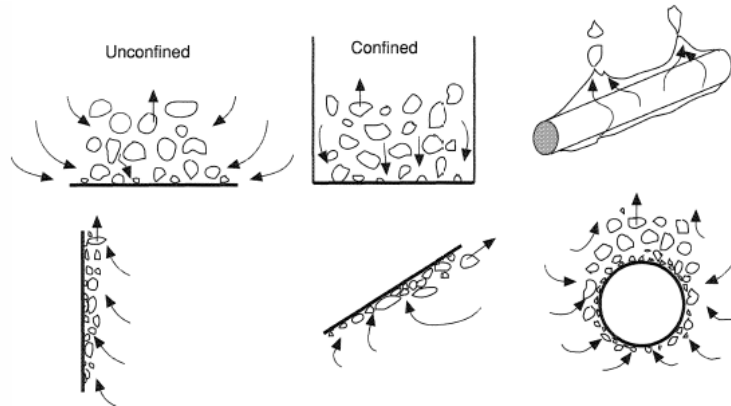


**Figure 2.9.** Heater geometry influence on boiling process (Kenning, thermopedia.com, 2019).

When pool boiling occurs in a saturated liquid, the vapor bubbles generated at the superheated surface rise and burst at the free surface. When pool boiling occurs in a subcooled liquid, the bubbles generated at the superheated wall condensate in the liquid. Figure 2.10 illustrates pool boiling of saturated and subcooled liquid.

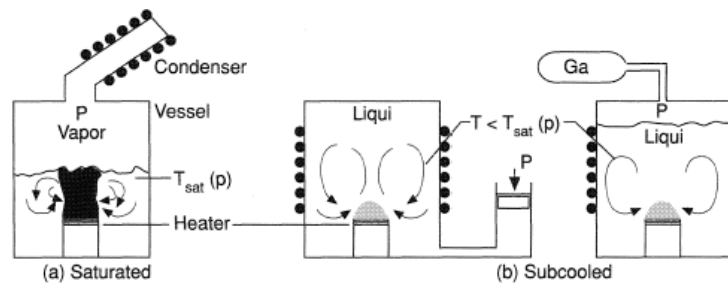


**Figure 2.10.** Saturated and subcooled liquid boiling methods (Kenning, thermopedia.com, 2019).

The micro-geometry, the wettability, and the confinement effects have a wide impact on nucleate and transition boiling when the pressure is large compared with the pressure of the triple point (Kenning, thermopedia.com, 2019).

#### II.2.4. Vapor generation process: falling film

Falling film is often used in components of absorption chillers and heat pumps (Mittermaier and Ziegler 2015). They are adaptable for various types of exchangers, such as for a falling-film desorber composed of flat vertical plates, vertical tubes, or horizontal tube arrays, along which the solution flows downward due to gravity and forms a film. The HTF circulates between the plates (alternating with the solution), or inside the tubes, and gives thermal energy to the falling-film solution flowing along the plates or around the tubes. Desorption takes place at the interface between the solution and the vapor, due to the thermophysical properties of the mixture in the exchanger (saturation temperature reached, pressure, and solution concentration). This kind of desorber provides a wide exchange surface between the HTF and the solution, and a wide interface surface between the solution and the vapor, thereby enhancing the heat and mass transfer.

There are two falling-film configurations: either both the solution and the vapor flows in a co-current direction from the top to the bottom, or the vapor rises, going in a counter-current direction versus the solution flow. Figure 2.11 shows the interactions involved in a falling film, in the case of a flat plate heat desorber, for a solution–vapor co-current configuration.

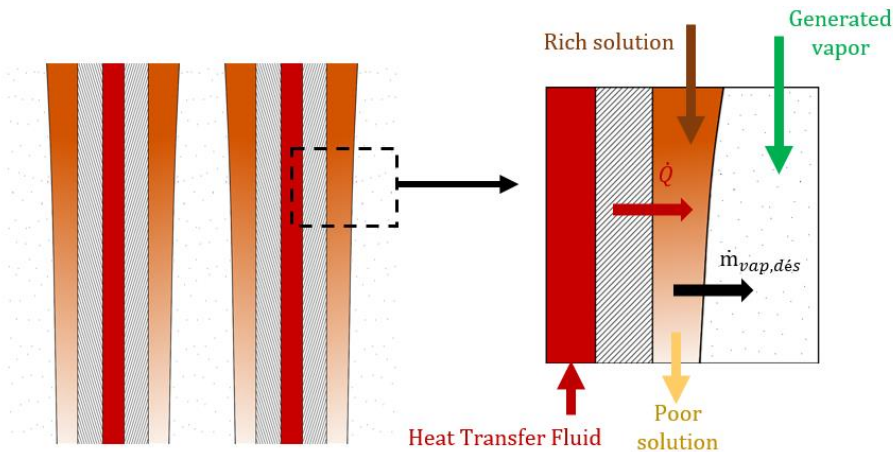


Figure 2.11. Schema of falling-film inside the generator: co-current configuration.

In co-current configuration, the solution flows downward, along the heated plates, and the generated vapor also flows downward. The HTF circulates between the plates, alternating with both the ammonia–water solution and the generated vapor. The rich solution of ammonia–water enters the desorber at the top, is heated along the plates by the heat rate  $\dot{Q}$  supplied by the HTF, after which the desorption phenomenon occurs. The solution flows in a thin film along the heated plates and reaches the bottom of the desorber as a poor solution, wherein the mass concentration of ammonia is lowered. During the desorption process, all along the interface between the solution and the vapor, ammonia vapor, almost pure but containing a small part of water, is released and evacuated at the bottom of the generator.

In counter-current configuration, the rich solution flows downward along the plates, whereas the ammonia vapor generated is evacuated upward. The process is the same as for the co-current configuration, except that the vapor is first generated at the bottom of the desorber, moves in a counter-current direction, and is evacuated at the top. Heat transfer between the HTF, plates, and solution is the same in both flow configurations. The heat and mass transfer occurring at the interface between the solution and vapor phases is also similar. According to (Golden 2012), a desorber performs better in a counter-current configuration than in a co-current flow design. Indeed, in a co-current configuration, the generated vapor exits downward, in equilibrium with the poor solution at a high temperature, and it includes a larger part of water stream than in the case of a counter-current flow. Thus, the input heat load is used more efficiently in the counter-current regime.

## Synthesis

The boiling vapor generation process and the falling-film process are widely used in various desorber and rectifier designs, and some technologies even use both. As mentioned earlier (*Sect II.2.1*), there are different heat exchanger geometries available, and among them the main designs employed for the desorption process in absorption chillers are the tubular exchangers, the heat plate exchangers, and the microchannel exchangers.

## II.3. Heat exchanger technologies used for vapor generation and purification

### II.3.1 Plate heat exchangers

A plate heat exchanger (PHE) is composed of a set of plates between which the HTF and the solution alternate. The heat brought by the HTF goes through the metal plates and provides the solution with the thermal energy needed to desorb the refrigerant vapor. According to (Abou Elmaaty et al. 2017), the plate-type heat exchangers are widespread in many industrial markets, thanks to their high thermal efficiency, their flexibility, their ease of maintenance, and their low cost. The plate surfaces can be enhanced by adding extended surfaces like fins, or by employing interrupted surfaces such as corrugations. The most

common surface pattern used is the chevron design. Different manners of sealing the PHE exist: welded, gasketed, brazed etc. According to (Abu-Kader 2012), the welded PHEs developed are able to overcome the pressure and the limitations of gasketed plate-and-frame exchangers. Figure 2.12 shows the example of a corrugated PHE consisting of a number of gasketed plates compressed between two supports. Most of the time, the PHEs use the falling-film process. The main advantage of this technology, as compared to tube- or microchannel-based heat exchangers, is the improvement in the heat and mass transfer thanks to the significant wetted exchange surface.

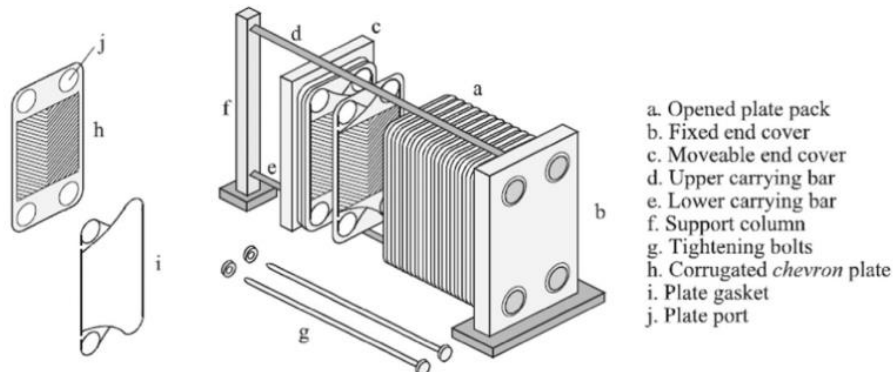


**Figure 2.12.** Gasketed chevron plates exchanger (Abou Elmaaty et al. 2017).

However, two main phenomena must be avoided in the PHE for a better operation of the desorption process: the fouling and, particularly in counter-current configuration, the flooding that limits the heat and mass exchanges. Indeed, the vapor rises upward in contact with the solution flowing downward, and if the vapor flowrate exceeds a certain threshold, some of the solution could be carried away by the rising vapor. Thus, (Golden 2012) explained that flooding depends on the flowrates of both phases, on the hydraulic fluid properties and on the geometry of the channels. These parameters must be carefully chosen. The fouling phenomenon has a complex behavior in a flat PHE, it depends on the plate geometry and on the fluid velocity, and it results in hydraulic and thermal disturbances. It creates the need for cleaning operations. Most of the time, the fouling phenomenon is caused by an unequal solution flow distribution between the channels. This underlines that an equal distribution of the solution over the plates is a crucial parameter to be considered.

(Yang et al. 2017) found that geometric dimensions play an important role in heat transfer characteristics. They proposed a generalized correlation of single-phase heat transfer performance of PHEs based on experimental and literature data. They found that the herringbone angle is the most influential factor; the heat transfer is enhanced with the increase of this angle.

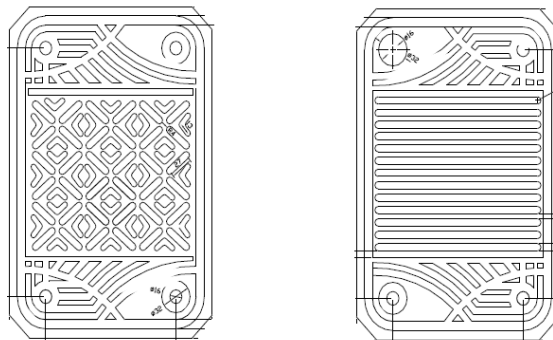


**Figure 2.13.** Heat exchangers with asterisk and corrugated surfaces (Durmus et al. 2009).

(Durmus et al. 2009) led an experimental study on the impact of a heat exchanger design on the efficiency and pressure drop of the system. The efficiency of the heat exchanger increases with the increase in the fluid's contact surface. The heat gained from a corrugated-type heat exchanger is greater than that gained from a flat or an asterisk type of exchanger. Accordingly, the pressure drop also rises, which increases the capital costs. However, the high heat exchanger efficiency makes it possible to reduce the system dimensions and thus decrease the production costs.

(Hessami 2000) investigated the impact of the size and of the corrugation orientation on the heat transfer performance of a PHE. The heat transfer and the isothermal pressure drop data in a single-pass U-type counter-flow PHE, at a low Reynolds number, are presented with various chevron plate arrangements.

All these studies (Yang et al. 2017; Durmus et al. 2009; Hessami 2000) propose new correlations and show results that are mainly based on previous experiments and well-established empirical correlations. The main parameters affecting the PHE behavior are summarized in Table 2.5.

Thermal hydraulic parameters	Geometric parameters
Working fluid	Herringbone angle
Flow distribution	Surface enlargement factor
Pressure drop	Corrugation profile
Friction factor	Aspect ratio
Reynolds and Nusselt numbers	

**Table 2.5.** *Main parameters affecting PHE behavior.*

Although PHE is an effective geometry for falling-film desorption, for its compactness and performance, there is still scant literature available on flat plate falling-film generators, and fewer still focusing on ammonia–water desorption. (Taboas et al. 2010) developed a vertical brazed PHE, operating as a generator, for an ammonia–water absorption chiller supplied at a low-temperature source by solar energy or waste heat. The saturated flow boiling heat transfer and the associated frictional pressure drop of the ammonia–water mixture are investigated for a pressure between 7 and 15 bar, and an inlet ammonia concentration between 0.42 and 0.62. The mean vapor quality varies between 0.0 and 0.22, the heat flux from 20 to 50 kW.m<sup>-2</sup>, and the mass flux from 70 to 140 kg.m<sup>-2</sup>.s<sup>-1</sup>. The results showed that boiling heat transfer coefficient is highly dependent on the mass flux, while for a high vapor quality, it is barely affected by the heat flux, the ammonia concentration, or the pressure. The pressure drop increased with the mass flux and with the vapor quality.

### II.3.2 Microchannel exchanger

A microchannel exchanger has an ultra-thin design and most of the time a cross-flow tubes profile. It is commonly used when a highly compact component is needed, allowing the air pressure drop and fluid quantity to be reduced. It enhances the heat and mass transfer effectiveness thanks to the high surface area-to-volume ratio provided by the channels.

(Determan and Garimella 2011) led an experimental and analytical study on the ammonia–water desorption processes occurring in a microchannel tube device operating as a generator for a residential heat pump system of 17.5-kW heat load. The parallel pass arrangement of the microchannel tubes makes it possible to achieve the heat performance with a heat transfer coefficient between 388 and 617 W.m<sup>-2</sup>.K<sup>-1</sup>, and with low coolant pressure drops. While rising through this highly compact component (178 mm, 178 mm, 0.508 m), the vapor that is generated is cooled by interacting with the ammonia–water solution film flowing downward, and reaches a high ammonia concentration at the outlet. A model simulating the heat and mass transfer of a crossflow well-mixed falling film over horizontal tubes allows one to predict the temperature, the concentration, and the mass flowrate profiles in the exchanger. The authors found that the wetted area ratio ranging from 25 to 69% of the tube arrays limits the performance of the generator, even if the mass transfer resistance lies in the vapor phase. This study was in line with previous studies demonstrating its operation as an absorber, thus it underlines the versatility of the concept.

### II.3.3 A tubular exchanger: the distillation column

Distillation columns are commonly used in industrial processes. The development of a desorber, rectifier, or combined desorber–rectifier component for absorption chillers is often achieved with the technology of columns. Distillation columns are divided into different groups according to their geometries and internal processes of vapor generation: tray columns, structured or randomly packed columns, flooded columns, etc. A distillation column takes advantage of the significant exchange surface between the spread solution and the vapor generated. The wider the contact surface between the vapor rising and the solution falling, the better the heat and mass transfer. The repetitive interactions between the solution and the vapor facilitates cooling of the vapor and increasing its purity.

#### II.3.3.1 Tray columns

A staggered tray or branched tray column design employs falling-film and pool boiling processes. The rich solution flows downward as a film along the wall surface, and along its path to the bottom it undergoes pool boiling in several alternating trays holding up the boiling liquid mixture. An HTF flows in adjacent channels, and provides the heat needed for the vapor generation. Along the plates, there are downcomers helping the solution to circulate downward to lower plates and forcing the vapor generated to rise through the pool boiling areas. An optimal balance is established between the vapor desorbed at the falling-film interface and the vapor generated by the pool boiling process. One main advantage of this method is that it causes only low instabilities. Figure 2.14 provides a scheme of the liquids and vapor flows in a branched tray column.

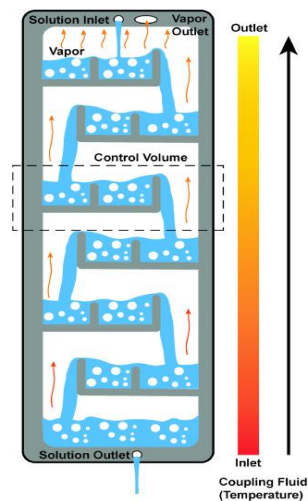


Figure 2.14. Example of a branched tray design (Keinath et al. 2019).

#### II.3.3.2 Packed columns

The structured or randomly packed columns are composed of various shapes and material packing, arranged to provide a uniform distribution of the falling solution and of the rising vapor, so as to obtain an optimal contact to enhance the interface transfers. The weir fixes the pressure drop.

(Fernandez–Seara et al. 2002) developed a mathematical model based on heat and mass transfer and mass and energy balance equations, to simulate the behavior of a packed distillation column operating as a rectifier in an ammonia–water absorption chiller. In this model, the column is composed of a stripping section, directly supplied by the solution, and of a rectifying section, supplied by a liquid reflux from a condenser. The ammonia vapor generated ahead enters at the bottom and is purified by interacting with the solution while rising in counter-current flow from it. A net molar flux is transferred at the interface. The authors found that the liquid mass transfer resistance is negligible, and the vapor mass transfer coefficient has the most significant effect on the ammonia concentration generated, as well as on the length of the rectifier section, which has to be much longer than the stripping section length, at fixed geometric parameters and operating conditions.

### II.3.3.3 Flooded columns

Moreover, a heat plate or tubular exchanger can be partly flooded. The solution falls, in a falling-film shape, into a heated retention tank, and undergoes pool boiling, causing desorption of one component of the mixture, based on the volatility differences, e.g., the flooded column uses this principle of this combination of processes. The HTF flows into microchannels tubes, warming up the pools where the refrigerant vapor is generated. The solution moves downward through other tubes, falls into the pools, boils, and generates vapor, which moves in counter-flow direction. This design is intended to operate under flooded conditions, with a vigorous mixing of liquid and gas phases.

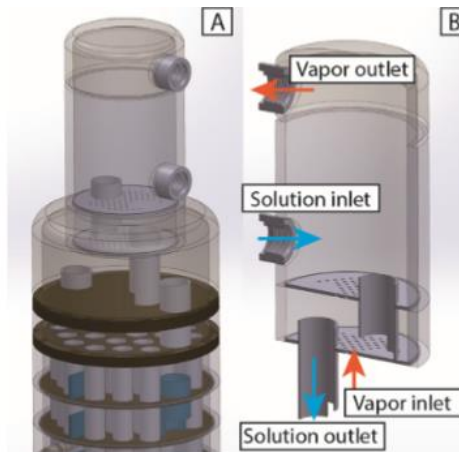


**Figure 2.15.** Flooded column design (Staedter and Garimella 2018a).

(Golden 2012) developed a model for a counter-current desorber of an ammonia–water flooded column where refrigerant vapor is generated through a combination of falling-film and pool boiling. He validated his model with an experimental study on a constructed design. Results showed that this configuration yielded higher heat transfer during pool boiling, and new boiling correlations are suggested. However, limitations of the system performance related to the design are highlighted, and a study focusing on the falling-film process could help to remove some of the constraints.

Refrigerant vapor generation is a well-developed process through many technologies. However, the vapor produced is not always pure enough to yield a good performance of the absorption chiller. In order to enhance the purity of the vapor produced, various technologies of rectifier are developed.

### II.3.4 Rectifier

Partial condensation of the vapor is a purification solution: If the refrigerant vapor is cooled by contact with a surface that is cooled below the vapor dew point, a concentration of the absorbent (here water) will condense out of the vapor stream, because it has a higher boiling point (Fernandez-Seara et al. 2013). The authors developed a finite-difference numerical model of a helical coil rectifier for an ammonia–water absorption chiller. The interface temperature is nearly equal to the bulk liquid temperature, which implies that heat transfer resistance in the liquid film is negligible. Water always condenses as it descends through the rectifier.

Recent studies have focused on distillation columns or PHEs with a rectification and a generation section, to replace both components, in order to gain compactness, to decrease the operating and maintenance costs, and to increase efficiency of the system.

### II.3.5 Combined technologies: vapor generation and purification in the same component

#### II.3.5.1 Distillation columns

Usually, the rectifier and the desorber are used as two separate components; however, they can also be combined into one component, as done for certain column technologies. For example, the vertical column design is one of generator–rectifier assembly, which involves the falling-film heat transfer technology. The rich solution is introduced in the middle of the column and moves downward, through the generator section. The heat provided by the HTF to the solution makes it possible to generate vapor in this section. A rectifier section is located above, enabling condensation of the absorbent contents in the rising vapor that is generated. This section can be adiabatic, or cooled by a fluid flowing through channels, or plates, depending on the chosen geometry.

(Fernandez–Seara and Sieres 2006) carried out an experimental study quantifying the impact of the residual water contents in the refrigerant vapor on the effectiveness and reliability of a single-stage ammonia–water absorption system. The study was performed considering a system with complete condensation by reflux and including a distillation column, composed of a rectifying section over the column feed point, an adiabatic stripping section below the feed point, and a heated generator section at the bottom. The separation efficiency (Murphree efficiency) of the distillation column and the impact of the system operating conditions are investigated based on modeling of the absorption chiller behavior. Higher efficiency in the stripping and rectifying sections results in higher ammonia vapor concentration as well as higher system COP, pressure, and solution concentration. The use of a rectifying section has a greater effect on the vapor concentration, while the use of a stripping section showed a greater effect on the system COP. The authors underlined that the purification process is required for applications of low evaporation temperature (otherwise, the COP would be too low, and operation of the system might even not be possible). However, for applications of high evaporation temperature, the ammonia vapor purification is not critical but is recommended, especially if the absorber temperature is high.

(Zavaleta–Aguilar and Simoes–Moreira 2015) experimentally studied a falling-film distiller, composed of a generator and of a rectifier section, designed for an ammonia–water absorption chiller. Their parametrical study showed that the distilled ammonia vapor concentration decreases with the rectifier or with the generator temperature increase, while it is improved with increase in the concentrated solution mass flowrate, in the concentration, or in the subcooling, reaching a maximum of 0.9974. The distilled ammonia mass flowrate decreases with the rectifier temperature or with the concentrated solution mass flowrate increase, and it is improved with an increase in the concentrated solution or in the generator temperature. The authors proposed a new Nusselt number correlation for the ammonia–water falling-film over the generator tube bundle.

Minimization of small-capacity ammonia–water absorption chiller size necessarily leads to a reduction in the size and combination of the components. Concerning the vapor production and purification, more and more studies (presented in the following paragraphs) focus on the combination, in the same component, of a desorber section at the bottom, sometimes topped with an analyzer section spreading the solution over the heated desorption part, and of a rectifier section at the top. This concept has the advantage of high heat transfer coefficients, enabling the reduction of the component size, and the production of a high-quality ammonia vapor, which induces lower rectification loads and lower operating costs (Delahanty et al. 2015).

(Delahanty et al. 2015) developed a compact desorber composed of a series of vertical columns. The solution flows downward as a falling-film, heated by a coupling fluid flowing counter-current in a vertical microchannel array. The vapor generated rises to the rectifier section, where a cold coupling fluid flowing in an adjacent microchannel array cools it. In the same configuration of HTF, solution and vapor flows, the authors also developed an other combined component, composed of a series of branched trays, where the solution falling in the trays undergoes pool boiling. They also modeled the heat and mass transfer occurring, in order to investigate the profile of the temperature and concentration in the component. (Keinath et al. 2015) built a branched tray desorber for a 3.5-kW space-conditioning system, consisting of an array of alternating plates with integral microscale features enclosed between cover plates. They showed that the production of refrigerant vapor increases with the increase in the HTF temperature and in the solution and HTF mass flowrates.

(Staedter and Garimella 2018a) designed a direct- and gas-coupled diabatic distillation column, providing a favorable solution for small-capacity systems (with high vapor purification and gas-side heat transfer coefficient). Moreover, they performed a statistical analysis comparing various thermal compressor configurations using thermodynamic modeling based on a control algorithm (Staedter and Garimella 2018b). They defined the diabatic distillation as the optimal design for desorption and rectification phases and the HTF temperature as a critical variable of control. The model they developed can be extended as a tool to guide other system designs. The authors then developed a diabatic distillation concept for a non-equilibrium 3.5-kW cooling capacity model (Staedter and Garimella 2018c). On the basis of parametric studies, they underlined that the heat source temperature variations make it possible to minimize the exergy destruction, reduce the rectifier heat duty, and improve the overall system performance. They also identified that the mass flowrate is a crucial control variable, because the condensation heat transfer coefficient in the rectifier part and the global vapor purification efficiency are highly sensitive to it. (Staedter and Garimella 2018d) introduced and validated correlations for pool boiling heat transfer coefficients, and proposed new correlations for liquid mass transfer and for binary mixture correction coefficients. In the same study, they developed an effective design rectification solution through a packed bed geometry, and developed the sensible vapor heat transfer coefficient.

In their transient-regime model for a small-capacity ammonia–water absorption heat pump, (Roeder et al. 2019) investigated the impact of branched-tray geometry operating parameters on the system functioning. They found that the ammonia vapor generation is highly impacted by the HTF temperature and by the flowrates of the solution and HTF. This also underlined the flexibility of the desorber behavior according to inlet operating conditions.

These concepts showed a definite advance in the development of compact desorption systems for small-capacity ammonia–water absorption chillers, through the ability of including the rectifier and the generator in a single component and a scalability to fit various applications. The construction costs are reduced, and the implementation potential is improved. However, the cooling of the rectifier part induces load needs, and reduces the absorption chiller COP.

### *II.3.5.2 Micro-scale systems*

In the meantime, the area of microscale systems is receiving more interest, and some studies are focusing on the development of extremely compact absorption chillers, as standalone units including a desorber and rectifier as a heat exchanger combined component. For example, (Garimella et al. 2016) developed a compact  $\text{NH}_3\text{-H}_2\text{O}$  absorption heat pump standalone unit for space-conditioning applications, that is able to reach a cooling power of 3.3 kW for a COP of 0.47. It included a combined generator–rectifier, which provides a refrigerant purity over 0.99. They observed that the vapor mass flowrate increases with the concentrated solution mass flowrate and with the temperature of the HTF until 180°C.

(Staedter and Garimella 2018e) developed a highly compact ammonia–water absorption chiller, integrating only two monolithic blocs composed of microchannel heat and mass exchangers. The vapor generation unit was designed on the basis of previous work by (Delahanty et al. 2015) and was enlarged to obtain higher vapor generation rates. The system produces 7 kW of cold for a cooling COP reaching 0.44, which is close to the initially designed capacity, predicted by the segmented model developed to choose the size. It depends on thermodynamic properties simulated and on the number of channels, which specify the overall cross-sectional area needed for the fluid flow. The non-optimal operation of the desorber–analyzer–rectifier block could explain the gap between the predicted COP and the measured COP, and this component needs to be further investigated (size and weight reduction) to reach a better COP. (Keinath et al. 2019) confirmed the potential of compact desorbers providing a high purity of ammonia vapor for small capacity  $\text{NH}_3\text{-H}_2\text{O}$  absorption chillers. They continued their experimental investigation of the heat and mass transfer occurring in a micro-scale vertical column and branched tray. The branched tray shows a better performance in regard to ammonia vapor purity and heat duty.

(Delahanty et al. 2021a, 2021b) demonstrated the opportunity to develop highly compact vapor generation units for small-scale  $\text{NH}_3\text{-H}_2\text{O}$  absorption chillers by conducting an experimental study of two novel

counter-flow geometry components. Both of the components are composed of a desorber, an analyzer, and a rectifier. The branched tray is characterized by the pool boiling process in the desorber section, and by the falling-film process in the analyzer and rectifier sections. The vertical column relies entirely on the falling-film process. The solution enters with a flowrate between 0.7 and 1.3 g.s<sup>-1</sup>, and with an ammonia concentration between 0.4 and 0.55, while the HTF inlet temperature range is 170–190°C. Heat and mass transfer coefficients were investigated, and the branched tray design showed a better performance than the vertical column. The average deviations for the heat transfer coefficient correlations proposed are under 18% compared with the literature. The liquid-side mass transfer resistance was dominant, the liquid mass transfer coefficients predicted by the literature result in an average deviation of -5% and 9% for the branched tray and the vertical column, respectively. The vapor mass transfer coefficients correspond to -1% and 11%. The flooding limits determined were in good agreement with the available correlations. The ideal cooling capacities and COP obtained for the branched tray and the vertical column are 430 and 320 W, and 0.56 and 0.50, respectively. The models predict correctly the performance of the components.

These studies prove the ability to build highly compact absorption chillers, using microscale heat exchangers for residential-scale applications.

### II.3.6 Concept versatility

Desorption and absorption processes are closely related. Indeed, the kind of heat exchangers used as desorbers or absorbers in absorption chillers are the same, and they can have similar geometries. Thus, the heat and mass transfer occurring in these heat exchangers are very similar too. (Mittermaier and Ziegler 2015) conducted research on the comparison between absorption and desorption processes both for absorption heat pumps and for reverse absorption heat pumps. They focused their work particularly on the liquid–vapor interface transfers, through a comprehensive model combining heat, mass, and momentum transfers. They found that, in absorption chillers, the vapor generation process occurs at a higher pressure and a higher temperature than the absorption process. Therefore, in a desorber, the viscosity is lowered and the mass diffusivity is increased, leading to the evolution of a thinner and better performing film during desorption than absorption. Moreover, (Determan and Garimella 2011) proved that the microchannel heat and mass transfer technology can be successfully used for both desorption and absorption thanks to the easy versatility of the concept.

### II.3.7 Combined generator studied

The development of desorber and rectifier technologies for ammonia–water absorption chillers is gaining renewed attention, with the design of compact and effective combined components providing high ammonia vapor at lower energetic costs of the chiller, such as the counter-flow distillation column and some geometries of microchannel PHEs. According to (Staedter and Garimella 2018a), the choice of the desorber configuration strongly depends on its specific application. In this PhD study, the absorption machine developed produces 5 kW of cold and works with an ammonia–water solution. The study and state of the art of the different patterns and parameters led to the choice of designing a desorber with flat corrugated plates, chosen for the performance and compactness of the PHEs. In order to reduce the size, the costs and the complexity of the absorption chiller, the study focuses on the development of a new concept of a combined generator, bringing together the generation and purification of the ammonia vapor in the same component.

Besides the design of the generation and the purification sections inside the same component, another important part of the system to be designed is the distribution system of the solution, which should be in accordance with the internal design of the new combined generator.

## II.4. Distribution system

An equal distribution of the solution is a key element in a plate heat generator. Indeed, the desorption efficiency increases with the increase of the solution exchange surface (Durmus et al. 2009), and the wide wettability of the plates for effective heat and mass transfer depends on the homogeneous solution distribution provided by the distributor. The distribution system is located on top of the exchanger. For a counter-current configuration PHE, the distributor geometry is designed to allow free circulation of the solution and the vapor at the same time. The perfect liquid distribution consists in providing an equal quantity of solution per unit area of plates, in order to uniformly wet them. It must also provide means to maintain a low pressure drop (Wang J. and H. 2015). It represents an infinite number of solution streams with an identical flow. According to (Strobbe and Van Egmond 1989), a well-designed distributor needs to respect the following criteria:

- + Provide a uniform solution distribution over the packing;
- + Consider the proper operation range;
- + Limit the vapor phase pressure drop;
- + Resist plugging and fouling;
- + Maintain a minimal solution residence time.

The main design limitations are the orifice size, the fouling potential, and the mechanical construction.

A distribution system can be simple or multi-stage, for a more precise distribution of the solution. Some examples of distributors are provided in the following paragraphs. Figure 2.16 shows various types of top distributors, where the initial liquid flow inlet is separated into multiples streams (KOCH–GLITSCH 2009).

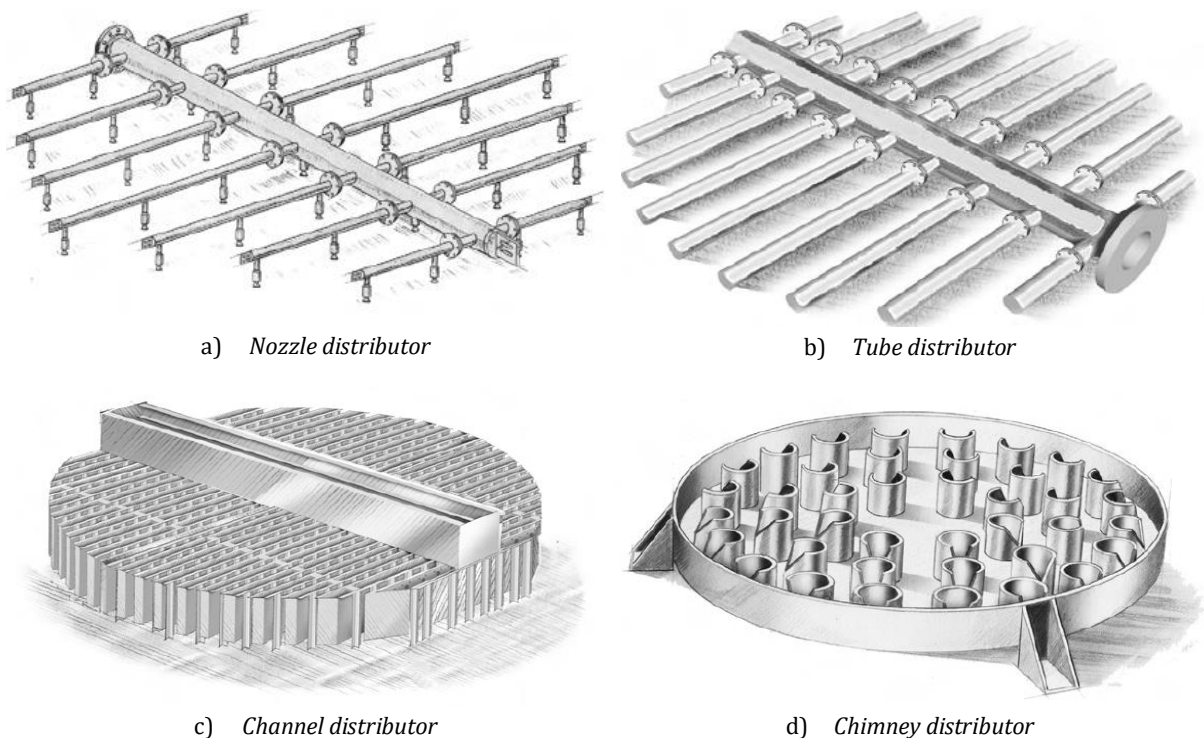


**Figure 2.16.** Various types of top distributor (Koch–Glitsch 2009).

In order to enhance the efficiency of the distribution system, a second part is implemented at the bottom of the distributor. This secondary distribution can be composed of a sieve tray, for example, made from a flat perforated plate, which allows the passage of vapor through the liquid; a structured pack; or a packing support, which is a slatted type of support, with a very large open area to let the vapor and the solution flow uniformly.

Most of the time, at the inlet of the distribution system, the first and larger stream of solution needs to be pre-distributed uniformly into several smaller streams. A manifold can be used for that purpose; four types are identified in Figure 2.17.

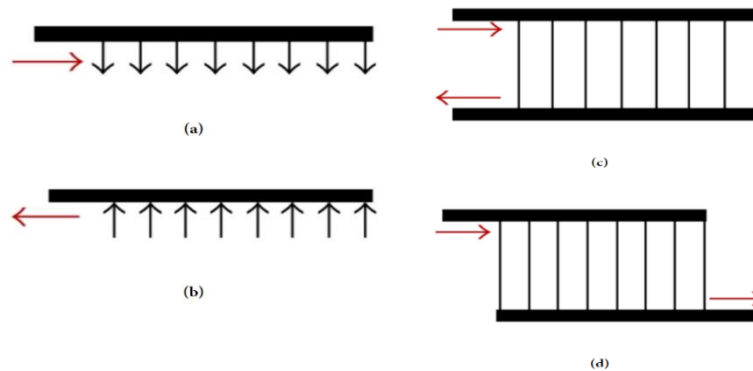


**Figure 2.17.** Different types of flow manifolds: (a) dividing, (b) combining, (c) U-manifold, (d) Z-manifold (Hassan et al. 2014).

Parallel- and reverse-flow manifolds (the Z and U type, respectively) are associated with dividing and re-combining of the streams and are commonly used in PHEs. (Wang J. and H. 2015) led an experimental study to evaluate and compare the uniformity of the flow distribution and the pressure drop for both U-type and Z-type arrangements. The results show that the uniformity is generally better in the U-type.

A uniform flow distribution requirement is a common issue in many engineering contexts such as for PHEs. Therefore, a substantial number of experimental and numerical studies deal with flow in manifolds. (Bassiouny and Martin 1984a, 1984b) presented an analytical solution for the prediction of flow and pressure distribution in both intake and exhaust conduits of heat exchangers. (Hassan et al. 2014) led a numerical and experimental study for different outlets and configurations, namely, circular and tapered cross-section. At the outlet of the manifold with a circular cross-section, the flow distribution is clearly non-uniform, whereas the flow through the manifold with a tapered cross-section is found to be nearly uniform. The results also show that Reynolds number has a slight effect on the uniformity of the mass effusion from the outlets.

(Wen et al. 2006) conducted a particle image velocimetry experimental study on the behavior of a flow field in a plate-fin exchanger, depending on its header. The fluid maldistribution in classic industrial headers has proved to be important. The header configuration containing a punched baffle (with holes) clearly improves the uniformity both in the y and z directions as shown in Figure 2.18.

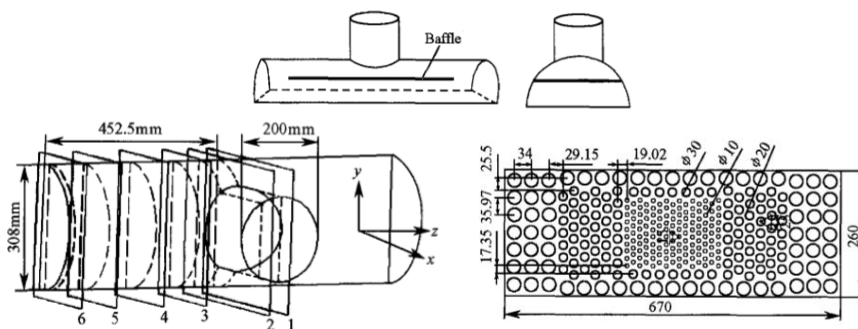


**Figure 2.18.** Baffle position and construction in the header (Wen et al. 2006).

(Jiao et al. 2003) proved that the use of a second header linked to the first header improves the flow distribution in a plate–fin heat exchanger. A schematic drawing of the second header is shown in Figure 2.19.

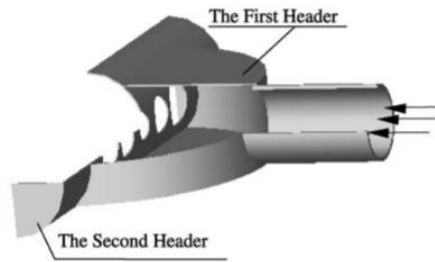


**Figure 2.19.** Double-header configuration (Jiao et al. 2003).

(Kim and Byun 2013) published a review of 10 studies on the impact of horizontal or vertical headers on vertical micro-channels tubes configuration. For both flow directions, the best flow distribution is obtained from a vertical inlet configuration. Three different inlet configurations are presented in Figure 2.20.

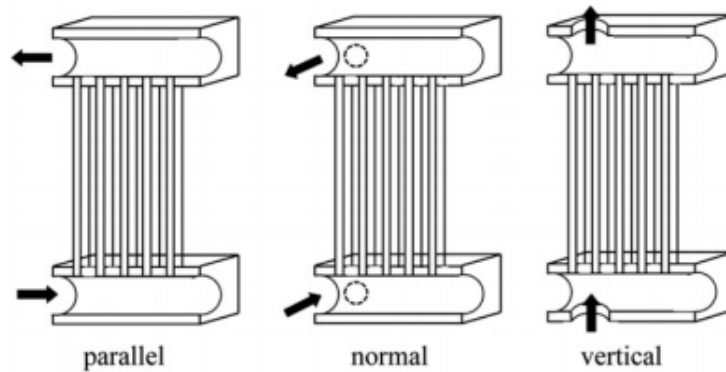


**Figure 2.20.** Flow inlet configurations (Kim and Byun 2013).

One of the main causes of deterioration in the heat exchanger efficiency is the non-uniformity of the flow field. Indeed, the non-uniformity of the flow field is closely linked to the temperature field. A bad flow distribution, thus a bad temperature distribution, can intensify the longitudinal wall heat conduction and the distribution of the interior temperature is then lowered. It can also induce a pressure drop.

## II.5. Synthesis of the generator and rectifier systems presented

Several experimental and numerical studies focus on ammonia vapor desorption and purification systems for  $\text{NH}_3\text{-H}_2\text{O}$  absorption chillers. These studies investigate the heat and mass transfer occurring inside the components and explore the impacts of various factors such as geometry design and the influence of inlet parameters on the behavior of the component as well as on the global absorption chiller performance.

This state of the art of the generation and purification systems details different designs such as the plate exchanger, the microchannel exchanger, and the tubular exchanger. Two main vapor generation processes can take place, the pool boiling and the falling-film process, or both. The PHE is a flexible technology, with easy maintenance, low costs, and a high wetted exchange surface that facilitates improvement in the thermal and mass transfer. The microchannel exchangers have a high surface area-to-volume ratio, reducing the quantity of the fluid and being profitable for highly compact systems. The tubular exchangers, like the distillation columns, used widely in industrial processes, include various types of geometry and offer a wide exchanger surface between the spreading solution and the vapor; yet, they are often not compact.

With these technologies, the system is either composed of a generator and a rectifier as separate components or both can be assembled in the same component. The ability to design efficient (in terms of high-quality ammonia vapor production) and compact components, combining the generation and the rectification of the vapor in the same component, is proven. The role of the solution distribution system is also highlighted, through a review of different sorts of manifolds. Analysis of the existing distribution technologies helps to design an adequate distributor.

However, as the importance of the desorption process has been proven, through the influence of the refrigerant vapor purity on the whole absorption system, and because there are only few and recent studies available in the literature on the desorption process in an ammonia–water absorption chiller, further investigations are needed so as to enhance these systems. In order to improve the technological advances in the design of efficient and compact desorbers, a complete understanding of the thermophysical processes occurring inside the system is necessary.

To this end, the next section focuses on the dynamics transfers inside the falling film, through the heat and mass transfer development, the definition of the fluid's properties, and the flowing models occurring in a falling-film and plate exchanger.

### III. Dynamics of transfers inside the falling film

#### III.1. Physical properties of the falling film

Numerous studies have been carried out on the hydrodynamic behavior and the physical mechanisms involved within a falling film. Mostly, in the studies focusing on coupled heat and mass transfer within a falling film, the flow is assumed to be established and two-dimensional, the equilibrium conditions at the interface are considered at the saturation temperature,  $T = T_i = T_{sat}(x, P_i)$ , and the physical properties and thickness of the film are assumed to be constant. However, (Mittermaier and Ziegler 2015) underlined that assuming a constant thickness of the film or constant properties of the fluids can lead to an underestimation of the absolute mass transferred during desorption. Thus, in this study, the physical properties and the thickness of the film are calculated along the flow.

#### III.2. Flow on a vertical plate

##### III.2.1 Film thickness

In the two following sections, a vertical plate is considered with the x-axis fixed along the length of the plate and the y-axis normal to the plate. The flow is assumed bi-dimensional and permanent. The fluid is incompressible and viscous. There is no pressure gradient in the fluid flow. The longitudinal gradient of velocity is assumed much smaller than the transverse velocity gradient (Tsay and Lin 1995). Thus, the steady laminar momentum equation is written:

$$\mu_L \cdot \frac{\partial^2 v}{\partial y^2} + \rho g = 0 \quad (2.6)$$

Figure 2.21 represents the velocity field of a solution flow along a vertical plate, under the gravity effect.

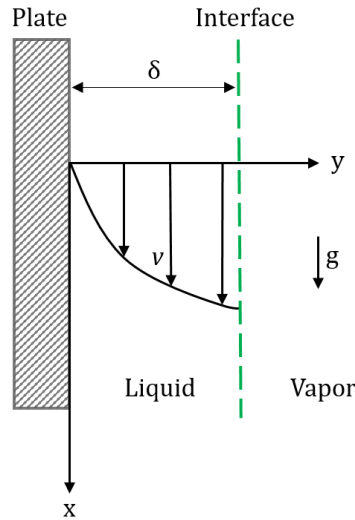


Figure 2.21. Flow profile along a vertical plate, under the gravity effect.

The following boundary conditions are considered:

- ✦ *Kinematic condition:* For  $Re < 400$ , the flow is laminar ( $Re$  is defined in Sect III.2.4), then, the kinematic viscosity is constant. Due to the viscosity, there is no slip at the plate wall ( $y=0$ ) and the velocity of the solution is equal to zero:

$$v(0) = 0 \quad (2.7)$$

- ✦ *Dynamic conditions:* there is no surface tension at the interface ( $y=\delta$ ):

$$\sigma = 2\mu_L \cdot \frac{\partial v(\delta)}{\partial y} = 0 \quad (2.8)$$

After integration, the velocity can be written:

$$v(y) = -\frac{\rho \cdot g \cdot y^2}{2 \cdot \mu_L} + a_1 \cdot y + a_2 \quad (2.9)$$

with the kinematic limit, at the plate:  $v(0) = a_2 = 0$

with the dynamic limit, at the interface:  $v'(\delta) = -\frac{\rho \cdot g \cdot \delta}{\mu_L} + a_1 = 0 \Leftrightarrow a_1 = \frac{\rho \cdot g \cdot \delta}{\mu_L}$

Then, the velocity profile is parabolic.

$$v(y) = \frac{\rho \cdot g}{\mu_L} \cdot \left( \delta \cdot y - \frac{y^2}{2} \right) \quad (2.10)$$

When a solution film flows on a plate, heated or cooled at the wall and interacting with the vapor at the liquid-vapor interface, the film-flow field and the film thickness play important roles in the mass and thermal resistances. On the basis of the study of (Nusselt 1916), the film thickness is written:

$$\delta = \left( \frac{3 \cdot \mu_L \cdot \dot{m}'}{\rho_L^2 \cdot g \cdot \sin\left(\frac{\pi \cdot \beta}{180}\right)} \right)^{1/3} \quad (2.11)$$

with  $\beta$  the inclination angle of the plates, here equal to  $90^\circ$ . The film thickness of vertical plates is then:

$$\delta = \left( \frac{3 \cdot \mu_L \cdot \dot{m}'}{\rho_L^2 \cdot g} \right)^{1/3} \quad (2.12)$$

where  $\dot{m}'$  is the liquid film flowrate along the plate per unit width. It can be defined by integrating the parabolic velocity profile between the plate wall and the interface:

$$\dot{m}' = \int_0^\delta \rho \cdot v(y) dy \quad (2.13)$$

### III.2.2 Shear stress at the solution-vapor interface

The impact of the contact between the solution falling-film and the vertical wall on the flow is characterized by the shear stress:

$$\tau_L(y) = \mu_L \cdot \frac{dv(y)}{dy} \quad (2.14)$$

$\frac{dv(y)}{dy}$  is the velocity gradient. The solution velocity is written as a polynomial function  $v(y) = a + b \cdot y + c \cdot y^2$ , with the following boundary conditions imposed:

$$v(0) = 0 \quad ; \quad \frac{dv(\delta)}{dy} = 0 \quad ; \quad w \cdot \int_0^\delta v(y) dy = \frac{Qv_L}{n} \quad (2.15)$$

with  $w$  the width of the plates,  $Qv_L$  the total volume solution mass flowrate, and  $n$  the number of the plates. Then, the shearing stress of the solution on the wall  $\tau_L$  is defined as:

$$\tau_L = \tau_L(0) = \mu_L \cdot \frac{3 \cdot Qv_L}{w \cdot n \cdot \delta} \quad (2.16)$$

Between two plates of an exchanger and for a two-phase system, another shear stress exists, between the liquid and the vapor. The characterization of this constraint allows us to determine the impact of the vapor flow on the solution flow. It is important to evaluate it, particularly when the vapor flows counter-current from the liquid, because the solution could be driven upstream by the vapor.

The vapor flow between two vertical plates of an exchanger, assuming the solution film thickness as negligible, is represented in Figure 2.22.

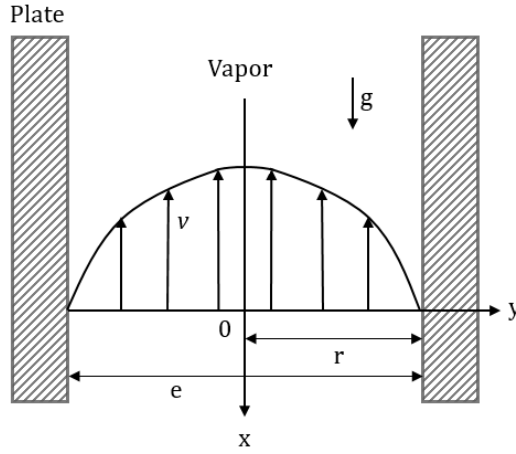


**Figure 2.22.** Schematic profile of the vapor flow between two plates.

The shear stress between the vapor and the falling-film solution is characterized by:

$$\tau_V(y) = \mu_V \cdot \frac{\partial v(r)}{\partial y} \quad (2.17)$$

Where the vapor velocity is defined as a polynomial function  $v(y) = a + b.y + c.y^2$ , and the following boundary conditions are imposed:

$$v(r) = 0 \quad ; \quad \frac{\partial v(0)}{\partial y} = 0 \quad ; \quad w \cdot \int_{-r}^r v(y) dy = \frac{Q_{vV}}{n} \quad (2.18)$$

With  $e$  the space between two plates, the shear stress of the vapor flow on the solution film  $\tau_V$  is defined as:

$$\tau_V = \tau_V(r) = -\mu_V \cdot \frac{6 \cdot Q_{vV} \cdot e^4}{w \cdot n} \quad (2.19)$$

### III.2.3 Surface tension

The surface tension of the ammonia–water solution mixture  $\sigma$  characterizes the forces applied between the solution and the vapor phases. It is useful particularly to determine the flow boiling point of the falling film. (Conde 2004) gave the following equations, formulated by (King et al. 1930):

$$\sigma_{mix} = \tilde{x} \cdot \sigma_{NH3} + (1 - \tilde{x}) \cdot \sigma_{H2O} + \Delta\sigma_{T,mix} \quad (2.20)$$

where,

$$\Delta\sigma_{T,mix} = -(\sigma_{H2O} - \sigma_{NH3}) \cdot F(\tilde{x}) \quad (2.21)$$

and,

$$F(x) = 1.442 \cdot (1 - \tilde{x}) \cdot (1 - e^{-2.5 \cdot \tilde{x}^4}) + 1.106 \cdot \tilde{x} \cdot (1 - e^{-2.5 \cdot (1 - \tilde{x})^6}) \quad (2.22)$$

with  $\tilde{x}$  the molar concentration of ammonia in the solution and  $\sigma_{NH3}$  and  $\sigma_{H2O}$  the surface tensions of the pure components determined by (Straub et al. 1980).

$$\sigma_{pure\ component} = \sigma_0 (1 - b \cdot T_{reduced}) \cdot T_{reduced}^\mu \quad (2.23)$$

$T_{reduced}$  is the reduced temperature of the solution considered, and  $\sigma_0$ ,  $b$  and  $\mu$  are constants for each pure component, given by (Conde 2004).

### III.2.4 Head losses

The liquid head losses  $\Delta P_L$  between the plates of an exchanger are determined by:

$$\Delta P_L = \frac{\lambda_p \cdot \rho_L \cdot v_L^2 \cdot L}{2 \cdot D_{hL}} \quad (2.24)$$

where  $L$  is the length of each plate, assuming the plates are straight, and  $\lambda_p$  is the head losses coefficient without unity, depending on the Reynolds number of the fluid: If  $Re_L$  is inferior to 1600, then  $\lambda_p$  is determined by Poiseuille's relation:  $\lambda_p = 64/Re_L$ .

The Reynolds number compares frictional and inertia forces. For a liquid falling-film flowing along a plate, it is defined:

$$Re_L = \frac{4 \cdot \dot{m}_L}{L_{sp} \cdot \mu_L} = \frac{4 \cdot \dot{m}'_L}{\mu_L} \quad (2.25)$$

If the maximal Reynolds number of the liquid is  $Re_{L,max} < 300$  then, the solution flow is smooth laminar.

In the same way as for the liquid head losses, the vapor head losses  $\Delta P_V$  between the plates of an exchanger are determined by:

$$\Delta P_V = \frac{\lambda_p \cdot \rho_V \cdot v_V^2 \cdot L}{2 \cdot D_{hV}} \quad (2.26)$$

$\lambda_p$  is the head losses coefficient, depending on the Reynolds number of the vapor: If  $Re_V$  is inferior to 2300, then  $\lambda_p$  is determined by Poiseuille's relation:  $\lambda_p = 64/Re_V$ .

For the vapor flowing against the falling film:

$$Re_V = \frac{\rho_V \cdot v \cdot D_{hV}}{\mu_V} \quad (2.27)$$

with the hydraulic diameter:

$$D_{hV} = \frac{4 \cdot Sect_V}{Per_V} \quad (2.28)$$

The mass flowrate of the vapor between the plates is  $\dot{m}_V = \rho_V \cdot v \cdot Sect_V$

Then, the Reynolds number for the vapor phase is:

$$Re_V = \frac{4 \cdot \dot{m}_V}{Per_V \cdot \mu_V} \quad (2.29)$$

If the maximal Reynolds number of the vapor is  $Re_{V,max} < 2.300$  then, the vapor flow is laminar.

### III.2.5 Flooding

In a two-phase flow, there are different flowing configurations. In a solution-vapor flow as described here, the presence of a deformable interface between the two fluids is determining for the definition of the flows. The geometry of the desorber induces a narrow space for the liquid and the vapor to flow in, and the smaller the cross-sectional section, the higher the velocities of the fluids. If the liquid flows down in a smooth laminar way and the vapor flows upward without affecting the solution flow, then there is no flooding. However, for example, if the velocity of the vapor flow becomes too high as compared to the velocity of the solution flow, then the solution flow is impacted. When waves appear at the liquid-vapor interface, the phenomenon of "flooding" begins. In the counter-current configuration, the liquid flow is driven backward by the vapor flow. (Jayanti and Hewitt 1992) reviewed the parameters characterizing the transition from a slug flow to a churn flow and then defined a flooding criterion for various multiphase patterns.

When the pressure effect due to the head losses along the plates is low, and can be neglected, the correlation for flooding is derived from the correlation of (Wallis 1961) and is written as:

$$v_V^{*0.5} + m \cdot v_L^{*0.5} = C \quad (2.30)$$

where the two non-dimensional parameters  $v_V^*$  and  $v_L^*$  are defined as:

$$v_V^* = v_V \cdot \rho_V^{0.5} \cdot (g \cdot de \cdot (\rho_L - \rho_V))^{-0.5} \quad (2.31)$$

$$v_L^* = v_L \cdot \rho_L^{0.5} \cdot (g \cdot de \cdot (\rho_L - \rho_V))^{-0.5} \quad (2.32)$$

where  $v_V$  and  $v_L$  are the velocities of the vapor and of the solution flows, respectively, and  $de$  is the diameter of the duct.

In this case, since there is no tubular column but rectangular ducts, the equivalent diameter  $de$  is introduced:

$$de = 1.30 \cdot \frac{(a \cdot b)^{0.625}}{(a+b)^{0.25}} \quad (2.33)$$

where  $a$  and  $b$  are the width of the section of the rectangular duct.

(Eq. 2.30) characterizing the flooding in vertical columns takes into account the length effect. The coefficient  $m$  depends on the ratio between the length of the plate and the equivalent diameter and is given by:

If  $\left(\frac{L}{de}\right) \leq 120$ ,

$$m = 0.1928 + 0.01089 \cdot \left(\frac{L}{de}\right) - 3.754 \cdot 10^{-5} \cdot \left(\frac{L}{de}\right) \quad (2.34)$$

If  $\left(\frac{L}{de}\right) > 120$ ,

$$m = 0.96 \quad (2.35)$$

After experimental tests on various previous methods and studies, (Jayanti and Hewitt 1992) determined that the flooding coefficient  $C$  should not be greater than 1 to avoid the formation of waves at the liquid–vapor interface. Then, while the coefficient  $C < 1$ , the ammonia vapor generated and the ammonia–water solution flow in the desorber without the appearance of flooding.

The correlation of (Wallis 1961) is one of the first to be established; however, further studies have stressed that it does not take into account the surface tension effects (Guichet and Jouhara 2020). At intermediate and high liquid film Reynolds numbers, flooding has to be correlated with the surface tension at the liquid–vapor interface, because its impact on the film flow becomes significant (El-Genkand Saber 1997).

Thus, (Faghri et al. 1989) determined a new correlation using the Bond number:

$$Bo = de \cdot \left(\frac{g \cdot (\rho_L - \rho_V)}{\sigma}\right)^{0.5} \quad (2.36)$$

with  $\sigma$  the surface tension at the liquid–vapor interface. The onset of the entrainment of the solution in the vapor flow is characterized by the maximal heat rate in the liquid–vapor mixture:

$$\dot{Q}_{flooding} = K \cdot S_{exch} \cdot Lv \cdot \rho_V^{0.5} \cdot (\sigma \cdot g \cdot (\rho_L - \rho_V))^{0.25} \cdot \left(1 + \left(\frac{\rho_V}{\rho_L}\right)^{0.25}\right)^{-2} \quad (2.37)$$

with  $S_{exch}$  the exchange surface,  $Lv$  the latent heat of vaporization, and  $K$  defined as:

$$K = \left(\frac{\rho_L}{\rho_V}\right)^{0.14} \cdot \tanh^2(Bo^{0.25}) \quad (2.38)$$

(Guichet and Jouhara 2020) recommend the use of this correlation that has a good reliability with several working fluids. The falling-film heat transfer coefficient depends on the thickness of the film, the flow regime, and the interface interactions between liquid and vapor. It takes into account the shear stress, particularly when vapor flows counter-current from the liquid.

### III.3. Heat and mass transfer at the solution-vapor interface of an ammonia-water solution falling film

Besides the Reynolds number introduced in *Sect.III.2.1*, other relevant non-dimensional parameters are used to characterize the dynamics of the falling-film flow and the heat and mass transfer occurring between the film and the vapor flow.

#### III.3.1 Characteristic numbers

The Nusselt number characterizes the importance of the convection heat transfer compared to the conduction heat transfer, with  $L_{sp}$  the characteristic length,  $h$  the convective heat transfer coefficient, and  $\lambda$  the thermal conductivity in the liquid film.

$$Nu = \frac{h \cdot L_{sp}}{\lambda} \quad (2.39)$$

The Prandtl number measures the ratio of momentum diffusion to thermal diffusion in the liquid film, with  $C_p$  the specific capacity.

$$Pr = \frac{C_p \cdot \mu}{\lambda} \quad (2.40)$$

The Sherwood number is used to characterize the mass transfer between a fluid and an interface. It is written as the ratio between convection mass transfer and diffusion mass transfer, with  $D$  the mass diffusivity.

$$Sh = \frac{k \cdot L_{sp}}{D} \quad (2.41)$$

The Schmidt number characterizes fluid flows in which momentum and mass diffusion convection processes occur. It is written as the ratio of momentum diffusivity ( $\nu$  the kinematic viscosity) to mass diffusivity.

$$Sc = \frac{\nu}{D} \quad (2.42)$$

The Weber number characterizes the fluid flow at the interface of a multiphase system. It is written as the ratio between the inertia force and the surface tension force, with  $\rho_{mix}$  the density of the homogeneous mixture, and  $G$  the mass flowrate per cross section area.

$$We = \frac{\dot{m}''^2 \cdot Dh_L}{\sigma \cdot \rho_{mix}} \quad (2.43)$$

The Froude number, defined as the ratio between the kinetic and the potential energies, is mainly used to characterize the free-surface flows.

$$Fr = \frac{\dot{m}''^2}{g \cdot Dh_L \cdot \rho_{mix}} \quad (2.44)$$

### III.3.2 Heat and mass transfer inside a falling film

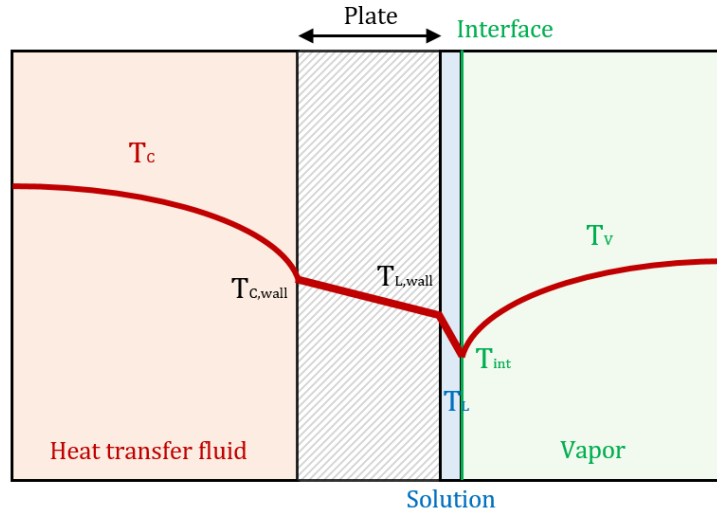


**Figure 2.23.** Temperature profile during desorption phenomenon in a falling-film.

At the solution–vapor interface, four main types of transfers take a part. The heat transfer from the liquid to the vapor phase, the heat transfer from the vapor to the liquid phase, the mass transfer at the liquid side and the mass transfer at the vapor side.

According to (Goel and Goswami 2005), who use the correlation previously established by (Yih and Chen 1982), the mass transfer coefficient for the liquid phase  $k_L$  is:

$$k_L = (0.01099 \cdot Re_L^{0.3955} \cdot Sc_L^{0.5}) \cdot \left( D_L \cdot \left( \frac{g}{\nu_L^2} \right)^{1/3} \right) \quad (2.45)$$

This correlation can be applied for a Reynolds number in the range of  $49 < Re_L < 300$ . The model was developed for laminar, wavy and turbulent falling film, near the liquid–vapor interface, solely in the case of fully developed conditions, and the values of the constants were established by fitting experimental data from 11 researchers, for falling film over a pipe of 183 cm.

The convective heat transfer coefficient between the vapor and the interface was established by (Kakaç et al. 1987), solely for fully developed profiles of velocity and temperature. The correlation is based on laminar flow conditions inside a parallel plate channel. The temperature at the interface is assumed to be uniform, and the edge effects due to the finite dimensions of the plates are neglected.

The convective heat transfer coefficient  $h_V$  is:

$$h_V = 7.541 \cdot \frac{\lambda_V}{D_{hV}} \quad (2.46)$$

The heat and mass transfer analogy developed by (Chilton and Colburn 1934) (Eq. 2.47) can be applied in (Eqs. 2.45–2.46) to obtain the heat transfer coefficient between the liquid phase and the interface (Eq. 2.48), and to obtain the mass transfer coefficient of the vapor phase (Eq. 2.49).

$$h = C_p \cdot k \cdot \rho \cdot \left(\frac{Sc}{Pr}\right)^{2/3} \quad (2.47)$$

$$h_L = C_{p,L} \cdot k_L \cdot \rho_L \cdot \left(\frac{Sc_L}{Pr_L}\right)^{2/3} \quad (2.48)$$

$$k_V = \frac{h_V}{C_{p,V} \cdot \rho_V} \cdot \left(\frac{Pr_V}{Sc_V}\right)^{2/3} \quad (2.49)$$

The study of the heat and mass transfer occurring at the liquid–vapor interface is a common topic of research for many solution–vapor absorption and desorption processes.

### III.3.3 Falling-film boiling

In the falling film of the generator, the heat flux coming from the HTF slowly increases the solution temperature, leading to the evaporation process. However, if the heat flux is high, causing a quick increase in solution temperature, it can lead to the boiling of the falling film. An evaluation of the first occurrence of the film boiling is essential to check that the processes occurring in the desorber are still those of the evaporation process. Indeed, heat transfer correlations used to characterize evaporation are different from those used to characterize boiling. As for the pool boiling process, the bubbles are first created inside the falling film, at the plate wall. Assuming that the temperature of the solution has to be superheated to allow the bubbles to grow from the equilibrium bubble radius  $r^*$ , (Rohsenow 1998) gives the following condition:

$$T_L - T_{sat} = \frac{2 \sigma \cdot T_{sat}}{r^* \cdot L_v \cdot \rho_V} \quad (2.50)$$

where  $T_{sat}$  is the saturation temperature of the solution falling-film.

Two boiling temperature differences can be calculated: either when the saturation temperature is the temperature of the interface between the liquid and vapor phases, or when the saturation temperature corresponds to the solution properties at the wall.

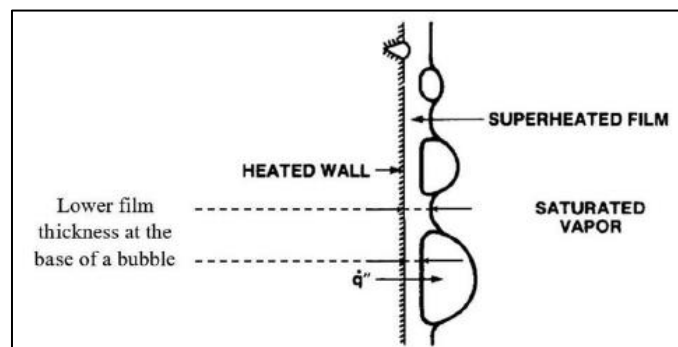


Figure 2.24. Falling-film boiling representation by (Cerza and Semas 1985).

### III.3.4 Notion of dry-out of the plate

(Madrid et al. 2007) proved the existence of a unique dry-out critical velocity where the interface between liquid and vapor becomes unstable. The vapor flow could drive some liquid with it and for high velocities the liquid falling film could break away from the wall. At this point, the heat transfer coefficient value decreases drastically. The total superficial velocity inside a channel is defined in the critical conditions where a dry-out can appear by:

$$j = \frac{\dot{m}_{tot}}{A \cdot \rho_{2ph}} \quad (2.51)$$

with  $\dot{m}_{tot} = \dot{m}_L + \dot{m}_V$  the overall mass flowrate of the two phases,  $A$  the cross section area, and  $\rho_{2ph}$  the homogeneous density of the two phases written as:

$$\rho_{2ph} = \left( \frac{y}{\rho_V} + \frac{1-y}{\rho_L} \right)^{-1} \quad (2.52)$$

$\rho_V$  and  $\rho_L$  are the densities of vapor and liquid phase, respectively, and  $y$  is the ammonia vapor concentration. Then, the superficial velocity  $j$  is given by:

$$j = \frac{\dot{m}_{tot} \cdot y}{A \cdot \rho_V} + \frac{\dot{m}_{tot} \cdot (1-y)}{A \cdot \rho_L} \quad (2.53)$$

The appearance of dry patches is directly linked to the shear stress between falling-film solution and counter-current flow vapor that could carry away the solution; to the evaporation process that can quickly reduce the thickness of the film; to the good wettability of the plates; to the potential boiling of the film; and to the difference of surface tension along the film (Rohsenow 1998). The highly heated wall causes the appearance of dry surfaces at local points. (Hartley and Murgartroyd 1964) gave the minimum linear wetting flowrate  $\dot{m}'_{wett,crit}$  that must be reached in order to avoid those dry patches:

$$\dot{m}'_{wett,crit} = 1.69 \cdot \left( \frac{\mu_L \cdot \rho_L}{g} \right)^{1/5} \cdot (\sigma \cdot (1 - \cos\theta))^{3/5} \quad (2.54)$$

Then, it corresponds to a critical thickness of the falling film, written as:

$$\delta_{crit} = 1.72 \cdot \left( \frac{\mu_L}{g \cdot \rho_L} \right)^{2/5} \cdot \left( \frac{\sigma \cdot (1 - \cos\theta)}{\rho_L} \right)^{1/5} \quad (2.55)$$

(Norman 1960) defined the contact angle between the liquid and the wall as  $\theta = 10^\circ$ , in order to have a sufficient linear wetting rate, allowing the solution to wet the whole plate and avoid dry patches.

However, boiling is another process, different from falling-film evaporation, purposely applied to a solution for releasing the ammonia vapor from the mixture (see Sect.II.2.3 for the pool boiling process description).

### III.3.5 Heat and mass transfer during the pool boiling of ammonia–water solution

Many correlations and models are available in the literature for flow boiling and pool boiling. Depending on the wall superheat temperature; the process of pool boiling occurs through four different mechanisms: natural convective boiling, nucleate boiling, transition boiling, and film boiling.

The wall superheat temperature is defined as the difference between the wall temperature and the solution saturation temperature:

$$\Delta T_{w,sat} = T_w - T_{sat} \quad (2.56)$$

### III.3.5.1 Pool boiling mechanisms

In this study, two main mechanisms of pool boiling are investigated: convective boiling and nucleate boiling.

Convective boiling occurs when the solution temperature at the heated wall is a few degrees above its saturation temperature. At the solution–vapor interface, there is a heat transfer with the phase change occurring by evaporation, and the vapor formation is maintained because the liquid–vapor interface temperature is also over the saturation temperature. The motion of the solution is induced by natural free convection and eventually by the bubble growth and detachment, when the temperature of the onset of nucleate boiling is reached.

Nucleate boiling occurs when the wall superheat temperature increases. Vapor bubbles form at the heated wall, after which they break away and flow to the solution surface. The heat generated at the wall surface during the bubble formation is carried directly into the solution, thus enhancing the heat transfer process in the solution.

The heat transfer coefficient correlations are classified depending on the dominant boiling, either one of the mechanisms is dominant, as for the convective boiling correlation developed by (Inoue and Monde 2008) or two boiling phases can contribute to the heat transfer as for the convective boiling combined with the nucleate boiling in the correlation of (Chen 1966). The correlations developed and used in this study are presented in *Chapter IV, Part IV*, of the manuscript.

### III.3.5.2 Review of some boiling models.

Various studies focusing on the nucleate boiling and natural or forced convective boiling of refrigerant binary mixtures are available in the literature, leading to the development of many heat transfer correlations. (Stephan and Korner 1969) determined a nucleate boiling heat transfer coefficient based on a correlation taking into account the mixture through the concentration of refrigerant contained in the liquid and vapor phases. (Calus and Rice 1972) developed a correlation for pool boiling of a binary liquid mixture (with acetone, isopropanol, and water), and found that the nature and the structure of the heat transfer surface significantly affects their correlation. (Benett and Chen 1980) formulated a correlation of heat transfer coefficient for forced convective boiling of aqueous mixtures of ethylene glycol and pure fluids in the annular flow regime, taking into account the mass transfer and the Prandtl number effects. (Mishra et al. 1981) developed heat transfer coefficient correlations of forced convection evaporation of R-12 and R-22 mixtures in a horizontal tube. (Jung and Radermacher 1993) studied the predictability of heat transfer coefficients of refrigerant mixtures in horizontal tubes for an evaporating temperature range from -10° to 10°C. When the mixture quality is lower than 20%, the heat transfer is mainly due to nucleate boiling, while for higher qualities, the convective evaporation mechanism prevails over the nucleate boiling process. At a microscopic level, (Kandlikar 1998) evaluated the mixture effects on heat transfer for pool boiling, involving a volatility parameter. For this, he derived the heat transfer coefficient, by analytical prediction of the interface temperature and equilibrium concentration of growing bubble, and took into account the mass diffusion effects. His model, compared to other models, can predict heat transfer coefficients of azeotrope mixtures and water-based mixtures.

Although many correlations were developed to define boiling heat transfer, they are not specifically established for ammonia–water mixture. More recently, interest in ammonia–water boiling grew, with the renewal of studies on absorption chillers. (Khair et al. 2005b) conducted an experimental study on forced convective boiling heat transfer of ammonia–water inside a vertical smooth tube, testing the predictability of three literature models. They showed the significant influence of the heat and mass fluxes on the heat transfer coefficient, and confirmed the accuracy of various literature models with their measurements. (Sathyabhama and Ashok Babu 2011) led an experimental study on the visualization of bubble nucleation of an ammonia–water mixture on the external surface of a heated vertical cylinder. The increase in ammonia concentration led to the decrease in boiling heat transfer coefficient. (Taboas et al. 2007) made a bibliographic review of the literature available on correlations for ammonia–water nucleate pool boiling. They found a good agreement in the literature experimental data for the heat transfer coefficients of pure

water, but not for pure ammonia or for the mixture; thus, they developed a new correlation of the pool boiling heat transfer coefficient of the mixture based on experiments. (Kaern et al. 2016) applied many heat transfer correlations established in the literature for flow boiling of ammonia–water mixtures, and compared their influence on the design of a heat exchanger. They observed that the nucleate boiling contribution to the heat transfer is significant for low mass fluxes, low vapor qualities, and high heat fluxes; otherwise, the convective boiling contribution is dominant in the conditions of the ammonia–water boilers studied.

## IV. Synthesis

The second part of this work, the state of the art, introduces the technologies studied through an overall view and focuses on the most recent developments. The following points are investigated:

- + The single-effect absorption chiller operation with details on the roles and performances of its main components;
- + The choice of ammonia–water as the working fluid pair through a short review;
- + The existing technologies of generator, rectifier, and component combining the refrigerant vapor generation and purification functions, with a focus on the designs and fluid flows occurring inside these components;
- + The importance of the solution distribution system through the presentation of various designs of manifolds;
- + The characteristic phenomena of falling-film flow;
- + The heat and mass transfer occurring in a falling film through the correlations of the literature and the characteristic numbers of solution flow and of heat and mass transfer;
- + A review of pool boiling studies.

The presentation of various technologies and the related thermophysical phenomenon led to the following main conclusions:

- + In light of the current energy environment, and more particularly in terms of energy saving for air-conditioning systems, absorption chillers are an interesting alternative to the use of electric air-conditioners. This technology is a heat-driven system producing cold from heat that comes from different technologies and processes such as heat recovery, heating networks, and solar energy. Thermal compression, instead of mechanical compression, makes it possible to reduce the primary energy consumed. Absorption chillers already have a place on the air-conditioning systems market; however, they are only slightly competitive in terms of operating and maintenance costs, compactness, and performance (mainly the COP and cooling capacity). Thus, this technology performance and compactness should be improved, to enhance its attractiveness on the market;
- + The performance of the absorption chiller, and particularly of the generator, depends on the fluids used to operate it. The use of ammonia–water as a working pair allows the absorption chiller to operate at high pressure and in a large range of external source temperatures. Moreover, this working pair is favorable to optimization of internal heat and mass transfer, to limitation in pressure drops, to reductions in fluid quantity, and thus to a compact machine design;
- + Machine performance gains can be obtained by optimizing the generator–rectifier assembly, components that are often not widely studied in absorption machines. However, the study of the desorption process in an absorption chiller remains a relatively new topic with only few related publications; therefore, the desorption and rectification technologies and models should be studied;
- + Various designs of heat exchangers are developed such as tubular, plate, and microchannel exchangers. They involve either one main process of vapor generation, such as the pool boiling or the falling-film process, or both. The PHEs take advantage of the flexibility, easy maintenance, and low costs, and they enhance the thermal and mass transfer;
- + The generator and the rectifier are used for refrigerant vapor production and purification, respectively. Recent studies focus on bringing together both functions in the same component, in order to improve the vapor production and quality, while reducing the component size. Experiments and models developed have shown interesting results, for example the impact of the various desorber parameters on the performance of the absorption chillers studied;
- + A falling-film and plate combined generator, merging the generation and the purification of the ammonia vapor in the same component, appears to be a promising solution, in order to reduce the size, the costs, and the complexity of the absorption chiller;
- + The distribution of the solution in the exchanger is crucial, and in this regard, many studies investigate the impact of various manifold designs and their operation on the solution spreading. The distributor and headers presented are helping to design a new distribution system, which fits best the new plate heat generator studied;
- + In order to improve the comprehension of the ammonia vapor generation and purification processes, a precise description of the coupled heat and mass transfer occurring has to be developed. It should

include the several physical phenomena related to the falling film, such as the flow development, the solution-vapor surface tension and head losses, the mass transfers, the heat exchanges, the potential dry-out of the plates, and the appearance of boiling.

This synthesis leads to the objective of this PhD work, which consists in developing a falling-film and plate combined generator, bringing together both the generation and purification of ammonia vapor, producing a sufficient quantity of pure ammonia vapor not to use a rectifier at its outlet, to improve the performance, the compactness, and the costs of the  $\text{NH}_3\text{-H}_2\text{O}$  absorption chiller in which it is integrated.

A numerical model describing heat and mass transfer will be developed to design the combined generator. The model will be validated thanks to an experimental investigation on the integration of this new component in an  $\text{NH}_3\text{-H}_2\text{O}$  absorption chiller of 5-kW cooling capacity.

## V. References

- Abou Elmaaty T. M., Kabeel A. E., Mahgoub M., (2017), "Corrugated plate heat exchanger review", *Renewable and Sustainable Energy Reviews* 70, 852–860
- Abu-Khader M.M., (2012), "Plate heat exchangers: Recent advances", *Renewable and Sustainable Energy Reviews* 16, 1883–1891
- AFNOR. Norme EN 378 (2016) fixant les exigences de sécurité et d'environnement pour les systèmes frigorifiques mobiles et fixes de toutes tailles
- Balmer R.T., (2011), "Modern Engineering Thermodynamics", 14.10 *Absorption refrigeration*
- Bassiouny M. K., Martin H., (1984a), "Flow distribution and pressure drop in plate heat exchangers-I U-type arrangement", *Chemical Engineering Science* 39, 693–700
- Bassiouny M. K., Martin H., (1984b), "Flow distribution and pressure drop in plate heat exchangers-II Z-type arrangement", *Chemical Engineering Science* 39, 701–704
- Bennett D. L., Chen J.C., (1980), "Forced convective boiling in vertical tubes for saturated pure components and binary mixtures", *Applied International Chemical Journal* 26, 454–461
- Calus W. F., Rice P., (1972), "Pool Boiling-Binary liquid Mixtures," *Chemical Engineering Science* 27, 1687–1697
- Cerza M., Sernas V., (1985), "A bubble growth model for nucleate boiling in thin, falling, superheated, laminar, water films", *International Journal of Heat and Mass Transfer* 28, 1307–1316
- Chen J.C., (1966), "Correlation for boiling heat transfer to saturated fluids in convective flow", *Industrial and Engineering Chemistry Process Design and Development* 5, 322–329
- Chilton T.H., Colburn A.P., (1934), "Mass Transfer (absorption) coefficients", *Industrial and Engineering Chemistry Research* 26, 1183–1187
- Conde Engineering, (2004), "Thermophysical properties of NH<sub>3</sub>/H<sub>2</sub>O solutions for the industrial design of absorption refrigeration equipment"
- Delahanty J.C., Garimella S., Garrabrant M., (2015), "Design of compact microscale geometries for ammonia-water desorption", *Science and Technology for the Built Environment* 21, 365–374
- Delahanty J.C., Hughes M., Garimella S., (2021a), "Desorber and rectifier geometries for ammonia-water absorption systems; Part I: Experimental approach and heat transfer", *International Journal of Refrigeration* 123, 114–123
- Delahanty J.C., Hughes M., Garimella S., (2021b), "Desorber and rectifier geometries for ammonia-water absorption systems; Part II: Mass transfer, flooding, and component performance", *International Journal of Refrigeration* 122, 245–255
- Determan M.D., Garimella S., (2011), "Ammonia-water desorption heat and mass transfer in microchannel devices", *International Journal of Refrigeration* 34, 1197–1208
- Durmus A., Benli H., Kurtbas I., Gul H., (2009), "Investigation of heat transfer and pressure drop in plate heat exchangers having different surface profiles", *International Journal of Heat and Mass Transfer* 52, 1451–1457
- El-Genk M., Saber H.H., (1997), "Flooding limit in closed, two-phase flow thermosyphons", *International Journal of Heat and mass transfer* 40, 2147–2164
- Faghri A., Chen M-M., Morgan M., (1989), "Heat transfer characteristics in two-phase closed conventional and concentric annular thermosyphons", *Journal of Heat Transfer* 111, 611–618
- Fernandez-Seara J., Sieres J., Vazquez M., (2002), "Simultaneous heat and mass transfer of a packed distillation column for ammonia-water absorption refrigeration systems", *International Journal of Thermal Sciences* 41, 927–935
- Fernandez-Seara J., Sieres J., Vazquez M., (2003), "Heat and mass transfer analysis of a helical coil rectifier in an ammonia-water absorption system", *International Journal of Thermal Sciences* 42, 783–794

- Fernandes-Seara J., Sieres J., (2006), "The importance of the ammonia purification process in ammonia-water absorption systems", *Energy Conversion and Management* 47, 1975–1987
- Garimella S., Keinath C., Delahanty J.C., Hoysall D.C., Staedter M.A., Goyal A., Garrabrant M.A., (2016), "Development and demonstration of a compact ammonia-water absorption heat pump prototype with microscale features for space-conditioning applications", *Applied Thermal Engineering* 102, 557–564
- Goel N., Goswami D.Y., (2005), "Analysis of a counter-current vapor flow absorber", *International Journal of Heat and Mass Transfer* 48, 1283–1292
- Golden J. H., (2012), "Ammonia-water desorption in flooded columns", *Georgia Institute of Technology*
- Guichet V., Jouhara H., (2020), "Condensation, evaporation and boiling of falling-films in wickless heat pipes (two-phase closed thermosyphons): a critical review of correlations", *International Journal of Thermofluids* 1–2, 100001
- Hassan J.M., Mohamed T.A., Mohammed W.S., Alawee W.H., (2014), "Modeling the uniformity of manifold with various configurations", *Journal of Fluids* 11, 1–9
- Hartley D.E., Murgatroyd W., (1964), "Criteria for the break-up of thin liquid layers flowing isothermally over solid surfaces", *International Journal of Heat and Mass Transfer* 7, 1003–1015
- Herold K.E., Radermacher R., Klein S.A., (2016), "Absorption chillers and heat pumps, second edition", *CRC Press, Taylor and Francis Group*
- Hessami Ma., (2000), "Surface temperature and heat transfer measurements in cross corrugated plate heat exchangers", *Iran J Sci Technol* 24, 283–97
- Inoue T., Kawae N., Monde M., (1998), "Characteristics of heat transfer coefficient during nucleate pool boiling of binary mixtures", *Heat and Mass Transfer* 33, 337–344
- Inoue T., Monde M., (2008), "Prediction of pool boiling heat transfer coefficient in ammonia-water mixtures", *Transactions of the Japan Society of Mechanical Engineers, Part B* 74, 1114–1118
- Jayanti.S, Hewitt.G.F, (1992), "Prediction of the slug-to-churn flow transition in vertical two-phase flow", *International Journal of Multiphase Flow* 18, 847–860
- Jiao A., Zhang, R., Jeong S., (2003), "Experimental investigation of header configuration on flow maldistribution in plate-fin heat exchanger", *Applied Thermal Engineering* 23, 1235–1246
- Jung D. S., Radermacher R., (1993), "Prediction of heat transfer coefficient of various refrigerants during evaporation", *International Journal of Refrigeration* 16, 201–209
- Kaern M.R., Modi A., Jensen J.K., Andreasen J.G., Haglind F., (2016), "An assessment of in-tube flow boiling correlations for ammonia-water mixtures and their influence on heat exchanger size", *Applied Thermal Engineering* 93, 623–638
- Kakaç S., Shah R.C., Aung W., (1987), "Handbook of Single-phase Convective Heat Transfer", *John Wiley and Sons Inc.*
- Kandlikar S.G., (1998), "Boiling heat transfer with binary mixtures: Part I–A theoretical model for pool boiling", *Journal of Heat Transfer* 120, 380–387
- Keinath C.M., Hoysall D., Delahanty J.C., Determan M.D., Garimella S., (2015), "Experimental assessment of a compact branched tray generator for ammonia-water desorption", *Science and Technology for the Built Environment* 21, 348–356
- Keinath C.M., Nagavarapu K.A., Dalahanty J.C., Garimella S., Garrabrant M.A. (2019), "Experimental assessment of alternative compact configurations for ammonia-water desorption", *Applied Thermal Engineering* 161, 113852
- Kenning D.B.R., (2019), "Pool Boiling", [www.thermopedia.com](http://www.thermopedia.com)
- Kherris S., (2008), "Simulation des cycles de machines frigorifiques à absorption", *Magister, Université Ibn Khaldoun-Tiaret, Algérie*
- Khir T. Brahim A., Jassim R., (2005), "Boiling by forced convection of water ammonia mixtures in a vertical tube", *Canadian journal of chemical engineering* 83, 466–476

- Khair T., Jassim R., Gahffour N., Ben Brahim A., (2005), "Experimental study on forced convective boiling of ammonia–water mixtures in a vertical smooth tube", *Arabian Journal for Science and Engineering* 30
- Kim N., Byun H., (2013), "Effect of inlet configuration on upward branching of two-phase refrigerant in a parallel flow heat exchanger", *International Journal of Refrigeration* 36, 1062–1077
- King H.H., Hall J.L., Ware G.C., (1930), "A study of the density, surface tension and adsorption in the water ammonia system at 20°C" *Journal of the American Chemical Society* 52, 5128–5135
- Koch–Glitsch, (2009), Liquid distribution data sheet
- Kuznetsov V., (2018), "Two-Phase Heat Exchangers", *Handbook of Thermal Science and Engineering*. Springer, 1473–1500
- Lima A.A.S., Leite G.N.P., Alvaro A. V. Ochoa A.A.V., Dos Santos C.A.C., Da Costa J.A.P., Michima P.S.A., Caldas A.M.A., (2021), "Absorption refrigeration systems based on ammonia as refrigerant using different absorbents: review and applications", *Energies* 14 (1)
- Madrid F., Caney N., Marty P., (2007), "Study of a Vertical Boiling Flow in Rectangular Mini-Channels", *Heat Transfer Engineering* 28, 753–760
- Marciss R.A., Gutraj J.M., Zawacki T.S., (1988), "Absorption fluid data survey: final report on worldwide data", *ORLN/sub/8447989/3–Inst. Gas Tech*
- Mishra M. P., Varma H. K., and Sharma C. P., (1981), "Heat Transfer Coefficients in Forced Convection Evaporation of refrigerants mixtures", *Letter in Heat and Mass Transfer* 8, 127–136
- Mittermaier M., Ziegler F., (2015), "Theoretical evaluation of absorption and desorption processes under typical conditions for chillers and heat transformers", *International Journal of Refrigeration* 59, 91–101
- Norman W.S., (1960), "Heat transfer to a liquid film on a vertical surface", *Transactions of the Institution of Chemical Engineers* 27, 301–307
- Nusselt W., (1916), "Die oberflächenkondensation des wasserdampfes", *Z. Vereines Deutsch* 60, 541–575
- Roeder A., Goyal A., Garimella S. (2019), "Transient simulation of ammonia–water mixture desorption for absorption heat pumps", *International Journal of Refrigeration* 100, 354–367
- Rohsenow W.M., Hartnett J.P., Cho Y.I., (1998), "Handbook of heat transfer", Third Edition, McGraw-Hill
- Sathyabhama A., Ashok Babu T.P., (2011), "Nucleate pool boiling heat transfer measurement and flow visualization for ammonia–water mixture", *Journal of Heat Transfer* 133, 101506
- Schlünder EU., (1983), "Heat transfer in nucleate boiling of mixtures", *International Chemical Engineering* 23, 589–599
- Shakir R. and S., (1987), "New Correlation for Nucleate Boiling of Binary Mixtures", *AIChE Symposium Series*
- Spindler K., (2010), "Overview and discussion on pool boiling heat and mass transfer and correlations of ammonia", *International journal of refrigeration* 33, 1292–1306
- Srikhirin P., Aphornratana S., Chungpaibulpatana S., (2001), "A review of absorption refrigeration technologies" *Renewables and Sustainable Energy Reviews* 5, 343–372
- Staedter M. A., Garimella S., (2018a), "Direct-coupled desorption for small capacity ammonia–water absorption systems", *International Journal of Heat and Mass Transfer* 127, 196–205
- Staedter M.A., Garimella S., (2018b), "Thermodynamic considerations for optimal thermal compressor design", *International Journal of Refrigeration* 91, 28–38
- Staedter M.A., Garimella S., (2018c), "Design and modeling of a microscale diabatic distillation column for small capacity ammonia–water absorption systems", *International Journal of Refrigeration* 94, 161–173
- Staedter M.A., Garimella S., (2018d), "Heat and mass transfer in microscale diabatic distillation columns for ammonia–water desorption and rectification", *International Journal of Refrigeration* 95, 10–20
- Staedter M.A., Garimella S., (2018e), "Development of a micro-scale heat exchanger based, residential capacity ammonia–water absorption chiller", *International Journal of Refrigeration* 89, 193–103

- Stephan K., Abdelsalam M., (1980), "Heat transfer correlation for natural convection boiling", *International Journal of Heat and Mass Transfer* 23, 73–87
- Stephan K., Korner M., (1969), "Calculation of heat transfer in evaporating binary liquid Mixtures", *Chemie Ingenieur Technik* 41, 409–417
- Straub J., Rosner N., Grigull U., (1980), "Oberflächenspannung von leichten und schweren Wasser", *Wärme und stoffübertragung* 13, 241–252
- Strobbe M., Van Egmond J., (1989), "European patent application, Splash plate liquid distributor", *Dow Chemical*
- Sun J., Fu L., Zhang S., (2012), "A review of working fluids of absorption cycles", *Renewable and Sustainable Energy Reviews* 16, 1899–1906
- Taboas F., Valles M., Bourouis M., Coronas A., (2007), "Pool boiling of ammonia–water and its pure components: Comparison of experimental data in the literature with the predictions of standard correlations", *International journal of Refrigeration* 30, 778–788
- Taboas F., Valles M., Bourouis M., Coronas A., (2010), "Flow boiling heat transfer of ammonia–water mixture in a plate heat exchanger", *International journal of Refrigeration* 33, 695–705
- Triché D., (2016), "Étude numérique et expérimentale des transferts couplés de masse et de chaleur dans l'absorbeur d'une machine à absorption ammoniac-eau", *Université de Grenoble Alpes*
- Tsay Y.L., Lin T.F., (1995), "Evaporation of a heated falling liquid film into a laminar gas stream", *Experimental Thermal and Fluid Science* 11, 61–71
- Wallis G. B., (1961), "Flooding velocities for air and water vertical tubes", *UKAA Report, AEEW-R123*
- Wang J., Wang H., (2015), "Discrete method for design of flow distribution in manifolds", *Applied Thermal Engineering* 89, 927–945
- Wen J., Li Y., Zhou A., Ma Y., (2006), "PIV Investigations of flow patterns in the entrance configuration of plate–fin heat exchanger", *Chinese Journal of Chemical Engineering* 14, 15–23
- Yang J., Jacobi A., Liu W., (2017), "Heat transfer correlations for single-phase flow in plate heat exchangers based on experimental data", *Applied Thermal Engineering* 113, 1547–1557
- Yih S.M., Chen K.Y., (1982), "Gas absorption into wavy and turbulent falling liquid films in a wetted-wall column", *Chemical Engineering Communication* 17, 123–136
- Zavaleta–Aguilar E.W., Simoes–Moreira J.R., (2015), "Horizontal tube bundle falling-film distiller for ammonia–water mixtures", *International Journal of Refrigeration* 59, 304–316



## **Part III: Design and performance predictions**

*The third part of this manuscript is dedicated to the design of the combined generator and the prediction of the performance of the absorption machine equipped with this new exchanger.*

*This part is divided in two chapters. The first chapter presents the numerical model developed to describe the combined generator performances, its validation, and its use to determine the best operating conditions. In the second chapter, the results of the model are used to estimate the performance of the  $\text{NH}_3\text{-H}_2\text{O}$  absorption chiller equipped with the combined generator on the basis of an effectiveness method.*



# Chapter I

## Design of a new falling-film and plate combined generator

---

### Objective:

*The purpose of the first chapter is to expose the design methodology of a new compact combined generator able to replace a flooded generator-separators-rectifier assembly in an  $\text{NH}_3\text{-H}_2\text{O}$  absorption chiller dedicated to air-conditioning.*

### Based on:

Wirtz M, Stutz B, Phan H.T., Boudéhenn F.

“Numerical modeling of falling-film plate generator and rectifier designed for  $\text{NH}_3\text{-H}_2\text{O}$  absorption machines”

*Heat and Mass Transfer* 58, 431–446 (2022)

<https://link.springer.com/article/10.1007%2Fs00231-021-03111-z>



*This chapter presents the development of a new generator-rectifier component, called “combined generator”, designed to be integrated and operated in a compact single-stage absorption chiller of approximately 5-kW cold capacity for air-conditioning. This new falling-film and plate heat exchanger combines an upper adiabatic part dedicated to the vapor purification and a lower heated part dedicated to the vapor generation.*

*First, the heat and mass processes occurring along the falling film are modeled using correlations from the literature, equilibrium condition at the solution-vapor interface, as well as mass, species, and energy balances. Then, co-current and counter-current operation modes are simulated and compared in order to determine the most performant configuration. Then, the model is used to investigate the impact of the operating conditions of the combined generator on its performance, such as the ammonia concentration in the vapor produced and the combined generator efficiency as a function of the inlet temperatures or mass flowrate of the heat transfer fluid. The impacts of the combined generator geometry are also examined through the length and number of plates, as well as the adiabatic/heated ratio of the plates. Finally, some aspects of the operating costs for cooling capacity are discussed, involving the influence of the combined generator geometry.*

## 1 Introduction

As explained in the *Part II. State of the art*, the performance of an  $\text{NH}_3\text{-H}_2\text{O}$  absorption chiller depends on the quantity and purity of the ammonia vapor transferred to the condenser. Thus, vapor rectification is usually needed to remove the water traces in the vapor produced by the generator. The heat and mass losses induced by the rectification process affects the coefficient of performance of the  $\text{NH}_3\text{-H}_2\text{O}$  absorption chillers which is lower than that of the  $\text{LiBr-H}_2\text{O}$  machines. The heat rejected at the rectifier level is as important as the fraction of water in the vapor at the exit of the generator is important.

Combining a generator and a rectifier is a way to optimize the design of  $\text{NH}_3\text{-H}_2\text{O}$  absorption chillers, which allows one to reduce operating costs and at the same time avoids the need for separators and pipes at the generator outlet. Multiples technologies are presented in the *Part II. State of the art*, as the flooded desorption column combining generation and rectification of  $\text{NH}_3$  vapor (Staedter and Garimella 2018). Another way to combine a generator and a rectifier is to take advantage of the opportunities offered by plate heat exchangers (*PHE*). They are known for their high thermal efficiency, flexibility, and low production and maintenance costs (Abou Elmaaty et al. 2017). They allow the use of falling-film design, which has proven to be efficient thanks to the high heat transfer rates (Golden 2012). In addition, their performance can be adjusted by modifying the number of plates, their length, and the plate spacing (Hessami 2000), which can also improve the absorption chiller compactness. The counter-current flow configuration (i.e., when the ammonia solution flows downward while the vapor rises from the bottom of the desorber to the top) has proved to be a better configuration. The system efficiency is enhanced through the partial absorption of the water traces by the solution film (Determan and Garimella 2011).

A falling-film plate combined generator associating generation and purification of refrigerant vapor appears to be a promising configuration for  $\text{NH}_3\text{-H}_2\text{O}$  absorption machines. It makes it possible to limit the water fraction in the vapor produced, by stimulating the heat and mass exchanges while being compact. This chapter focuses on the design of a combined generator for  $\text{NH}_3\text{-H}_2\text{O}$  compact absorption chillers of small cooling capacity (approximately 5 kW). The combined generator, represented in Figure 3.1, is composed of two sets of vertical plates (the adiabatic on top of the heated), involving falling-film. The ammonia-water mixture with a high concentration of ammonia is injected at the top, and flows downward along the plates. In the heated part, the HTF flows in counter-current mode compared to the falling-film. The generated vapor circulates from the bottom to the top of the exchanger, and interacts with the falling-film.

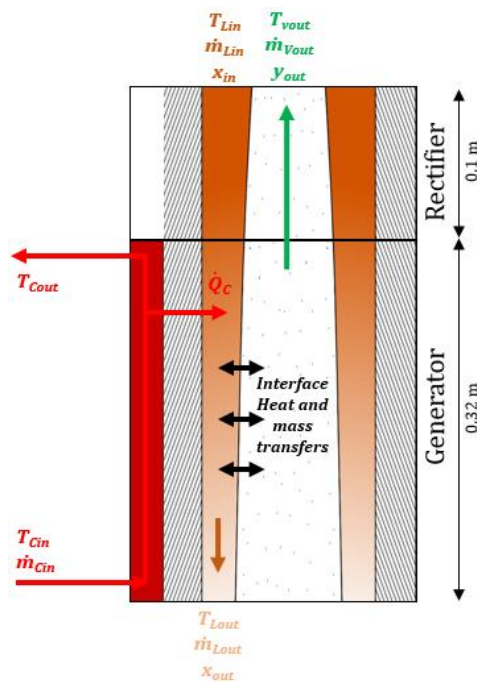


**Figure 3.1.** Schematic view of the combined generator with its main inputs and outputs, its dimensions, and the heat and mass transfers involved.

First, a one-dimensional model simulating the heat and mass transfer occurring in the combined generator is developed and validated through experimental measurements in absorption configuration. Then, the influence of the operating conditions and of the design parameters on the performance of the component is studied.

## 2 Numerical model

A numerical model is developed to describe heat and mass transfers in any type of falling-film plate heat exchanger. The ammonia–water solution flows down along the plates, heated or cooled by the HTF, which circulates in the same or opposite direction. The vapor generated or absorbed by the solution can circulate either in co-current or in counter-current configuration in relation to the solution flow. The numerical model is a one-dimensional model, describing the transfers within the heat exchanger through correlations from the literature and the use of balance equations and equilibrium equations at the interface between the solution falling-film and the generated vapor flow. The exchanger is discretized in “n” segments along its height. This model is based on the preliminary work of (Triché 2016), limited to the descriptions of heat and mass transfers for falling-film absorbers characterized by a co-current flow configuration. (Goel and Goswami 2005) and (Fernandez–Seara et al. 2005) studied the coupled heat and mass transfer processes occurring during the absorption of ammonia into a solution falling-film, using a finite-differential mathematical model, for a counter-current plate absorber and for a co-current vertical shell and tubes absorber, respectively. They led parametric analysis showing the impact of the design and operating conditions on the absorber performances. Authors show the high impact of the coolant inlet temperature on the absorber performance, as well as the inlet solution temperatures and mass flowrate (Fernandez–Seara et al. 2005).

The following assumptions are made, drawn from classic hypotheses found in the literature (Triché 2016; Goel and Goswami 2005; Fernandez–Seara et al. 2005), and the hypothesis 1 to 4 will be verified in part 4.2:

1. The calculations are performed in steady-state conditions;
2. The pressure does not vary along the plates (negligible pressure losses);
3. The flow regime of the falling-film is laminar smooth;
4. The plates are completely wet (no dry areas considered);
5. The generator is thermally insulated (negligible thermal losses);
6. The flows are homogeneously distributed between plates and according to their width;
7. The liquid–vapor interface is assumed to be in thermodynamic equilibrium.

(Goel and Goswami 2005) and (Fernandez–Seara et al. 2005) found that the liquid mass transfer resistance controls the overall absorption process. The effect of coolant flowrate and coolant inlet temperature on the reduction of the absorber’s size is found to be more significant than the effect of solution inlet temperature. Concentration gradients at the interface of the falling-film, at thermodynamic equilibrium between the solution and the vapor lead to NH<sub>3</sub> and H<sub>2</sub>O mass transfers through the interface (Goel and Goswami 2005):

$$dM_{NH_3} + dM_{H_2O} = k_L \cdot \rho_L \cdot dA_i \cdot \ln \left( \frac{z-x}{z-x_i} \right) = k_V \cdot \rho_V \cdot dA_i \cdot \ln \left( \frac{z-y_i}{z-y} \right) \quad (3.1)$$

Where  $dM_{NH_3}$  and  $dM_{H_2O}$  are the mass flowrates of ammonia and water transferred through the interface, both they can be absorbed or desorbed.  $x$  and  $y$  are the ammonia concentrations in the liquid and in the vapor phase, respectively.  $z$  is the mass flow fraction of ammonia that passes through the interface:

$$z = \frac{dM_{NH_3}}{dM_{NH_3} + dM_{H_2O}} \quad (3.2)$$

In the case of ammonia desorption,  $dM_{NH_3}$  is positive. Either water is desorbed ( $dM_{H_2O}$  is positive) and  $z < 1$  or water is absorbed ( $dM_{H_2O}$  is negative) and  $z > 1$ . In the case of ammonia absorption,  $dM_{NH_3}$  is negative. Either water is desorbed ( $dM_{H_2O}$  is positive) and  $z > 1$  or water is absorbed ( $dM_{H_2O}$  is negative) and  $z < 1$ .

The ammonia mass flowrate  $|dM_{NH_3}|$  transferred at the interface is greater than the water mass flowrate  $|dM_{H_2O}|$  transferred due to the higher volatility of ammonia. At the operating conditions of the combined generator, the vapor desorbed or absorbed at the interface, assumed in equilibrium with the solution, has an ammonia concentration superior to 95%.

At the interface, the ammonia concentration in the solution and in the vapor phase are calculated on the basis of the equations developed by (El-Sayed and Tribud 1985), which describe the bubble temperature and the dew temperature as a function of the ammonia concentration in the solution and in the vapor phase and of the pressure.

(Eqs. 3.3–3.6) describe the mass and species balances for the solution film and the generated vapor on one segment. Indices 1 and 2 refer to the upper and lower sections of the segment, respectively (see Figure 3.2).

$$\dot{m}_{L,1} - dM_{NH_3} - dM_{H_2O} = \dot{m}_{L,2} \quad (3.3)$$

$$\dot{m}_{V,1} + dM_{NH_3} + dM_{H_2O} = \dot{m}_{V,2} \quad (3.4)$$

$$\dot{m}_{L,1} \cdot x_1 - dM_{NH_3} = \dot{m}_{L,2} \cdot x_2 \quad (3.5)$$

$$\dot{m}_{V,1} \cdot y_1 + dM_{NH_3} = \dot{m}_{V,2} \cdot y_2 \quad (3.6)$$

Heat transfers inside the exchanger are described through transfer coefficients drawn from the literature (Goel and Goswami 2005). (Eqs. 3.7–3.9) present the heat transfer between the solution and the HTF, between the solution film and the liquid–vapor interface, and between the liquid–vapor interface and the vapor, respectively:

$$\dot{Q}_C = dAi \cdot U \cdot (T_{C,1} - T_{L,1}) \quad (3.7)$$

$$\dot{Q}_{sen,L} = h_L \cdot dAi \cdot (T_i - T_L) \quad (3.8)$$

$$\dot{Q}_{sen,V} = h_V \cdot dAi \cdot (T_i - T_V) \quad (3.9)$$

Where  $U$  is the global heat transfer coefficient taking into account the convective heat transfer between the HTF and the plate, the conduction within the plate, and the convective heat transfer between the plate and the solution film.  $h_L$  and  $h_V$  correspond to the heat transfer coefficient between the interface and the solution and between the interface and the vapor.

(Eqs. 3.10–3.12) give enthalpy balances for the HTF, the solution falling-film, and the generated vapor, respectively:

$$\dot{m}_{C,1} \cdot H_{C,1} - \dot{m}_{C,2} \cdot H_{C,2} - \dot{Q}_C = 0 \quad (3.10)$$

$$\dot{Q}_{sen,L} + \dot{Q}_C + \dot{m}_{L,1} \cdot H_{L,1} - \dot{m}_{L,2} \cdot H_{L,2} - dM_{NH_3} \cdot H_{L,NH_3,parti} - dM_{H_2O} \cdot H_{L,H_2O,parti} = 0 \quad (3.11)$$

$$\dot{Q}_{sen,V} + \dot{m}_{V,1} \cdot H_{V,1} - \dot{m}_{V,2} \cdot H_{V,2} + dM_{NH_3} \cdot H_{V,NH_3,i} + dM_{H_2O} \cdot H_{V,H_2O,i} = 0 \quad (3.12)$$

Where  $H_{L,NH_3,parti}$  and  $H_{L,H_2O,parti}$  are the partial enthalpies of ammonia and water in the solution at the liquid–vapor interface. In addition,  $H_{V,NH_3,i}$  and  $H_{V,H_2O,i}$  are partial enthalpies of ammonia and water in the vapor phase at the interface (corresponding to the enthalpies of pure ammonia vapor and pure water vapor). The enthalpies of the ammonia–water mixture are calculated from the Gibbs free energy method defined by (Ziegler and Trepp 1984).

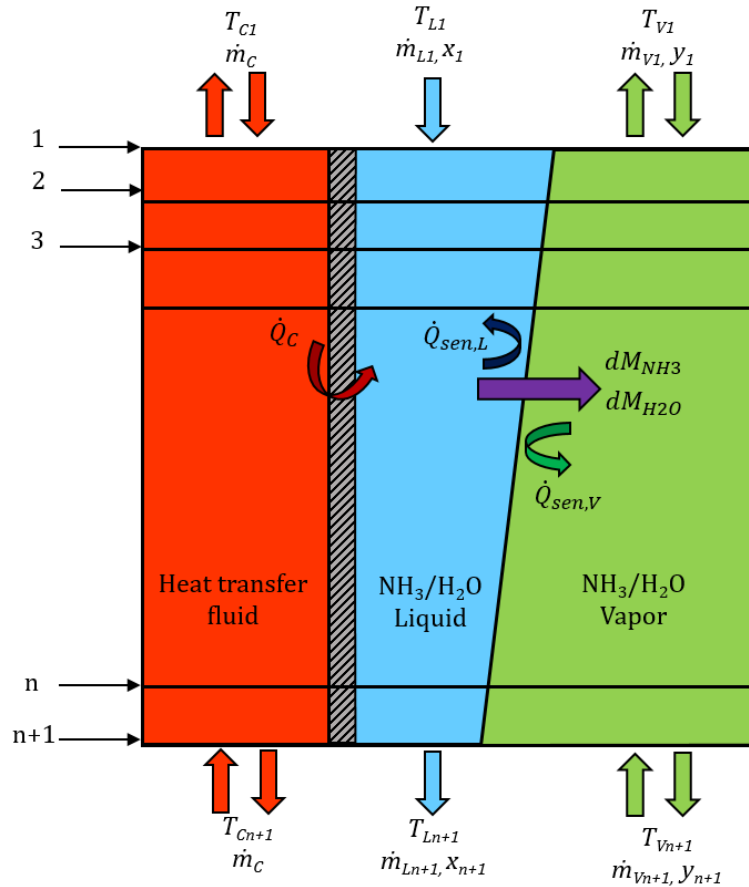


**Figure 3.2.** Schematic view of the heated part of the combined generator with the three fluid flows and the heat and mass transfers occurring in each segment.

All the thermodynamic properties of the ammonia, the water, and the mixture are calculated through Gibbs free energy, developed by (Ziegler and Trepp 1984). The numerical model is developed using Scilab software. The combined generator is discretized in 100 segments.

Three fluids circulate in each segment: the heat transfer fluid, the solution and the vapor flow. The balance equations (Eqs. 3.3–3.6) and (Eqs. 3.10–3.12) are used to calculate the state and the flowrate of each fluid at the outlet of the segment (in the direction of flow of the fluid considered) knowing the state and the flowrate of each fluid at the inlet of the segment. As no mass transfer can develop between the HTF and the solution, the mass flowrate and the composition of the HTF are constant and correspond to the values imposed at the exchanger inlet. Thus, 7 variables characterize the state of the fluid at the inlet and outlet of the segment:  $\dot{m}_L, \dot{m}_V, x, y, T_C, T_L, T_V$ .

A stationary method is used to solve the problem as illustrated in Figure 3.3 First, the geometrical parameters, the flowrate and the state of the fluid are set at their inlet in the exchanger. An initial distribution of the inlet flowrates and states of the fluids is assumed for each segment. The distribution of the outlet flowrates and states of the fluids is then calculated for each segment, integrating two iterative procedures, one on the interface temperature, and the other on the mass flow fraction. The results of the calculation are used as inlet conditions to perform a new iteration. The process is repeated until convergence of calculations.

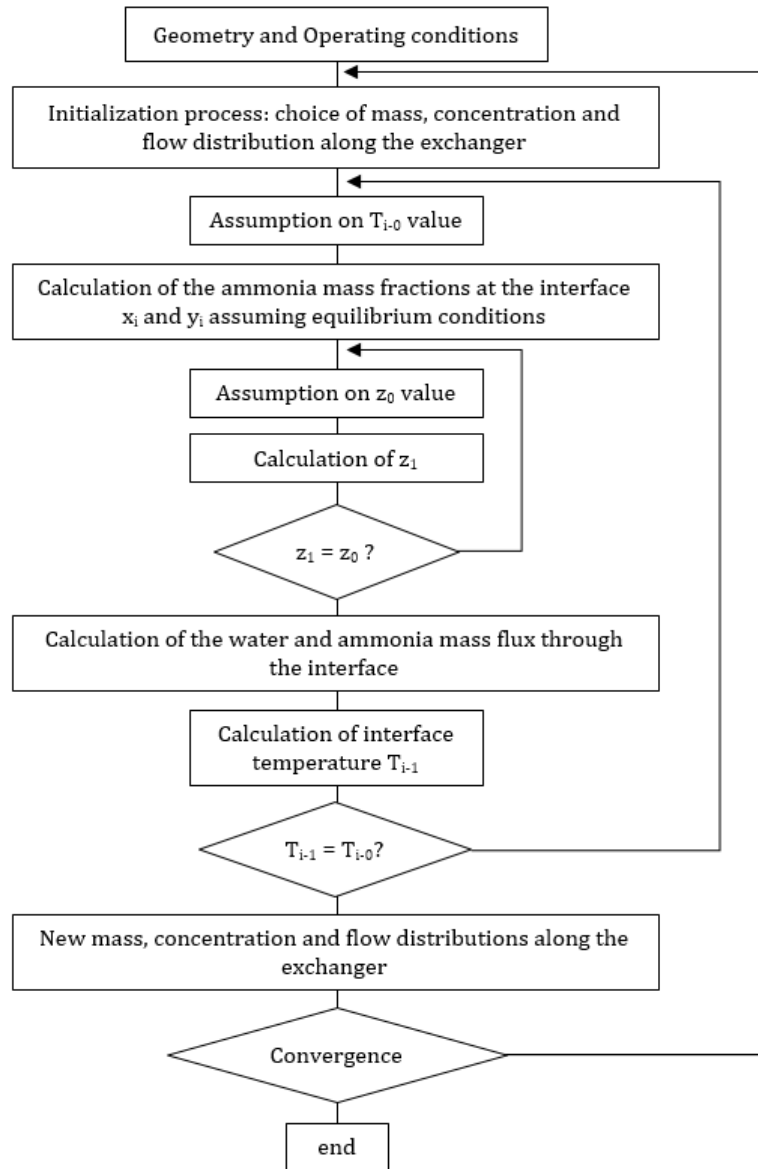


Figure 3.3. Numerical calculation scheme.

## 2.1 Boiling appearance

The onset of boiling depends on many parameters such as the cavity sizes, the wettability of the surface by the solution, and the temperature distribution within the liquid film. The appearance of boiling in the falling-film is estimated using the model developed by (Hsu 1962). The cavity radius range that could generate bubbles is given by (Eq. 3.13).

$$\left( \begin{matrix} r_{c,min} \\ r_{c,max} \end{matrix} \right) = \frac{\delta}{4} \cdot \left( 1 - \frac{T_{sat} - T_i}{T_w - T_i} \right) \sqrt{\left( 1 - \frac{T_{sat} - T_i}{T_w - T_i} \right)^2 - \frac{12.8 \cdot \sigma \cdot T_{sat}}{\rho_L \cdot Lv \cdot \delta \cdot (T_w - T_i)}} \quad (3.13)$$

Where  $T_w$  is the temperature at the wall,  $T_{sat}$  is the saturation temperature of the solution falling-film, and  $T_i$  is the temperature of the liquid-vapor interface.  $Lv$  is the latent heat of vaporization,  $\rho_L$  is the density of the solution,  $\sigma$  is the surface tension, and  $\delta$  is the thickness of the falling-film.

If the wall superheat becomes greater than the onset of boiling superheat ( $T_w - T_{sat} > T_{sat,ONB}$ ), boiling can occur. Heat and mass transfer occurring during boiling differs significantly from heat and mass transfer occurring during vaporization along the film interface, and thus new modeling has to be introduced.

Figure 3.4 presents the range of active cavity sizes that generate bubbles calculated using (Eq. 3.13) and the superheat of the wall, as a function of the position along the heated plates of the combined generator in the nominal case. The position along the combined generator corresponds to the distance covered by the solution along the plates from top to bottom. The heated part is located at 0.1 m downstream of the inlet of the combined generator. The plate is heated in counter-current mode in relation to the falling-film. The wall superheat is a maximum at 0.04 m downstream of the top of the heated plate, and due to the high ammonia concentration in this location, the film temperature increases first. It decreases downstream due to the decrease in the ammonia concentration (increase in the saturation temperature) even if the temperature of the solution increases. The range of active cavity lies between 0.2  $\mu\text{m}$  and 0.13 mm. In order to avoid the boiling process, the cavity radius of the plates has to be greater than 0.13 mm or smaller than 0.2  $\mu\text{m}$ . In this numerical study, it is assumed that the roughness of the plates is low enough (smooth surface) to avoid the appearance of nucleate boiling. Thus, the evaporation process correlations are applied along the plates.

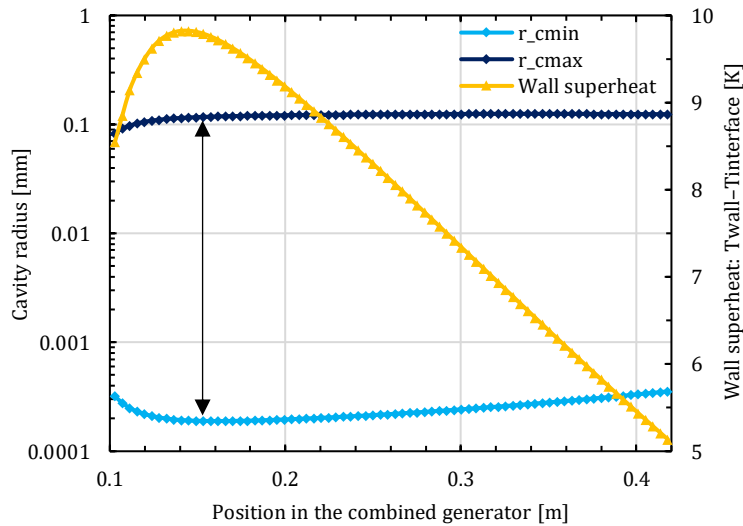


**Figure 3.4.** Range of active cavity radius and superheat of the wall as a function of the position in the combined generator.

Along the plates, the thickness of the falling-film, combined with the highly heated wall, can cause the appearance of dry surfaces at local points. (Eq. 2.54) gives the minimum linear wetting rate  $\Gamma_{\text{wett,crit}}$  estimated by (Hartley and Murgartroyd 1964) that must be reached in order to avoid dry patches and have a good wettability. In this study, the linear mass flowrate of the solution along the plates is higher than the linear wetting rate. Thus, the whole plates are considered wet and there are no dry patches, which validates hypothesis 4.

### 3 Model validation

The numerical model is validated through the experimental results obtained by (Triché 2016) involving an absorber plate with an ammonia–water solution falling-film. The absorber geometry is given in Table 3.1.

<b>Plate length</b>	0.668 [m]	<b>Number of plates</b>	16
<b>Plate width</b>	0.096 [m]	<b>Plate thickness</b>	0.5 [mm]

**Table 3.1.** Geometrical data of the absorber studied by (Triché 2016).

The operating conditions of the absorber corresponding to the inlet variables for the 10 tests run in a representative operation range are listed in Table 3.2.

Tests	$\dot{m}_{v,in}$ [kg/s]	$\dot{m}_{L,in}$ [kg/s]	$T_{v,in}$ [K]	$T_{L,in}$ [K]	$x_{in}$ [-]	$y_{in}$ [-]	P [MPa]	$T_{C,in,abs}$ [K]	$\dot{m}_{C,in,abs}$ [kg/s]
<b>Error</b>	$\pm 0.33 \%$	$\pm 0.35 \%$	$\pm 0.18 K$	$\pm 0.18 K$	$\pm 0.82 \%$	$\pm 1 \%$	$\pm 0.9 \%$	$\pm 0.15 K$	$\pm 1.16 \%$
<b>2-1</b>	$5.13 \cdot 10^{-3}$	$1.57 \cdot 10^{-2}$	298.60	312.19	0.458	0.998	0.607	300.11	$3.30 \cdot 10^{-1}$
<b>2-2</b>	$3.83 \cdot 10^{-3}$	$1.70 \cdot 10^{-2}$	297.89	317.41	0.488	0.995	0.629	304.12	$3.30 \cdot 10^{-1}$
<b>2-3</b>	$6.08 \cdot 10^{-3}$	$1.47 \cdot 10^{-2}$	298.37	309.19	0.433	0.998	0.598	297.11	$3.31 \cdot 10^{-1}$
<b>2-4</b>	$4.41 \cdot 10^{-3}$	$1.65 \cdot 10^{-2}$	298.34	310.27	0.500	0.998	0.621	300.18	$3.24 \cdot 10^{-1}$
<b>2-5</b>	$4.58 \cdot 10^{-3}$	$1.63 \cdot 10^{-2}$	298.28	313.69	0.463	0.997	0.578	300.19	$3.24 \cdot 10^{-1}$
<b>2-6</b>	$5.52 \cdot 10^{-3}$	$2.37 \cdot 10^{-2}$	294.68	315.60	0.490	0.992	0.603	300.13	$3.32 \cdot 10^{-1}$
<b>2-7</b>	$5.53 \cdot 10^{-3}$	$2.65 \cdot 10^{-2}$	293.66	317.36	0.498	0.991	0.604	300.14	$3.32 \cdot 10^{-1}$
<b>2-8</b>	$3.84 \cdot 10^{-3}$	$1.70 \cdot 10^{-2}$	296.53	318.48	0.473	0.998	0.629	300.06	$1.02 \cdot 10^{-1}$
<b>2-9</b>	$5.48 \cdot 10^{-3}$	$1.53 \cdot 10^{-2}$	300.7	311.4	0.447	0.999	0.609	300.29	$4.38 \cdot 10^{-1}$
<b>2-10</b>	$5.21 \cdot 10^{-3}$	$1.56 \cdot 10^{-2}$	295.1	312.5	0.452	0.993	0.603	300.16	$3.27 \cdot 10^{-1}$

**Table 3.2.** Operating conditions of the absorber studied by (Triché 2016).

The ability of the model to predict heat and mass transfer is analyzed through a comparison of the results from the experiments. Figure 3.5a and Figure 3.5b depicts the comparisons between this model and (Triché 2016) measurements, for the absorber internal power and the vapor mass flowrate absorbed, respectively.

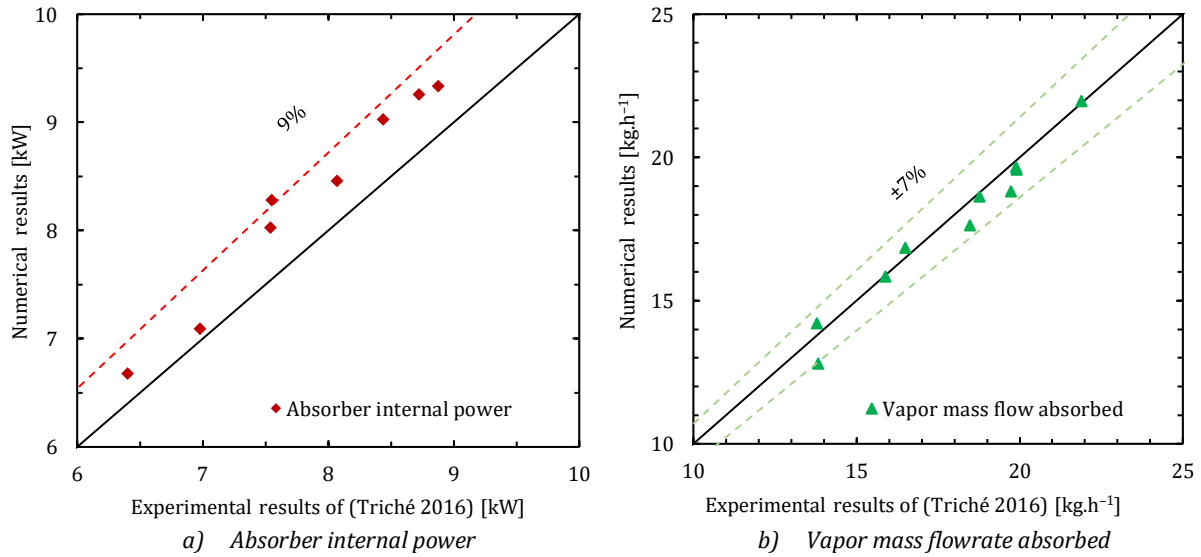


**Figure 3.5.** Comparison of absorber internal power and vapor mass flow absorbed.

The maximum deviation between the measurements and the calculations for the heat rate transferred to the HTF (absorber internal power) is about 9%. The maximum deviation between the experimental and numerical values of the vapor flow absorbed is equal to 7%. The deviations are mostly related to the hypotheses adopted in this model such as perfect wetting, no pressure drop, no heat losses, etc. However, a relative deviation under 10% is acceptable for model validation since the measurement uncertainties are approximately 12%.

## 4 Numerical results in nominal case

### 4.1 Co-current and counter-current cases

The present modeling work aims to design a flat-plate falling-film generator for a 5-kW  $\text{NH}_3\text{-H}_2\text{O}$  absorption machine. The model integrates the heat and mass transfer based on balance equations and equilibrium conditions at the liquid–vapor interface as described in *Sect 2*. The behavior of the generator is studied under nominal conditions for two directions of vapor flow in relation to the solution film: either the vapor is generated from the bottom to the top of the exchanger (counter-current flow) or from the top to the bottom (co-current flow). The HTF is set to flow upward, in the opposite direction of the solution film.

The generator geometry is presented in Table 3.3. Nominal operating conditions of the generator are presented in Table 3.4, corresponding to the absorption chiller prototype of our laboratory (Boudéhen et al. 2016).

<b>Plate length</b>	0.32 [m]	<b>Number of plates</b>	14
<b>Plate width</b>	0.150 [m]	<b>Plates thickness</b>	0.006 [m]

**Table 3.3.** Dimensions of the generator.

		<b>Mass flowrate</b> $\dot{m}$ [kg.h <sup>-1</sup> ]	<b>Temperature</b> $T$ [K]	<b>Ammonia concentration</b> $x, y$ [-]	<b>Pressure</b> $P$ [bar]
<b>Heat transfer fluid</b>	Inlet	0.44	372	-	12
<b>Solution</b>	Inlet	0.038	344	0.58	12
<b>Vapor</b>	Inlet	0	358	0.99	12

**Table 3.4.** Initial operating conditions in the generator.

The profile of the temperatures and the ammonia concentrations along the generator for the two vapor flow configurations are shown in Figures 3.6 and 3.7.

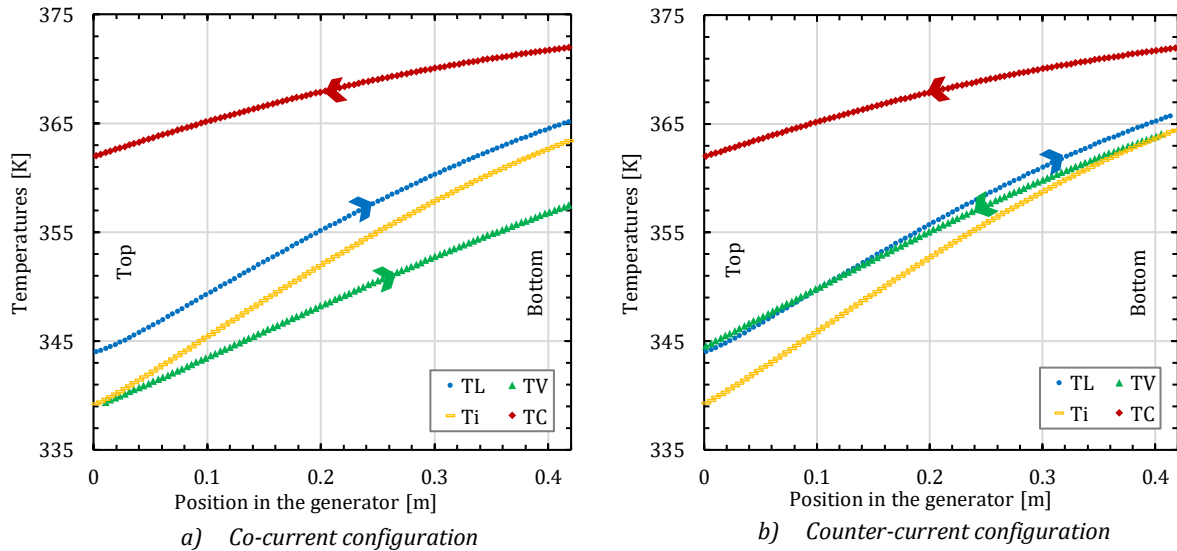


**Figure 3.6.** Temperatures profile along the generator.

The HTF heats the solution along the exchanger, leading to a decrease in its temperature  $T_c$  from bottom (0.4 m) to top (0 m) and to an increase in the solution temperature  $T_l$  from top to bottom. The desorption at the liquid–vapor interface limits the increase in the solution temperature and thus  $T_l$  evolves between  $T_c$  and the interface temperature  $T_i$ , which is maintained in thermodynamic equilibrium.  $T_i$  depends on the pressure and the ammonia concentrations in both liquid and vapor phases  $x_i$  and  $y_i$ . The heat transfer coefficient between the interface and the solution is higher than that between the HTF and solution (due to

convection resistance and conduction through the wall), thereby  $T_L$  is closer to  $T_i$  than to  $T_c$ . The vapor flowrate is zero at the top of the generator in co-current configuration, and zero at the bottom in counter-current configuration. At these positions, vapor generation starts and its temperature  $T_V$  corresponds to the interface temperature  $T_i$ . Along the exchanger, the profile of the vapor temperature  $T_V$  depends on the temperature of the interface where it is generated and on the temperature of the vapor produced upstream. Thus,  $T_V$  increases from top to bottom while remaining lower than  $T_i$  for co-current configurations, and decreases from bottom to top while remaining higher than  $T_i$  for counter-current configurations.

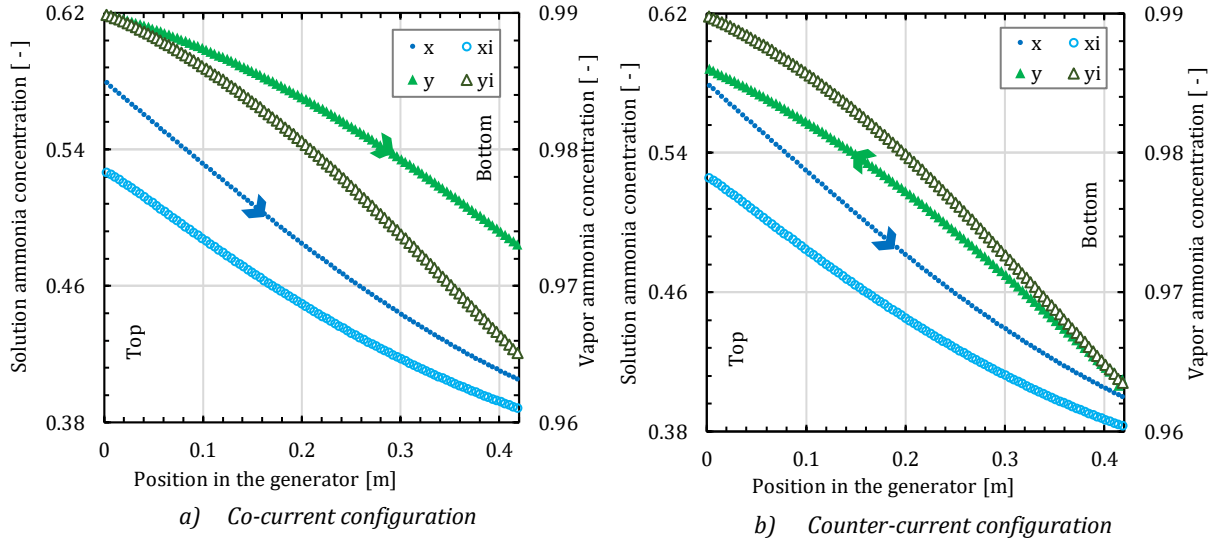


Figure 3.7. Profile of ammonia concentrations along the generator.

According to the thermodynamic conditions, the vapor generation is mainly composed of ammonia. As a result, in both co- and counter-current configurations, the ammonia concentration within the film  $x$  and the ammonia concentration at the liquid interface  $x_i$  decrease along the desorption process. The ammonia concentration in the vapor phase  $y$  at the beginning of the vapor generation (at the top for co-current and at the bottom for counter-current) corresponds to the equilibrium concentration at the vapor interface  $y_i$ . The ammonia concentration in the vapor along the exchanger depends on the vapor concentration at the interface where it is generated and on the concentration of the vapor produced upstream. Thus,  $y$  decreases from top to bottom while remaining higher than  $y_i$  in co-current mode, but increases from bottom to top while remaining lower than  $y_i$  in counter-current mode.

The ammonia concentration of the vapor produced by the generator in counter-current configuration reaches 0.986 and is higher than in co-current flow configuration where it reaches 0.973. The vapor mass flowrate leaving the generator is  $11.70 \text{ g}\cdot\text{s}^{-1}$  in the co-current configuration, while it is  $11.59 \text{ g}\cdot\text{s}^{-1}$  in the counter-current configuration. The performance of an absorption chiller depends on the quality of the refrigerant vapor sent to the condenser. For the machine under consideration, the acceptable water content in the refrigerant is approximately 0.5%. In order to purify the ammonia vapor produced by the generator, the use of a rectifier at the outlet of the generator is necessary. Let us consider a rectifier placed at the exit of the generator, cooling down the temperature of the vapor to reach  $y_{out,rect} = 0.995$ . The co-current and counter-current operating modes are compared, calculating the heating needs of the generator per unit mass of vapor leaving the rectifier. The results are presented in Table 3.5 (the combined generator results correspond to the concept described in Sect. 4.2).

Vapor flow configuration	$y_{out,gen}$ [-]	$\dot{m}_{v,out,gen}$ [g·s <sup>-1</sup> ]	$\dot{m}_{v,out,rect}$ [g·s <sup>-1</sup> ]	$\dot{Q}_c/\dot{m}_{v,out,rect}$ [kJ·kg <sup>-1</sup> ]
Co-current mode	0.973	11.70	11.09	1672
Counter-current mode	0.986	11.59	11.35	1591
Combined generator	0.991	9.26	9.18	2150

Table 3.5. Comparison of the performances of co- and counter-current vapor flow configurations.

The counter-current operation mode generates a higher amount of vapor at 99.5% ammonia and at a lower energy cost compared with the co-current operation mode. As the ammonia concentration at the outlet of the generator is higher in the counter-current configuration than in the co-current configuration, it enables one to reduce the capacity and thus the size of the rectifier.

## 4.2 Combined generator concept

In order to reduce the amount of water contained in the vapor produced by the generator, an adiabatic plate section is added above the heated plates of the generator presented previously. This new exchanger configuration will be called “combined generator” in the following. The solution entering the combined generator first flows over adiabatic plates where a rectification process occurs, before being heated and subject to desorption on the heated plates.

In the reference design, the length of the adiabatic and heated plates is, respectively, 0.1 m and 0.32 m. The gap between the plates is fixed to 4 mm to ensure negligible pressure losses in the vapor phase and to avoid flooding effects. The inlet conditions correspond to those previously presented in Table 3.4, except for the temperature of the solution at the inlet of the combined generator. Indeed, in order to enhance the rectification process occurring in the adiabatic part, the solution has to enter the combined generator in subcooled conditions. On the basis of preliminary calculations, the liquid inlet temperature is fixed to  $T_{Lin} = 310$  K in nominal conditions.

Figures 3.8a and 3.8b show the profile of the temperature and the ammonia concentration, respectively, according to the position inside the combined generator.

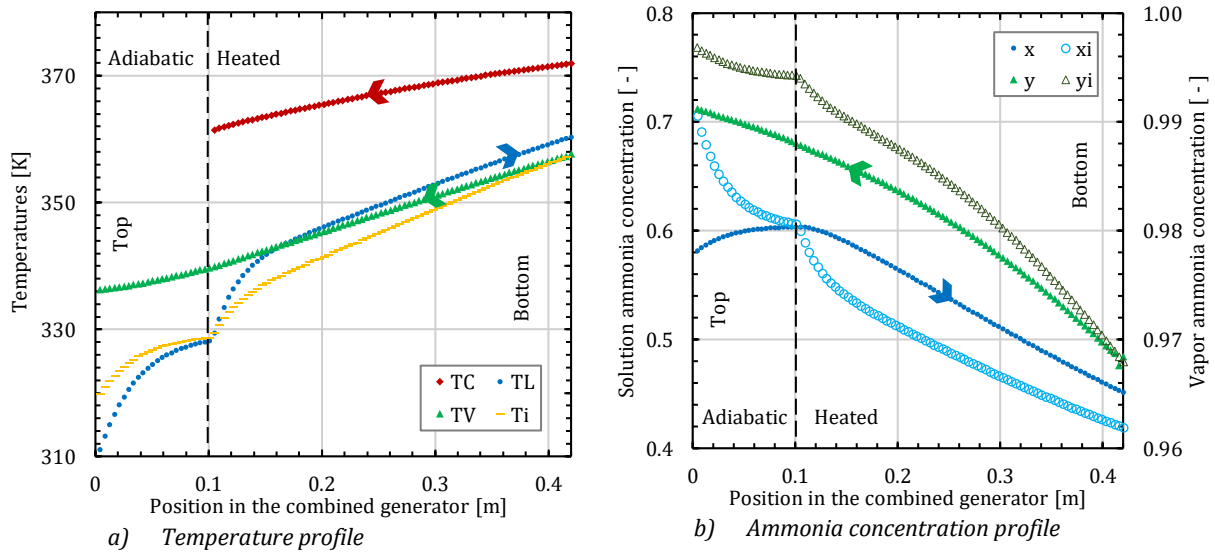


**Figure 3.8.** Profile of temperatures and ammonia concentrations along the combined generator for nominal case.

The temperatures of the HTF, the solution, and the vapor in the heated section evolve in the same way as that described in Sect. 4.1 (see Figures 3.6b and 3.7b).

In the adiabatic section, part of the vapor generated by the heated film is absorbed by the subcooled solution flowing on the adiabatic plates ( $T_L < T_i$ ). The interface of the solution film is in equilibrium. The heat released by the absorption process heats the subcooled solution. Thus, the temperature of the interface is higher than that of the subcooled solution. The temperature of the solution increases along the film and tends toward the equilibrium temperature. The solution leaving the adiabatic plates is very close to equilibrium, limiting the energy impact of the initial solution subcooling on the heating process. The temperature of the vapor decreases regularly as it flows along the exchanger.

The concentration of ammonia within the liquid film  $x$  increases along the adiabatic plates during the absorption process and decreases during the desorption process. The decrease in the interface temperature from the bottom to the top leads to an increase in the ammonia concentration at the interface in the vapor phase. The reduction of the water mass fraction at the interface diffuses into the vapor and results in a continuous increase of the ammonia concentration in the vapor throughout the exchanger. The ammonia concentration is at a minimum at the bottom of the combined generator, where it is equal to the equilibrium concentration at the interface  $y = y_i = 0.968$ . It then increases along the exchanger to reach 0.987 at the outlet of the heated part and reaches maximum at the top of the combined generator where  $y = 0.991$ . Indeed, the rectifier section allows the mass fraction of water in the vapor to be reduced. This demonstrates the value of integrating the adiabatic rectification into the combined generator.

To compare the performance of various operating conditions and combined generator designs, an ideal rectifier is simulated at the exit of the combined generator, cooling down the vapor produced until reaching a vapor concentration of  $y_{out,rect} = 0.995$ . The mass flowrate of the vapor at the exit of the rectifier and the heating needs for the combined generator per unit mass of vapor leaving the rectifier are listed in Table 3.5. At the outlet of the combined generator, the concentration of ammonia in the vapor is higher than for fully heated exchangers, whereas the mass flowrate of vapor produced is lower. The energy cost needed to reach  $y_{out,rect} = 0.995$  is more significant, and the mass flowrate of the vapor purified is lower. These results indicate that a high subcooling of the solution at the inlet of the combined generator is not the optimal configuration concerning the energy supply and the final mass flowrate of vapor produced. This shows the importance of taking into account the impact of the temperature that should be imposed at the solution inlet.

The pressure losses calculated along the vapor flow have no significant impact on the operating pressure ( $\Delta P = 5.35 \cdot 10^{-3} \text{ bar} \ll 12 \text{ bar}$ ) and thus on the thermodynamic equilibrium conditions at the interface of the film, validating hypothesis 2. The Reynolds numbers of the solution along the plate are lower than  $Re < 330$ , corresponding to wavy laminar regime in case of large flat plates. In the present case, flows develop along 4 mm width grooves to ensure high wettability of each plate (Huaylla et al. 2019). Instabilities can increase by a factor 2 the heat and mass transfer at the interface, in case of particular frequency excitation (Yoshimura et al. 1995). The presence of the lateral walls limits the development of the interface instabilities and no particular vibration excitation is introduced. Therefore, the intensification effects due to the wavelet development are assumed to be negligible, corresponding to hypothesis 1 and 3.

## 5 Parametric studies

### 5.1 Impact of the inlet conditions

Operating conditions affect the quality and the quantity of vapor produced by the combined generator. Subsequently, the quality of the vapor produced will be described by its ammonia concentration. The mass flowrate of the vapor produced will be analyzed through the mass effectiveness of the combined generator. The combined generator mass effectiveness is defined as the ratio of the vapor mass flowrate generated at the outlet of the combined generator and the maximum vapor mass flowrate that could be generated.

$$\varepsilon_{mass} = \frac{\dot{m}_{v,out}}{\dot{m}_{v,out,max}} \quad (3.14)$$

The maximum heat rate that can be transferred and the maximum vapor mass flowrate that can be generated are obtained in an infinitely long exchanger, where the HTF and solution flow in counter-current (the exchanger behaves like a usual counter-current thermal exchanger) while the vapor and the solution flow in co-current. They depend on the fluid that limits the transfers.

The limiting fluid is determined thanks to the equilibrium factor (Eq. 3.15) defined as the ratio between the maximum heat rate which can be transferred by the HTF  $\dot{Q}_{C,max}$ , assuming the solution as non-limiting, to the maximum heat rate that can be transferred by the solution  $\dot{Q}_{L,max}$ , assuming the HTF non-limiting.

$$R_{eq} = \frac{\dot{Q}_{C,max}}{\dot{Q}_{L,max}} = \frac{\dot{m}_C [H_{C,in} - H_C(T_{C,out,min})]}{\dot{m}_{L,out} \cdot H_L(T_{C,in},P) + \dot{m}_{v,out,max} \cdot H_V(T_{C,in},P) - \dot{m}_{L,in} \cdot H_L(T_{L,in};x_{in})} \quad (3.15)$$

If  $R_{eq} > 1$ , the solution is the limiting fluid and thus the maximum transferable heat corresponds to the one obtained with an infinitely long isothermal generator, for which the HTF imposes the temperature to the solution and vapor at the exit. The maximum solution temperature is  $T_{L,out,max} = T_{V,out,max} = T_{C,in}$  (i.e.,  $T = 372$  K for the nominal case). The solution is at the equilibrium state with the vapor at the exit of this ideal generator. The ammonia concentrations of the solution and the vapor are given by  $x_{out} = x_{eq}(T_{C,in}, P)$  and  $y_{out} = y_{eq}(T_{C,in}, P)$ . The mass flowrates of the solution and the vapor exiting the combined generator ( $\dot{m}_{L,out,min}$  and  $\dot{m}_{V,out,max}$ ) are deduced from mass and species balances (Eqs. 3.16–3.17).

$$\dot{m}_{L,in} = \dot{m}_{L,out,min} + \dot{m}_{V,out,max} \quad (3.16)$$

$$\dot{m}_{L,in} \cdot x_{in} = \dot{m}_{L,out,min} \cdot x_{eq}(T_{C,in}, P) + \dot{m}_{V,out,max} \cdot y_{eq}(T_{C,in}, P) \quad (3.17)$$

The maximum heat transferable is given by (Eq. 3.18):

$$\dot{Q}_{max} = \dot{Q}_{L,max} = \dot{m}_{L,out,min} \cdot H_{L,out}(T_{C,in}, P, x_{out}) + \dot{m}_{V,out,max} \cdot H_{V,out}(T_{C,in}, P, y_{out}) - \dot{m}_{L,in} \cdot H_{L,in} \quad (3.18)$$

If  $R_{eq} < 1$ , the HTF is the limiting fluid and thus the maximum heat rate transferred to the solution corresponds to the sensible heat released by the HTF when its temperature varies from its inlet temperature to its minimum outlet temperature,  $T_{C,out,min}$  (Eq. 3.19):

$$\dot{Q}_{max} = \dot{Q}_{C,max} = \dot{m}_C [H_{C,in} - H_C(T_{C,out,min})] = \dot{m}_C \cdot Cp_C \cdot (T_{C,in} - T_{C,out,min}) \quad (3.19)$$

The state of the solution (subcooled or superheated solution) at the inlet of the combined generator depends on the operating pressure, the temperature and the concentration. The deviation of the solution from the equilibrium conditions with the vapor phase can be represented by the solution equilibrium deviation temperature (Eq. 3.20):

$$\Delta T_{L,eq} = T_L - T_{eq}(x, P_V) \quad (3.20)$$

If the solution enters in the combined generator with a temperature lower than the equilibrium solution temperature ( $\Delta T_{L,eq,in} < 0$ ) (subcooled state), the minimal outlet temperature that can reach the HTF corresponds to the inlet solution temperature:  $T_{C,out,min} = T_{L,in}$ .

If the solution enters in the combined generator with a temperature higher than the equilibrium solution temperature ( $\Delta T_{L,eq,in} > 0$ ) (superheated state), the minimum outlet temperature that can be reached by the HTF corresponds to one reached by the solution after adiabatic desorption ( $T_{C,out,min} = T_{L,ad}$ ). Liquid and vapor are in an equilibrium state where,  $x = x_{eq,ad}$  and  $y = y_{eq,ad}$ . This temperature is deduced from mass, species and enthalpy balances (Eqs. 3.21–3.23):

$$\dot{m}_{L,in} = \dot{m}_{L,ad} + \dot{m}_{V,ad} \quad (3.21)$$

$$\dot{m}_{L,in} \cdot x_{in} = \dot{m}_{L,ad} \cdot x_{eq}(T_{L,ad}, P) + \dot{m}_{V,ad} \cdot y_{eq}(T_{L,ad}, P) \quad (3.22)$$

$$\dot{m}_{L,in} \cdot H_{L,in} = \dot{m}_{L,ad} \cdot H_{L,eq}(T_{L,ad}, P) + \dot{m}_{V,ad} \cdot H_{V,eq}(T_{L,ad}, P) \quad (3.23)$$

In nominal flowing conditions,  $R_{eq} = 3.77$ , thus, the solution is the limiting fluid. For the following studies, unless specified, the solution is always the limiting fluid.

5.1.1 Impact of the inlet temperature and the ammonia concentration of the solution

Figure 3.9 presents the evolution of the ammonia vapor concentration,  $y_{out}$ , at the outlet of the combined generator as a function of the combined generator mass effectiveness  $\epsilon_{mass}$  for various values of the inlet ammonia concentration  $x_{in}$  and the inlet temperature of the solution  $T_{L,in}$ .

As expected, the mass effectiveness of the combined generator increases with the decrease in the solution subcooling at the inlet for nominal conditions at a fixed inlet concentration. Indeed, the lower the inlet subcooling of the solution, the lower the energy to heat the solution needed per kilogram of vapor emitted. For a given superheating of the inlet solution, the mass effectiveness increases with the increase in ammonia concentration. This shows the impact of physical properties of the solution such as viscosity, thermal conductivity, and mass diffusivity on transfer when varying the inlet conditions. The temperature of the solution at the inlet should be lower than the equilibrium temperature for the absorption process to occur in the adiabatic part of the exchanger.

For a given ammonia concentration of the solution at the inlet of the exchanger, the variation of the ammonia concentration of the vapor at the outlet of the exchanger decreases with the increase in the solution subcooling until it becomes zero. Strong inlet subcooling of the solution is therefore to be avoided insofar as the increase in the solution subcooling degrades also the mass effectiveness of the combined generator.

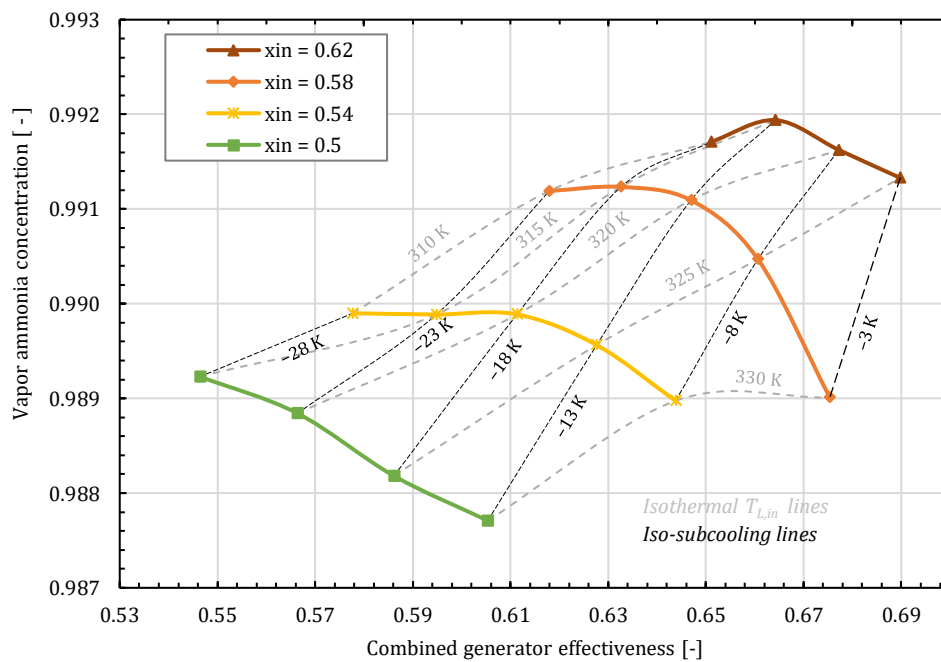


**Figure 3.9.** Evolution of the ammonia vapor concentration at the exit as a function of the combined generator mass effectiveness for various inlet conditions (ammonia concentration and temperature of the solution).

In order to find the optimal subcooling of the solution, an ideal rectifier is placed at the exit of the combined generator, cooling the temperature of the vapor until it reaches  $y_{out,rect} = 0.995$ . The heating needs (called "energy costs") per unit mass of vapor leaving the rectifier are plotted in Figure 3.10 as a function of the inlet conditions.

## Combined generator design

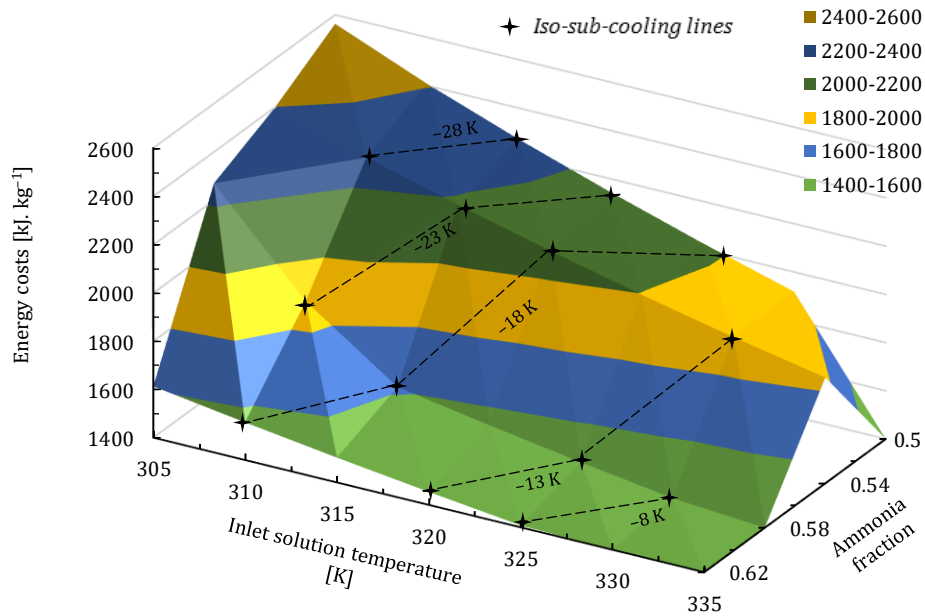


**Figure 3.10.** Evolution of energy costs as a function of the inlet values of both the ammonia concentration and temperature of the solution.

The energy cost decreases with the increase in the inlet ammonia concentration of the solution. Indeed, the higher the inlet ammonia concentration, the greater the mass effectiveness and the outlet ammonia concentration of the vapor. Thus, the rectification process needs less energy supply. The best compromise between the purity of the ammonia vapor produced and the energy cost is obtained with the solution inlet temperature  $T_{L,in}$  lying between 315 and 320 K, and the ammonia concentration lying between 0.58 and 0.62.

### 5.1.2 Impact of the heat transfer fluid temperature

Figure 3.11 presents the evolution of the ammonia vapor concentration  $y_{out}$  at the outlet of the combined generator and the energy cost per unit mass of vapor leaving the rectifier (heating needs per unit mass of vapor leaving the rectifier placed at the exit of the combined generator in order to reach  $y_{out,rect} = 0.995$ ) as a function of the inlet temperature of the HTF  $T_{C,in}$ , for the inlet solution temperature and concentration, respectively, equal to  $T_{L,in} = 310$  K and  $x_{in} = 0.58$ . The mass flowrate of the HTF is equal to  $0.44$  kg.s<sup>-1</sup>. The values of the combined generator mass efficiencies  $\epsilon_{mass}$  are reported in the figure.

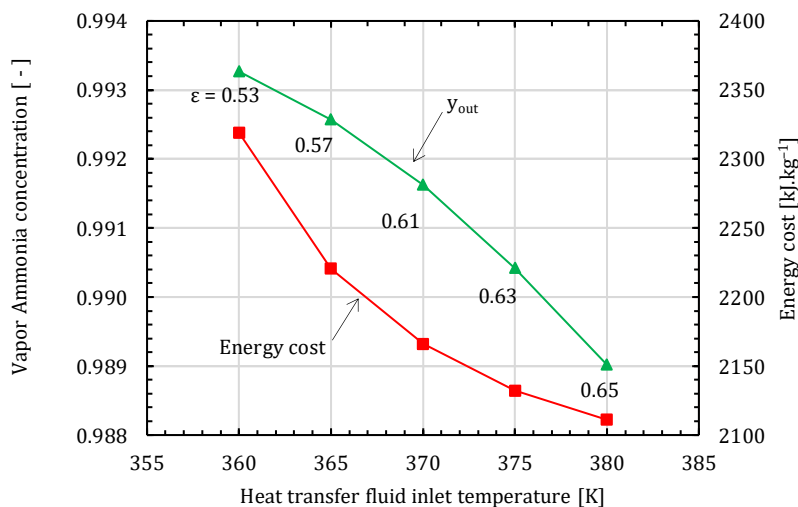


**Figure 3.11.** Evolution of ammonia vapor concentration and energy cost as a function of HTF inlet temperature.

As expected, the ammonia vapor concentration at the exit of the combined generator increases with the decrease in the HTF inlet temperature, whereas the combined generator mass effectiveness increases. The energy cost needed to generate the desired vapor quality (i.e.,  $y_{out,rect} = 0.995$ ) decreases with the increase in the HTF temperature. It should be noted that this decrease is attenuated with the increasing HTF temperature, and it is likely that an optimum is reached at higher temperatures.

### 5.1.3 Impact of the heat transfer fluid flowrate

Figure 3.12 presents the evolution of the ammonia vapor concentration leaving the combined generator  $y_{out}$  and the energy cost per unit mass of vapor leaving the rectifier (heating needs per unit mass of vapor leaving the rectifier placed at the exit of the combined generator in order to reach  $y_{out,rect} = 0.995$ ) as a function the HTF mass flowrate  $\dot{m}_c$ . The ammonia solution temperature and concentration at the combined generator are, respectively, equal to  $T_{L,in} = 310$  K and  $x_{in} = 0.58$ . The HTF temperature is equal to 372 K at the inlet. For an HTF mass flow over  $0.117$   $\text{kg}\cdot\text{s}^{-1}$  ( $R_{eq}=1$ ), the solution is the limiting fluid. For an HTF mass flow under  $0.117$   $\text{kg}\cdot\text{s}^{-1}$ , the HTF is the limiting fluid.

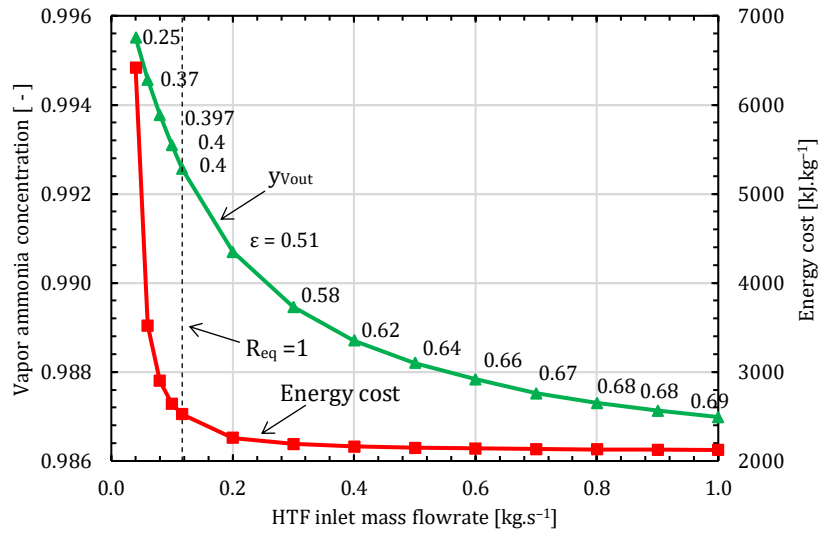


**Figure 3.12.** Evolution of ammonia vapor concentration and energy cost as a function of HTF mass flowrate.

The increase in the HTF mass flowrate increases the amount of vapor generated and decreases the ammonia concentration of the vapor generated by the combined generator. The ammonia vapor concentration decrease is related to the increase in the ammonia solution temperature with the increase in the HTF mass flowrate. The ammonia vapor concentration reaches 0.995 for very low HTF mass flowrates (i.e.,  $\dot{m}_c = 0.05$   $\text{kg}\cdot\text{s}^{-1}$ ). The mass flowrate of the ammonia vapor is then very low and equal to  $2.10^{-3}$   $\text{kg}\cdot\text{s}^{-1}$ . The combined generator mass effectiveness increases with the increase in the HTF mass flow because of the increase in the convective heat transfer coefficient with the HTF flowrate.

It is necessary to reduce the HTF flowrate to  $0.05$   $\text{kg}\cdot\text{s}^{-1}$  to achieve an ammonia concentration at the combined generator outlet equal to 0.995. The combined generator mass effectiveness is then equal to 0.249. By contrast, the mass flowrate of ammonia vapor generated reaches  $1.10^{-2}$   $\text{kg}\cdot\text{s}^{-1}$  for  $\epsilon_{mass} = 0.68$ , while the concentration drops to 0.987.

The heating needed per unit mass of vapor leaving the rectifier reaches  $6400$   $\text{kJ}\cdot\text{kg}^{-1}$  when  $\dot{m}_c = 0.05$   $\text{kg}\cdot\text{s}^{-1}$ . It decreases with the increase in the HTF mass flowrate, and stabilizes at around  $2150$   $\text{kJ}\cdot\text{kg}^{-1}$  for  $\dot{m}_c > 0.3$   $\text{kg}\cdot\text{s}^{-1}$ . A good compromise between ammonia vapor purification, combined generator mass effectiveness, and energy costs is achieved when the HTF mass flowrate varies between  $[0.4$  and  $0.6$   $\text{kg}\cdot\text{s}^{-1}]$  with  $y_{out} \approx 0.988$ ,  $\epsilon_{mass} \approx 0.64$ , and  $\dot{Q}_C / \dot{m}_{V,out,rect} = 2100$   $\text{kJ}\cdot\text{kg}^{-1}$ .

### 5.2 Impact of design parameters

This section highlights the influence of the geometric design of the combined generator on its performance. Attention is drawn to the influence of the number of plates and the adiabatic/heated ratio. In order to make coherent comparisons, the total exchange surface and the plate thickness are kept constant and equal to those of the nominal configuration (i.e., 0.72 m<sup>2</sup> and 0.006 m, respectively; the parametric study will then be carried out with the same material costs). Given the plate width constant, the number of plates impacts the mass flow of solution per plate, thus the thickness of the solution film, and the transfer resistance. Keeping the exchange surface constant, an increase in the number of plates affects the plate length and thus the residence time of the solution along the plate. The adiabatic/heated ratio affects the rectification-desorption balance. Since the number of plates is related to their length, an aspect ratio (*AR*) defined by (Eq. 3.24) is introduced. The plate lengths of the generator-rectifier studies are reported in Table 3.6. The adiabatic/heated plates length ratio (equal to 24% in the nominal case) will be called "AHR" in the following.

$$AR = \frac{\text{Length of plates}}{\text{Number of plates} \cdot \text{width of plates}} \quad (3.24)$$

Number of plates	2	5	10	15	20	30
Length of the plates [m]	2.4	0.96	0.48	0.32	0.24	0.16
Aspect ratio	8	1.280	0.320	0.142	0.080	0.036

Table 3.6. Combined generator geometrical parameters.

The simulations are made with the same initial values of inlet temperature, ammonia concentration, and mass flowrate as in the nominal case presented in Table 3.4 in Sect. 4.2.

Figure 3.13 shows the evolution of the ammonia vapor concentration at the combined generator outlet as a function of its mass effectiveness for various plate numbers and various adiabatic/heated surface ratios.

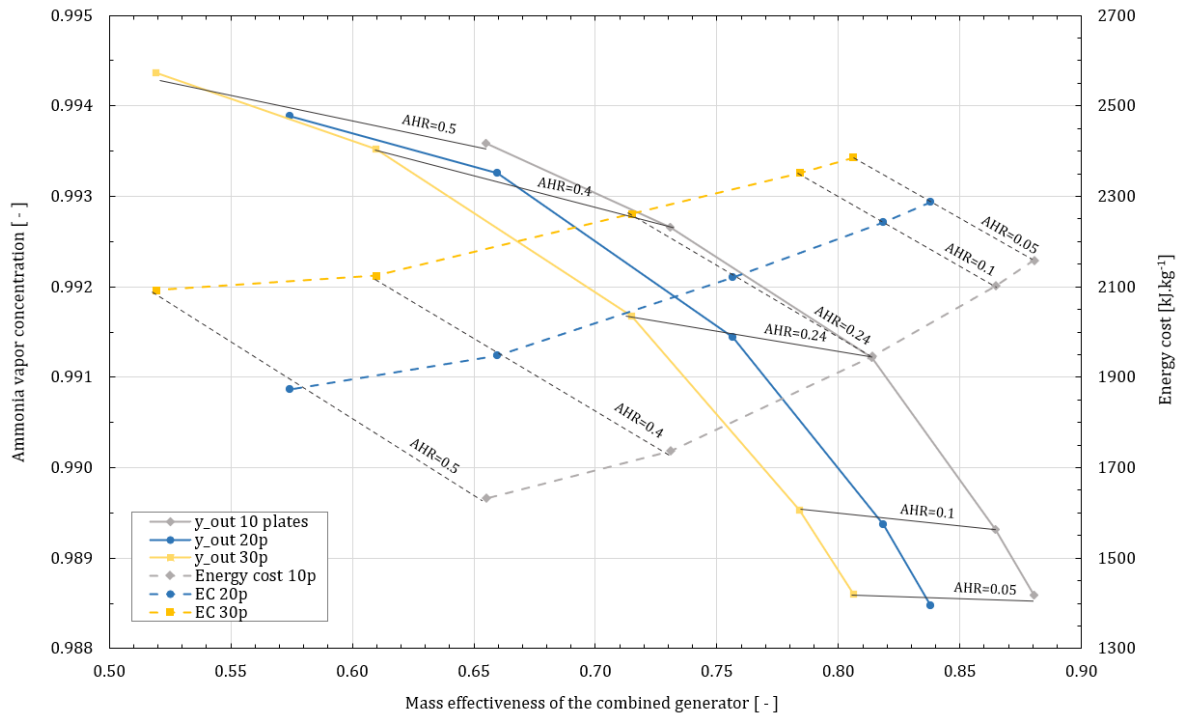


Figure 3.13. Evolution of ammonia vapor concentration and energy costs as a function of the combined generator mass effectiveness for various geometrical configurations.

The ammonia vapor concentration and thus the effectiveness of the rectification process increases as expected with the increase in the AHR. For a given AHR, the increase in the plate numbers appears to increase the ammonia vapor concentration. Since the space between the plates is kept constant, an increase in the number of plates results in a decrease in the HTF flowrate per unit width of plate, leading to a decrease in the heat transfer coefficient. The increase in the plate numbers thus reduces the temperature of the falling-film, leading to an increase in the vapor ammonia concentration. This also explains why, by contrast, the mass effectiveness increases with the decrease in the number of plates, keeping the AHR constant.

For a given AHR, the energy cost per unit mass of vapor produced at the exit of the rectifier decreases with the decrease in the number of plates. For a given number of plates, the energy cost decreases with the increase in the AHR. Thus, a high aspect ratio and AHR are beneficial for reducing the energy cost to produce vapor at the desired ammonia concentration.

For desired vapor ammonia concentration at the outlet and length of the combined generator plates, this application allows determining the mass effectiveness and the energy cost associated. This tool could be useful for an industrial design of an exchanger; however, it should include the exchange surface variation, which is fixed in this study.

### 5.3 Study of energy costs

Figure 3.14 shows the evolution of the cooling capacity per kilowatt of heat supplied to the combined generator as a function of the heat exchange surface per kilowatt of cooling capacity (the cooling capacity is defined as the product of the vapor mass flowrate at the exit of the ideal rectifier multiplied by its latent heat of condensation under operating conditions).

This figure depicts the evolution of the operating cost for cold power production (directly related to the heat supplied to the generator) as a function of the investment cost (related to the surface of the plate needed at the combined generator level for the machine to produce 1 kW cold capacity). The figure shows the influence of the number of plates and of the AHR.

The ammonia concentration and the mass flow of the solution, as well as the mass flow and the temperature of the HTF, correspond to those set in nominal conditions. Two inlet solution temperatures are investigated:  $T_{L,in} = 310$  K (Figure 3.14a) and  $T_{L,in} = 330$  K (Figure 3.14b) corresponding to 20°C subcooling and to the saturation condition, respectively. The AHR varies between 0 and 0.4, whereas the number of plates varies between 2 and 30.

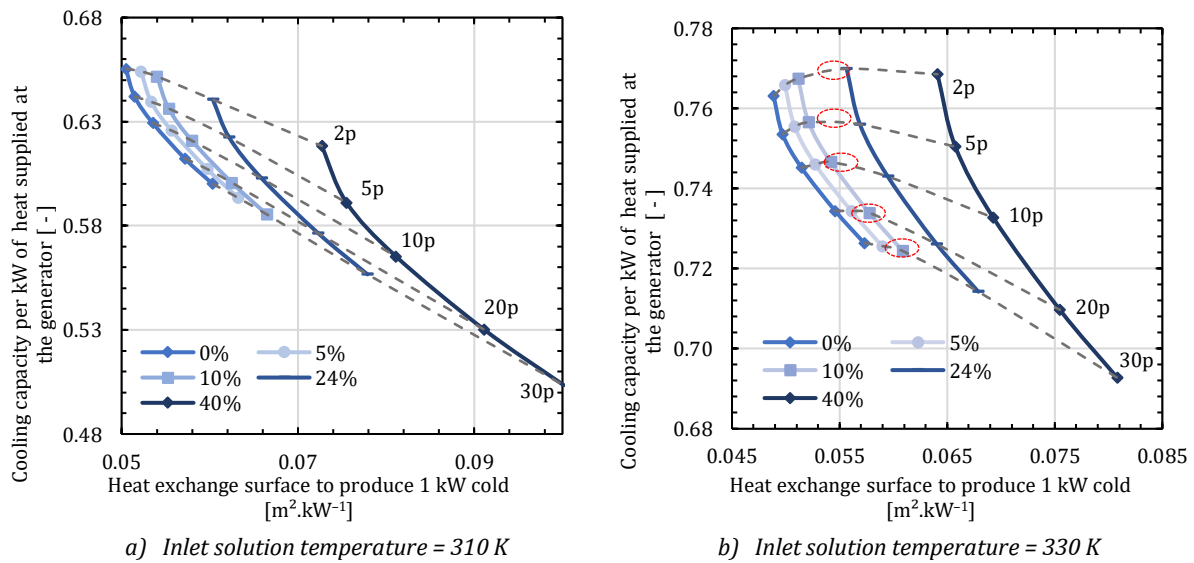


**Figure 3.14.** Evolution of the cold power production per kW of heat supplied in the combined generator according to the plate.

The heat exchange surface needed to generate 1 kW of cooling capacity increases with the increase in the AHR, thus leading to an increase in the combined generator cost. On the other hand, the increase in the AHR induces a reduction in the rectifier capacity (since the ammonia concentration is larger at the exit of the rectifier) and thus a reduction in its cost. The cooling capacity per kilowatt of heat is higher for the configuration of a few long plates compared with several small plates. This is partly due to the reduction in the convection heat transfer of the HTF when increasing the number of plates, as described previously. Although they facilitate good performance, the configurations with two and five plates are not operational due to their size (equal to 1.2 and 0.96 m, respectively).

The AHR leading to the maximum cooling capacity depends on the temperature of the solution at the inlet of the combined generator. It lies between 10% and 24% when the solution enters the combined generator in saturation conditions, and is equal to 0% (no adiabatic plates) when the solution enters the combined generator with 20 K of subcooling. This underlines the role of the inlet liquid temperature in the optimization of the combined generator.

The maps represented in Figure 3.12, 3.13 and 3.14 are intended to be a first basis for sizing tools that have to be completed to become fully operational.

## 6 Conclusion

The performance of a generator and of a combined generator falling-film plate exchanger for  $\text{NH}_3\text{-H}_2\text{O}$  absorption chillers is studied through a numerical model. The developed model validated using experimental results allows simulating desorption and absorption processes through various geometrical and inlet parameters. The counter-current configuration (vapor generated from bottom to top) appears to be more efficient than the co-current configuration. The implementation of adiabatic plates above the heated plates makes it possible to increase the ammonia concentration at the exit of the exchanger.

The rectification process is all the more efficient when the temperature of the solution at the inlet of the exchanger is low. However, the subcooling of the solution at the inlet of the combined generator has to be limited so as not to have a significant impact on the energy cost of the process. The nominal design shows a good compromise between ammonia vapor purity and desorption efficiency for a subcooling of the inlet solution of approximately 15°C.

Initial estimations of the cooling capacities per injected heat highlight the impact of the combined generator geometry and of the inlet liquid temperature on the performance of the combined generator. The high aspect ratio is beneficial for reducing the operating cost. The increase in the adiabatic/heated ratio increases the investment cost. Its impact on the operating cost depends on the subcooling of the solution at the inlet of the exchanger.

The study presented in this chapter gives insights to design a combined generator, considering its integration in an absorption chiller, and taking into account the variations of the inlet parameters.

## 7 References

- Abou Elmaaty T.M., Kabeel A.E., Mahgoub M., (2017), "Corrugated plate heat exchanger review", *Renewable and Sustainable Energy Reviews* 70, 852–860
- Boudéhenn F., Triché D., Demasles H., Bonnot S., Perier-Muzet M., Lefrançois F., (2016), "Development and performances overview of ammonia–water absorption chillers with cooling capacities from 5 to 100 kW", *Energy Procedia* 91, 707–716
- Determan M.D., Garimella S., (2011), "Ammonia–water desorption heat and mass transfer in microchannel devices", *International Journal of Refrigeration* 34, 1197–1208
- El-Sayed Y.M., Tribud M. A., (1985), "Theoretical Comparison of the Rankine and Kalina cycles," *ASME Publication* 1, 97–102.
- Fernandez–Seara J., Sieres J., Rodriguez C., Vazquez M., (2005), "Ammonia–water absorption in vertical tubular absorbers", *International Journal of thermal sciences* 44, 277–288
- Goel N., Goswami Y., (2005), "Analysis of a counter-current vapor flow absorber", *International Journal of Heat and Mass Transfer* 48, 1283–1292
- Golden J.H., (2012), "Ammonia–water desorption in flooded columns", *Georgia Institute of Technology*
- Hartley D.E., Murgatroyd W., (1964), "Criteria for the break-up of thin liquid layers flowing isothermally over solid surfaces", *International Journal of Heat and Mass Transfer* 7, 1003–1015
- Hessami Ma., (2000), "Surface temperature and heat transfer measurements in cross corrugated plate heat exchangers", *Iran Journal of Science and Technology* 24–3, 283–97
- Hsu Y. Y., (1962), "On the Size Range of Active Nucleation Cavities on a Heating Surface", *Journal of Heat Transfer* 84, 207–213
- Huaylla F., Le Pierrès N., Stutz B., (2019), "Numerical and experimental analysis of falling-film exchangers used in a LiBr–H<sub>2</sub>O interseasonal heat storage system", *Heat Transfer Engineering* 40–11, 879–895
- Norman W.S., (1960), "Heat transfer to a liquid film on a vertical surface", *Transactions of the Institution of Chemical Engineers* 27, 301–307
- Staedter M. A., Garimella S., (2018), "Direct-coupled desorption for small capacity ammonia–water absorption systems", *International Journal of Heat and Mass Transfer* 127, 196–205
- Triché D., (2016), "Étude numérique et expérimentale des transferts couplés de masse et de chaleur dans l'absorbeur d'une machine à absorption ammoniac-eau", PhD thesis, *Université de Grenoble Alpes*
- Yoshimura P.N., Nosoko T., Nagata T., (1995), "Enhancement of mass transfer into a falling film by two dimensional surface waves–Some experimental observations and modeling", *Chemical Engineering Science* 51, 1231–1240
- Ziegler B., Trepp C., (1984), "Equation of state for ammonia–water mixtures ", *International Journal of Refrigeration* 7, 101–106





# Chapter II

## Evaluation of the NH<sub>3</sub>-H<sub>2</sub>O absorption chiller performance equipped with the combined generator

---

### Objective:

*The goal of the second chapter is to investigate numerically the improvement of the performance of an NH<sub>3</sub>-H<sub>2</sub>O absorption chiller dedicated to air-conditioning equipped by the combined generator developed in Chapter I.*

### Based on:

Wirtz M., Stutz B., Phan H.T., Boudéhenn F.

“Study of the impact of a combined generator on the performance of an NH<sub>3</sub>-H<sub>2</sub>O absorption machine thanks to the effectiveness method”

*Applied Thermal Engineering (Submitted 2021)*



*This chapter presents the numerical estimation of the performance of a 5-kW single-stage NH<sub>3</sub>-H<sub>2</sub>O absorption chiller equipped with the combined generator model presented in Chapter I.*

*First, a numerical model describing the performance of the original NH<sub>3</sub>-H<sub>2</sub>O absorption chiller is developed. The model is validated using experimental data. Then, the evolutions of the combined generator performances as a function of the operating conditions is described through the establishment of mass, thermal, and species effectiveness correlations, which involve three non-dimensional numbers: an energy ratio, an NTU, and a modified Jakob number. The effectiveness are then integrated in the global simulation tool of the machine. Finally, the impact of the combined generator on the machine performance (COP and cooling capacity) is studied for various inlet operating conditions; heat transfer fluid and rich solution temperatures and mass flowrates. The influence of the rectifier located at the outlet of the combined generator is also investigated.*

## 1 Introduction

Various studies relate to absorption systems, and while some include one PHE among the components, only a few focus on ammonia–water small-capacity systems containing only PHE technology. (Boudéhenn et al. 2012) were the first to use only brazed PHEs for the development of a compact NH<sub>3</sub>–H<sub>2</sub>O absorption chiller of 5-kW cooling capacity. Their numerical and experimental data are in good agreement providing encouraging results, with some points being optimized later by the work on the absorber of (Triché 2016). Later, (Neyer et al. 2018) tested a combined single- and half-effect NH<sub>3</sub>–H<sub>2</sub>O absorption system built with flat PHEs. The system produces cold at 12°C with a cold power of 18.4 kW and 10.6 kW, and an energy effectiveness ratio of 0.57 and 0.27 in single- and half-effect mode, respectively. This chiller was later successfully implemented in a solar-driven cooling system. More recently, (Jiménez et al. 2019) conducted an experimental study on an NH<sub>3</sub>–H<sub>2</sub>O single-stage absorption machine, designed for food conservation or air-conditioning applications and composed of PHEs. It produces 2.6 kW of cold, with a thermal COP of 0.61 at an evaporation temperature of –19°C. Their study shows the appeal of developing very compact and efficient machines.

The present chapter investigates the advantage of replacing a generator-separators-rectifier assembly in a 5-kW ammonia–water absorption machine by the unique innovative combined generator developed and presented in *Chapter 1*. This combined generator consists of a falling-film PHE that has a double function of ammonia vapor generation and purification. The global performance of the combined generator is characterized with mass, thermal, and species effectiveness. The impact of the new component on the performance of the absorption machine is investigated through numerical modeling. Furthermore, the impact of the operating conditions on the performance of the absorption cycle is analyzed.

## 2 Absorption chiller

### 2.1 Absorption chiller model

The present work aims to improve the performances of a 5-kW NH<sub>3</sub>–H<sub>2</sub>O PHE absorption chiller implemented in the laboratory (Boudéhenn et al. 2012), by replacing a flooded boiling generator with a combined falling-film generator. The absorption machine is composed of five PHEs connected to three external sources: (i) a falling-film absorber designed and tested by (Triché 2016), a flat plate condenser, and a rectifier, which are cooled by a water circuit at ambient temperature 22°–33°C; (ii) a flat plate evaporator that cools a chilled water circuit between 5°C and 22°C; (iii) a flooded generator heated by a hot water loop at 80°–120°C. The generator and the rectifier are connected to a vapor-liquid separator. The scheme of the absorption chiller is presented in Figure 4.1.

The internal operating conditions and the performance of the machine are described using temperature pinches or thermal efficiencies, and the following assumptions are made:

- + The heat losses are not taken into account.
- + The pressure losses are not taken into account.
- + The expansion valves are isenthalpic and the pump is isentropic.
- + The volumes of liquids within the tubes, the accumulators, and the separators are not taken into account.

The solution leaving the flooded generator is assumed to be at equilibrium with the vapor. The generator performance is calculated using the temperature pinch between the inlet HTF and the ammonia-poor solution exiting the component after desorption ( $\Delta T_{gen} = T_{C,gen,in} - T_{L,gen,out}$ ).

The rectifier purifies the vapor produced by the generator. Its performance is calculated through the thermal effectiveness  $\varepsilon_{rect}$ , defined as the ratio between (a) the effective heat rate transferred between the vapor exiting the generator and the HTF and (b) the maximum heat rate that could be exchanged ideally (Eq. 4.1).

$$\varepsilon_{rect} = \frac{\dot{Q}_{rect}}{\dot{Q}_{rect,max}} \quad (4.1)$$



$$\sum \dot{m}_{in} = \sum \dot{m}_{out} \quad (4.4)$$

$$\sum(\dot{m}_{L,in} \cdot x_{in}) + \sum(\dot{m}_{V,in} \cdot y_{in}) = \sum(\dot{m}_{L,out} \cdot x_{out}) + \sum(\dot{m}_{V,out} \cdot y_{out}) \quad (4.5)$$

$$\sum((\dot{m}_{L,in} \cdot H_{L,in}) - (\dot{m}_{L,out} \cdot H_{L,out})) + \sum(\dot{Q}) = 0 \quad (4.6)$$

The fluid properties of the ammonia solution are given by (Ziegler and Trepp 1984), and the model is developed using SciLab 6.0.2.

## 2.2 Validation of the model on experimental values

The absorption chiller was characterized by (Triché 2016). The nominal temperature of the external circuits is 90°C at the generator inlet; 27°C at the absorber, condenser, and rectifier inlets; and 13°C at the evaporator outlet. The nominal mass flowrate of the rich solution is 75 kg.h<sup>-1</sup>.

The various parameters of the model were determined with the measurements for several operating conditions.

$$\Delta T_{gen} = 10 \text{ } ^\circ\text{C} \quad (4.7)$$

$$\Delta T_{cond} = 0.627 \cdot \dot{Q}_{cond} \quad (4.8)$$

$$P_{high} = P_{eq,NH_3}(1, T_{L,cond,out}) + 10.58 \cdot y_{cond,in} - 10 \quad (4.9)$$

$$\Delta T_{ab} = 10 \text{ } ^\circ\text{C} \quad (4.10)$$

$$\Delta T_{ev} = 5 \text{ } ^\circ\text{C} \quad (4.11)$$

$$\Delta T_{eq, ev} = 5 \text{ } ^\circ\text{C} \quad (4.12)$$

$$P_{low} = P_{eq}(y_{ev,out}, T_{C,ev,out} - \Delta T_{ev}) \quad (4.13)$$

On the basis of a previous study, the effectiveness of the rectifier, subcooler, and economizer is fixed at  $\varepsilon_{rect} = 0.95$ ,  $\varepsilon_{sub} = 0.8$ , and  $\varepsilon_{eco} = 0.9$ , respectively. The effectiveness of the rectifier appears to be high as compared to normally expected effectiveness. The thermal COP of the absorption chiller (Eq. 2.1) and the cooling capacity are used for comparison between the experimental data reported by (Triché 2016) and the numerical results of the model.

Figure 4.2 compares the COP and the cooling capacity predicted by the model with the experimental results as functions of the HTF temperature at the inlet of the absorber. The deviations between the experimental and the numerical results are lower than the measurement uncertainty range for absorber temperatures included between 22°C and 31°C.

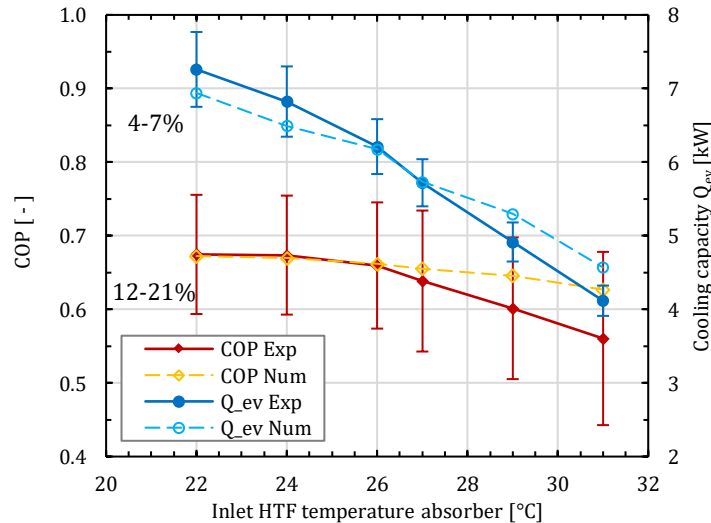
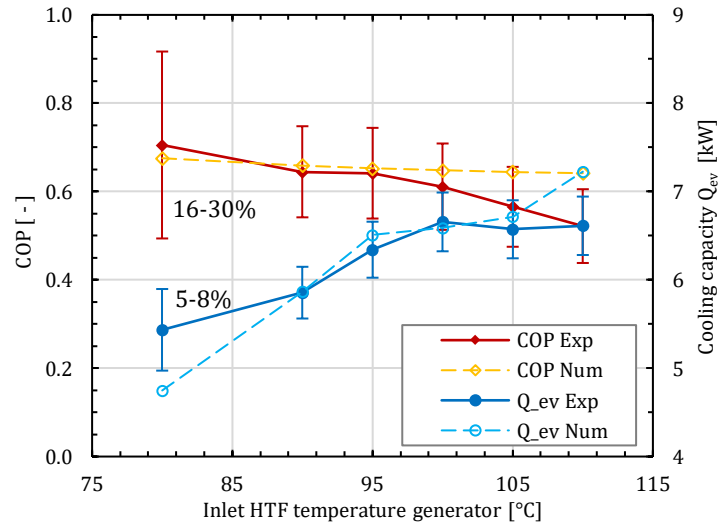


Figure 4.2. COP and cooling capacity as a function of the inlet absorber HTF temperature.

Figure 4.3 **Erreur ! Source du renvoi introuvable.** displays the COP and the cooling capacity predicted by the model and the experimental results as functions of the HTF temperature at the inlet of the generator. The deviations between the experimental and the numerical results are lower than the measurement uncertainty range for generator temperatures included between 80°C and 105°C. For high temperatures, the results deviate and the model needs to be improved.



**Figure 4.3.** COP and cooling capacity as a function of the inlet generator HTF temperature.

The deviations between the experimental and numerical data may be explained mainly by the hypothesis related to the pressure drop and heat losses considered in the model presented in *Chapter I*. However, the relative deviations observed are acceptable for the model validation since they are lower than the measurement uncertainties. The absorption chiller model can therefore be used with high reliability for the HTF temperature ranges of 80°–105°C at the generator inlet and 22°–31°C at the absorber inlet.

### 3 Development of the correlations for the novel falling-film combined generator

#### 3.1 Combined generator concept

In order to gain compactness and to decrease the operating costs, the innovative heat exchanger called a “combined generator” presented in *Chapter I* and associating both generation and purification of the refrigerant vapor in the same bloc is used. This concept makes it possible to replace the two PHEs used for the generator and the rectifier as well as two associated phase-separators by only one component (see Figure 4.1). The new exchanger is also composed of flat plates but uses falling-film technology. The ammonia–water solution with a high concentration of ammonia (rich solution) enters the combined generator through a distributor, and is spread downward along adiabatic plates, where a partial reabsorption of the vapor moving upward occurs, purifying it. Then, the solution flows along the heated plates and generates the vapor, which moves upward. The HTF and the vapor flow counter-currently to the solution. The detailed 1-D model describing the heat and mass transfer occurring in this exchanger is presented in *Chapter I*. The results provided by this model with the geometry shown in Figure 4.4 are used in the following sections.

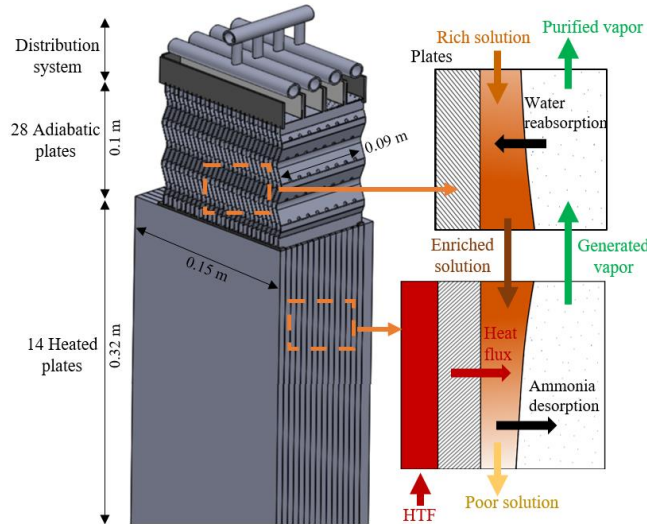


Figure 4.4. Combined generator geometry and heat and mass transfer involved.

In the case of flooded plate generators, the assumption of equilibrium of the solution with the vapor at the outlet of the exchanger is very realistic. Knowing the temperature pinch between the solution and the HTF is then sufficient for determining the flowrate of vapor generated as well as the concentrations of the solution and the vapor at the outlet of the flooded generator, as presented previously. This assumption is no longer valid in the case of falling-film and plate combined generators where the vapor flows against the solution. The concentrations and temperatures of the solution and the vapor leaving the exchanger are no longer linked by equilibrium conditions. It is therefore necessary to use other parameters than temperature pinch to describe their evolution. In the case of salt solution combined generators, such as lithium bromide-water solution, the vapor is composed only of refrigerant. The performance of falling-film and plate combined generators can then be described by means of the mass and the thermal effectiveness (Perier-Muzet and Stutz 2021). These quantities enable the calculation of the generated vapor flowrate as well as the temperatures of the solution. In the case of a solution containing a volatile sorbent such as water in the water-ammonia working pair, a new unknown appears: the concentration of refrigerant in the vapor leaving the exchanger. It is then necessary to introduce an additional component of effectiveness: the species effectiveness.

### 3.2 Definition of effectiveness characterizing the combined generator

#### 3.2.1 Mass, thermal, and species effectiveness

The combined generator mass effectiveness is defined (Eq. 3.14).

The combined generator thermal effectiveness, is defined as the ratio of the actual heat transferred to the maximum transferable heat (Eq. 4.14).

$$\varepsilon_{th} = \frac{\dot{Q}}{\dot{Q}_{max}} \quad (4.14)$$

The combined-generator species effectiveness is defined by a ratio of ammonia concentration differences: the vapor ammonia concentration at the exit of the combined generator and the minimum ammonia concentration  $y_{out,min}$  reachable at the outlet, divided by the difference between the maximum ammonia concentration  $y_{out,max}$  and the minimum ammonia concentration reachable at the outlet (Eq. 4.15). The calculation of  $y_{out,min}$  and  $y_{v,out,max}$  is explained in Sect. 3.2.3.

$$\varepsilon_{sp} = \left( \frac{y_{out} - y_{out,min}}{y_{out,max} - y_{out,min}} \right) \quad (4.15)$$

### 3.2.2 Equilibrium factor $R_{eq}$

The maximum heat rate that can be transferred and the maximum vapor mass flowrate that can be generated are described in *Chapter 1, Sect. 5.1*, depending on the fluid that limits the transfers, which is determined thanks to the equilibrium factor  $R_{eq}$ , defined (Eq. 3.15).

If the solution is the limiting fluid,  $R_{eq} > 1$ ,  $T_{L,out,max} = T_{V,out,max} = T_{C,in}$ , the mass flowrates of the solution and the vapor exiting the combined generator are those defined (Eqs. 3.17–3.18), and the corresponding maximum transferable heat is given by (Eq. 3.19).

If the HTF is the limiting fluid,  $R_{eq} < 1$ , either the solution enters in the combined generator in the subcooled state:  $T_{C,out,min} = T_{L,in}$ , or the solution enters in the combined generator in the superheated state:  $T_{C,out,min} = T_{L,ad}$  deduced from (Eqs. 3.22–3.24), and the corresponding maximum heat rate transferred to the solution is given by (Eq. 3.20).

### 3.2.3 Application to the 5-kW absorption machine

The combined generator was designed so that the HTF is never the limiting fluid (i.e.  $R_{eq} > 1$ ). The thermal effectiveness and mass effectiveness are given by (Eqs. 4.16–4.17), respectively:

$$\varepsilon_{th} = \frac{\dot{Q}}{\dot{m}_{L,out,min} \cdot H_{L,out}(T_{C,in}, P) + \dot{m}_{V,out,max} \cdot H_{V,out}(T_{C,in}, P) - \dot{m}_{L,in} \cdot H_{L,in}} \quad (4.16)$$

$$\varepsilon_{mass} = \frac{\dot{m}_{V,out}}{\dot{m}_{V,out,max}} = \frac{\dot{m}_{V,out}}{\dot{m}_{PS} \cdot \frac{(x_{RS,sat} - x_{PS})}{(y_{out} - x_{RS,sat})}} \quad (4.17)$$

The calculation of the species effectiveness required the calculation of maximal and minimal ammonia concentration in the vapor phase. The maximum ammonia concentration of the vapor is calculated at the lowest temperature that can be reached by the solution in the combined generator, assuming the vapor and solution are in equilibrium at that point. If the solution enters in a superheated state,  $T_{C,out,min} = T_{L,ad}$  then:

$$y_{out,max} = y_{eq}(T_{L,ad}, P) \quad (4.18)$$

If the solution enters in equilibrium or in a subcooled state,  $T_{C,out,min} = T_{L,in}$  then:

$$y_{out,max} = y_{eq}(T_{L,in}, P) \quad (4.19)$$

The minimum ammonia concentration that can be reached by the vapor at the exit of the combined generator  $y_{out,min}$  is obtained for an infinitely long generator for which the HTF flows in countercurrent mode to the solution, and the vapor in co-current mode to the solution. The solution and the vapor are then in equilibrium state at the exit, and the temperature is maximum  $T_{L,out,max}$ . If the solution is the limiting fluid, then  $T_{L,out,max} = T_{C,in}$  and the minimum ammonia concentration is given by (Eq. 4.20):

$$y_{out,min} = y_{eq}(T_{C,in}, P) \quad (4.20)$$

If the HTF is the limiting fluid,  $T_{L,out,max}$  is calculated by solving the heat and mass balances (Eqs. 4.21–4.23).

$$\dot{m}_{L,in} = \dot{m}_{L,out,min} + \dot{m}_{V,out,max} \quad (4.21)$$

$$\dot{m}_{L,in} \cdot x_{in} = \dot{m}_{L,out,min} \cdot x_{eq}(T_{L,out,max}, P) + \dot{m}_{V,out,max} \cdot y_{eq}(T_{L,out,max}, P) \quad (4.22)$$

$$\dot{Q}_{C,max} + \dot{m}_{L,in} \cdot H_{L,in} - \dot{m}_{L,out,min} \cdot H_{L,out}(T_{L,out,max}, P, x_{i,out}) - \dot{m}_{V,out,max} \cdot H_{V,out}(T_{L,out,max}, P, y_{i,out}) = 0 \quad (4.23)$$

And the minimum ammonia concentration is calculated by (Eq. 4.24):

$$y_{out,min} = y_{eq}(T_{L,out,max}, P) \quad (4.24)$$

### 3.3 Characterization of the effectiveness

The evolution of the thermal effectiveness of heat exchangers is described through two non-dimensional parameters: the number of heat transfer units,  $NTU$ , and the ratio of heat capacity rate. We propose to adapt this approach to describe the performance of the heated part of the combined generator, and to introduce a new non-dimensional number to take into account the influence of the adiabatic part of the exchanger.

The  $NTU$  is replaced by an adapted  $NTU$  based on the flow capacity of the HTF and defined by (Eq. 4.25):

$$NTU = \frac{U \cdot S_{exch}}{(\dot{m}_C \cdot Cp_C)} \quad (4.25)$$

Wherein  $U$  is the overall heat transfer coefficient,  $S_{exch}$  is the heat transfer area,  $\dot{m}_C$  is the HTF mass flowrate and  $Cp_C$  the HTF heat capacity. The ratio of heat capacity rate is replaced by the equilibrium factor defined by (Eq. 3.15).

The mass transfer between the solution and the vapor in the adiabatic part of the combined generator depends on the sorption heat of the solution, on its sensible heat, and on the equilibrium concentration variation as a function of the temperature at the operating pressure. For the given working fluid and machine operating conditions, this latter physical property is almost constant. The ability of the solution to purify the vapor in the adiabatic part of the exchanger is assumed to be a function of the adapted Jakob number defined by (Eq. 4.26):

$$Ja = \frac{\rho_L \cdot Cp_L \cdot (T_{L,in} - T_{L,eq}(x_{L,in}, P))}{\rho_V \cdot (H_V(T_{eq}, y_{eq,in}, P) - H_L(T_{eq}, x_{L,in}, P))} \quad (4.26)$$

Where,  $\rho_L$  and  $\rho_g$  are the densities of the solution and vapor respectively,  $Cp_L$  is the heat capacity of the solution,  $T_{L,eq}$  is the equilibrium temperature of the solution at the inlet concentration and  $\Delta H_{VL}$  is the sorption heat of vapor at the interface.

When  $Ja > 0$ , the solution enters the combined generator in a superheated state; when  $Ja < 0$ , the solution enters in a subcooled state. The Jakob number reflects the sorption solution potential along the adiabatic part of the combined generator. Thus, the higher the Jakob number, the higher the adiabatic absorption capacity of the solution.

Figure 4.5 illustrates the capacity of the adapted Jakob number to describe the impact of the adiabatic rectification of the vapor on the mass, thermal, and species effectiveness. To this end, the Jakob number was varied over a large range (through pressure ( $P = 9-14$  bar), concentration ( $x_{in} = 0.4-0.7$ ), and inlet solution temperature ( $T_{L,in} = 37-87^\circ\text{C}$ ) variation) and keeping the  $NTU$  and the ratio of heat capacity rate almost constant (the mass flowrates of the HTF and of the solution are fixed to  $\dot{m}_{C,in} = 1600 \text{ kg}\cdot\text{h}^{-1}$  and  $\dot{m}_{L,in} = 136 \text{ kg}\cdot\text{h}^{-1}$ , respectively; the HTF inlet temperature is fixed to  $T_{C,in} = 100^\circ\text{C}$ ). A total of 370 random combinations of operating conditions involving the pressure, concentration, and temperature of the ammonia solution at the inlet were studied.

The solution state (subcooled or superheated) at the inlet of the combined generator does not significantly affect the thermal effectiveness, which lies between 0.65 and 0.69. The combined generator behaves like a standard countercurrent heat exchanger. The mass effectiveness increases linearly with the increase in the temperature at the inlet of the combined generator, and becomes higher than 0.7 for a superheat of over  $20^\circ\text{C}$  (corresponding to  $Ja > 5$ ). The length of the adiabatic part is sufficient for the solution to reach the equilibrium state at the inlet of the heated part (see the geometry in Figure 4.4). When the solution enters the combined generator close to equilibrium with the vapor, the heat transfer and mass transfer between the solution and the vapor in the adiabatic part become very small and the purification process is very limited. The mass effectiveness is then very close to the thermal effectiveness, the difference between both is due to the small degree of superheating of the solution at the exit. The mass effectiveness increase with the Jakob number is directly related to the heat and mass exchanged between the vapor and the solution in the adiabatic part, as expected. The species effectiveness  $\varepsilon_{sp}$  also shows an almost constant trend when the

solution is superheated at the inlet of the combined generator ( $Ja > 0$ ). For subcooled inlet conditions ( $Ja < -1.5$ ), the results are more scattered and vary in the range of 0.74–0.81. When the solution enters the combined generator close to the equilibrium state, most of the points of  $\varepsilon_{sp}$  show a positive slope with the Jakob number and fluctuate in the range of 0.81–0.90.

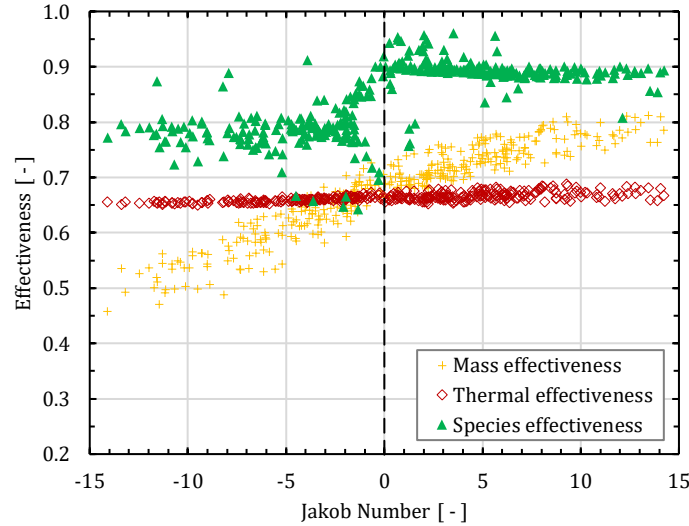


**Figure 4.5.** Effectiveness evolutions as a function of the Jakob number.

Two regimes appear in the adiabatic part of the combined generator: the desorption regime when the solution enters in a superheated state ( $Ja \geq 0$ ) and the absorption regime when the solution enters in a subcooled state ( $Ja \leq 0$ ). One correlation for each regime and each effectiveness is then proposed.

The power-law given by (Eq. 4.27) is proposed to describe the evolution of the different combined generator effectiveness as a function of the operating conditions:

$$\varepsilon_i = A_i \cdot Re_n^{a_i} \cdot (Ja + B_i)^{b_i} \cdot NTU^{c_i} \quad (4.27)$$

Where  $\varepsilon_i$  is the mass, thermal, or species effectiveness, and  $A_i$ ,  $B_i$ ,  $a_i$ ,  $b_i$ , and  $c_i$  are constants for each effectiveness. The constants and exponents were calculated using the root mean square method on the basis of numerical simulations. Table 4.1 shows the values of the constants of (Eq. 4.27). Overall, 265 random combinations of operating conditions involving pressure, temperature, and mass flowrate variations enclosed in the operating range of the machine (i.e.,  $P = 11\text{--}13.5$  bar,  $T_{C,in} = 80^\circ\text{--}105^\circ\text{C}$ ,  $\dot{m}_{C,in} = 800\text{--}2000$  kg.h<sup>-1</sup>,  $T_{L,in} = 50^\circ\text{--}100^\circ\text{C}$ , and  $\dot{m}_{L,in} = 80\text{--}140$  kg.h<sup>-1</sup>) were applied.

	<i>Effectiveness</i>	<i>B</i>	<i>A</i>	<i>a</i>	<i>b</i>	<i>C</i>
<b>Superheated state</b> ( $Ja \geq 0$ )	$\varepsilon_{mass}$		0.4744	0.3501	0.0344	0.3043
	$\varepsilon_{th}$	0	0.4440	0.3902	-0.0114	0.3313
	$\varepsilon_{sp}$		0.9015	-0.0294	-0.0028	0.0183
<b>Subcooled state</b> ( $Ja \leq 0$ )	$\varepsilon_{mass}$		0.1365	0.5057	0.3576	0.4144
	$\varepsilon_{th}$	16	0.2357	0.4073	0.2107	0.3343
	$\varepsilon_{sp}$		4.0713	-0.3553	-0.5090	-0.3083

**Table 4.1.** Constant values for the mass, thermal, and species effectiveness correlations.

The capacity of the correlations to describe the evolutions of the mass, thermal, and species effectiveness was validated through simulations involving 154 new random combinations of operating conditions. Figure 4.6 presents these new effectiveness predicted by the correlation as a function of the effectiveness calculated with the modeling.

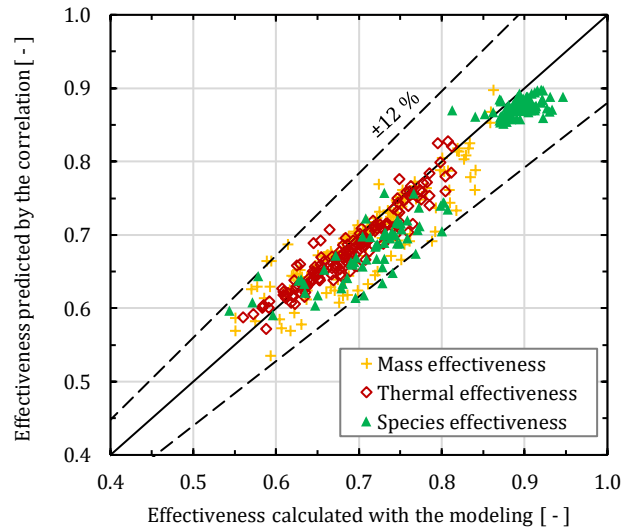


**Figure 4.6.** Comparison of the effectiveness predicted by the correlations and the modeling.

The deviations between the effectiveness calculated with the modeling and that predicted with the correlations are lower than 12%, 7%, and 12%, respectively, for the mass, thermal, and species effectiveness. Figure 4.7 presents the distribution of the number of values in each range of the error rate between the effectiveness calculated with the correlations and with the modeling.

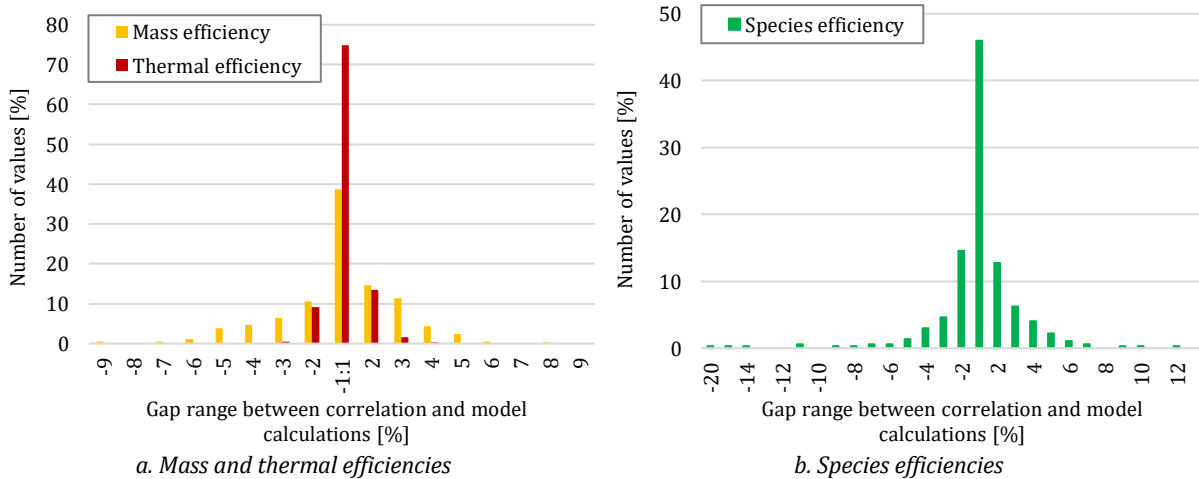


**Figure 4.7.** Error rate between the effectiveness calculated with the correlations and the modeling, distribution for the number of values in each range.

For the mass effectiveness, 96.8% of the values are under 5% of difference between the correlation and the model calculations, for the thermal effectiveness, 97.6% of the values are under 2% of difference and for the species effectiveness, 94.6% of the values are under 5% of difference.

Thus, the correlations determining the mass, thermal and species effectiveness are validated with more than 94% of the values comprised in the range of 0 to 5% of error in comparison to the model.

Considering the ability of the correlation to describe the evolution of the effectiveness as functions of the operating conditions, it has been decided to simulate performances of the absorption chiller with the new combined generator is evaluated thanks to the modeling described in Sect. 2 and the effectiveness correlations presented in Sect. 3.

#### 4 Performances of the absorption chiller equipped with the combined generator

The nominal operating conditions of the absorption chiller (AC) are defined in Table 4.2. The ammonia concentration of the solution introduced in the machine is fixed to  $x_{in} = 0.56$ .

	Generator	Absorber/Condenser	Rectifier	Evaporator	Rich solution
Temperature [°C]	Inlet: 95	Inlet: 27	Inlet: 27	Outlet: 13	-
Inlet mass flowrate [kg.h <sup>-1</sup> ]	1600	-	12	-	100

Table 4.2. Operating inlet conditions of the absorption chiller.

##### 4.1 Performance comparison

The performance of the absorption chiller equipped with the combined generator is compared with the performance of the machine including the flooded generator and a rectifier (Figure 4.8), through the COP of the machine and the ammonia vapor concentration at the inlet of the condenser. The simulations are made for a hot water temperature range of 80°–105°C and a heat rejection temperature range of 22°–31°C.

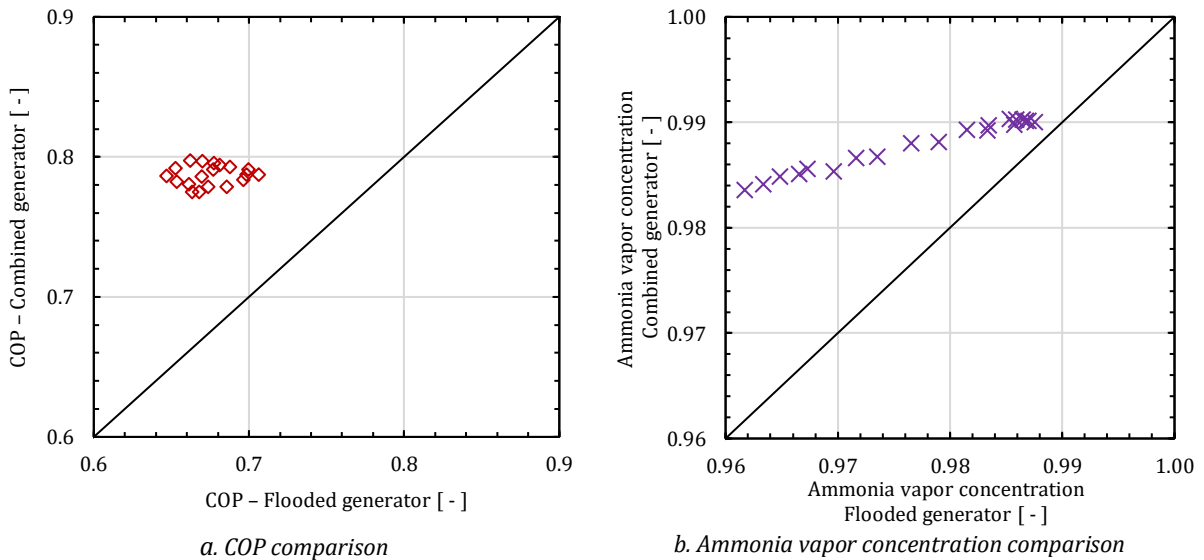


Figure 4.8. Comparison of the absorption chiller COP and of the refrigerant ammonia concentration at the inlet of the condenser for the machine equipped with the combined generator vs. the machine equipped with the flooded generator and rectifier.

The new combined generator improves the performance coefficient of the machine by 11–18%, and increases the purity of the ammonia by up to 2%. The behavior of the machine equipped with the new combined generator as a function of the operating conditions is investigated in detail in the following section in order to identify the new optimum operating conditions.

#### 4.2 Impact of the rectification at the combined generator outlet

A rectifier can be installed downstream of the exchanger to purify the vapor through the partial condensation of the vapor. Either it works (the rectifier thermal effectiveness is fixed to  $\varepsilon_{th,rect} = 0.95$ ) or it is by-passed (the rectifier thermal effectiveness is fixed to  $\varepsilon_{th,rect} = 0$ ).

To further investigate the impact of the active rectification, Figure 4.9a presents the evolution of the ammonia concentration and of the mass flowrate of the vapor produced, as a function of the rectifier effectiveness. Figure 4.9b presents the evolution of the COP and the cooling capacity of the machine.

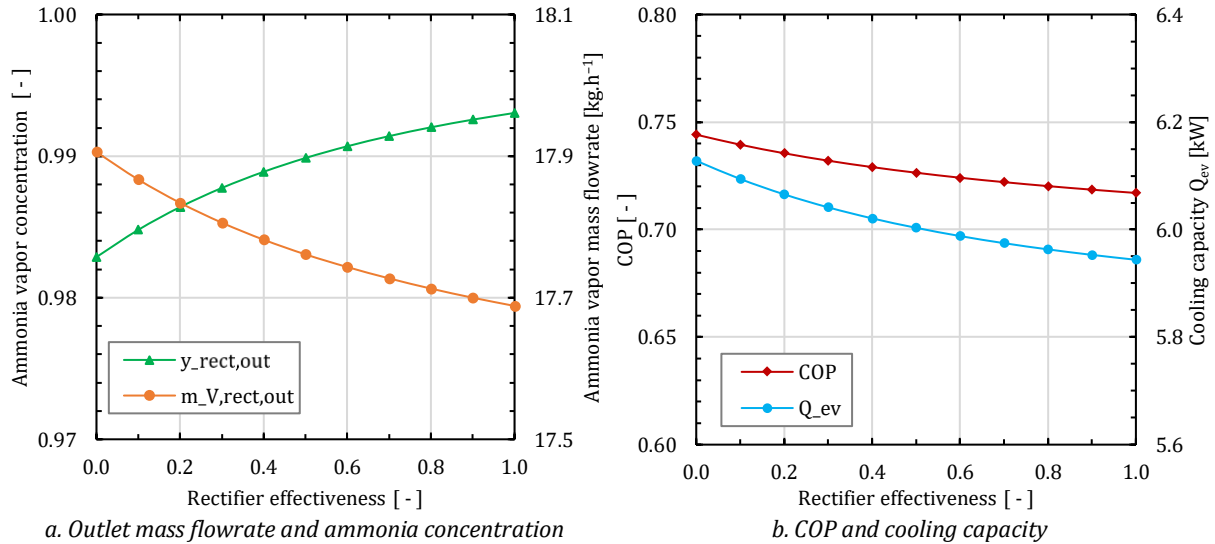


**Figure 4.9.** Refrigerant mass flowrate and concentration, COP and cooling capacity as a function of the rectifier effectiveness.

The vapor produced by the combined generator is characterized by an ammonia concentration higher than 0.98. The purification of the vapor results in a reduction in the amount of ammonia flowing to the evaporator, and thus affects the cooling capacity. The greater the rectifier effectiveness, the greater the ammonia purity and the lower the ammonia vapor mass flowrate.

In the present air-conditioning application characterized by positive temperatures at the evaporator, the rectification process downstream of the combined generator degrades the performance of the machine (relative reduction of the COP of approximately 3%). The rectifier does not have a positive impact on the performance of the machine equipped with the new combined generator and is therefore removed from the installation in the rest of the study.

#### 4.3 Impact of the inlet HTF temperature

The evolution of the performance coefficient of the machine as well as of the cooling power produced at the evaporator as functions of the HTF temperature at the inlet of the combined generator is shown in Figure 4.10.

The cooling capacity increases consistently as expected with the increase in the HTF temperature. The thermal COP of the absorption chiller (Eq. 2.1) shows a relatively low sensitivity to the temperature of the HTF. It reaches a maximum of 0.79 for an HTF temperature of 80°C, before decreasing and reaching 0.77 for an HTF temperature of 102°C.

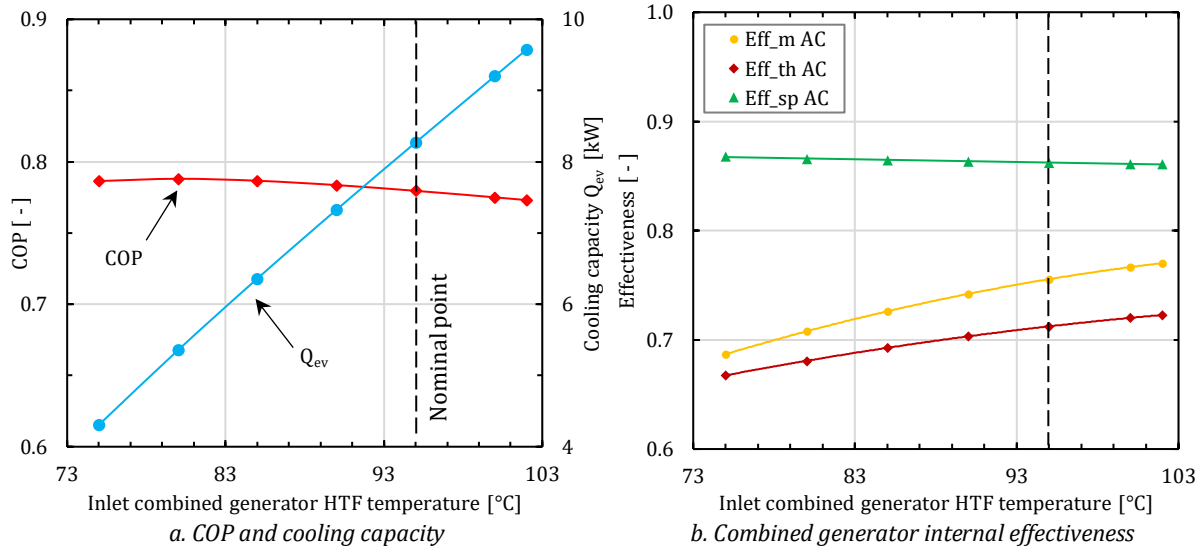


**Figure 4.10.** COP, cooling capacity, and effectiveness evolution as a function of the HTF temperature at the inlet of the combined generator.

The increase in the vapor generated causes a reduction in the falling-film thickness, a reduction in the thermal resistance between the HTF and the vapor, and thus an increase in the thermal effectiveness. The solution that enters the combined generator is slightly superheated, leading to a higher mass effectiveness of the generator than the thermal effectiveness (Figure 4.10b). The superheating of the solution at the inlet of the combined generator increases with the rise in the HTF temperature, leading to an increase in the amount of vapor generated in the adiabatic part and thus in the mass effectiveness compared with the thermal effectiveness. The species effectiveness remains quasi-unchanged when varying the HTF temperature, as shown in Figure 4.10.

#### 4.4 Impact of the inlet solution temperature

The solution superheat at the inlet of the combined generator has a major impact on the ammonia vapor concentration leaving the generator and flowing to the condenser by affecting mass transfer in the adiabatic part. It is possible to modify this temperature by varying the effectiveness of the economizer or by implementing a heat exchanger between the economizer and the combined generator, on the ammonia-rich solution circuit, downstream of the economizer. The first solution consists in reducing the economizer effectiveness, which leads to an increase in the solution temperature at the absorber inlet. The second solution makes it possible to keep the temperature quasi-unchanged at the inlet of the absorber and thus limits the undesirable effect on the machine that would be caused if the performance of the economizer was reduced. The impact of the inlet solution superheat on the machine performance is presented in Figure 4.11.

In the nominal operating conditions (when the solution exchanger located downstream of the economizer does not work), the temperature of the superheated solution entering the combined generator is approximately 9°C. The cooling capacity of the machine increases with the increase in the solution superheat and reaches 9.1 kW for a combined generator inlet solution superheat of 34°C. This tendency is the result of two contrary effects: an increase in the vapor mass flowrate that is proportional to the cooling capacity in the case of a constant ammonia concentration of the vapor leaving the generator; a decrease in the ammonia concentration of the vapor produced by the generator that induces a decrease in the cooling capacity in the case of a constant vapor mass flowrate leaving the generator. The heat injected into the solution through the exchanger to achieve a solution superheat greater than 9°C is taken into account in the calculation of the performance coefficient of the machine. This explains why there is almost no variation in the COP when the solution is heated downstream of the economizer, whereas the cooling capacity increases and the heat provided in the heated part remains almost constant.

The cooling of the solution downstream of the economizer makes it possible to enhance the ammonia concentration of the vapor leaving the generator, as well as to reduce the amount of vapor and enhance the

heat provided by the generator in the heated part, leading to a continuous decrease in the performance coefficient of the machine. The cooling capacity appears to be minimally affected by the subcooling of the solution at the inlet of the combined generator, with the subcooling being compensated by an increase in the heating power in the heated part of the combined generator.

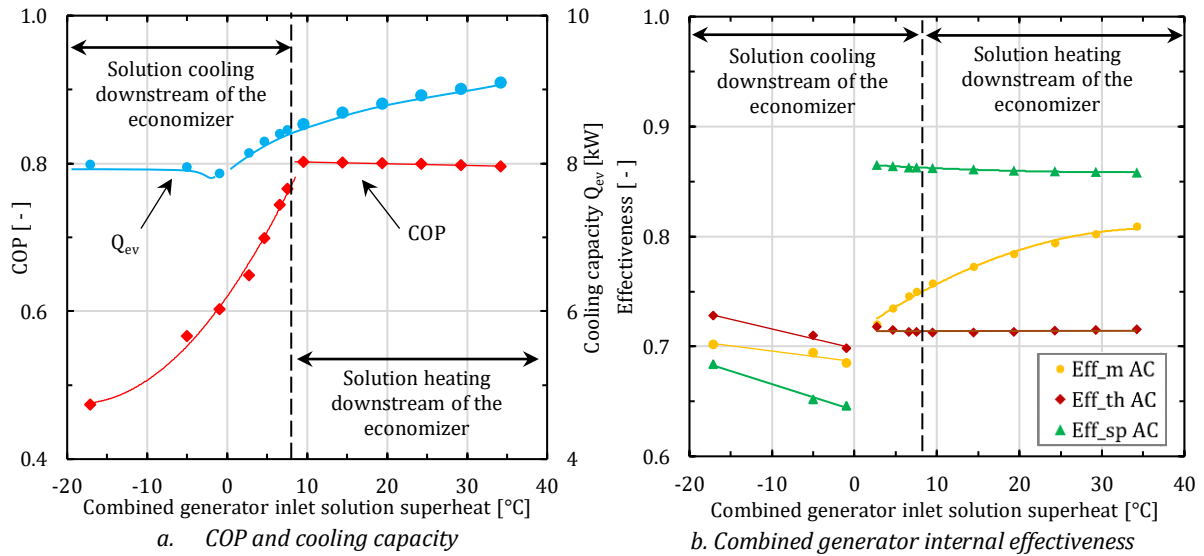


**Figure 4.11.** COP, cooling capacity, and effectiveness evolution as a function of the solution superheating at the inlet of the combined generator.

The evolution of the effectiveness as a function of the superheat of the solution at the inlet of the combined generator is similar to the one shown in Figure 4.5. The dispersion of the points in Figure 4.5 is explained by the variation of a large number of parameters, whereas in Figure 9b, the change in the variable is limited.

#### 4.5 Impact of the equilibrium factor of the combined generator

As mentioned in Sect. 3, the equilibrium factor has an impact on the effectiveness of the combined generator. The influence of this parameter is investigated at the nominal operating point by keeping the temperature of the external sources constant as well as the parameters of the machine, except the mass flowrate of the HTF. Figure 4.12a and Figure 4.12b present the evolution of the absorption chiller performance (COP and cooling capacity) as well as the evolution of the combined generator effectiveness as a function of the equilibrium factor of the combined generator.

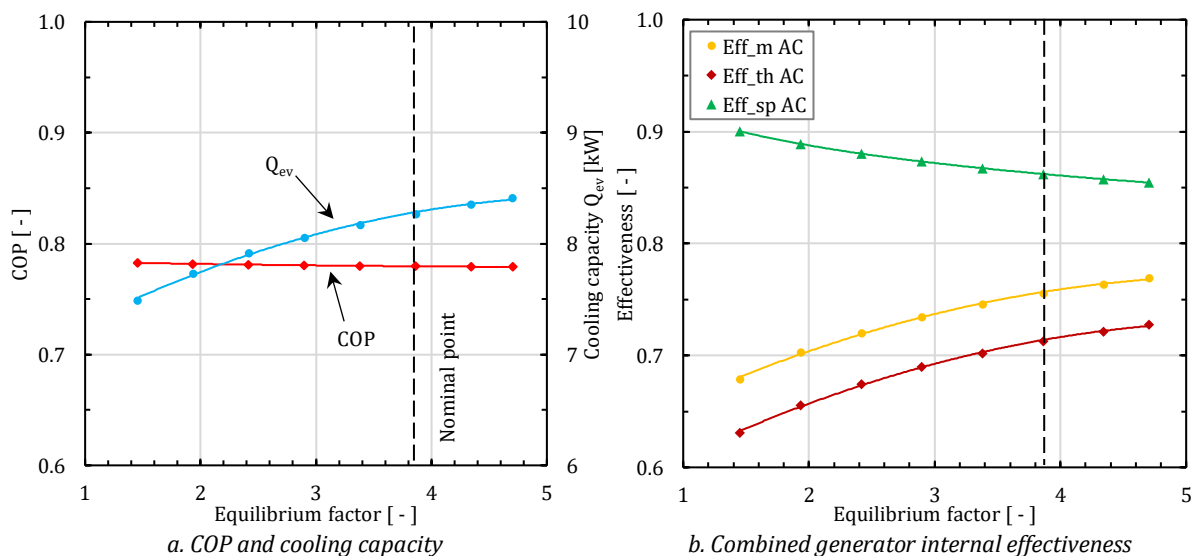


**Figure 4.12.** COP, cooling capacity, and effectiveness evolution as a function of the equilibrium factor.

For the nominal operating condition, the equilibrium factor is close to 4. This means that the mass flowrate of the HTF is fourfold higher than the one theoretically needed to impose its temperature on the solution at the exit of an infinitely long countercurrent generator.

The cooling capacity increases consistently from 7.5 kW to 8.4 kW with the increase in the mass flowrate of the HTF, and thus of the equilibrium factor from 1.4 to 4.7. The COP of the machine is almost not affected by the variation in the equilibrium factor. When the HTF mass flowrate increases, the heating mode on the heated plates of the generator tends to approach the isothermal conditions: It reduces the temperature difference between the inlet and the outlet and increases the heat transfer coefficient between the HTF and the plate, which is an ideal solution concerning the heat and mass transfer with HTF heating mode. The increase in the HTF mass flowrate, however, involves additional energy consumption by the circulation pumps that depends on the system in which the absorption machine is integrated. A further study must then be carried out to identify the optimal operating conditions. Thus, the optimum energy for the system does not necessarily correspond to the highest equilibrium factor.

The increase in the HTF mass flowrate results in an increase in the overall heat transfer coefficient between the HTF and the solution. It increases the heat rate transferred from the HTF to the solution, whereas the maximum heat rate transferable decreases slightly (the equilibrium factor being greater than 1). This leads to an increase in thermal effectiveness. This effect is amplified for the mass effectiveness, the solution at the inlet of the combined generator being superheated. The absorption potential of the solution in the adiabatic part remains almost constant whereas the vapor mass flowrate exiting the heated part of the generator increases with the HTF temperature increase. This explains the evolution of the species effectiveness as a function of the equilibrium factor.

#### 4.6 Impact of the inlet solution mass flowrate

A way to regulate the cooling capacity of absorption machines is to vary the mass flowrate of the solution between the absorber and the generator. The effectiveness of this regulation method is confirmed by the evolution shown in Figure 4.13: The cooling capacity of the machine varies linearly with the increase in the solution mass flowrate at the inlet of the combined generator, whereas the COP remains almost unchanged and equal to 0.78.

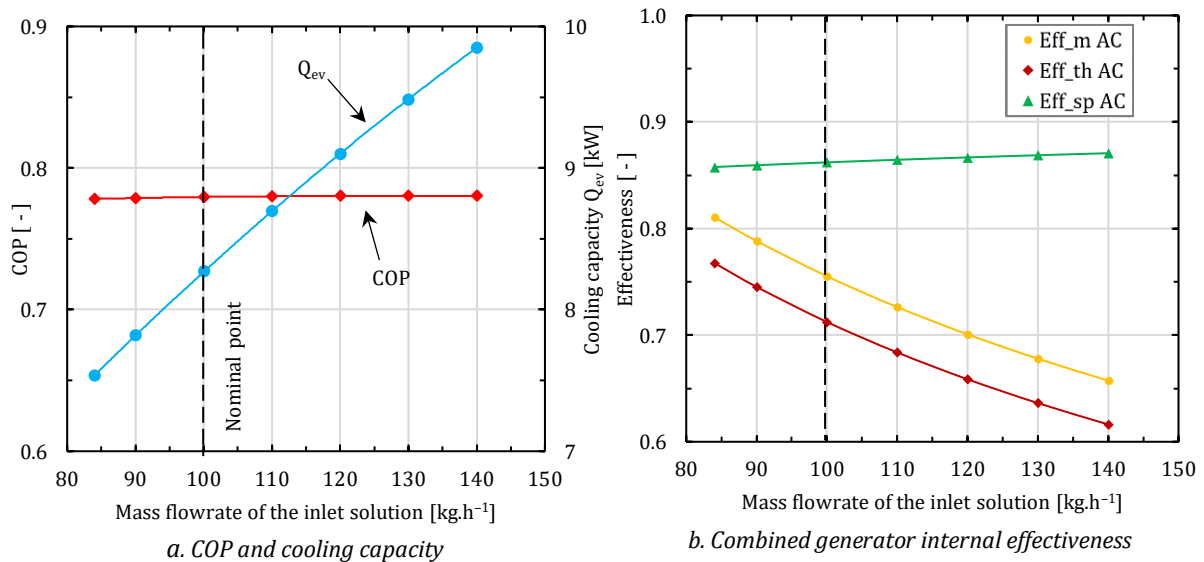


**Figure 4.13.** COP, cooling capacity, and effectiveness evolution as a function of the solution mass flowrate at the combined generator inlet.

The increase in the solution mass flowrate induces an increase in the thickness of the falling film, and thus a decrease in the heat transfer coefficient between the plate and the vapor, and a decrease in the residence time of the solution over the plate. The first effect reduces the heat rate between the HTF and the solution.

The second one increases the maximum heat rate that can be transferred between the HTF and the solution ( $Re_q > 1$ ). These two effects explain the decrease in the thermal effectiveness when varying the solution mass flowrate. The mass effectiveness follows the same evolution as the thermal effectiveness, the difference between the two being due to the superheating of the solution at the inlet of the combined generator.

The increase in the absorption potential in the adiabatic part of the combined generator, due to the increase in the solution mass flowrate, makes it possible to compensate the increase in vapor generation in the heated part. This enables the combined generator to maintain a good purification process of the vapor in the adiabatic part, and leads to an increase in the species effectiveness.

## 5 Conclusion

The improvement of an  $\text{NH}_3\text{-H}_2\text{O}$  absorption machine dedicated to air-conditioning is studied on the basis of replacing a flooded generator-separators-rectifier assembly by the unique combined generator involving falling-film over adiabatic and heated plates developed in *Chapter 1*. The vapor mass flowrate generated as a function of the operating conditions is predicted through mass effectiveness and thermal effectiveness. The ammonia concentration of the vapor at the exit of the combined generator is predicted through species effectiveness. The evolution of the different effectiveness as a function of the operating conditions is described using correlations involving a set of three non-dimensional numbers: an energy ratio, an adapted NTU, and a modified Jakob number. The deviation between the calculated effectiveness and the effectiveness predicted by the correlation is lower than 12%, 7%, and 12%, respectively, for the mass, thermal, and species effectiveness.

A model simulating the behavior of the  $\text{NH}_3\text{-H}_2\text{O}$  absorption chiller equipped with the flooded generator is validated experimentally for a wide range of operating conditions. The impact of the combined generator on the performance of the absorption machine is investigated numerically through mass, thermal, and species effectiveness. The absorption chiller equipped with the novel exchanger shows a significant improvement in the performance coefficient of approximately 15%. The vapor purification process in the adiabatic part of the combined generator is good enough to remove the rectifier. The implementation of the new combined generator in the machine reduces the number of components, increases the compactness of the system, and improves its performance. The influence of the solution flowrate, the heat transfer flowrate, the temperature of the solution at the inlet of the combined generator, and the temperature of the heat sources on the performance of the machine is investigated. The cooling capacity of the machine can be controlled by varying the solution mass flowrate or by varying the temperature of the heat source, keeping the performance of the machine nearly constant. The ammonia concentration at the exit of the generator can be controlled through the temperature of the solution at the inlet of the combined generator. For air-conditioning applications, it is not necessary to control the temperature at the exit of the economizer.

The implementation of the new combined generator in the machine reduces the number of components, increases the compactness of the system, and improves its performance. This chapter yields preliminary numerical results on the behavior of an absorption chiller that uses the novel flat-plate falling-film combined generator. The experimental work follows, producing data that confirm the present numerical observations.

## 6 References

- Boudéhenn F., Demasles H., Wyttenbach J., Jobard X., Chèze D., Papillon P., (2012), "Development of a 5kW cooling capacity ammonia–water absorption chiller for solar cooling applications", *Energy Procedia* 30, 35–43
- Jiménez-García J.C., Rivera W., (2019), "Parametric analysis on the experimental performance of an ammonia/water absorption cooling system built with plate heat exchangers", *Applied Thermal Engineering* 148, 87–95
- Neyer D., Ostheimer M., Hauer N., Halmdienst C., Pink W., (2018), "Application of an adapted single- half-effect NH<sub>3</sub>–H<sub>2</sub>O absorption chiller in tri-generation and solar cooling systems", *Solar Energy* 173, 715–727
- Perier-Muzet M., Stutz B., (2021), "Numerical study of the effectiveness of a vertical falling plate film absorber for an absorption chiller", *International Journal of Refrigeration* 127, 221–229
- Triché D. (2016), "Étude numérique et expérimentale des transferts couplés de masse et de chaleur dans l'absorbeur d'une machine à absorption ammoniac-eau", PhD thesis, *Université de Grenoble Alpes*
- Ziegler B., Trepp C., (1984), "Equation of state for ammonia–water mixtures ", *International Journal of Refrigeration* 7, 101–106



## **Part IV: Experimental characterization and model validation**

*The fourth part of this manuscript is dedicated to the characterization of the performances of the combined generator and of the absorption chiller equipped with this new exchanger.*

*This part is divided in two chapters. The first chapter presents the experimental characterization of the combined generator and its impact on the performance of the  $\text{NH}_3\text{-H}_2\text{O}$  absorption chiller. The second chapter provides a comparative analysis of the performances of a flooded generator and of the combined generator.*



# Chapter III

## Experimental characterization of the NH<sub>3</sub>-H<sub>2</sub>O absorption chiller equipped with the combined generator

---

### Objective:

*The goal of the third chapter is to characterize experimentally the combined generator and its impact on the performance of the NH<sub>3</sub>-H<sub>2</sub>O absorption chiller.*

### Based on:

Wirtz M., Stutz B., Phan H.T., Boudéhenn F.

“Experimental study of the impact of a combined generator behavior on NH<sub>3</sub>-H<sub>2</sub>O absorption chiller performance”  
*International Journal of Refrigeration (Submitted 2021)*

Wirtz M., Boudéhenn F., Phan H.T., Stutz B.

“Générateur comprenant une fonction de rectification, une machine à absorption comprenant ledit générateur et un procédé de production de vapeur de fluide frigorigène par ledit générateur” (2021a)  
*European patent, EP 3 885 672 A1*

Wirtz M., Chandez B., Phan H.T., Stutz B.

“Dispositif de rectification comprenant un rectifieur et un dispositif de distribution, et machine à absorption comprenant ledit dispositif de rectification” (2021b)  
*European patent, EP 3 885 673 A1*



*This chapter presents the impact of the novel falling-film and plate combined generator associating vapor production and purification on the performance of an NH<sub>3</sub>-H<sub>2</sub>O absorption chiller. Two operating modes of the combined generator are analyzed: partly flooded and unflooded mode.*

*First, the impact of two operating parameters (i.e. the heat transfer fluid mass flowrate and solution subcooling at the generator inlet) on the performance of the absorption chiller is analyzed in order to fix them for the rest of the study. Then, the impact of the operating conditions of the machine (i.e. inlet temperatures of the heating, chilling, and heat rejection sources, as well as mass flowrate of the rich solution) on the combined generator performance is studied using a design of experiments. Then, two correlation forms are developed and compared with experimental data. Moreover, the performances of the machine equipped with the initial generator-separators-rectifier assembly and equipped with the combined generator are compared using the Carnot-COP approach. The influence of the solution mass flowrate on the COP and cooling capacity is studied. Finally, a practical application of an office air-conditioning involving the absorption chiller is developed to compare the performances of the different machine configurations and the associated energy gains.*

## 1 Introduction

The performance of absorption chillers is highly dependent on the temperature of the heat sources and sinks, whose variations depend on the climate and conditions of use. Therefore, users need reliable information on the long-term behavior of the system they want to implement, for known external operating conditions (Lazrak et al. 2016). Modeling absorption chillers helps to evaluate the system performance evolution when the operating conditions differ from the nominal conditions. To that purpose, some studies were led, presenting the modeling of absorption chillers with experimental validations, as the studies of (Ziegler et al. 1999; Boudéhenn et al. 2012; and Franchini et al. 2015).

The absorption chiller performance relies on the operation (and thus on the technology) of its components, mainly the absorber and the desorber, whose performance is more influential (Mittermaier and Ziegler 2015). For  $\text{NH}_3\text{-H}_2\text{O}$  machines, a rectifier or a suitable architecture such as a packing column can address the problem of water traces in the generated ammonia vapor. However, this involves more components in the machine, making its architecture more complex and reducing its compactness. Aiming to improve the performance and to reduce the size of the machine, various desorption technologies were developed during the past few years, such as microchannel, vertical tubes or plates exchangers (Altamirano et al. 2020).

The present experimental work investigates the effect of integrating the innovative combined generator presented in *Chapter I* and *Chapter II*, on the performance (especially the thermal COP and cooling capacity), of an  $\text{NH}_3\text{-H}_2\text{O}$  absorption chiller of 5-kW cooling capacity. The combined generator produces sufficiently high ammonia vapor quality to avoid the use of a rectifier. The impact of partial flooding of the combined generator is investigated. A design of experiments is applied to a wide range of external and internal operating conditions, to characterize the performance of the combined generator. The ability of two correlation forms to predict the performance of the combined generator is compared using complementary measurements points. The impact of the solution mass flowrate and the heating temperature on the chiller operating limits and performance is studied through the presentation of the advantages and drawbacks of various case studies.

## 2 Integration of the combined generator in an $\text{NH}_3\text{-H}_2\text{O}$ absorption chiller of 5-kW cooling capacity

### 2.1 The $\text{NH}_3\text{-H}_2\text{O}$ absorption chiller

The objective of this experimental work is to enhance the performance of a single-effect  $\text{NH}_3\text{-H}_2\text{O}$  absorption chiller, with 5-kW cold capacity, by replacing the vapor generation and purification device by an innovative combined generator. The experimental tests are conducted in the  $\text{NH}_3\text{-H}_2\text{O}$  absorption chiller, chiller developed by CEA, at the National Institute of Solar Energy (Boudéhenn et al. 2012). The absorption chiller was intended to be low-cost, compact, and has to respond to specific performance and industrial characteristics as being scalable to large temperature ranges, in order to meet the air-conditioning needs of a single-family home.

The absorption chiller comprised four main plate heat exchangers: the absorber, the flooded generator, the evaporator, and the condenser. Three additional classic exchangers are implemented to enhance the performance of the machine: a sub-cooler (that cools the liquid refrigerant before its evaporation and superheats the vapor before it enters the absorber); an economizer (that heats the rich ammonia-water mixture entering the generator and cools the poor solution entering the absorber); and a rectifier (that purifies the vapor produced by the generator). A pump drives the mass flowrate of the rich solution, and two expansion valves are located at the inlet of the evaporator and of the absorber. Two accumulators are included in the machine to absorb the variations of the coolant and of the rich solution, depending on the operating conditions. Two separators are implemented at the exit of the generator to separate the vapor from the poor solution and at the exit of the rectifier to separate the ammonia vapor from water condensate.



**Figure 5.1.** Single-stage  $\text{NH}_3\text{-H}_2\text{O}$  absorption chiller implemented in the CEA laboratory.

The machine is connected to a characterization bench to determine its performance over the desired operating range. Independent hydraulic loops fix the temperatures and the mass flowrates of the heat transfer fluids (HTFs) that flow inside the generator, the condenser, the absorber, and the evaporator. The temperature ranges of the heating and chilling sources and of the intermediate heat sink are, respectively,  $T_{hot} = [80\text{-}120^\circ\text{C}]$ ,  $T_{cold} = [5\text{-}22^\circ\text{C}]$ , and  $T_{medium} = [22\text{-}33^\circ\text{C}]$ .



**Figure 5.2.** The single-stage  $\text{NH}_3\text{-H}_2\text{O}$  absorption chiller and the external hydraulic modules.

## 2.2 Implementation of the combined generator

### 2.2.1 The heated plates

The initial boiling generator used was a flooded heat plate exchanger. A rectifier was implemented at its outlet to purify the refrigerant vapor for a better performance of the machine. Two separators located between the generator and the rectifier, and at the rectifier exit completed the ammonia vapor generation and purification system. A combined falling-film generator, involving vapor generation and purification functions is designed to replace this assembly of four components (see Figure 5.1).

The new exchanger is built with stainless steel, to resist the ammonia corrosion and the high temperatures of operation. Its global dimensions are 0.65 m high, 0.27 m width, and 0.16 m thick when assembled. Figure 5.3a shows an exploded view of the combined generator, including the front face plate where all the fluids enter and exit (1), one of the HTF plates (2), one of the solution plates (3), and the back face plate (4).

The combined generator is composed of a stack of 15 alternating plates: the HTF circulates in 8 channels and the ammonia concentrated solution falling-film flows through 7 channels between the plates. The HTF enters at the bottom of the heated plates in C (Figure 5.3a), flows upward in counter-current mode compared to the solution falling-film it heats, and exits in D at the top of the heated plate part.

The ammonia-rich solution enters at the top in A, crosses the distribution-rectification system and flows downward the heated and corrugated plates. The ammonia-poor solution exits in B and goes back to the absorber. The solution flows along the heated plates within 4 mm thick grooves insuring negligible head losses and a laminar flow, and keeping an acceptable level of wetting of the plates by limiting the phenomena of solution aggregation under the effect of the superficial tension (rivulets formation).

The heat transferred allows generating ammonia vapor with small water content from the bottom of the combined generator. This ammonia vapor flows upward interacting with the heated falling-film and goes through the distribution-rectification system to exit in E.

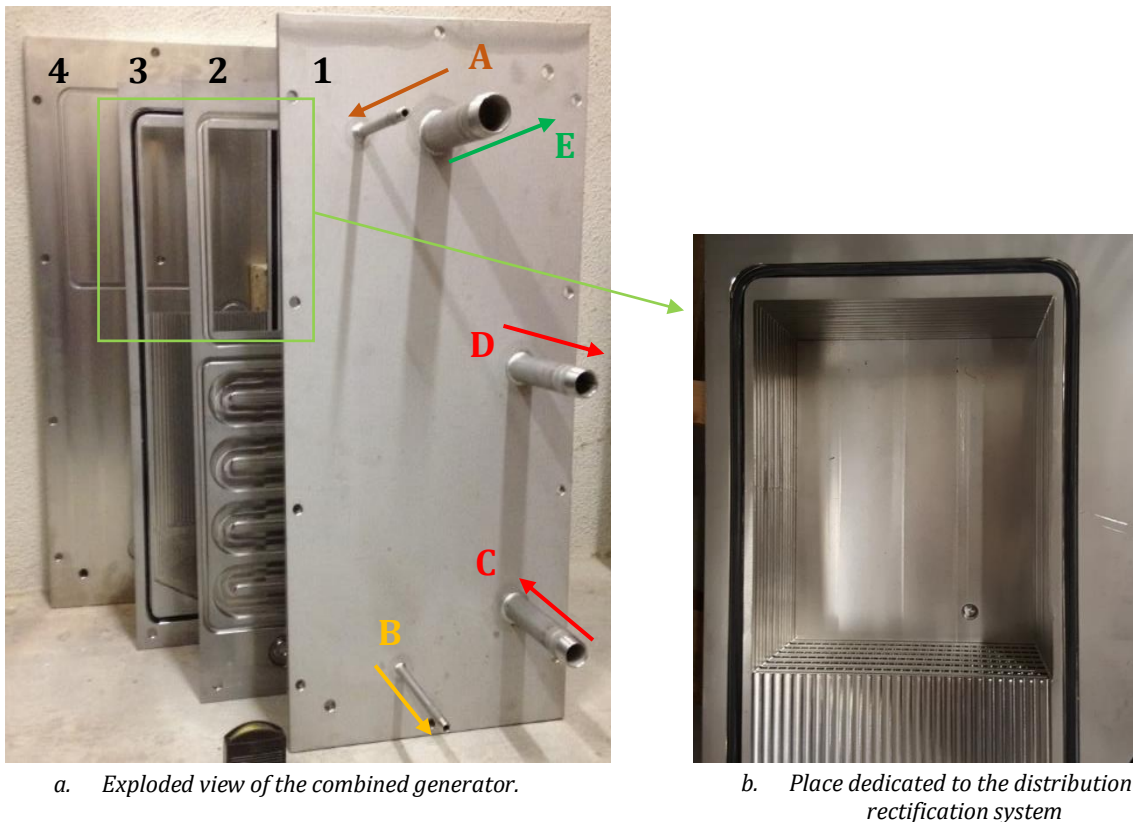


**Figure 5.3.** Interior of the combined generator before integrating the distribution-rectification system.

On top of the heated plates section, a space is left for the distribution–rectification system integration (Figure 5.3b).

### 2.2.2 Distribution–rectification system

For better thermal transfers between the HTF and the falling-film, the ammonia–water solution has to be homogeneously distributed over all the grooves of the solution plates. A distribution system is designed to divide uniformly the solution in all the grooves of each plate, and to let the ammonia vapor generated evacuating upward after exiting from the heated plates. This system combines also the function of ammonia vapor rectification by providing a sufficient exchange surface between solution and vapor, for a partial reabsorption of the vapor by the solution, reducing the water content in the vapor and thus purifying it. This distribution–rectification system is fixed on the top of the heated plates.

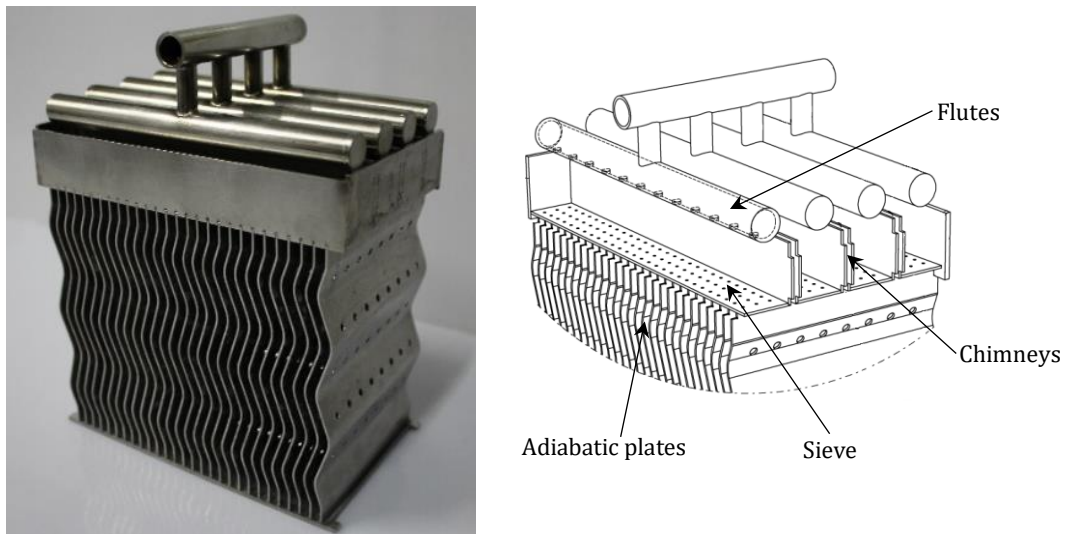


**Figure 5.4.** Distribution–rectification system (patent EP 3 885 673 A1).

The rich solution is injected in the upper part of the system, in an assembly of flutes, primarily distributing the solution in a retention tank. The bottom of the tank is composed of a sieve, designed to let the solution spread over the entire sieve, before passing through the holes. Then the solution flows underneath, along plates of 0.1 m high. The distribution plates are curved and perforated to allow a uniform distribution of the fluid on both sides of the plates. It ensures an important surface of exchange between the solution and the vapor, for an efficient rectification process; indeed, the solution partially reabsorbs the vapor, and particularly the fraction of water it contains, and thus purifies it.

The distribution system is designed to allow the second distribution of the solution over the heated plates. Indeed, it includes 28 curved plates, disposed to correspond to the grooves of the heated plates, to avoid vapor head losses and to let enough space between them for the vapor flow escape without causing the shearing of the solution. The distribution–rectification system is placed perpendicularly to the heated plates for a better contact and a better distribution of the solution in each groove. The system is set thanks to combs, placed at the lower part of the plates, preventing the risk of movement of the curved plates, by fixing the space between them.

The implementation of three rectangular chimneys located through the retention tank allows the purified vapor to exit from the curved plates through three exits. Thus, the evacuation surface is wide and well dispersed on the whole sieve.

The head losses due to the geometry of the distribution–rectification system are calculated in a nominal case of operation of the combined generator for both liquid and vapor flows and correspond to  $\Delta P_L = 0.11136 \text{ bar}$  and  $\Delta P_V = 1.44 \cdot 10^{-3} \text{ bar}$ , respectively. As the pressure in the component varies between 11 and 13 bar, the head losses are negligible. The detail of the head losses calculations is provided in *Appendix 6.2*.

2.2.3 Combined generator operation

The lower third of the heated plates can be flooded by the solution. Thus, either the combined generator operates with only falling-film process along the heated plates, or it operates in the partly flooded configuration, which combines falling-film and boiling transfers. Figure 5.5 shows a photo of the prototype interior with the fluids circulation, and the geometry of the combined generator with its dimensions.

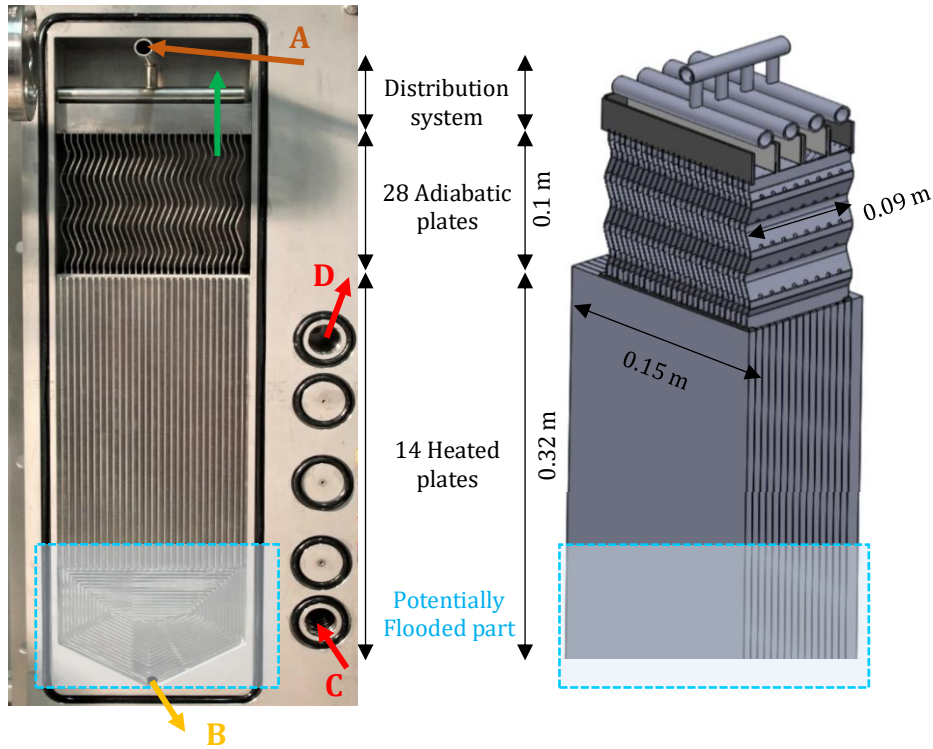


**Figure 5.5.** Combined generator (patent EP 3 885 672 A1) and fluids circulation.

The combined generator presented is built and integrated in the absorption chiller. As shown in Figure 5.1, it replaces the flooded generator-separators-rectifier assembly. In the following, the absorption chiller works with the new combined generator.

### 2.3 Measurements

The location of the different measurements is represented in the absorption chiller PID in Figure 5.6.

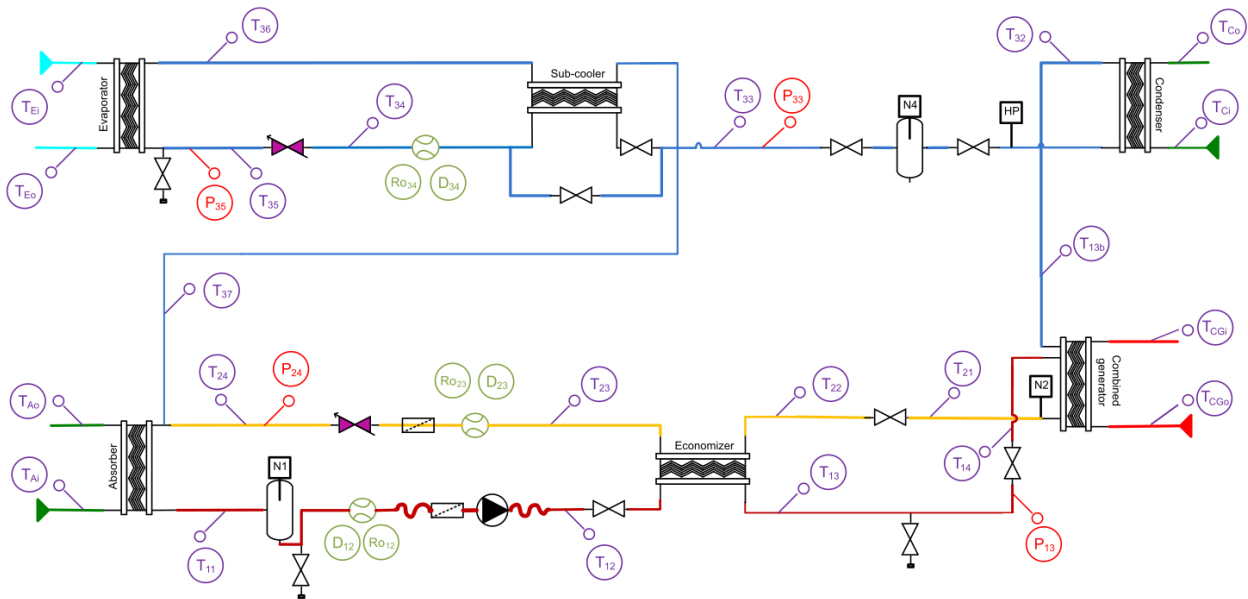


Figure 5.6. PID of the  $\text{NH}_3\text{-H}_2\text{O}$  absorption chiller.

The operating range and the uncertainties of the measurements are given in Table 5.1. The measurement uncertainties take into account the stability, the repeatability, the resolution, and the accuracy of the system. The measurement and calibration uncertainties are detailed in *Appendix 6.1*. The ammonia concentration in the rich solution, the poor solution, and the refrigerant is calculated using correlations established with the temperature and density measurements.

Sensor	Quantity	Measurement	Name	Range	Uncertainty
Pressure sensor	2	High pressure [bar]	P <sub>13</sub> , P <sub>33</sub>	0–20	± 0.82%
	2	Low pressure [bar]	P <sub>24</sub> , P <sub>35</sub>	0–10	± 0.41%
Thermocouples	15	Internal temperatures [°C]	T <sub>11</sub> –T <sub>37</sub>	0–125	± 0.19°C
	8	External temperatures [°C]	T <sub>Ai</sub> –T <sub>Ro</sub>	-20–130	± 0.14°C
Coriolis flowmeter	Rich solution	Flowrate [kg.h <sup>-1</sup> ]	D <sub>12</sub>	0–160	± 0.20%
		Density [kg.m <sup>-3</sup> ]	RO <sub>12</sub>	600–1100	± 0.38%
	Poor solution	Flowrate [kg.h <sup>-1</sup> ]	D <sub>23</sub>	0–160	± 0.20%
		Density [kg.m <sup>-3</sup> ]	RO <sub>23</sub>	600–1100	± 0.38%
	Refrigerant	Flowrate [kg.h <sup>-1</sup> ]	D <sub>34</sub>	0–40	± 0.38%
Density [kg/m <sup>3</sup> ]		RO <sub>34</sub>	600–1100	± 0.38%	
Electromagnetic flowmeter	Generator	Heating water flowrate [kg.h <sup>-1</sup> ]		0–5000	± 0.30%
	Evaporator	Cooling water flowrate [kg.h <sup>-1</sup> ]		0–5000	± 0.15%
	Absorber	Ambient water flowrate [kg.h <sup>-1</sup> ]		0–2500	± 0.47%
	Condenser	Ambient water flowrate [kg.h <sup>-1</sup> ]		0–2500	± 0.47%

Table 5.1. Range of values of parameters measured and uncertainties.

### 3 Experimental comparison of the absorption chiller performance, equipped with the combined generator and with the generator-separators-rectifier assembly

(Triché 2016) experimentally tested the former configuration of the absorption chiller containing the assembly of the generator, the rectifier, and the separators. The absorption chiller equipped with the new combined generator is run for the same inlet parameters. The nominal operating conditions for the external circuits HTFs, and the solution mass flowrate are presented in Table 5.2.

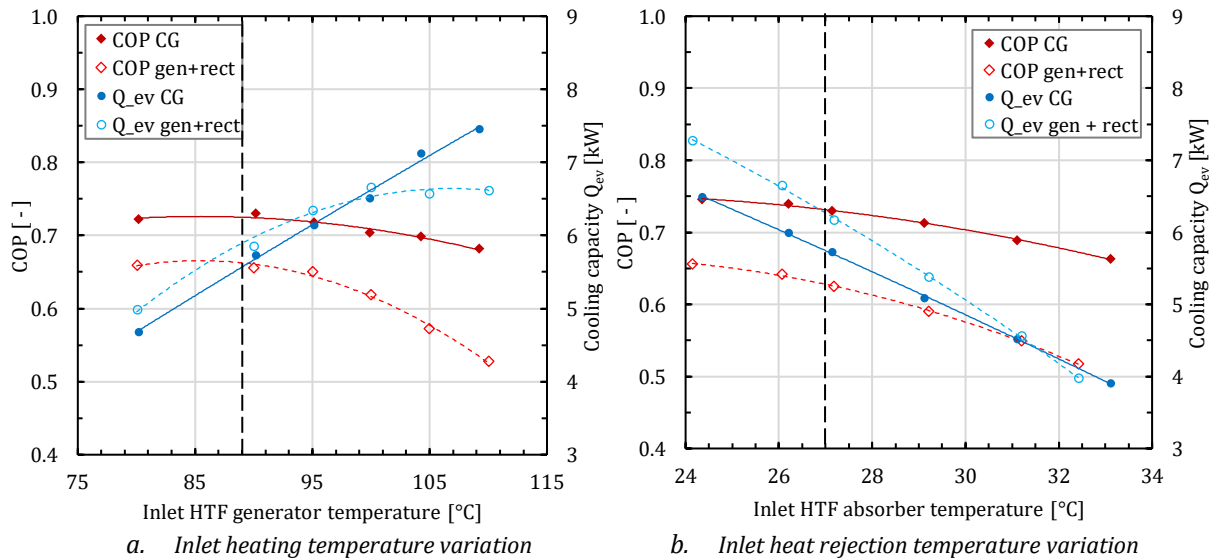
	Generator	Absorber/Condenser	Rectifier	Evaporator	Rich solution
Temperature [°C]	90	27	27	18	-
Mass flowrate [kg.h <sup>-1</sup> ]	1120	1190	12	1110	75

**Table 5.2.** Inlet nominal operating conditions and ranges of operating conditions of the absorption chiller.

The two main parameters used to compare the performance of the absorption chiller equipped with the former assembly (*gen+rect*) and equipped with the combined generator (*CG*) are the COP (defined Eq. 4.14) and the cooling capacity ( $Q_{ev}$ ) at the evaporator level.

Figure 5.7a, Figure 5.7b, and Figure 5.7c represent the COP and cooling capacity as a function of the heating temperature at the generator inlet ( $T_{hot}$ ), of the heat rejection temperature at the absorber inlet ( $T_{medium}$ ), and of the chilling temperature at the evaporator inlet ( $T_{cold}$ ), respectively. Figure 5.7d shows the COP and cooling capacity as a function of the inlet solution mass flowrate ( $\dot{m}_{RS}$ ).

Between  $T_{hot} = [75-100 \text{ °C}]$ , cooling capacity in both configurations of the absorption chiller increases at a very close value ( $\sim 0.3 \text{ kW}$ ). When  $T_{hot} > 100 \text{ °C}$ , cooling capacity in the absorption chiller equipped with the combined generator still increases while it reaches a maximum of 6.5 kW for the absorption chiller equipped with the former configuration. The COP of the absorption chiller equipped with the combined generator is 0.07 to 0.16 higher than the COP of the absorption chiller including the former components assembly. They reach the maximum values of 0.73 at  $T_{hot} = 90 \text{ °C}$ , and 0.66 at  $T_{hot} = 85 \text{ °C}$ , respectively. Thus, the combined generator needs less heat input to produce the same amount of cold.



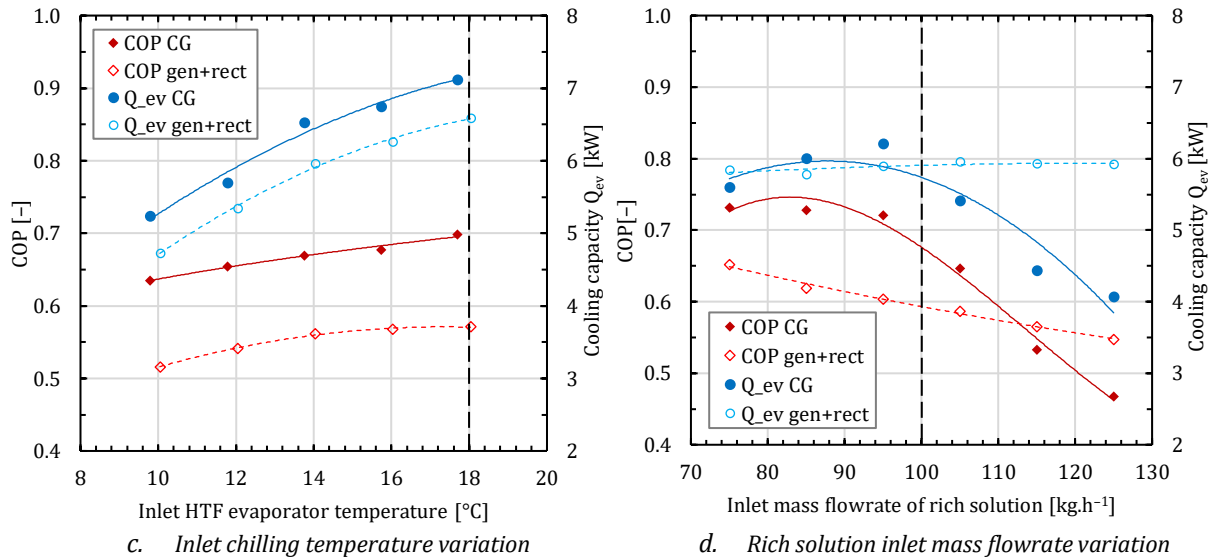


**Figure 5.7.** COP and cooling capacity evolution as a function of the inlet temperatures of the external circuits and of the inlet solution mass flowrate, for the absorption chiller equipped with the former assembly and equipped with the combined generator.

The COP and cooling capacity decrease with the increase in the heat rejection source temperature at the absorber level, with a value of the COP 0.08 to 0.15 higher when the combined generator works. For low values of  $T_{medium}$ , the absorption chiller equipped with the former assembly produces more cold.

When the inlet chilling temperature varies, the inlet heating temperature is fixed at  $T_{hot} = 105^{\circ}\text{C}$  and the other inlet operating conditions are presented in Table 5.2. The COP and cooling capacity decrease consistently with the decrease of the chilling temperature, with higher values of COP and cooling capacity for the machine equipped with the combined generator (+0.12 and +0.5 kW, respectively).

Regardless of the solution mass flowrate increase from 75 to 125 kg.h<sup>-1</sup>, the cooling capacity of the absorption chiller including the former generator and rectifier assembly is almost constant at 5.9 kW. The COP decreases linearly from 0.65 to 0.55. For the absorption chiller equipped with the combined generator, the COP increases until  $\dot{m}_{RS} \approx 84$  kg.h<sup>-1</sup> to reach a maximum value of 0.73, and cooling capacity increases until  $\dot{m}_{RS} \approx 87$  kg.h<sup>-1</sup> to reach a maximum value of 6 kW; then they quickly decrease until  $\dot{m}_{RS} = 125$  kg.h<sup>-1</sup> reaching 0.47 and 4.1 kW, respectively. The decrease of the performance of the combined generator for a solution mass flowrate  $\dot{m}_{RS} > 90$  kg.h<sup>-1</sup> is rather unexpected. This might be due to distribution problems at high mass flowrate. This hypothesis should be confirmed by additional experiments at atmospheric pressure including flow visualization.

The NH<sub>3</sub>-H<sub>2</sub>O absorption chiller equipped with the flooded generator-separators-rectifier assembly produces a slightly superior amount of cold than the machine equipped with the new combined generator, except at high heating temperatures values ( $T_{hot} > 100^{\circ}\text{C}$ ). For solution mass flowrate lower than  $\dot{m}_{RS} < 115$  kg.h<sup>-1</sup>, the integration of the combined generator upgrades the performance of the machine: the combined generator needs less heat power input than the former generator-rectifier assembly for similar cooling capacity.

Thus, the combined generator takes the advantage on the former assembly of being less energy-consuming, leading to the improvement of the machine performance, and to the reduction of the operating costs; in addition to being more compact, which leads to the reduction of the machine size and design costs. Then, the nominal inlet operating conditions of the absorption chiller need to be adapted to the new combined generator for an optimal functioning of the machine.

In the following, the absorption chiller is equipped with the combined generator and the machine performance is investigated for two operating modes of the combined generator.

## 4 Parametric analysis

The impact of the combined generator control variables on the performance of the absorption chiller is investigated, for the unflooded (*UF*) and the partly flooded (*PF*) configurations of the combined generator.

### 4.1 Mass flowrate of the heat transfer fluid

The maximum heat rate that can be transferred in the combined generator depends on the mass flowrates and enthalpies of the HTF and of the solution that enter the exchanger. Their calculations are detailed in *Chapter I (Eqs. 3.18–3.19)*. The limiting fluid can be determined through the equilibrium factor (*Eq. 3.15*).

The heat exchangers of the absorption machine in which the combined generator is implemented were sized to operate with sufficiently large HTF flowrates so as not to be limiting. The optimum flowrate of the HTF supplying the combined generator was the subject of a specific study that will be presented hereafter. This optimum flowrate is fixed by applying the COP, calculated in (*Eq. 2.1*), and the cooling capacity of the absorption chiller.

Figure 5.8 shows the evolution of the COP and of cooling capacity with the HTF mass flowrate at the inlet of the combined generator. The HTF mass flowrate range studied is [600–1800 kg.h<sup>-1</sup>]. The equilibrium factor corresponding to this operating range is [1.1–3.4]. The solution is the limiting fluid on the entire range of the HTF flowrate studied.

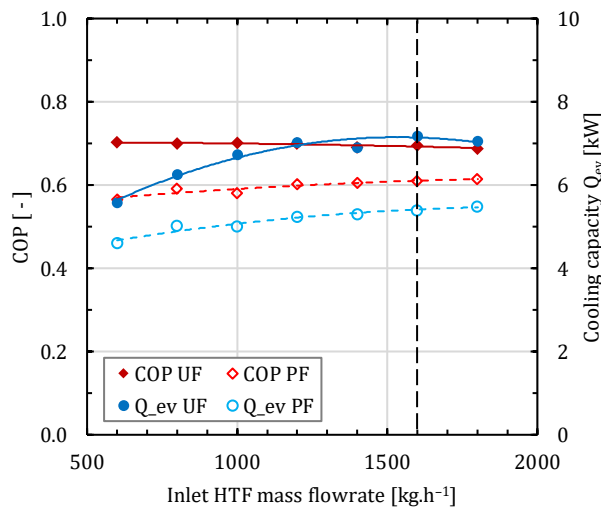


**Figure 5.8.** Evolution of COP and cooling capacity as a function of the inlet HTF mass flowrate for both configurations of combined generator.

The performance of the partly flooded combined generator is lower than that of the unflooded configuration. The COP difference is approximately 0.1, whereas the cooling capacity difference is on average equal to 1.5 kW. For the unflooded configuration, the increase in the HTF mass flowrate leads to a small COP decrease from 0.70 to 0.69, whereas cooling capacity reaches a maximum of 7.2 kW for an HTF mass flowrate of 1600 kg.h<sup>-1</sup>. Considering these changes, the operating condition relative to the HTF mass flowrate at the generator was fixed at  $\dot{m}_{hot} \approx 1600 \text{ kg.h}^{-1}$  for the unflooded operating configuration.

For the partly flooded configuration, the COP and cooling capacity increase consistently, from 0.57 to 0.61 and from 4.6 kW to 5.5 kW, respectively. This behavior suggests that the optimum operating condition for this mode is the isothermal configuration. Considering the moderate impact of the HTF mass flowrate on the performance of the combined generator operating with the partial flooding configuration, the operating condition relative to the HTF mass flowrate at the generator was also fixed at  $\dot{m}_{hot} \approx 1600 \text{ kg.h}^{-1}$ .

## 4.2 Nominal operating conditions

The nominal operating conditions for the HTF and the solution mass flowrate are summarized in Table 5.3.

	Combined generator	Absorber	Evaporator	Rich solution
	$T_{hot}, \dot{m}_{hot}$	$T_{medium}, \dot{m}_{medium}$	$T_{cold}, \dot{m}_{cold}$	$\dot{m}_{RS}$
Temperature [°C]	95	27	18	-
Mass flowrate [kg.h <sup>-1</sup> ]	1600	1230	1110	100

**Table 5.3.** Nominal operating parameters of the absorption chiller.

The temperatures and mass flowrates of the HTF and of the solution are the four main inlet operating parameters of the combined generator which impacts on the absorption chiller performance can be investigated. The temperature of the solution injected in the combined generator depends on the chiller operation, however, as showed in *Chapter II, Sect 4.4*, it is an interesting parameter to investigate, because the colder the solution entering the exchanger, the purer the ammonia vapor produced.

## 4.3 Impact of the solution subcooling on the absorption chiller performance

As explained in *Chapter II, Sect 4.4*, implementing a heat exchanger downstream of the economizer makes it possible to cool the solution entering the combined generator while keeping the temperature quasi-unchanged at the inlet of the absorber. Hereafter, we present the analysis of the impact of the solution superheat at the inlet of the generator. The analysis is based, on the one hand, on the machine performance determined by the COP and cooling capacity, and on the other hand, on the performance of the combined generator determined by the ammonia concentration and mass flowrate of the vapor emitted. The ammonia vapor mass flowrate is calculated on the basis of the temperature and the density of the liquid refrigerant measured by a Coriolis flowmeter before entering the evaporator.

A 3-kW capacity heat plate exchanger is placed between the economizer and the combined generator. Externally connected to a cold-water network, it cools the solution to the desired temperature before entering the combined generator. Figure 5.9a displays the evolution of the COP and of cooling capacity of the absorption chiller as a function of the temperature gap between the inlet solution temperature and the saturation temperature of the solution, calculated for the ammonia concentration and the pressure measured at the inlet. The solution reaches its maximum superheat when the cooling exchanger is not supplied with coolant. The impact of the solution cooling is observed until instabilities are generated in the absorption chiller operation. The subcooling limits are then, respectively,  $-15$  and  $-12^{\circ}\text{C}$  for the unflooded and the partly flooded configurations. Figure 5.9b presents the evolution of the ammonia vapor concentration and the mass flowrate as a function of the saturation temperature gap. For an easier operation of the absorption chiller, the chilling temperature at the evaporator was fixed at  $T_{cold} = 14^{\circ}\text{C}$ . The other operating parameters of the absorption chiller are presented in Table 5.3.

As can be seen in Figure 5.9, the operating configuration of the combined generator has a significant impact on the performance of the machine. When there is no cooling of the solution downstream of the economizer, the ammonia fraction and the superheat of the solution at the inlet of the combined generator are, respectively, 99.4% and 5°C for the unflooded configuration and 99.2% and 11°C for the partly flooded configuration.

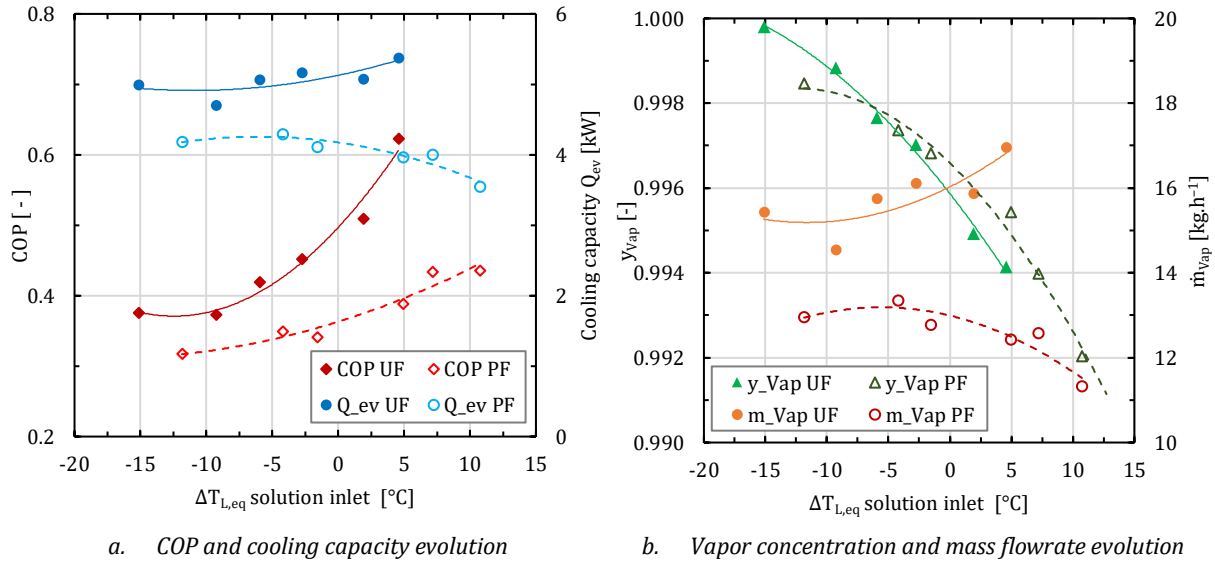


**Figure 5.9.** COP, cooling capacity, vapor concentration, and mass flowrate as a function of the saturation temperature gap at the inlet of the combined generator.

For the unflooded configuration, the solution cooling at the inlet of the combined generator leads to an ammonia vapor concentration increase that reaches 99.96% for the highest solution subcooling  $\Delta T_{L,eq} = -15^\circ\text{C}$ . The intensification of the purification due to the partial vapor reabsorption in the adiabatic part is accompanied by a reduction in the vapor mass flowrate emitted by the exchanger: This flowrate decreases from 17 to 15  $\text{kg}\cdot\text{h}^{-1}$  when  $\Delta T_{L,eq}$  varies from 5 to  $-15^\circ\text{C}$ . It results in a slight decrease in cooling capacity from 5.4 to 5 kW. The reduction in cooling capacity has an impact on the COP, which decreases from 0.623 to 0.376.

For the partly flooded configuration, the solution cooling at the inlet of the combined generator also causes an increase in the ammonia vapor concentration, reaching 99.83% at  $\Delta T_{L,eq} = -12^\circ\text{C}$ . The mass flowrate reaches a maximum of  $\dot{m}_{vap} \sim 13 \text{ kg}\cdot\text{h}^{-1}$  for  $\Delta T_{L,eq} = -5^\circ\text{C}$ . Cooling capacity is then at a maximum and equal to 4.3 kW. This behavior is still not well understood. It could be the result of an indirect effect linked to the impact of the increase in ammonia concentration of the vapor emitted by the generator and then transmitted to the condenser and the evaporator, by affecting the pressures and the regulation of the system. However, this effect is only observed in the partly flooded generator configuration. The COP decreases consistently from 0.436 to 0.317 with the solution cooling.

The significant decrease in COP (40% for the unflooded configuration and 30% for the partly flooded configuration) observed with the cooling of the solution indicates that it is preferable not to cool the solution at the inlet of the combined generator for this machine, which produces positive cold for air-conditioning. Two other sets of experiments were conducted, varying the heating temperature and the solution mass flowrate.

#### 4.4 Experimental performance of the absorption chiller

The nominal operating parameters of the absorption chiller are detailed in Table 5.3, for the external sources temperatures and mass flowrates, and for the rich solution mass flowrate. For the unflooded and partly flooded configurations, Figure 5.10a and Figure 5.10b, present the evolutions of the thermal COP and cooling capacity measurements with the HTF temperature and with the rich solution mass flowrate at the inlet of the combined generator.

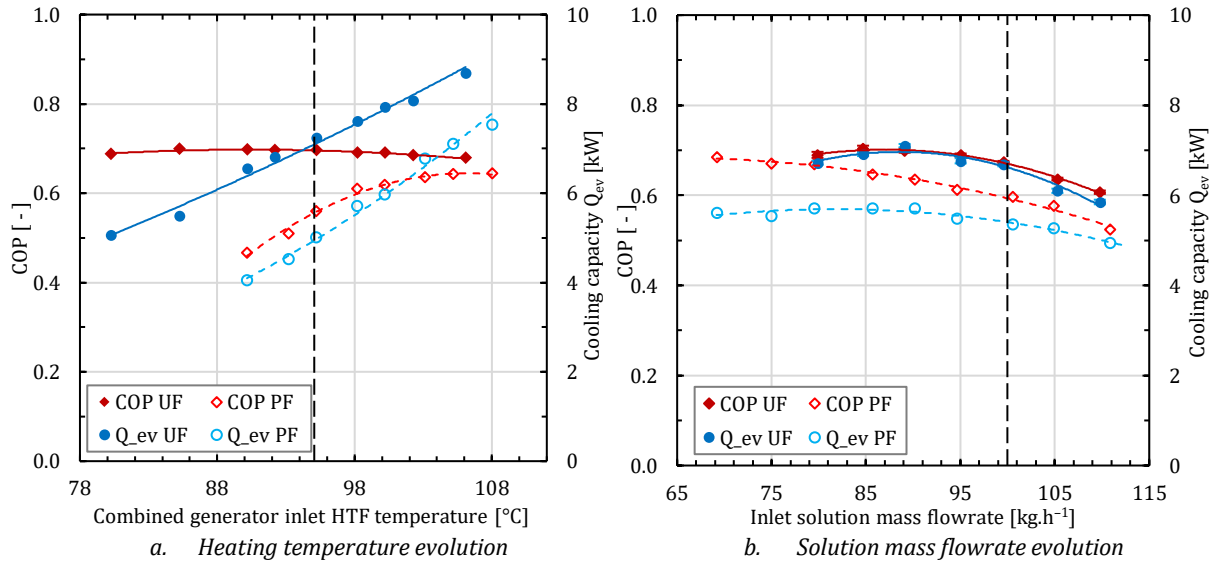


**Figure 5.10.** COP and cooling capacity measured as a function of the inlet HTF temperature and of the solution mass flowrate at the inlet of the combined generator, for unflooded and partly flooded configurations.

For the unflooded configuration, the COP reaches a maximum of approximately 0.7 in the range of HTF inlet temperature of [85–95°C]. At lower or higher inlet HTF temperature, the COP decreases slightly. For the partly flooded configuration, the COP increases from 0.465 at  $T_{hot} = 90^\circ\text{C}$  until reaching a maximum of 0.643 at  $T_{hot} = 105^\circ\text{C}$ . The cooling capacity increases with the HTF inlet temperature, and is higher when the combined generator is not flooded, reaching 8.7 kW at  $T_{hot} = 106^\circ\text{C}$  while it reaches 7.5 kW at  $T_{hot} = 108^\circ\text{C}$  for the partly flooded configuration.

For the unflooded configuration, the COP reaches a maximum of 0.7 when  $\dot{m}_{RS} = [85\text{--}90 \text{ kg.h}^{-1}]$ , and cooling capacity a maximum of 7.1 kW at  $90 \text{ kg.h}^{-1}$ . When the mass flowrate of the solution is higher, both decrease. When  $\dot{m}_{RS} = 75 \text{ kg.h}^{-1}$ , the absorption chiller operation becomes unstable. For the partly flooded configuration, the COP decreases from 0.69 to 0.52 for an increase of the solution mass flowrate from [70–110 kg.h<sup>-1</sup>]. The cooling capacity varies slightly, reaching a maximum of 5.7 kW when  $\dot{m}_{RS} = [80\text{--}90 \text{ kg.h}^{-1}]$ .

For all the experiments performed, the partial flooding of the combined generator degrades the performance of the machine, between 5 and 33% for the COP and between 15 and 38% for cooling capacity. Since the falling-film operation mode shows a better performance than the partly flooded mode, the rest of the study will focus only on the unflooded configuration.

The other operating parameters that mainly affect the combined generator behavior need to be investigated. For that purpose, a design of experiments (DOE) is led to characterize the combined generator performance, for various operating conditions corresponding to external factors such as the temperatures of the external sources, and internal factors such as the mass flowrate of the solution entering the combined generator.

## 5 Design of experiments

### 5.1 Description of the design of experiments

The absorption machine dedicated to air-conditioning aims to meet the desired cooling requirements depending on the cold and rejection temperature levels. To achieve this objective in the most efficient way possible, it is foreseen that the operator can act on two operating parameters: the temperature of the heat sources and the solution flowrate between the absorber and the desorber (the HTF flowrates are fixed by the system).

The ranges of the four operating conditions studied —the heat source temperature at the combined generator inlet ( $T_{hot}$ ), the heat rejection temperature at the absorber and the condenser inlets ( $T_{medium}$ ), the chilling temperature at the evaporator inlet ( $T_{cold}$ ), and the solution mass flowrate ( $\dot{m}_{RS}$ )— are defined according to air-conditioning requirements established in European countries (Table 5.4).

The HTF mass flowrates are kept constant and fixed at 1600 kg.h<sup>-1</sup>, 1100 kg.h<sup>-1</sup>, and 1230 kg.h<sup>-1</sup> for the heating, the chilling, and the heat rejection sources, respectively. The superheat of the refrigerant at the inlet of the expansion valve is fixed at 6°C.

	$T_{hot}$ [°C]	$T_{cold}$ [°C]	$T_{medium}$ [°C]	$\dot{m}_{RS}$ [kg.h <sup>-1</sup> ]
<b>Minimum value (-1)</b>	80	10	22	75
<b>Medium value (0)</b>	95	16	27	110
<b>Maximum value (1)</b>	110	22	32	145

**Table 5.4.** Range of values for the inlet variables of the DOE.

An adapted Doehlert DOE of second order is used to describe the performance of the combined generator implemented in the absorption machine in all possible operating conditions of the latter (Karam 2004).

### 5.2 Doehlert model and polynomial coefficients determination

The DOE is adapted insofar as the hot, cold, and heat rejection temperatures do not constitute directly the control parameters of the combined generator, but the control parameters of the machine. The parameters that directly affect the combined generator are the operating pressure  $P$  (related to the intermediate temperature via the condenser), the superheat of the HTF at the inlet  $\Delta T_{sat,HTF}$  (related to the heating temperature), the solution ammonia concentration at the inlet  $x$  (related to the intermediate and chilling sources temperatures), and the solution mass flowrate  $\dot{m}_{RS}$ . Three parameters are selected to describe the combined generator: the vapor mass flowrate  $\dot{m}_{vap}$  emitted by the exchanger, the ammonia fraction of this vapor  $y_{vap}$ , and the heat rate supplied to the exchanger  $Q_{CG}$ .

The DOE is based on an asymmetric matrix with a number of experiments  $N$  corresponding to equation:

$$N = v_n^2 + v_n + 1 \quad (5.1)$$

Where  $v_n$  is the number of variables.

In the case of four parameters studied, the second-order equation corresponds to that of (Eq. 5.2) given for the vapor mass flowrate emitted. In this equation, the coded variables (defined in a range between -1 and 1, where -1 corresponds to the lowest value and +1 corresponds to the highest value of the parameter) are conveniently used to objectively evaluate the impact of the different parameters in the experimental domain regardless of their units and dimensions. In this regard, the center of the experimental domain is defined as the point at which all the parameters are in the middle of their range (coded variable of zero, see Table 5.4).

A set of 15 coefficients are obtained for each parameter evaluated. When analyzing four variables, a minimum of 21 tests are required to obtain the polynomial of (Eq. 5.2). The least-squares method is used to determine the coefficients of the equation.

$$\begin{aligned} \dot{m}_{vap}(T_{hot}, T_{cold}, T_{medium}, \dot{m}_{RS}) = & a_0 + a_1 \cdot \dot{m}_{RS} + a_2 \cdot \Delta T_{sat,HTF} + a_3 \cdot P + a_4 \cdot x + \\ & a_{12} \cdot \dot{m}_{RS} \cdot \Delta T_{sat,HTF} + a_{13} \cdot \dot{m}_{RS} \cdot P + a_{14} \cdot \dot{m}_{RS} \cdot x + a_{23} \cdot \Delta T_{sat,HTF} \cdot P + a_{24} \cdot \Delta T_{sat,HTF} \cdot x + \\ & a_{34} \cdot P \cdot x + a_{11} \cdot \dot{m}_{RS}^2 + a_{22} \cdot \Delta T_{sat,HTF}^2 + a_{33} \cdot P^2 + a_{44} \cdot x^2 \end{aligned} \quad (5.2)$$

The matrix of experiments associated to the Doehlert network method with four factors, and the corresponding temperatures and mass flowrates, calculated thanks to the measurements are presented in Appendix 6.3.

### 5.3 Model prediction

The three investigated combined generator performances are interpolated thanks to the polynomial coefficients of the DOE, for the 21 tests led. Figure 5.11 presents the heat supplied calculated thanks to the DOE interpolation model as a function of the measurements. The more the scatter plot is closed to the first bisecting line of the plan, and the determination coefficient  $R^2$  is close to 1, the higher the model quality description.

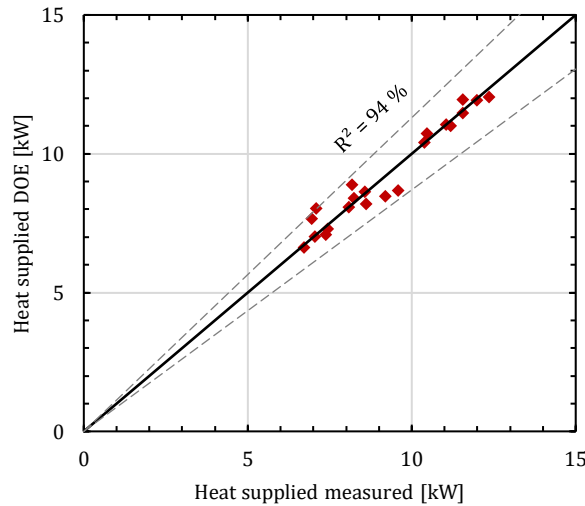


Figure 5.11. Heat supplied calculated through the DOE as a function of the measurements.

As detailed in Table 5.5, the confidence level for each parameter evaluated is higher than 91%.

Parameter evaluated	Confidence range %
$Q_{CG}$	94.4
$\dot{m}_{vap}$	91.0
$y_{vap}$	91.3

Table 5.5. Confidence ranges of each parameter evaluated.

The ammonia vapor mass flowrate and the ammonia vapor concentration present a good concordance with the model, and the injected heat is the most precise.

The descriptive quality of the model is sufficient for the three parameters evaluated. In order to confirm that statement, an ANalysis Of VAriance is led for each parameter, the test description and the results are provided in Appendix 6.3. In a statistical approach, the model is firstly validated for the ranges of heating, heat rejection, and chilling temperatures and for the rich solution mass flowrate detailed in Table 5.4. Then, in order to validate the model through other experiments, interpolations are applied to new sets of measurements.

## 5.4 Validation of the design of experiments

The ability of the second-order equations to describe the evolution in the performance of the combined generator is analyzed by comparing the performance predicted by the correlations with a set of approximately 30 complementary experimental results. For these tests, the temperatures and mass flowrates studied are within the ranges defined in Table 5.4. The parameters are fixed to the nominal condition except the studied parameter that varies. Figure 5.12 depicts the comparison between the predicted values and the experimental values of the heat rate supplied to the combined generator.

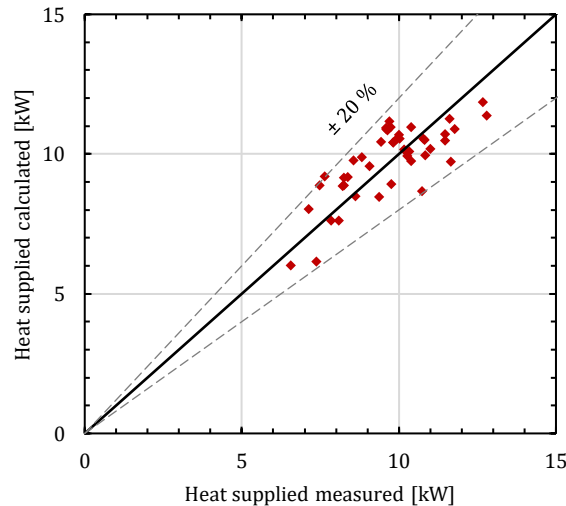


**Figure 5.12.** Comparison of the heat supplied, interpolated and measured.

The maximum deviations between the values predicted by the second-order equation and by the measurements are approximately 20% for the heat supplied, and approximately 25% for vapor mass flowrate values. The maximal deviation for the ammonia vapor concentration is  $\sim 0.005$ .

These results show the ability but also the limitations of these second-order equation formulations to describe the performance of heat and mass exchangers encountered in absorption machines. In the part that follows, the results obtained with this approach will be compared with a different approach that can be used for such components.

## 6 Parametric analysis of the combined generator

### 6.1 Adapted NTU method

To compare the generator performances, it is necessary to express them in a non-dimensional way, by comparing them with the asymptotic values that could be obtained in the presence of ideal exchangers. Therefore, the mass flowrate  $\dot{m}_{vap}$  and ammonia concentration  $y_{vap}$  of the vapor emitted by the exchanger, as well as the heat rate supplied to the combined generator  $Q_{CG}$ , will be expressed in the following in a non-dimensional form on the basis of mass, thermal, and species effectiveness developed in *Chapter II*. The mass effectiveness is defined in (Eq. 3.14), the thermal effectiveness is defined in (Eq. 4.14), and the species effectiveness is defined in (Eq. 4.15). The calculation of the different effectiveness as a function of the pressure and of the fluid characteristics at the inlet of the combined generator is detailed in *Chapter II, Sect.3.2*.

The measurement uncertainty in the ammonia mass fraction of approximately 1% is unfortunately too high to reliably determine the species effectiveness and to correlate its evolution with the operating conditions. Also, the evolution of this last criterion could not be studied within the framework of this study. Thus, only the mass and thermal effectiveness will be analyzed.

To complete the non-dimensional approach to describe the performance of the combined generator, the evolutions of the mass and thermal effectiveness are correlated with the operating conditions through the three non-dimensional parameters inspired from the NTU methods for heat exchangers:

- (1) the adapted NTU based on the flow capacity of the HTF and defined by (Eq. 4.25);
- (2) The equilibrium factor defined by (Eq. 3.15) and equivalent to the ratio of the heat capacity rate;
- (3) the Jakob number defined by (Eq. 4.26). This number is introduced to take into account the mass transfer between the solution and the vapor in the adiabatic part of the combined generator.

The power law (Eq. 4.27) is used to describe the evolution of the varying combined generator effectiveness as a function of the operating conditions. The constants and exponents were calculated using the root mean square method on the basis of numerical simulations. Table 5.6 shows the values of the constants calculated in the complementary experiments made. The solution at the inlet of the combined generator is then always superheated.

<i>Effectiveness</i>	<i>A</i>	<i>a</i>	<i>b</i>	<i>c</i>
$\epsilon_{mass}$	0.1760	1.2694	-0.3157	1.0577
$\epsilon_{th}$	0.1673	1.0319	-0.1683	0.8098

**Table 5.6.** Constant values for the mass and thermal effectiveness correlations.

The ability of the adapted NTU method to describe the evolution of the performance of the combined generator is analyzed by comparing the mass and thermal effectiveness predicted by the correlations with the complementary experimental results obtained (Figure 5.13).

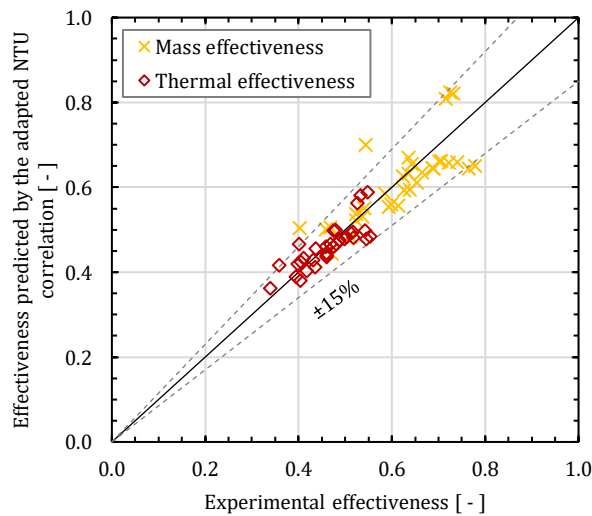


**Figure 5.13.** Comparison of the effectiveness predicted by the adapted NTU method correlations and the modeling.

Since the HTF flowrate was fixed at  $\dot{m}_{hot} = 1600\text{kg}\cdot\text{h}^{-1}$ , the modified *NTU* of the combined generator varies only slightly. Thus, the *NTU* term in (Eq. 4.27) is not meaningful and could be included in the constant  $A_i$ . The equilibrium factor  $R_{eq}$  depends essentially on the solution mass flowrate, but also varies according to the deviation from equilibrium of the solution at the inlet of the combined generator. The Jakob number  $Ja$  also depends on the superheating of the solution at the combined generator inlet. It varies according to the operating parameters of the machine, such as the pressure and the concentration of the poor solution.

## 6.2 Performance of the combined generator

Figure 5.14 presents the evolution of the mass and thermal effectiveness of the combined generator as a function of the equilibrium factor when varying the solution flowrate and of the Jakob number when varying the temperature at the evaporator level. The experimental effectiveness is compared with the values predicted by the second-order polynomial approach of the DOE and by the adapted NTU approach. The measurement uncertainties calculated for the mass and thermal effectiveness are between 6 and 8%.

For all the points considered, the mass effectiveness is higher than the thermal effectiveness. This effect is due to the slight superheated state of the solution at the inlet of the combined generator (between 1 and 6°C), which leads to a small flash desorption at the inlet of the combined generator, and thus to vapor generation without any heat supply from the HTF.

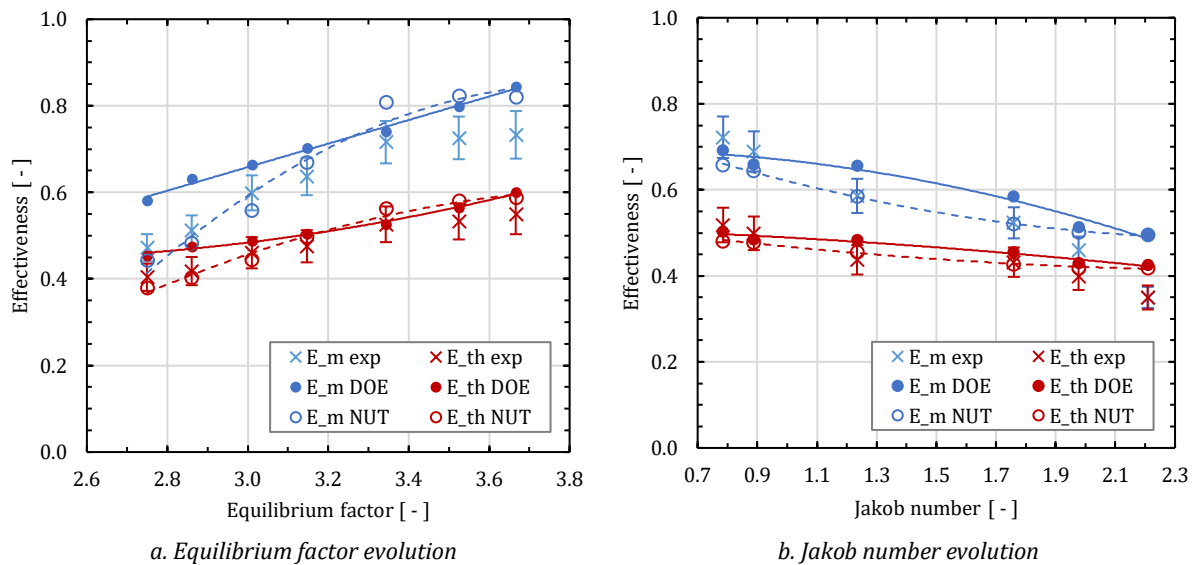


**Figure 5.14.** Comparison of mass and thermal effectiveness determined experimentally, with the values estimated using the second-order polynomial resulting from the adapted Doehlert design of experiment (DOE), and from the adapted Nusselt approach (NTU), in regard to the impact of the equilibrium factor and of the Jakob number.

The increase in the solution mass flowrate induces the thickening of the solution falling-film on the plate of the exchanger. It results in both a decrease in the heat transferred between the HTF and the solution (increase in the thermal resistance of the falling film) and an increase in the amount of vapor that can be generated by the exchanger (the solution is the limiting fluid). The decrease in the effectiveness with the increase in the solution mass flowrate can be seen in Figure 5.14a; with the HTF mass flowrate being fixed, the increase in the solution mass flowrate leads to a decrease in the equilibrium factor.

The increase in the solution superheat and therefore in the Jakob number at the inlet of the combined generator should lead to an increase in the mass effectiveness due to the flash evaporation process occurring in the distribution part of the exchanger. It should not affect the thermal effectiveness, since the solution that leaves the adiabatic part of the combined generator is close to the equilibrium, and the solution mass flowrate is almost unchanged. These trends are not observed experimentally when the evaporator temperature is varied from 22 to 12°C: The increase in the Jakob number from 0.8 to 2.2 at the inlet of the combined generator induced by the increase in the superheat of the solution from 2 to 6°C leads to a decrease in thermal and mass efficiency (Figure 5.14b). These tendencies may be due to the reduction in ammonia concentration from 0.6 to 0.55 during these changes in operating conditions, and it potentially affects the physical properties and thus the heat and mass transfer.

The best performance of the combined generator is obtained at a low solution flowrate when the resistance to transfer through the film is minimal, and when the solution is concentrated in ammonia.

The effects of the operating conditions (temperature of the HTF fluids and of the solution mass flowrate) on the combined generator performance are fairly well described by the adapted DOE correlation and the

adapted NTU method correlation. The NTU power law correlation appears to be more efficient than the adapted DOE correlation: The predicted values overlap with the confidence level of the experimental measurements except for low flowrates (high  $R_{eq}$  value) or low chilling temperatures (high Jakob number) that correspond to extreme operating conditions of the machine.

## 7 Parametric analysis of the absorption chiller performance

### 7.1 Performance of the machine

In the following, the absorption chiller performance is described through the COP and cooling capacity. The evolution of the machine performance as a function of the operating parameters will not be assessed using second-order equations implemented in the Doehlert experimental plans. These equations are not adapted for absorption machines. Indeed, in the DOE, the properties investigated (corresponding to the machine performances) are coupled to the operating parameters by a power law that is not representative of the thermodynamics. It was therefore decided to implement a far more relevant form from a thermodynamic point of view based on Carnot-COP ( $COP_{Carnot}$ ) and described by (Boudéhenn et al. 2012). In this way, the authors compare the performance of the machine with the Carnot-COP.

The COP and cooling capacity are described with a unique equation function of the Carnot-COP (Eq. 2.5) in which  $\omega_1$ ,  $\omega_2$ ,  $\tau_1$ ,  $\tau_2$ , and  $F_0$  are fitted parameters calculating either the machine's cooling capacity  $\dot{Q}_{ev}$  or its thermal COP.

$$F^{cfm} = \omega_1 \cdot e^{(-COP_{Carnot}/\tau_1)} + \omega_2 \cdot e^{(-COP_{Carnot}/\tau_2)} + F_0 \quad (5.3)$$

Figure 5.15 presents the evolution of the COP and cooling capacity of the machine equipped with the combined generator operating in unflooded mode as a function of the Carnot-COP. Three different values of the solution mass flowrate are compared:  $\dot{m}_{RS} = 75, 100, \text{ and } 110 \text{ kg}\cdot\text{h}^{-1}$ . The performance of the machine equipped with the combined generator is compared with that of the machine equipped with the previous flooded vapor generator and rectification system (FGS) that was operated with a mass flowrate of  $\dot{m}_{RS} = 75 \text{ kg}\cdot\text{h}^{-1}$ .

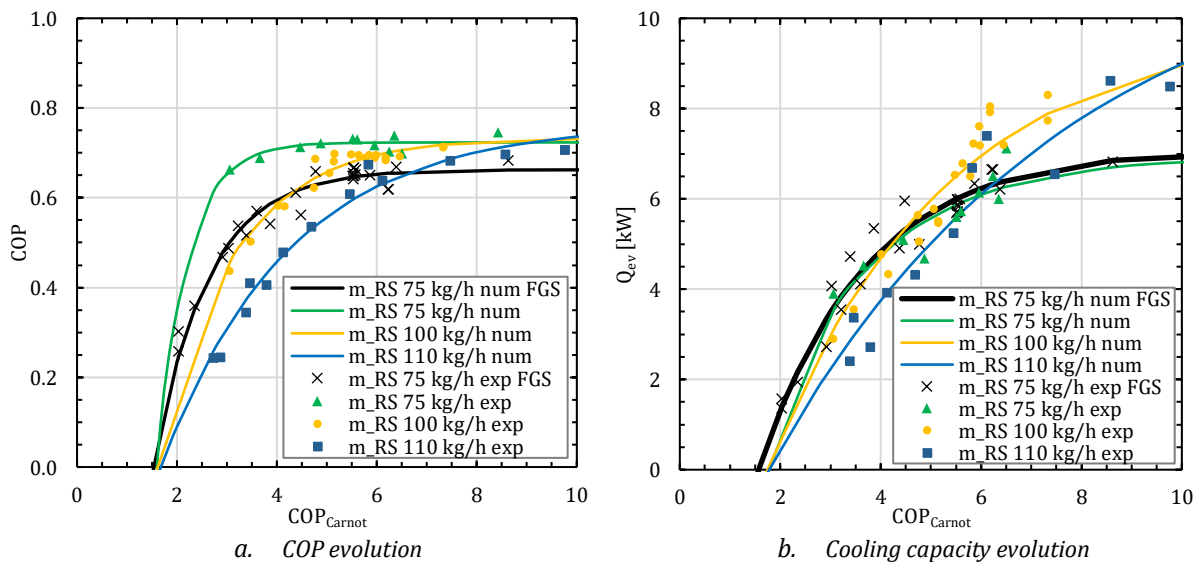


Figure 5.15. COP and cooling capacity as a function of the Carnot-COP, for various solution mass flowrates.

The evolution of the COP is strongly correlated with the Carnot-COP. The power and thus the COP of the machine tend toward zero for Carnot-COP of the order of 1.6; for example, for a chilling temperature of 12°C and a rejection temperature of 30°C, it corresponds to a heating temperature of 64°C. The COP tends toward an asymptotic value close to 0.72 for high values of Carnot-COP. The asymptotic value

is reached even more quickly when the solution flowrate is low. It appears that for each value of Carnot-COP, the maximum COP is reached when  $\dot{m}_{RS} = 75 \text{ kg.h}^{-1}$  for cooling capacity requirements below 6.8 kW. It also constitutes the flowrate limit below which the machine becomes unstable and no longer works properly. As can be seen in Figure 5.15b, cooling capacity is higher at a low solution mass flowrate for low Carnot-COP and at a high flowrate for high Carnot-COP.

The former configuration of the machine (represented in black), integrating the flooded generator-separators-rectifier assembly, reaches an optimal COP of 0.66, which is lower than the new configuration of the machine integrating the combined generator. However, the two absorption chiller configurations produce almost the same amount of cold when the solution mass flowrate is low ( $\dot{m}_{RS} = 75 \text{ kg.h}^{-1}$ ). The gain in performance of the machine equipped with the combined generator is between 10 and 20% under usual operating conditions. This gain is mainly due to the impact of the rectifier in the former absorption chiller configuration.

On the basis of the findings presented in Figure 5.15, it is possible to select the operating conditions that allow us to reach the desired cooling capacity with the best efficiency for the machine, knowing the cooling and heat rejection temperatures. Indeed, the Carnot-COP needed to produce the desired amount of cold can be determined for each solution mass flowrate using the data from Figure 5.15.b; and the COP of the machine running with the different mass flowrates can be compared using Figure 5.15.a.

## 7.2 Application case

The objective of this part is to estimate the performance of the absorption chiller operating for an air-conditioning application in an office. The test case is located in Chambéry, a small town in the French Alps with a district heating system heated by an incineration plant operating all year round. The system operates in the summer during office opening hours, from 9 a.m. to 6 p.m., 5 days a week, when the external ambient temperature  $T_{ext,amb}$  is  $\geq 25^\circ\text{C}$ . The external temperatures are determined using the meteorological measurements given by the database *Meteonorm V7*, for the months of June, July, and August during the period 2000–2009.

For the heat rejection at the absorber and condenser level, an alternative to a cooling tower system is considered: a shallow geothermal system. Indeed, this long-life, low-carbon and renewable energy system allows the electricity consumption to be reduced and is more environmentally friendly (Rosiek and Batlles 2012). Considering the results presented in the study by (Rosiek and Batlles 2012) showing the ability of the geothermal system to achieve efficient cooling of the absorption chiller for similar temperature ranges, the inlet temperature at the absorber level is fixed at  $T_{medium} = 27^\circ\text{C}$ .

The internal ambient temperature range is determined according to the *German DIN 1946 standard* and depends on the external ambient temperature. Air-conditioning operates when  $T_{ext,amb} \geq 25^\circ\text{C}$ . The setpoint temperature is fixed at  $T_{int,amb} = \frac{T_{ext,amb}}{3} + 14.5^\circ\text{C}$ . The blowing temperature in the office is fixed at  $(T_{int,amb} - 8^\circ\text{C})$  and the cold temperature of the HTF leaving the evaporator is fixed at  $T_{cold,out} = T_{int,amb} - 6^\circ\text{C}$ . The office is open for 650 hours, and among the data collected on external temperature, only 294 hours present a value of  $T_{ext,amb} \geq 25^\circ\text{C}$ , corresponding to the operating periods of the absorption chiller. The maximum external temperature measured is  $T_{ext,amb,max} = 34.5^\circ\text{C}$ , which corresponds to the maximum cooling capacity of 6.8 kW reachable by the machine for the lower solution mass flowrate. The minimum cooling capacity is fixed at 4.5 kW, for the minimum external temperature initiating the absorption chiller operation:  $T_{ext,amb,min} = 25^\circ\text{C}$ . Thus, for each external temperature, cooling capacity is required to be between 4.5 and 6.8 kW, corresponding to a chilling temperature at the evaporator inlet between 16.8 and 20°C. The number of cooling capacity occurrences required is presented in Figure 5.16.

Three different absorption chiller configurations are compared: the machine equipped with the former generator-separators-rectifier assembly (the solution mass flowrate is  $\dot{m}_{RS} = 75 \text{ kg.h}^{-1}$ ); and the machine equipped with the combined generator for two cases of solution mass flowrate:  $\dot{m}_{RS} = 75 \text{ kg.h}^{-1}$  and  $\dot{m}_{RS} = 100 \text{ kg.h}^{-1}$ . The energy consumption of the different absorption machines is computed as follows: the Carnot efficiency corresponding to the cooling capacity needed is determined on the basis of the cooling

power expected and the characteristic curves shown in Figure 5.15.b. The COP of the machines is calculated using the characteristic curves in Figure 5.15.a, which provide the value of the heat supplied to the absorption chiller. Two cumulative energetic gains (CEG) are represented in Figure 5.16: the gain achieved when using the combined generator in the absorption chiller instead of the former configuration for  $\dot{m}_{RS} = 75 \text{ kg}\cdot\text{h}^{-1}$  (CG vs. FGS operation); and the gain achieved when the solution mass flowrate is  $\dot{m}_{RS} = 75 \text{ kg}\cdot\text{h}^{-1}$  instead of  $\dot{m}_{RS} = 100 \text{ kg}\cdot\text{h}^{-1}$  when the machine is equipped with the combined generator (75 vs. 100 kg/h CG). The percentage of total energy saved (TES) for the two comparisons is represented in Figure 5.16.

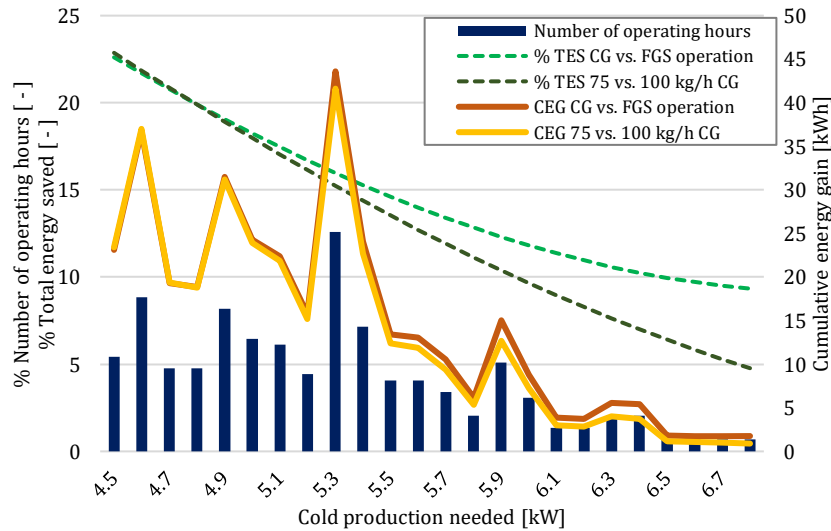


**Figure 5.16.** Number of operating hours required for each cooling capacity event of the absorption chiller, cumulative energetic gains, and % of total energy saved for the two comparisons made.

The highest energy gains (up to 23%) are obtained for a cooling capacity requirement when the machine is equipped with the combined generator and for a flowrate of  $75 \text{ kg}\cdot\text{h}^{-1}$ . The operation of the absorption chiller equipped with the combined generator leads to a cumulative energetic gain of approximately 352 kWh as compared to the operation of the machine equipped with the former assembly when the solution mass flowrate is  $\dot{m}_{RS} = 75 \text{ kg}\cdot\text{h}^{-1}$ . For the machine equipped with the combined generator, the gain when the mass flowrate of the solution is  $\dot{m}_{RS} = 75 \text{ kg}\cdot\text{h}^{-1}$  as compared to  $\dot{m}_{RS} = 100 \text{ kg}\cdot\text{h}^{-1}$  is approximately 332 kWh. The relative energy gains are equal to 16.3% and 15.3%, respectively.

The operation of the absorption chiller equipped with the combined generator with a low solution mass flowrate seems to be favorable for energy-saving; however, it requires a larger range of heating temperature to provide the required cooling capacity with  $T_{hot} = [72-118^\circ\text{C}]$ , as compared to the old configuration of the machine with  $T_{hot} = [72-100^\circ\text{C}]$ . This is explained by the fact that cooling capacity slowly tends toward its limit value for high Carnot-COP (see Figure 5.15b); then, the old machine configuration reaches 6.8 kW at  $\eta_{Carnot} = 8.2$ , corresponding to  $T_{hot} = 100^\circ\text{C}$ , while the new machine configuration reaches 6.8 kW at  $\eta_{Carnot} = 9.8$ , corresponding to  $T_{hot} = 118^\circ\text{C}$ . Moreover,  $\dot{m}_{RS} = 75 \text{ kg}\cdot\text{h}^{-1}$  constitutes the flowrate limit below which the machine becomes unstable.

For a solution mass flowrate fixed at  $\dot{m}_{RS} = 100 \text{ kg}\cdot\text{h}^{-1}$ , the temperature range needed for the heat source is very low  $[74-75^\circ\text{C}]$ . Thus, the machine is almost self-regulated, and a connection to a heat network would be favorable owing to the low heating temperature required.

To optimize the system, a compromise should be found between the energetic gains associated with the solution mass flowrate injected in the combined generator, the stability of the machine operation, and the variations in the heating temperature.

## 8 Conclusion

The experimental work led in this chapter investigated the impact of integrating the innovative falling-film and plate combined generator, associating ammonia vapor generation and purification, on the performance of an  $\text{NH}_3\text{-H}_2\text{O}$  absorption chiller of 5-kW cooling capacity. The combined generator is highly efficient in terms of ammonia vapor production and quality, and needs a lower heat supply. Thus, its integration in the machine made it possible to increase the cooling capacity, improve the COP, and reduce the size of the chiller (by the suppression of the rectifier and separators at the outlet of the combined generator).

The HTF mass flowrate of the combined generator affects the COP and cooling capacity slightly, and reaches its optimum at  $\dot{m}_{hot} \sim 1600 \text{ kg}\cdot\text{h}^{-1}$ . The subcooling of the solution at the inlet of the combined generator enables production of a purer ammonia vapor; however, it affects the COP significantly. Therefore, the solution subcooling is not recommended for air-conditioning applications.

The partial flooding of the combined generator degrades the performance of the machine, by up to 33% for the COP and by 38% for cooling capacity. Thus, the unflooded configuration is favorable.

A design of experiments is carried out over the external source temperatures and solution mass flowrate. The interpolation model built allows us to characterize the combined generator performance. The combined generator operation is highly impacted by the solution flowrate and the concentration of the solution. The adapted NTU model offers a better description of the combined generator performance.

A low solution mass flowrate ( $75 \text{ kg}\cdot\text{h}^{-1}$ ) makes it possible to reduce the energy consumption by approximately 15% but it requires a higher temperature for the heat source. The increase in the solution mass flowrate up to  $100 \text{ kg}\cdot\text{h}^{-1}$  degrades the performance but enables the machine to run with a low heat source ( $75 \text{ }^\circ\text{C}$ ) and leads to the self-regulation of the machine for air-conditioning applications.

## 9 References

- Altamirano A., Stutz B., Le Pierrès N., (2020), "Review of small-capacity single-stage continuous absorption systems operating on binary working fluids for cooling: Compact exchanger technologies", *International Journal of Refrigeration* 114, 118–147
- Boudéhenn F., Demasles H., Wyttenbach J., Jobard X., Chèze D., Papillon P., (2012), "Development of a 5kW cooling capacity ammonia-water absorption chiller for solar cooling applications", *Energy Procedia* 30, 35–43
- Boudéhenn F., Bonnot S., Desmales H., Lazrak A., (2014), "Comparison of different modeling methods for a single effect water-lithium bromide absorption chiller", *EuroSun Conference, Aix-les-Bains, France*
- Franchini G., Notarbartolo E., Padovan L.E., Perdichizzi A., (2015), "Modeling, Design and Construction of a Micro-scale Absorption Chiller", *Energy Procedia* 82, 577–583
- Karam S. (2004), "Application de la méthodologie des plans d'expériences et de l'analyse de données à l'optimisation des processus de dépôt", *Thèse de l'Université de Limoges*
- Mittermaier M., Ziegler F., (2015), "Theoretical evaluation of absorption and desorption processes under typical conditions for chillers and heat transformers", *International Journal of Refrigeration* 59, 91–101
- Rosiek S., Batlles F.J., (2012), "Shallow geothermal energy applied to a solar-assisted air-conditioning system in southern Spain: Two-year experience", *Applied energy* 100, 267–276
- Ziegler, F., Hellmann, H.M., Schweigler, C., (1999), "An approximative method for modeling the operating characteristics of advanced absorption chillers", *29th Int. Congress of Refrigeration, Sydney, Australia*



# Chapter IV

## Improvement of the modeling tools dedicated to the design of generators

---

### Objective:

*The goal of the fourth and last chapter is to provide a comparative analysis of the performance of a flooded plate generator and of the combined generator operating with two modes as a function of the operating conditions of the NH<sub>3</sub>-H<sub>2</sub>O absorption chiller.*

### Based on:

Wirtz M., Stutz B., Phan H.T., Boudéhenn F.

*“Characterization and modeling of a flooded generator for small capacity NH<sub>3</sub>-H<sub>2</sub>O absorption chillers.”  
Heat and Mass Transfer (Submitted 2022)*

Wirtz M., Stutz B., Phan H.T., Boudéhenn F.

*“Combined generator for an NH<sub>3</sub>-H<sub>2</sub>O absorption chiller”  
International Journal of Heat and Mass Transfer (Submitted 2022)*



*In this last chapter, the performance of two plate generators –a flooded generator and a combined falling-film generator– are investigated when they are integrated in a single-stage  $\text{NH}_3\text{-H}_2\text{O}$  absorption cooling system of 5-kW cold capacity.*

*First, the convective boiling mechanisms occurring in the flooded plate generator are modeled through the Chen superposition model adapted to ammonia–water binary mixture. The ability of the model to predict the experimental data is studied. The contributions of each boiling mechanism to the global heat transfer, and the pressure drop along the plates are investigated. Then, the combined generator model described in Chapter I is compared to the experiments presented in Chapter III. The impact of new physical phenomena on the combined generator performance is examined such as the wettability of the plates and the boiling occurrence in the bottom part of the combined generator when it operates in partly flooded mode. Finally, the impact of the operating parameters on the performance of the different generators are evaluated through their mass, thermal, and species effectiveness.*

## 1 Introduction

As detailed in *Sect. III* of the *Part II. State-of-the-art*, numerous researches focus on the nucleate boiling and convective boiling of refrigerant binary mixtures, and thus various heat transfer correlations were developed. However, they were not initially established for ammonia–water mixture, and it is only recently (with the renewal of interest in the absorption chillers), that experimental studies focused on ammonia–water, leading to the adaptation of former correlations and to the development of new ones.

For small capacity absorption chillers, the compactness of the system is essential, and the use of compact components as PHE is an appropriate option (Ziegler 1999). Moreover, plate heat exchangers are classic components that have been available for years and are used as standard in industry. In the absorption chiller domain, few studies focus on simple heat plate generators (Zacarias et al. 2010), and even less on boiling plate generators when ammonia–water is involved.

Thus, the present work investigates the behavior of two different generators integrated in the  $\text{NH}_3\text{-H}_2\text{O}$  absorption chiller of 5-kW cold capacity presented in *Chapter III*. The first model developed focuses on the flooded flat plate generator formerly used in the absorption chiller for the experiments of (Triché 2016). The numerical model simulates the heat and mass transfer occurring in the generator, through the development of the combined nucleate and convective boiling heat transfer processes. The pressure drop is also modeled. The second generator investigated is the falling-film and plate combined generator, whose model was already presented in *Chapter I*, and experimental results in *Chapter III*. The combined generator is examined through two operating modes: either the solution flows in falling film along the plates involving evaporation mechanisms; or the third bottom of the heated plates is flooded and pool-boiling mechanisms take place. The generators' performances calculated by the different models are compared to experimental data for various inlet operating conditions of the absorption chiller in which the generators are integrated. Finally, the impact of the inlet operating parameters of the generators on their effectiveness is investigated.

## 2 Experimental setup: the single-stage ammonia–water absorption chiller

The flooded generator is implemented in the single-effect  $\text{NH}_3\text{-H}_2\text{O}$  absorption chiller of 5-kW cold capacity presented in *Chapter III, Sect 2.1*. The initial architecture of the machine is used, involving the four components that were replaced by the new combined generator: the flooded generator studied, the rectifier, and the two separators dissociating the ammonia vapor from the poor solution and the water condensate. The hydraulic loops supplying the system are the same as already described (see Figure 5.2) including a medium temperature cooling loop [22–33°C], a heating loop [80–120°C], and a chilling loop [5–22°C]. (Triché 2017) gives details about the absorption chiller architecture and operation.

### 2.1 The flooded generator

The flooded generator implemented in the  $\text{NH}_3\text{-H}_2\text{O}$  absorption chiller is a plate heat exchanger composed of 20 plates (0.12 x 0.077 m), 2.48 mm thick. The HTF is injected at the top of the exchanger, and the solution enters at the bottom. Convective boiling develops in the ammonia–water solution in the channels, generating vapor. The liquid–vapor ammonia mixture exits at the top of the generator. The corrugation influence is considered through an intensification factor of 1.5, which is in accordance with the factors proposed by (Zacarias et al. 2010; Fernandes et al. 2008).

### 2.2 Inlet absorption chiller operating parameters–Flooded generator

In the framework of her thesis, (Triché 2016) conducted experiments on the  $\text{NH}_3\text{-H}_2\text{O}$  absorption chiller, including the flooded generator. Table 6.1 presents the nominal conditions and the ranges of operating conditions of the absorption chiller for 36 tests.

		Flooded generator	Absorber and Condenser	Evaporator	Rich solution
<i>Nominal</i>	Temperature inlet [°C]	90 / 105	27	18	-
	Inlet mass flowrate [kg.h <sup>-1</sup> ]	1118	1190	1100	75
<i>Range</i>	Temperature inlet [°C]	90–120	22–32	10–18	-
	Inlet mass flowrate [kg.h <sup>-1</sup> ]	1118	1190	1100	55–135

**Table 6.1.** Nominal conditions and ranges of operating conditions for the tests run with the flooded generator of (Triché 2016).

The temperature of the HTF at the generator inlet is fixed at  $T_{gen} = 90^{\circ}\text{C}$  when the HTF temperature of the rejection source ( $T_{abs}$ ), and the mass flowrate of the solution ( $\dot{m}_{RS}$ ) vary. It is fixed at  $T_{gen} = 105^{\circ}\text{C}$  when the chilling source temperature ( $T_{ev}$ ) at the evaporator inlet varies.

### 3 Numerical model

#### 3.1 Heat transfer model

A numerical model, describing the flow boiling of the ammonia–water solution, is developed. The vapor thermodynamic quality of the ammonia–water mixture that enters the generator is larger than 0. It is calculated assuming the solution at equilibrium with the vapor phase. The following ideal assumptions are made:

1. Ammonia and water are miscible at all concentrations;
2. The sensible heat gain of the liquid film and the vapor core are negligible compared to the latent heat of vaporization;
3. Steady-state conditions are assumed;
4. There is no liquid entrainment in the vapor phase;
5. Axial conduction is neglected;
6. Liquid and vapor are assumed to be at equilibrium at the interface;
7. Pressure gradient is negligible.

The well-known superposition correlation of (Chen 1966) is used to describe the profile of the heat transfer coefficient along the vertical channels. Two contributions are taken into account (Eq. 6.1), i.e., the convective boiling  $h_L$  with the enhancement factor  $F$  and the nucleate boiling  $h_{nb}$  with the suppression factor  $S$ .

$$h = h_{mac} + h_{mic} = F \cdot h_L + S \cdot h_{nb} \quad (6.1)$$

The convective heat transfer coefficient  $h_L$  is calculated using the Dittus-Boelter equation (Eq. 6.2):

$$h_L = 0.023 \cdot \frac{\lambda_L}{D_{hL}} \cdot Re_L^{0.8} \cdot Pr_L^{0.4} \quad (6.2)$$

Where the liquid phase Reynolds number is written:

$$Re_L = (1 - X) \frac{\dot{m}'' \cdot D_{hL}}{\mu_L} \quad (6.3)$$

With  $X$  the vapor weight composition of the two-phase flow and  $\dot{m}''$  the total mass flux of both liquid and vapor flows, corresponding to the total mass flowrate over the cross sectional area of the ducts.

The convective heat transfer enhancement factor  $F$  is written:

$$\text{If } \frac{1}{X_{tt}} > 0.1, \quad F = 2.35 \cdot \left(0.213 + \frac{1}{X_{tt}}\right)^{0.736} \quad (6.4)$$

$$\text{If } \frac{1}{X_{tt}} \leq 0.1, \quad F = 1 \quad (6.5)$$

Where the Lockhart-Martinelli parameters ( $X_{tt}$  or  $X_{ll}$ ) are defined by:

$$\text{If the solution flow is turbulent, } X_{tt} = \left(\frac{1-X}{X}\right)^{0.9} \cdot \left(\frac{\rho_V}{\rho_L}\right)^{0.5} \cdot \left(\frac{\mu_L}{\mu_V}\right)^{0.1} \quad (6.6)$$

$$\text{If the solution flow is laminar, } X_{ll} = \left(\frac{1-X}{X}\right)^{0.5} \cdot \left(\frac{\rho_V}{\rho_L}\right)^{0.5} \cdot \left(\frac{\mu_L}{\mu_V}\right)^{0.5} \quad (6.7)$$

The Chen's correlation was mainly developed for water flow boiling. Since the liquid Prandtl number is different from one fluid to another, (Bennett and Chen 1980) recommended modifying the macroscopic coefficient as:

$$h_{mac} = F \cdot h_L \cdot Pr_L^{0.296} \quad (6.8)$$

In order to consider the effect due to the binary mixture in the convective phenomenon, (Jung et al. 1989) introduced a correction factor taking into account the mass transfer resistance.

$$h_{mac} = F \cdot h_L \cdot C_{me} \cdot Pr_L^{0.296} \quad (6.9)$$

$$\text{With } C_{me} = 1 - 0.35 (\tilde{y} - \tilde{x})^{1.56} \quad (6.10)$$

(Inoue and Monde 2008) defined the heat transfer coefficient of nucleate boiling of a mixture  $h_{nb}$  (Eq. 6.11) through the ideal heat transfer coefficient  $h_{id}$  (Eq. 6.13) and the reduction heat transfer coefficient  $E$ .

$$\frac{h_{nb}}{h_{id}} = \frac{1}{1+E} = \frac{1}{1 + \frac{K_i \cdot k \cdot \Delta T_E}{\Delta T_{id}} + \frac{K_{sh} \cdot (y_{NH_3} - x_{NH_3})}{\Delta T_{id}} \cdot \left(1 - e^{-\left(\frac{B \cdot \dot{Q}''}{D \cdot \rho_L \cdot L_V}\right)}\right)} \cdot (T_{sat,H_2O} - T_{sat,NH_3}) \quad (6.11)$$

With  $\Delta T_E$  the temperature difference between the dew point and the bubble point.

(Inoue and Monde 2008) fixed the constants  $K_i = 0.15$  and  $K_{sh} = 0.25$ , and (Schlünder 1983) defined the constant  $B = 1$  and fixed the mass diffusivity to  $D = 0.0002 \text{ m}^2 \cdot \text{s}^{-1}$ . (Inoue et al. 1998) determined the correlation factor  $k$ , expressing the rise in bubble point temperature versus the corresponding maximum rise during boiling and limited by dew and boiling points temperatures difference (Eq. 6.12).

$$k = 1 - 0.75 \cdot e^{-0.75 \cdot 10^{-2} \cdot \dot{Q}''} \quad (6.12)$$

For the ammonia-water mixture, the ideal heat transfer coefficient  $h_{id}$  is given by:

$$\frac{1}{h_{id}} = \frac{h_{NH_3} \cdot h_{H_2O}}{h_{NH_3} \cdot x_{H_2O} + h_{H_2O} \cdot x_{NH_3}} \quad (6.13)$$

(Eq. 6.14) defines the ideal wall superheat  $\Delta T_{id}$ .

$$\Delta T_{id} = x_{NH_3} \cdot \Delta T_{w,sat,NH_3} + x_{H_2O} \cdot \Delta T_{w,sat,H_2O} \quad (6.14)$$

With  $\Delta T_{w,sat,NH_3}$  the wall superheat for pure ammonia and  $\Delta T_{w,sat,H_2O}$  the wall superheat for pure water.

$$\Delta T_{w,sat,NH_3} = (T_{w,NH_3} - T_{sat,NH_3}) \text{ and } \Delta T_{w,sat,H_2O} = (T_{w,H_2O} - T_{sat,H_2O}) \quad (6.15)$$

(Stephan and Abdelsalam 1980) determined the wall temperatures for ammonia (Eq. 6.16) and water (Eq. 6.17), with the constants  $C_1$  and  $C_4$  depending on the fluid used and as a function of the pressure.

$$T_{w,NH_3} = T_{sat,NH_3} + \frac{\dot{Q}''^{0.255}}{C_4} \quad (6.16)$$

$$T_{w,H_2O} = T_{sat,H_2O} + \frac{\dot{Q}''^{0.327}}{C_1} \quad (6.17)$$

(Bennett et al. 1980) modified the initial suppression factor defined by (Chen 1966).

$$S = \frac{1 - \exp(-F \cdot h_L \cdot X_0 / \lambda_L)}{F \cdot h_L \cdot X_0 / \lambda_L} \quad (6.18)$$

Where,

$$X_0 = 0.041 \cdot \left( \frac{\sigma}{g \cdot (\rho_L - \rho_V)} \right)^{0.5} \quad (6.19)$$

The heat rate supplied by the HTF is given by:

$$\dot{Q}_C = S_{exch} \cdot (T_C - T_{wall}) \cdot \frac{1}{\frac{1}{h_C} + \frac{t_h}{k_p}} \quad (6.20)$$

With  $h_c$  the heat transfer coefficient of the HTF given by:

$$h_C = 0.34365 \cdot Re_C^{0.694} \cdot Pr_C^{1/3} \cdot \frac{\lambda_C}{D h_C} \quad (6.21)$$

The exchanger is discretized into 100 segments. The mass flowrates and the concentrations of the liquid and of the vapor phases at the outlet of the segments are iteratively calculated thanks to the following mass and species equations:

$$\dot{m}_{L,out} = \dot{m}_{L,in} - dM_V \quad (6.22)$$

$$\dot{m}_{V,out} = \dot{m}_{V,in} + dM_V \quad (6.23)$$

$$dM_V = \frac{S_{exch} \cdot h \cdot (T_{wall} - T_{sat})}{L_v} \quad (6.24)$$

$$x_{out} = \frac{x_{in} \cdot \dot{m}_{L,in} - dM_V \cdot y_{sat}}{\dot{m}_{L,in} - dM_V} \quad (6.25)$$

$$y_{out} = \frac{y_{in} \cdot \dot{m}_{V,in} + dM_V \cdot y_{sat}}{\dot{m}_{V,in} + dM_V} \quad (6.26)$$

A stationary algorithm is developed and detailed in Figure 6.1. First, the geometrical parameters and the inlet operating conditions are set, and a flow distribution of the fluids is assumed for each segment. The outlet parameters are then calculated for each segment through an iterative procedure on the wall temperature inside the liquid film. The results are the new inlet conditions for the next iteration, and the algorithm is repeated until convergence of calculations with a residue lower than  $10^{-5}$ .

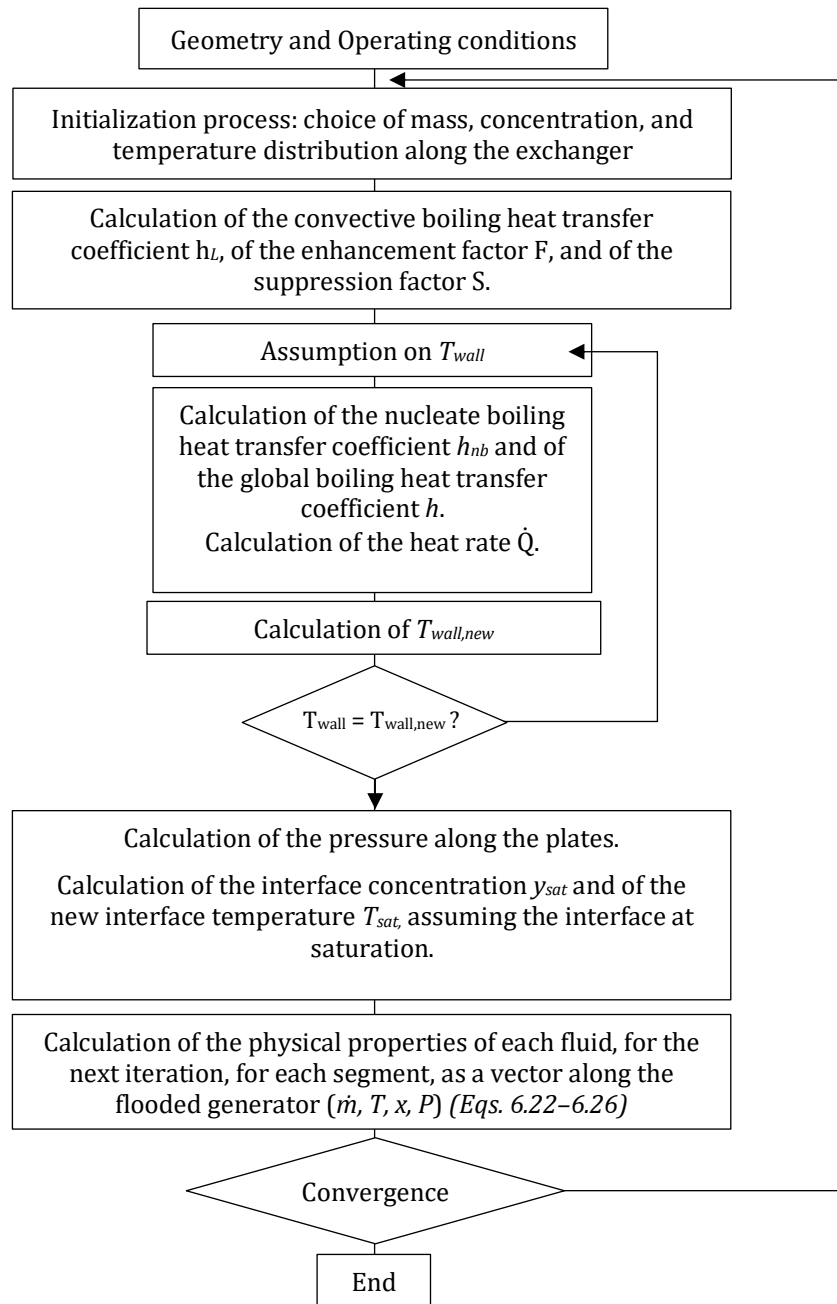
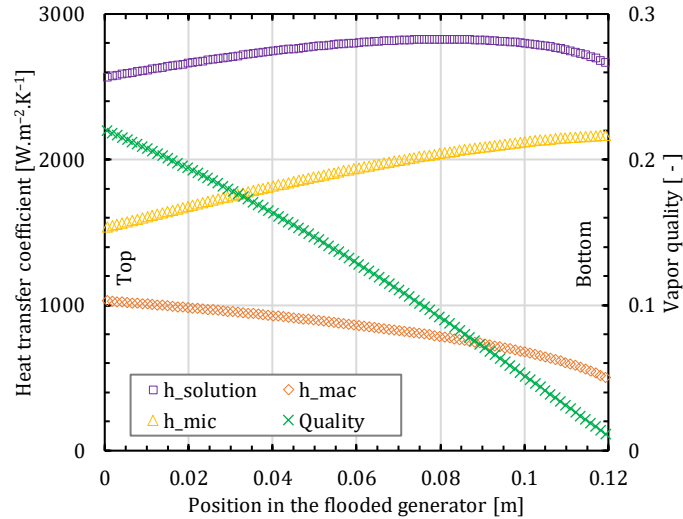


Figure 6.1. Numerical calculation scheme.

The input data of the model are the operating pressure ( $P$ ), the temperature and the mass flowrate of the HTF ( $T_{gen}$ ,  $\dot{m}_{gen}$ ) as well as the temperature, the mass flowrate, and the ammonia concentration of the rich solution ( $x_{RS}$ ) measured at the inlet of the generator.

### 3.2 Application to the nominal case

Figure 6.2 presents the profile of the boiling heat transfer coefficient along the plates, as well as its macroscopic and microscopic contributions, and the vapor quality. The position axis in the generator is oriented downward and its origin corresponds to the top of the exchanger (at the outlet of the solution).



**Figure 6.2.** Macroscopic and microscopic contributions, heat transfer coefficient, and quality vs. position.

The solution and the vapor flow from the bottom to the top, whereas the HTF flows in counter-current mode from the top to the bottom. The vapor quality varies from 1% at the bottom (flash desorption due to the superheat of the solution at the inlet) to 22% at the top. The microscopic contribution  $h_{mic}$ , through the nucleate boiling heat transfer coefficient  $h_{nb}$  clearly prevails on the macroscopic contribution  $h_{mac}$ . As found by (Kaern et al. 2016), this can be explained by the low mass flowrate of the solution in the flooded generator. As expected, the nucleate boiling heat transfer decreases and the convective boiling heat transfer increases with the increase in the vapor quality, which affects the velocity and the liquid film thickness (Jung and Radermacher 1993; Kaern et al. 2016). The solution heat transfer coefficient increases along the exchanger and reaches a maximum for a quality of 0.08 before decreasing in the downstream part of the generator due to diffusion effects and equilibrium temperature decrease.

The temperatures and the mass flowrates of the HTF, the solution and the vapor as well as the ammonia concentrations in the flooded generator are represented in Figure 6.3a, Figure 6.3b, and Figure 6.3c, respectively.

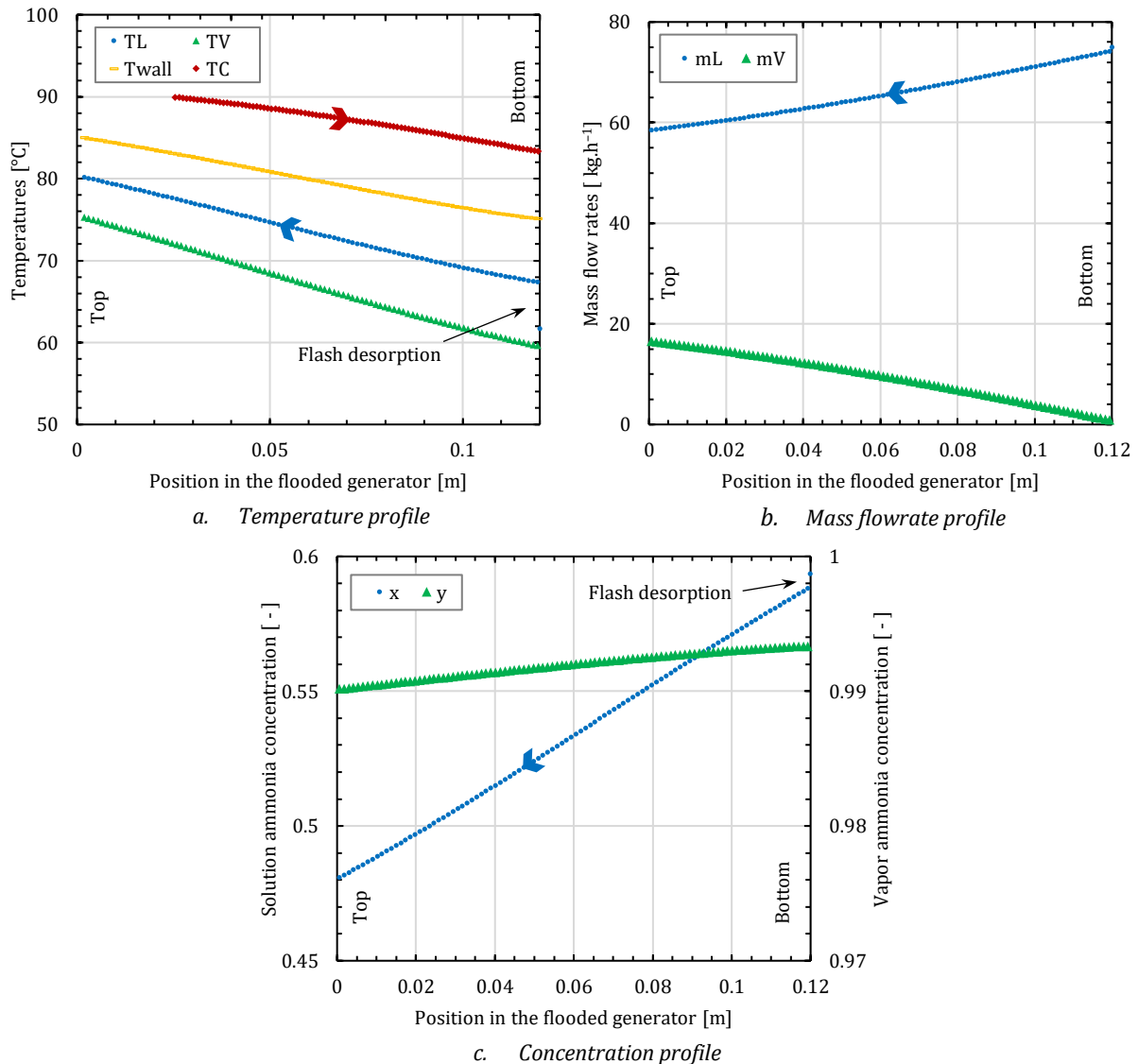


**Figure 6.3.** Temperature, ammonia concentration, and mass flowrate profile in the flooded generator.

The HTF heats the ammonia–water solution through the plates. Its temperature  $T_c$  decreases through its movement from the top to the bottom of the exchanger, leading to the heating of the solution, whose temperature  $T_l$  remains slightly under the wall temperature. The solution enters at the bottom of the flooded generator superheated by +2.2°C. It undergoes a “flash” desorption, leading to sudden drops in temperature and in ammonia concentration to recover the saturation concentration, and to the production of a small amount of vapor with high ammonia concentration (>0.993). The ammonia is more volatile than the water; thus, its concentration in the vapor emitted by the solution is larger than the one in the solution. Therefore, the ammonia concentration  $x$  in the solution decreases along the upward flow. It leads to an increase in the equilibrium temperature at the interface and thus to the increase in the vapor temperature. Due to phase change, the vapor is obviously colder than the solution. Its temperature follows the profile of the solution temperature with a difference of approximately 6°C. The vapor mass flowrate increases regularly from bottom to top. The vapor concentration  $y$  decreases along the flooded generator, due to the increase in the equilibrium temperature.

### 3.3 Pressure drop model

Three main phenomenon affect the pressure in the exchanger: friction losses, acceleration, and gravity. (Eq. 6.27) defines the overall pressure drop:

$$\frac{dP}{dz} = -\frac{2 \cdot f_{L0} \cdot \dot{m} \nu^2}{\rho_L \cdot Dh_L} \cdot \Phi_{L0}^2 - \dot{m} \nu^2 \cdot \frac{d}{dz} \left( \frac{X^2}{\alpha \cdot \rho_V} + \frac{(1-X)^2}{(1-\alpha) \cdot \rho_L} \right) - (\alpha \cdot \rho_V + (1-\alpha) \cdot \rho_L) \cdot g \quad (6.27)$$

The solution flow is laminar, thus the liquid only friction factor  $f_{L0}$  is given by (Eq. 6.28):

$$f_{L0} = \frac{16}{Re_{L0}} \text{ for } Re_{L0} = \frac{Dh_L \cdot \dot{m} \nu^2}{\mu_L} < 2000 \quad (6.28)$$

(Whalley 1987) recommended using the correlation of (Friedel 1979) to define the two-phase multiplier  $\Phi_{L0}$  (Eq. 6.29), if  $\frac{\mu_L}{\mu_V} < 1000$  (Eq. 6.32). Here  $\frac{\mu_L}{\mu_V} \approx 30$ .

$$\Phi_{L0}^2 = Ep + \frac{3.24 \cdot Fp \cdot Hp}{Fr^{0.045} \cdot We^{0.035}} \quad (6.29)$$

With

$$Ep = (1-X)^2 + X^2 \cdot \left( \frac{\rho_L \cdot f_{V0}}{\rho_V \cdot f_{L0}} \right) \quad (6.30)$$

$$Fp = X^{0.78} \cdot (1-X)^{0.24} \quad (6.31)$$

$$Hp = \left( \frac{\rho_L}{\rho_V} \right)^{0.91} \cdot \left( \frac{\mu_V}{\mu_L} \right)^{0.19} \cdot \left( 1 - \frac{\mu_V}{\mu_L} \right)^{0.7} \quad (6.32)$$

With the Weber ( $We$ ) and the Froude ( $Fr$ ) numbers given by (Eqs. 2.43 and 2.44), respectively, and where  $\rho_{mix}$  the density of the homogeneous mixture is defined by (Eq. 6.33).

$$\rho_{mix} = (1-\alpha) \cdot \rho_L + \alpha \cdot \rho_V \quad (6.33)$$

The solution-vapor flow circulating upward is stratified, thus it is composed of a liquid and a vapor phase with different velocities. The void fraction  $\alpha$  is defined by (Eq. 6.34).

$$\alpha = \frac{\Phi_L - 1}{\Phi_L} \quad (6.34)$$

(Chisholm 1967) defined the liquid-side two-phase multiplier  $\Phi_L$  (Eq. 6.35) on the basis of the graphic representations of the two-phase multipliers variations as a function of the Martinelli's parameter  $X_m$  (Eq. 6.36) established by (Lockart and Martinelli 1949). (Chisholm 1967) determined the dimensionless coefficient  $C$  depending on the flow regimes of the liquid and vapor phases. For a laminar-laminar solution-vapor flow,  $C = 5$ .

$$\Phi_L^2 = 1 + \frac{C}{X_m} + \frac{1}{X_m^2} \quad (6.35)$$

$$X_m^2 = \frac{1-X}{X} \cdot \sqrt{\frac{\rho_V \cdot f_L}{\rho_L \cdot f_V}} \quad (6.36)$$

$X$  is the vapor quality along the channel, and  $f_L$  and  $f_V$  are the liquid and vapor friction factors, respectively.

### 3.4 Application to the nominal case

Figure 6.4 represents the pressure gradient with its three terms, and the pressure profile along the flooded generator for the nominal case.

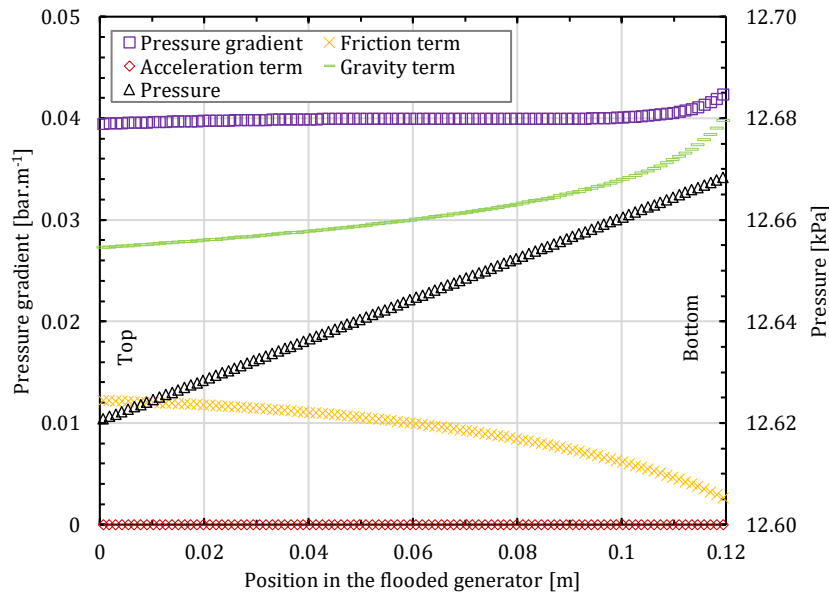


**Figure 6.4.** Pressure gradient and pressure profile along the flooded generator plates for the nominal case.

The local acceleration term (red) has no impact on the pressure drop. The gravity term (green) affects the pressure gradient at the bottom of the generator, where the mixture density is large ( $\alpha = 0.45$ ). It decreases along the exchanger and reaches a minimum at the exit where the void fraction is maximum ( $\alpha = 0.64$ ). The friction term (yellow) is all the more important that the vapor quality is large. The pressure gradient (purple) is slightly higher at the generator bottom ( $\sim 0.043 \text{ bar.m}^{-1}$ ) than at the top exit ( $\sim 0.039 \text{ bar.m}^{-1}$ ).

However, the total head losses does not exceed  $\Delta P = 0.0048 \text{ bar}$ . This represents  $\sim 0.038\%$  of the operating pressure ( $P_{in} = 12.669 \text{ bar}$ ), which is negligible, thereby validating hypothesis 7.

Two pressure sensors measure the high pressure in the absorption chiller: one on the rich solution pipe at the inlet of the flooded generator and the other on the refrigerant solution pipe at the outlet of the condenser. The relative measurement uncertainty is approximately  $\pm 0.9\%$ . For the nominal case, the measure of the pressure difference between the generator inlet and the condenser outlet is  $\Delta P = 0.3 \text{ bar} \pm 0.5 \text{ bar}$ , which represents  $\sim 2.1\%$  of the inlet pressure. It confirms the result predicted by the calculation. The pressure difference measured takes into account the singular and regular head losses related to the pipes and components between the generator and the condenser, which explains the greater head losses compared to those calculated inside the flooded generator.

#### 4 Comparison between measurements and simulations

Figure 6.5 shows a comparison between the numerical results predicted by the model and the measurements of (Triché 2016) presented in Table 6.1, (the heat supplied to the flooded generator; the ammonia vapor mass flowrate generated; the solution temperature differences between the outlet and the inlet; the ammonia concentration differences between the inlet and the outlet).

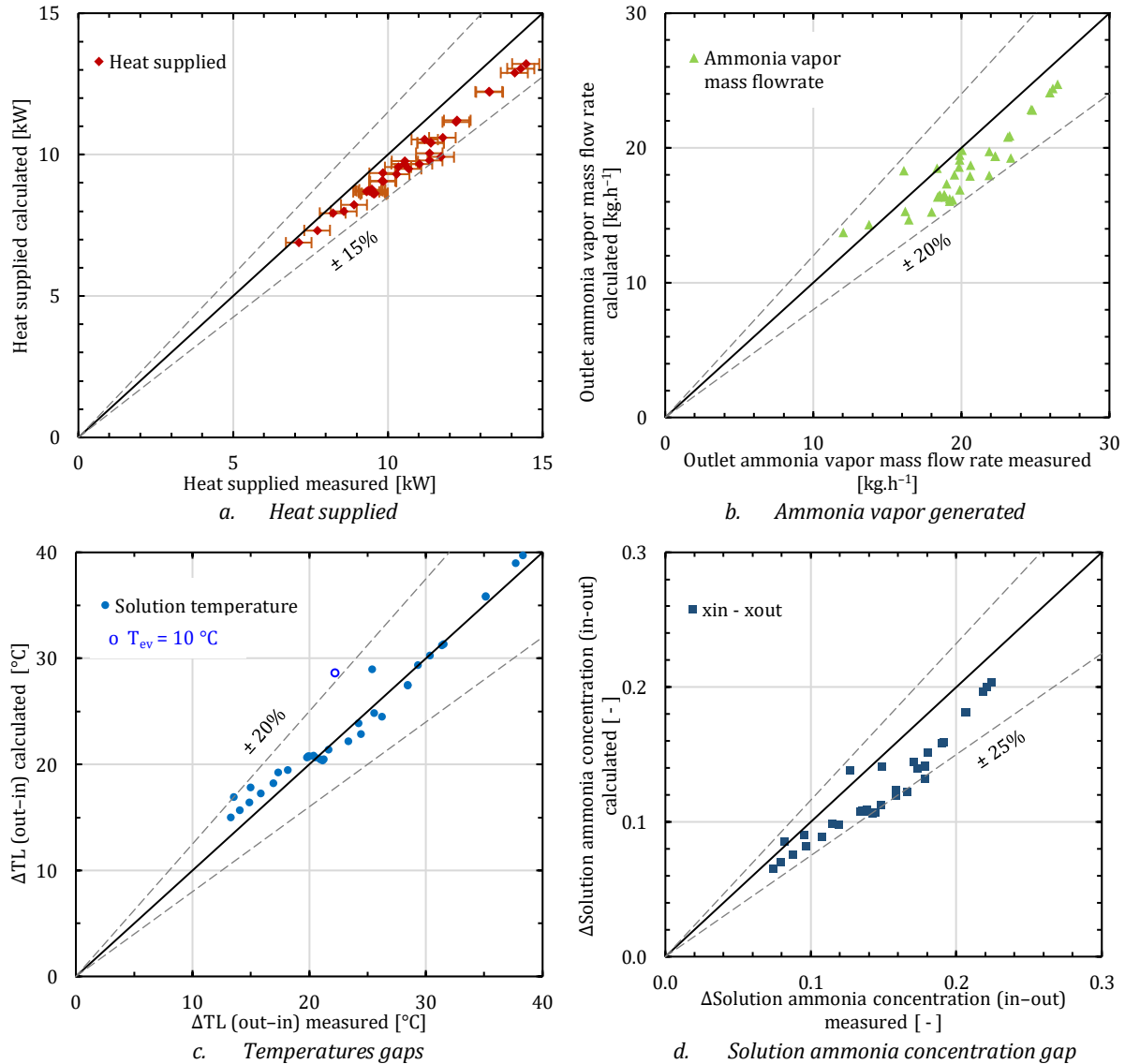


**Figure 6.5.** Numerical results vs. measurements for the flooded generator.

Figure 6.5a shows that the heat supplied to the generator is underestimated by the model. The uncertainties in the measurement of approximately  $\pm 4\%$  do not explain these differences on their own. The underestimation can be due to heat losses as well as to the choice of the enlargement factor used to describe the corrugation influence. However, the difference of a maximum 15% is small enough to be considered acceptable.

The ammonia vapor mass flowrate leaving the generator is measured by a flowmeter, located at the outlet of the condenser. The estimations of the ammonia vapor produced predicted by the simulations are underestimated compared to the experimental results. The maximum deviation is less than 18% and the measurement uncertainties are lower than 1%.

The model successfully predicts the increase in the solution temperature measured from the bottom of the flooded generator to the top. The temperature variations are included between 13 and 39°C for the experiments, and between 15 and 40°C for the simulations. The greatest difference corresponds to low chilling temperature at the evaporator level ( $T_{ev} = 10^\circ\text{C}$ ).

The ammonia concentration differences in the solution between the inlet and the outlet are predicted with a maximum relative error of 25%. (The ammonia concentration of the vapor produced is between 0.97 and 0.99). The ammonia concentration measured is determined through density and temperature measurements, and the use of a correlation describing the evolution of the concentration as a function of the temperature and the density. Measurements are performed at the inlet and outlet of the absorber. Unfortunately, no data are available to know the accuracy of the correlation.

A useful numerical tool is developed, simulating with a good accuracy the behavior of a flooded plate generator for an  $\text{NH}_3\text{-H}_2\text{O}$  absorption machine.

The model of the other generator designed for the  $\text{NH}_3\text{-H}_2\text{O}$  absorption chiller was already introduced in *Chapter I*: the combined generator falling-film model. The model developed in *Sect 3.1* of this chapter is implemented in the bottom part of the heated plates of the falling-film model, in order to investigate the impact of the boiling when the generator is partly flooded. The impact of the wettability of the plates in the falling-film section is also studied.

## 5 Unflooded combined generator model

### 5.1 Falling-film model and combined generator integration in the absorption chiller

The one-dimensional numerical model developed in *Chapter I* is used to predict the behavior of the combined generator implemented in the absorption chiller. It describes the coupled heat and mass transfer in a falling-film and plates heat exchanger, through literature correlations; mass, species, and energy balances; and equilibrium equations at the interface between the solution falling film and the ammonia vapor generated (*Eqs. 3.1 to 3.12*). The model is developed using SciLab 6.0.2, and Figure 3.3 shows the numerical calculation scheme. *Chapter III* provides the detailed description of the combined generator (*Sect. 2.2* with Figures 5.4 to 5.6) and of the absorption chiller in which it is integrated (*Sect 2.1* with Figures 5.1 and 5.2). The instrumenting of the absorption chiller is detailed in *Chapter III, Sect 2.3*.

### 5.2 Inlet absorption chiller operating parameters–Unflooded combined generator

The performance of the combined generator integrated in the  $\text{NH}_3\text{-H}_2\text{O}$  absorption chiller was characterized. Table 6.2 presents the nominal conditions and the ranges of operating conditions of the absorption chiller equipped with the combined generator operating in unflooded mode.

		Combined generator	Absorber / Condenser	Evaporator	Rich solution
<i>Nominal</i>	Temperature inlet [°C]	95	27	18	-
	Inlet mass flowrate [kg.h <sup>-1</sup> ]	1600	1190	1100	100
<i>Range</i>	Temperature inlet [°C]	80–106	22–31	10–22	-
	Inlet mass flowrate [kg.h <sup>-1</sup> ]	600–1800	1190	1100	75–125

**Table 6.2.** Nominal operating conditions and operating ranges of the  $\text{NH}_3\text{-H}_2\text{O}$  absorption machine used to characterize the combined generator operating in unflooded mode.

The temperatures and the mass flowrates of the HTF and of the rich solution  $T_{gen}$ ,  $T_{RS}$ ,  $\dot{m}_{gen}$ ,  $\dot{m}_{RS}$ , as well as the solution ammonia concentration  $x_{RS}$ , and the pressure  $P$  measured at the inlet of the combined generator in steady-state operating mode are used as input values for the modeling. A total of 52 experiments were performed to validate the model.

### 5.3 Comparison between measurements and simulations for the unflooded combined generator

Figure 6.6 compares experimental and numerical results (heat supplied to the combined generator in Figure 6.6a, mass flowrate of the ammonia vapor produced in Figure 6.6b, solution temperatures difference between the outlet and the inlet in Figure 6.6c, and ammonia solution concentration difference between the inlet and the outlet in Figure 6.6d).

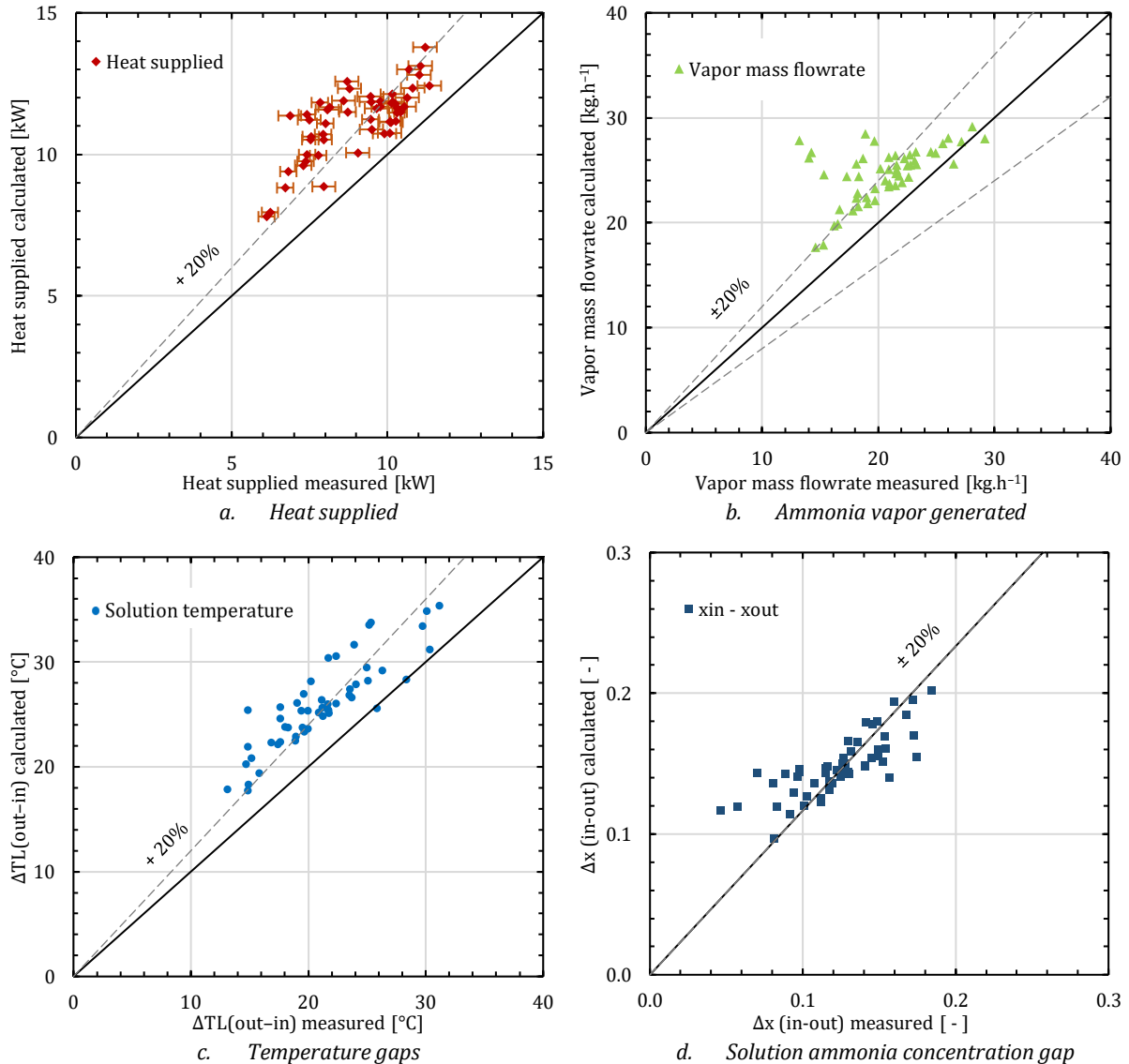


**Figure 6.6.** Comparison between measurements and simulations for the combined generator operating in unflooded mode.

The heat supplied to the combined generator is calculated through the temperatures and the mass flowrate of the HTF. The model overestimates the heat rate transmitted to the generator by 20% on average.

The ammonia vapor mass flowrate is determined experimentally using the mass balance performed between the inlet and the outlet of the solution flowrate. The experimental uncertainties are under 1% and are not presented in the figure. The model overestimates most of the value of the vapor mass flowrate generated by the exchanger by approximately 20%.

The simulations overestimate the solution temperature difference between the inlet and the outlet by approximately 20%. The temperature measurement uncertainties ( $< 0.1^{\circ}\text{C}$ ) are too small to be represented. The ammonia concentration in the solution is determined experimentally through density and temperature measurements of the solution entering and exiting the combined generator. The uncertainties are too small

to be represented in the figure. The simulations overestimate the solution ammonia concentration difference by approximately 20%.

The numerical model overestimates all the performances of the combined generator considered here by approximately 20%. This is most likely due to the drying effects of the walls that are not taken into account in the model and that affect the heat and mass transfer. In the next paragraphs, the impact of the wettability is investigated and discussed.

#### 5.4 Introduction of wettability in the model

Figure 6.7 presents two wetting configurations within the square grooves: an ideal completely wetted configuration and a partly wetted configuration, where the dry patches develop along the most highly superheated surfaces.

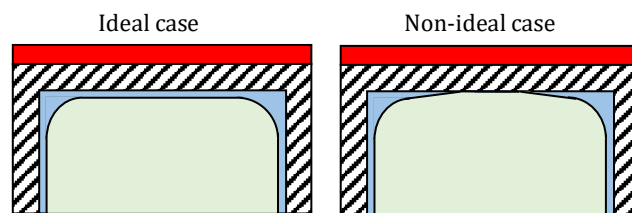


Figure 6.7. Schemes of completely wetted and partly wetted surfaces of the grooved plates.

The dry patches can be estimated thanks to the (Hartley and Murgartroyd 1964) correlation on the minimum linear wetting rate  $m'_{wett,crit}$  (Eq. 2.54).

In order to consider a sufficient linear wetting rate to avoid the appearance of dry patches, (Norman 1960) defined the contact angle between the liquid and the wall at  $\theta = 10^\circ$ .

To our knowledge, no data are available in the literature concerning the contact angle of ammonia–water solution flowing along heated vertical stainless-steel plates. Since ammonia–water is known to be a highly wetting fluid, the contact angle is assumed to be much lower than  $\theta \ll 90^\circ$ . Various simulations were performed by varying the contact angle between the solution and the wall. The contact angle is assumed to be fixed, and not dependent on the temperature and concentration. The local wetted area in the calculation depends on the local solution properties and on the local solution mass flowrate. A good agreement between the experimental results and the model results is obtained for a contact angle of  $\theta = 15^\circ$ .

The average percentage of the wetted area of the plates for the tests is presented in Figure 6.8.

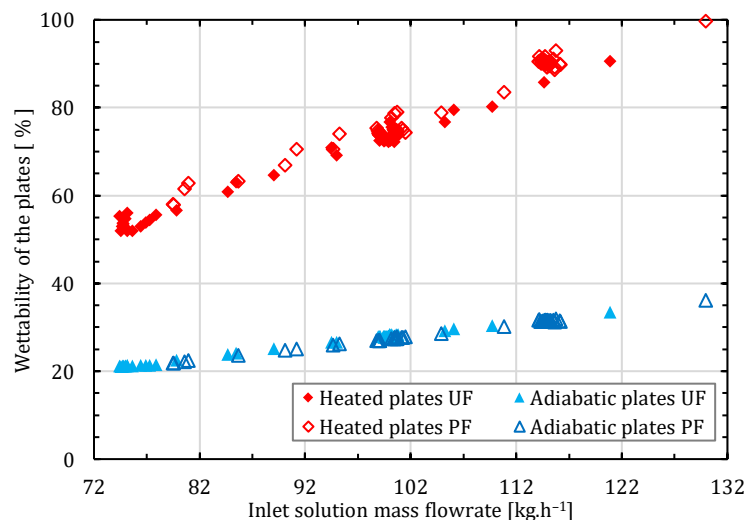


Figure 6.8. Percentage of the wetted area for the adiabatic and heated plates of the combined generator.

The minimum linear wetting rate mainly depends on the contact angle that is kept constant in the present study. The wetted area estimation corresponds to the ratio of the minimum linear wetting rate divided by the linear wetting rate when the plate is completely wetted. Thus, it varies linearly with the solution mass flowrate. These results could be significantly improved by knowing the impact of the contact angle evolution as a function of the operating conditions. The solution is distributed on both sides of the 28 adiabatic plates and on one side of the 14 solution heated plates. Thus, it explains the wetting difference between the adiabatic and heated plates.

### 5.5 New comparison between measurements and simulations

The same 52 tests are simulated for the inlet operating conditions presented in Table 6.2. Figure 6.9 presents the comparison between the experiments and the modeling taking into account the contact angle.

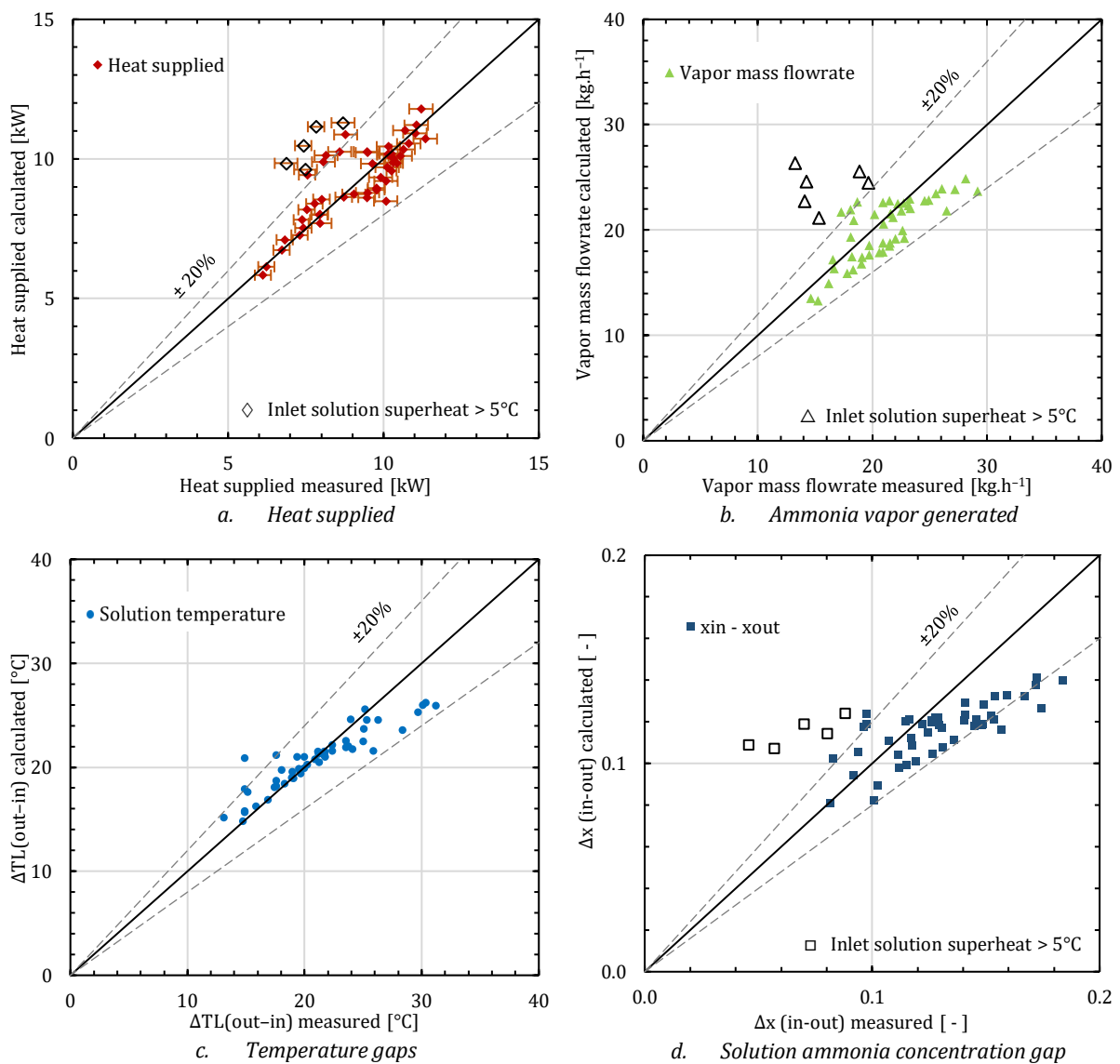


Figure 6.9. Numerical results vs. measurements for the unflooded combined generator, with reduced wettability.

The relative accuracy of the model prediction of the output of the combined generator with a confidence level of 90% is given in Table 6.3.

	Unflooded configuration	Partly flooded configuration
<i>Heat supplied</i>	24 %	17 %
$\dot{m}_{V,out}$	24 %	44 %
$T_{Lout}$	16 %	36 %
$x_{out}$	26 %	28 %

**Table 6.3.** Relative accuracy of the model in predicting the output of the combined generator with a confidence level of 90%.

The model results agree well with the experimental results, with deviations of less than 20%, except for a number of tests where the solution entering the combined generator has a superheat of more than +5°C. It is likely that for these conditions, the important flash desorption at the inlet of the distributor is accompanied by a malfunction of the latter.

The reduction of the contact surface of the falling film with the heated plates leads to a reduction of the heat transferred from the HTF to the solution, and thus to changes in all of the physical properties of the falling film. The introduction of the wettability improves significantly the predictability of the model.

However, in practice, the contact angle should vary along the plates, depending on the film properties (temperature and mass flowrate), and thus would be different for each point along the combined generator, and especially between the adiabatic and in the heated part. Taking into consideration the contact angle variations for the modeling could further improve the model predictability.

In the following section, the second operating mode of the combined generator is investigated. Considering the enhancement of the model predictability when the plate's wettability is taken into account, the next part involves the model with contact angle for the falling-film sections.

## 6 Partly flooded combined generator model

In this second operating mode of the combined generator, the lowest third part of the heated plates is flooded, leading to the development of the pool-boiling process

### 6.1 Boiling heat transfer model

The nucleate boiling heat transfer coefficient of a mixture  $h_{nb}$  (Eq. 6.11) defined by (Inoue and Monde 2008) through the reduction heat transfer coefficient  $E$  and the ideal heat transfer coefficient  $h_{id}$  (Eq. 6.13) is implemented in the falling-film model to characterize the heat and mass transfer occurring in the flooded part of the combined generator. The lowest third part of the exchanger is discretized into 13 segments. Along the falling film, the solution and the vapor are assumed to be at equilibrium at the liquid-vapor interface. The temperature of the interface is estimated thanks to the bubble point temperature corresponding to the operating pressure and concentration of the solution. The temperature gradient within the bubbles is neglected. In the flooded part, the solution temperature is estimated as the average between the wall temperature and the interface temperature. The mass flowrate of the vapor generated is calculated thanks to (Eq. 6.24), assuming a negligible influence of the sensible heat. The ammonia concentration of the vapor generated at the interface corresponds to the ammonia concentration bubble point. The mass flowrates and the concentrations in the liquid and vapor phases at the outlet of the segments are iteratively calculated through the mass balances (Eqs. 6.22 and 6.25) and the species balances (Eqs. 6.23 and 6.26).

Then, the simulations are compared to the experimental values of the partly flooded combined generator operating in the absorption chiller.

## 6.2 Inlet absorption chiller operating parameters–Partly flooded combined generator

Table 6.4 presents the nominal conditions and the ranges of operating conditions of the absorption chiller equipped with the combined generator operating in partly flooded mode.

		Combined generator	Absorber / Condenser	Evaporator	Rich solution
<b>Nominal</b>	Temperature inlet [°C]	95	27	18	-
	Inlet mass flowrate [kg.h <sup>-1</sup> ]	1600	1190	1100	100
<b>Range</b>	Temperature inlet [°C]	85–110	22–31	13–22	-
	Inlet mass flowrate [kg.h <sup>-1</sup> ]	600–1800	1190	1100	80–130

**Table 6.4.** Nominal operating conditions and operating ranges of the NH<sub>3</sub>-H<sub>2</sub>O absorption machine used to characterize the combined generator operating in partly flooded mode.

Overall, 59 experiments were conducted to study the performance of the machine equipped with the combined generator operating in partly flooded mode.

## 6.3 Partly flooded combined generator nominal case

Figure 6.10 shows the profiles of the temperature, the mass flowrate, and the ammonia concentration according to the position inside the partly flooded combined generator for the nominal case.

At the inlet of the combined generator, the solution is superheated by +8°C. It undergoes a “flash desorption” at the exit of the injecting flutes, resulting in a sudden drop of the solution temperature to the equilibrium temperature (see Figure 6.10a). Due to this flash desorption, the solution ammonia concentration drops from  $x_m = 0.59$  to the saturation concentration  $x_i = x = 0.575$ . The small amount of vapor generated is characterized by a high ammonia concentration ( $y > 0.993$ ). Thus, the solution ammonia concentration remains quasi-constant in the adiabatic section before decreasing downstream in the heated falling-film section until 0.487, and in the flooded section until 0.463.

The HTF heats the ammonia–water solution through the heated plates: It leads to a decrease in the HTF temperature  $T_c$  along the plates from the bottom to the top, to the development of a boiling regime in the lowest part of the heated plates, and to an evaporation regime in the falling-film part. The desorption process induces a decrease in the solution ammonia concentration and thus an increase in the interface temperature  $T_i$  along the film from the top to the bottom. The ammonia vapor concentration at the bottom of the exchanger corresponds to the equilibrium concentration (Figure 6.10.c). It mixes along the vapor flow with the ammonia generated at the interface and characterized by a higher ammonia vapor concentration. The temperature of the solution  $T_L$  flowing from the top to the bottom is heated at the wall level and cooled by the phase change process. Thus, it lies between the HTF temperature and the interface temperature.

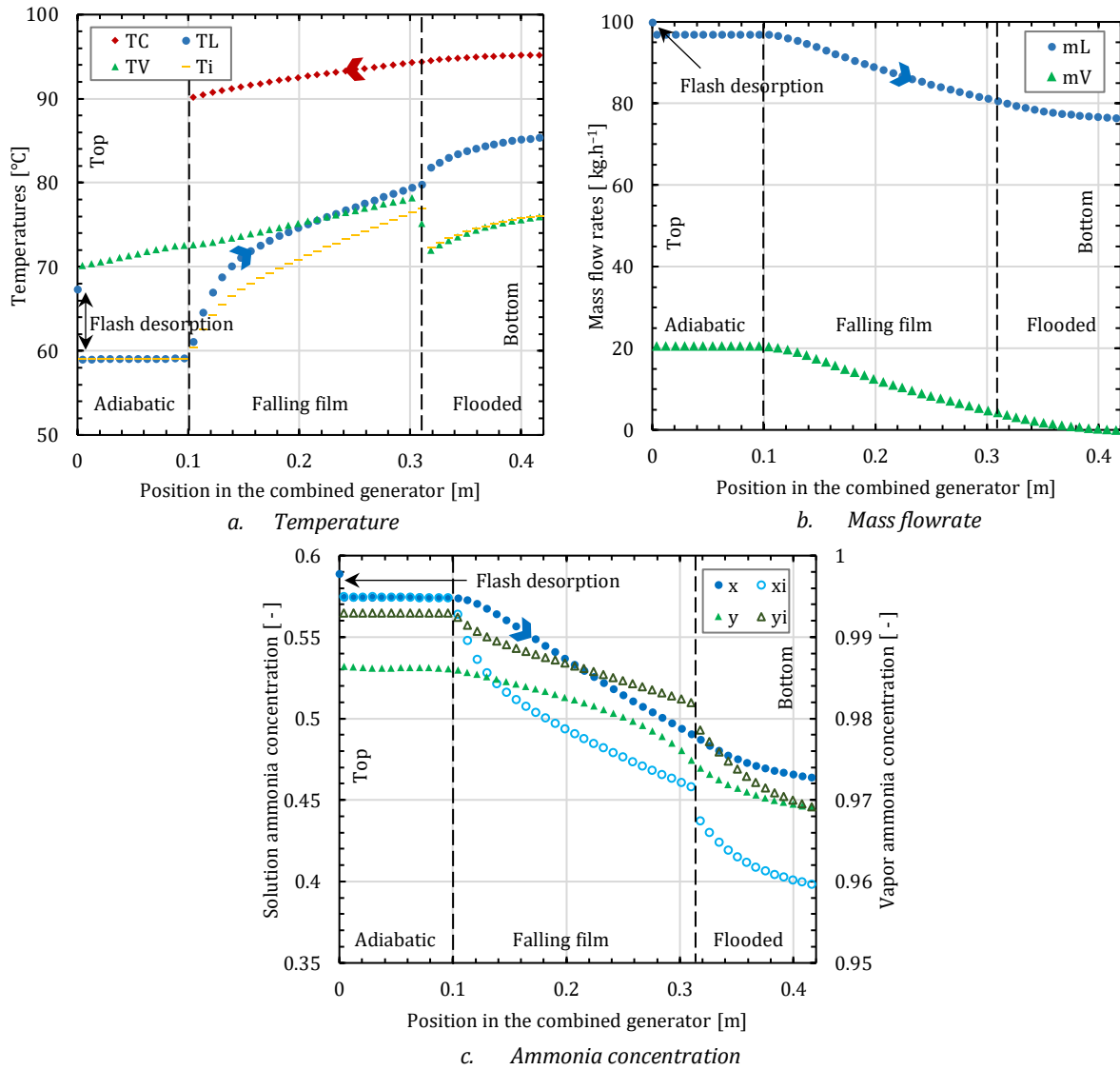


**Figure 6.10.** Temperature, mass flowrate, and ammonia concentration profile along the combined generator in partly flooded operating mode.

The transition from the falling-film part to the boiling part results in temperature drops on both the liquid and vapor sides. The temperature drop in the vapor side is due to the solution mixing when it enters in the flooded part, leading to an increase in the ammonia concentration at the interface and a reduction in the bubble point temperature. This temperature drop is overestimated by the model. Indeed, it integrates the diffusion effects in the heat transfer coefficient at the wall but does not estimate the vapor temperature accurately.

The heat transfer coefficient appears to be higher in the falling-film section as compared to the flooded section. This results in an inflection of the generated vapor flow (Figure 6.10.b).

In contrast to the case of the combined generator operating in unflooded mode, the adiabatic part seems to have almost no effect on the vapor purification. The solution stays in equilibrium condition until the end of the adiabatic part, and does not significantly transfer heat and mass with the vapor.

#### 6.4 Comparison between measurements and simulations for the partly flooded combined generator

The wettability of the plates is similar to the one obtained for the unflooded configuration as can be seen in the Figure 6.8.

Figure 6.11 presents the comparison between the experiments and the modeling, with the reduced wettability of the plates.

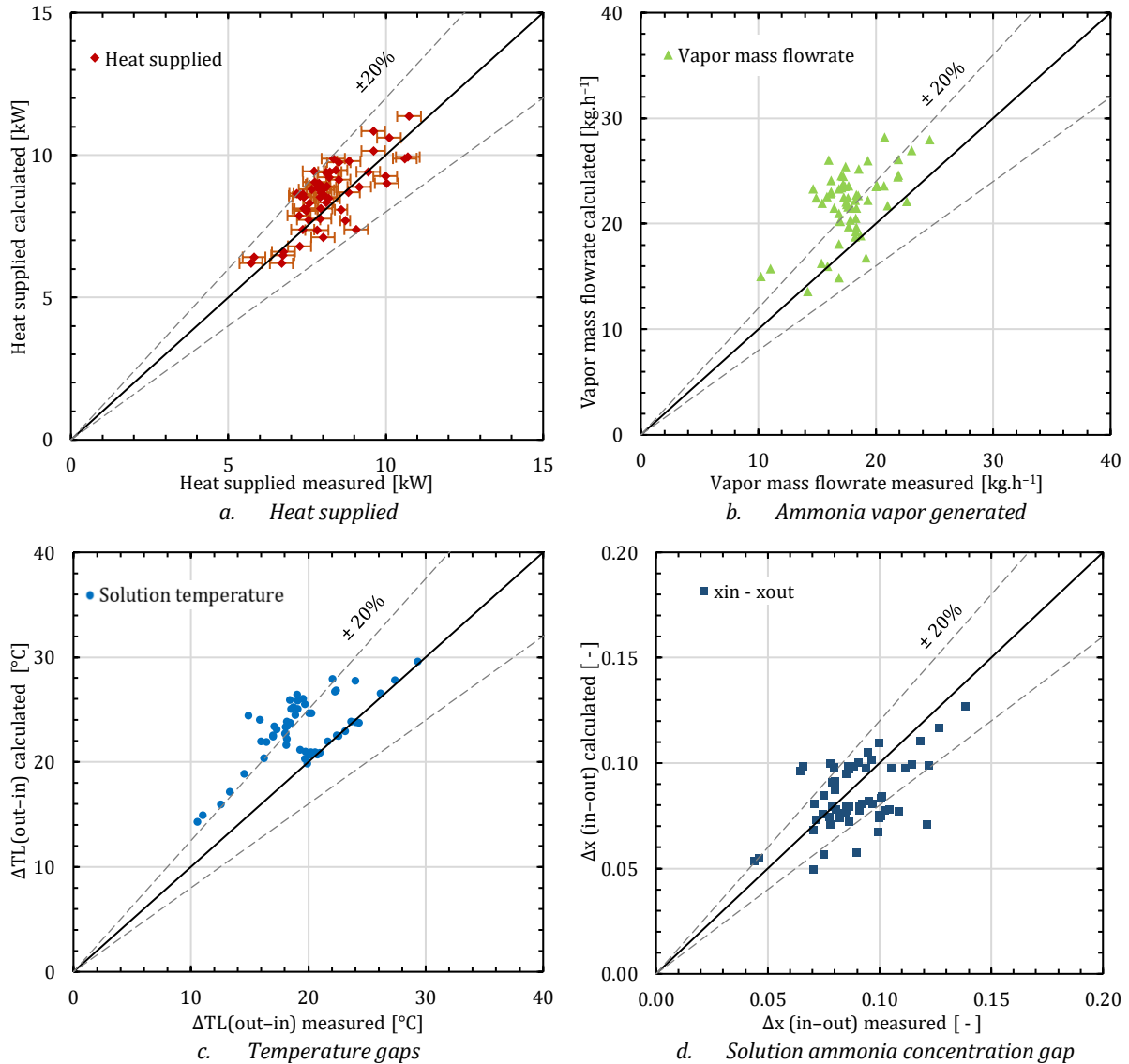


**Figure 6.11.** Numerical results vs. measurements for the partly flooded combined generator, with plate wettability reduced.

The relative accuracy of the model prediction of the combined generator outputs with a confidence level of 90% is given in Table 6.3.

The heat supplied to the combined generator predicted by the model agrees well with the experimental results (Figure 6.11a). The deviations are less than 20%, with measurement uncertainties of 2–7%.

The model overestimates the ammonia vapor production with an average of approximately 20% (Figure 6.11b). The deviations reach approximately 40% in some cases, highlighting the model limits. This might be due to the difficulties of modeling boiling heat transfers with binary mixtures. One approach would be to use a convective boiling model with a limiting factor for the nucleate boiling; however, this type of model is not well adapted in the case of counter-current flow configuration between the solution and the vapor. As for the unflooded model, the model could be improved using an adapted correlation describing the contact angle evolution as a function of the operating conditions.

The model overestimates the increase in the solution temperature from the top to the bottom by an average of 15% (Figure 6.11c). The deviations are mostly less than 30%. The model agrees well with the experiments at low solution mass flowrate ( $\dot{m}_{RS} < 100 \text{ kg.h}^{-1}$ ) but overestimates the temperature difference for higher solution mass flowrate.

The accuracy of the model in predicting the ammonia concentration at the outlet is approximately 28%. This accuracy depends on the model ability to predict the vapor mass flowrate generated.

Three models of generators are developed, allowing the prediction of their behaviors when they are integrated in an  $\text{NH}_3\text{-H}_2\text{O}$  absorption chiller of small capacity. In the following section, the performances of the flooded generator and of the combined generator with its two operating modes are compared, thanks to their effectiveness.

## 7 Comparison of performance between the flooded generator and the combined generator for its two operating modes

In *Chapter 2, Sect 3.2.1*, the mass effectiveness (Eq 3.15), the thermal effectiveness (Eq. 4.14), and the species effectiveness (Eq. 4.15) are defined. They enable the calculation of the ammonia vapor mass flowrate generated and its concentration, as well as the thermal energy required by the generator, depending on the operating conditions. In the following section, the performances of the flooded generator and of the combined generator are investigated through these three effectiveness.

### 7.1 Inlet operating conditions of the generators

In the previous sections, the inlet operating conditions of the generators were fixed by the absorption chiller operation (see Tables 6.1, 6.2, and 6.4). Considering the impact of the generator performance on the absorption machine operation, it was not possible to characterize the generator performance with the same operating conditions. The present part aims to compare the different generators performances using the numerical models at the same inlet operating conditions, which are presented in Table 6.5.

	Temperature [°C]	Mass flowrate [kg.h <sup>-1</sup> ]	Ammonia concentration [-]	Pressure [bar]
<b>Solution</b>	62	100	0.58	12
<b>HTF</b>	95	1600	-	3

**Table 6.5.** Nominal inlet operating conditions of the three generators.

The mass effectiveness (yellow), the thermal effectiveness (red), and the species effectiveness (green) are represented in Figures 6.12 to 6.14 as a function of the inlet operating conditions, for the flooded generator (*FG*), the unflooded combined generator (*UF*), and the partly flooded combined generator (*PF*).

The flooded generator shows globally higher mass, thermal, and species effectiveness compared to the combined generator. This appears counterintuitive compared to the results presented previously in this chapter. The impact of the generators performances on the machine performance will be presented later (*Sect. 7.5*) to confirm the trends experimentally observed.

In general, the unflooded combined generator shows higher thermal and mass effectiveness than the partly flooded combined generator. Concerning the species effectiveness, the two operating modes are characterized by similar performances.

However, the evolutions of the species effectiveness should be interpreted with caution. Indeed, accurate ammonia concentration measurement in the vapor emitted by the generator is very complex to achieve, and the current measurements accuracy is not high enough to validate the evolution of the species effectiveness predicted by the models. This is especially true for the flooded generator, which was implemented in the absorption machine with a rectifier.

## 7.2 Impact of the inlet HTF temperature

Figure 6.12 presents the mass, thermal, and species effectiveness of the flooded generator and of the combined generator for its two operating modes, as a function of the inlet HTF temperature.

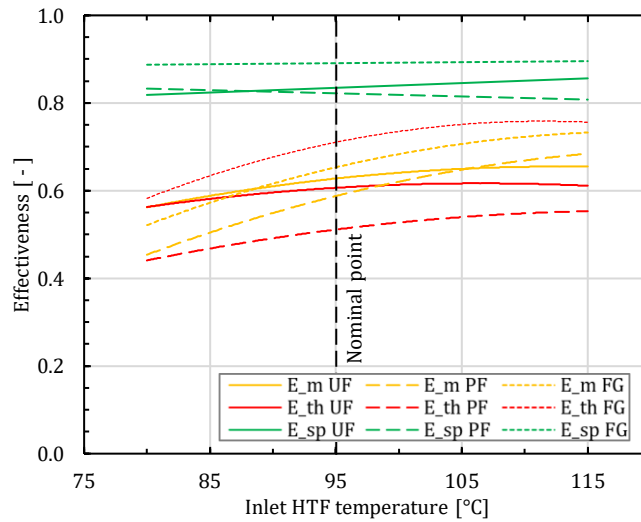


**Figure 6.12.** Mass, thermal, and species effectiveness vs. inlet HTF temperature evolution for the three generators.

In the flooded generator, the increase in the HTF temperature leads to the increase in the wall superheat and in the boiling heat transfer. Thus, as expected, the thermal effectiveness increases with the HTF temperature, and tends toward a maximum of 0.75 at  $T_{gen} = 110^{\circ}\text{C}$ . The solution exiting the flooded generator is slightly superheated ( $+4^{\circ}\text{C}$ ), thus, the thermal effectiveness is higher than the mass effectiveness, which seems to reach a maximum of 0.73 around  $T_{gen} = 115^{\circ}\text{C}$ . The water content in the vapor leaving the flooded generator increases with the temperature of the HTF. This increase appears to be proportional to the maximum water content that could be generated in an infinitely long flooded generator, keeping the species effectiveness constant.

The solution temperature enters the combined generator with a superheat of  $+3^{\circ}\text{C}$ . Therefore, a small amount of vapor is generated without any heat transfer, improving the mass effectiveness compared to the thermal effectiveness. On the other hand, the increase in the solution superheating at the exit of the combined generator promotes thermal effectiveness over mass effectiveness (since heat transfer can be performed without any mass transfer). Thus, the difference between the two types of effectiveness depends on the solution superheat at the inlet and outlet of the exchanger, weighted by the solution mass flowrate. The effect of the solution superheat at the exit will be all the more important that the solution mass flowrate is high (i.e., low vapor mass flowrate). This helps to explain the higher increase in the mass effectiveness compared to the thermal effectiveness when the HTF temperature increases.

For the unflooded mode, the mass effectiveness and the thermal effectiveness reach their maximum of  $\epsilon_{mass} \approx 0.65$  and of  $\epsilon_{th} \approx 0.61$  at  $T_{gen} = 110^{\circ}\text{C}$ . For the partly flooded mode, the thermal effectiveness reaches its maximum of  $\epsilon_{th} \approx 0.55$  at  $T_{gen} = 110^{\circ}\text{C}$ . The vapor mass flowrate generated increases with the increase in the HTF temperature (Figure 9.a). It is accompanied by a small decrease in the film thickness due to the decreases in the wetted areas. Therefore, for the unflooded operating mode, the increase in the heat transfer coefficient is limited, as is the increase in the thermal effectiveness with the HTF temperature increase. The boiling heat transfer coefficient increases significantly with the wall temperature increase, leading to the higher increase in thermal effectiveness with the HTF temperature increase for the partly flooded operating mode.

### 7.3 Impact of the inlet solution mass flowrate

Figure 6.13 presents the mass, thermal, and species effectiveness of the flooded generator and of the combined generator for its two operating modes, as a function of the inlet solution mass flowrate.

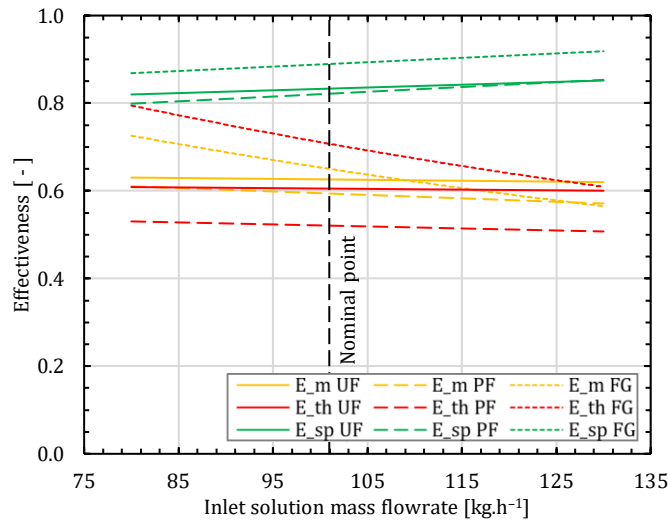


**Figure 6.13.** Mass, thermal, and species effectiveness vs. inlet solution mass flowrate evolution for the three generators.

The limiting fluid is the solution. The increase in its mass flowrate results in a direct increase in the maximum heat rate that can be transferred from the HTF to the solution. However, in the flooded generator, the impact of the decrease in transit time due to the increase in mass flowrate is not compensated by the increase in boiling heat and mass transfers. Thus, the increase in the mass flowrate of the solution results in a decrease in the mass and thermal effectiveness. The increase in the mass flowrate of the solution induces a reduction in the temperature of the solution, leading to the generation of a vapor with higher ammonia concentration, and thus to the increase in the species effectiveness.

The increase in the solution mass flowrate at the combined generator inlet leads to an increase in the desorption potential in the falling film. Moreover, it leads to an increase in the wetted surface for similar film thickness along the falling film; resulting in an equivalent increase in the vapor generated. Thus, for the unflooded operating mode, the mass and thermal effectiveness are almost unchanged when the solution mass flowrate varies. The boiling heat transfer is not affected by the solution mass flowrate. Therefore, the amount of vapor generated in the flooded part does not change when the solution mass flowrate increases. This explains why the thermal effectiveness and mass effectiveness decrease in the partly flooded operating mode. The increase in the solution mass flowrate increases the wetted area in the adiabatic part, and thus the purification process is enhanced, resulting in an increase in the species effectiveness with the solution mass flowrate increase. A mass flowrate of 130 kg.h<sup>-1</sup> appears to be the lower limit to wet entirely the heated plates and seems to be a good compromise for vapor generation and purification. For smaller solution flows, it would be interesting to reduce the number of plates to enable better wetting.

#### 7.4 Impact of the inlet solution superheat

Figure 6.14 presents the mass, thermal, and species effectiveness of the flooded generator and of the combined generator for its two operating modes, as a function of the inlet solution superheat.

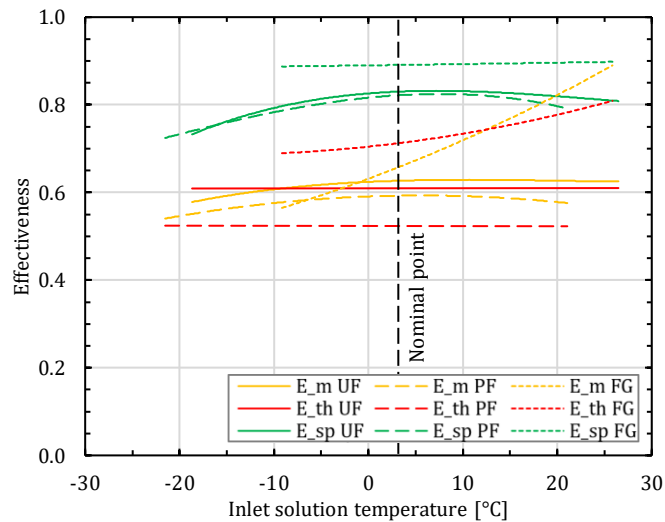


**Figure 6.14.** Mass, thermal, and species effectiveness vs. inlet solution superheat evolution for the three generators.

In the nominal operating conditions, the solution enters the flooded generator or is injected in the combined generator superheated by approximately +3°C.

The increase in this superheating increases the amount of vapor produced thanks to the flash desorption at the bottom of the flooded generator and reduces the amount of vapor produced along the plates. Thus, the impact of the thermal resistance between the HTF and the solution is reduced, leading to the increase in the mass effectiveness. The decrease in the maximum heat rate that can be transferred to the solution (due to increase of the solution superheating) leads to the thermal effectiveness increase. The increase in the solution temperature at the inlet of the exchanger decreases the maximum ammonia concentration reachable at the outlet while the ammonia concentration leaving the exchanger is almost constant; thus, it leads to an increase in the species effectiveness.

The subcooling or superheating of the solution at the combined generator inlet does not affect the thermal effectiveness, which stays constant at  $\varepsilon_{th} \approx 0.61$  and  $\varepsilon_{th} \approx 0.52$  for the unflooded and the partly flooded operating modes, respectively. Increasing the solution inlet temperature leads to an increase in the vapor production and in the ammonia vapor quality; however, when the superheat is higher than +3°C, the vapor ammonia concentration starts decreasing and its effect is greater than the increase in the vapor mass flowrate effect. Thus, the mass and species effectiveness increase with the solution temperature increase at the inlet of the combined generator until reaching the maximum before decreasing. A superheat of +5°C at the inlet of the combined generator seems to be the optimal entry condition for the solution, making it possible to obtain the highest thermal, mass, and species effectiveness.

## 7.5 Impact of the generators performances on the absorption chiller performance

The present section aims to compare the generators performances through their effectiveness. The accuracy of the partly flooded model is not sufficient to establish the advantage of this operation mode compared to the unflooded mode (see Sect. 6.4). Thus, the comparisons will focus only on the flooded generator vs. the unflooded combined generator.

The ammonia vapor concentrations simulated are higher than  $y_{out} > 0.98$  for both generators; however, as mentioned previously, the measurements are not accurate enough to validate the species effectiveness estimations thanks to the models. Furthermore, since the models used to calculate the ammonia vapor concentrations emitted by the generators are different, it is difficult to assess the best species effectiveness between the flooded generator and the combined generator. This is especially true because the boiling model used to characterize the flooded generator performance addresses the species transfer in a simplified way. Therefore, the following analysis is solely based on the evolution of the mass effectiveness and thermal effectiveness.

Figure 6.15 presents the mass effectiveness and thermal effectiveness, as well as the effectiveness ratio of the flooded generator and unflooded combined generator, as a function of the inlet HTF temperature and inlet solution mass flowrate. The evolutions are the same than in Figure 6.12 and Figure 6.13, respectively.

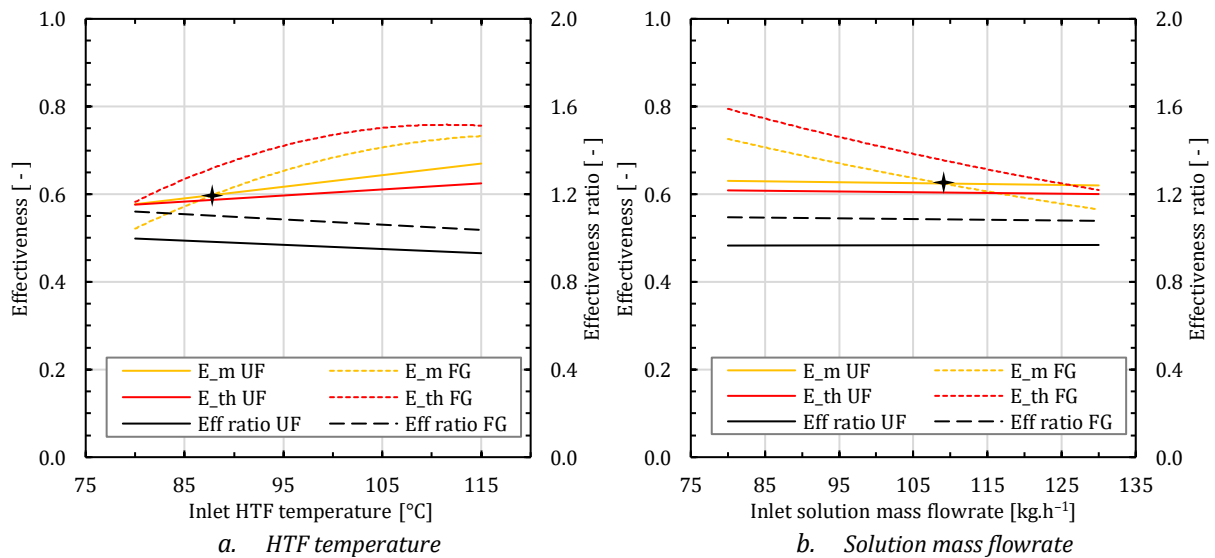


**Figure 6.15.** Mass and thermal effectiveness and effectiveness ratio vs. inlet HTF temperature and inlet solution mass flowrate evolution for the unflooded combined generator and the flooded generator.

A first operating point presenting the same mass effectiveness for both generators is compared:  $\epsilon_{mass} = 0.6$  at  $T_{gen} = 88^\circ\text{C}$  (see Figure 6.15a). The operating conditions are the same; thus, the maximum vapor mass flowrate producible is the same and the two generators produce the same vapor mass flowrate. The heat supplied to the generators for those operating conditions can be calculated thanks to the thermal effectiveness. Indeed, the maximum heat rate transferrable to the generators is equal. The thermal effectiveness of the flooded generator  $\epsilon_{th} = 0.67$  is higher than the thermal effectiveness of the unflooded combined generator  $\epsilon_{th} = 0.59$ . Thus, the heat required to produce the same amount of vapor is larger in the flooded generator ( $\sim 10$  kW) compared to the combined generator ( $\sim 9$  kW). Then, the COP is higher when the absorption machine is equipped with the combined generator compared to the flooded generator for this operating point (assuming equal ammonia concentrations in the vapor produced). Therefore, the results of the models confirm the experimental results observed previously in this chapter.

The same reasoning can be led for the operating point at  $\dot{m}_{RS} = 112$  kg.h<sup>-1</sup> (see Figure 6.15b).

In consequence, the performances of the generators must be evaluated through the joint analysis of the different effectiveness. In *Chapter I*, a first optimization approach was conducted on the combined generator via the introduction of an energy cost of vapor production. The same approach can be performed thanks to the effectiveness ratio  $ER$  between the thermal and mass effectiveness. The  $ER$  relates to the energy cost in a non-dimensional way. The two generators work under the same operating conditions, thus  $\dot{m}_{v,out,max}$  and  $\dot{Q}_{max}$  are the same for the two exchangers.

$$ER = \frac{\varepsilon_{th}}{\varepsilon_{mass}} = \frac{\dot{Q}}{\dot{m}_{v,out}} \frac{\dot{m}_{v,out,max}}{\dot{Q}_{max}} \quad (6.35)$$

For all the values, the effectiveness ratio of the unflooded combined generator is smaller than the one of the flooded generator. Thus, the combined generator has a better energy performance compared to the flooded generator.

## 8 Conclusion

Two numerical models of generators for  $\text{NH}_3\text{-H}_2\text{O}$  absorption chiller of small capacity (5 kW) were developed. The first one simulates the behavior of a flooded boiling plate generator. The solution is injected at the bottom and flows upward together with the vapor generated, while the HTF heats the solution in counter-current mode. The heat transfers are essentially due to the nucleate boiling. The heat transfer due to convective boiling is less intensive although it increases along the exchanger. The pressure in the flooded generator remains almost constant. The second model describes the heat and mass transfer in a falling-film section and in a flooded section where boiling heat transfers occur, in a combined plate generator. Thus, the combined generator operates in two different modes: unflooded and partly flooded. The impact of the plate's wettability on the combined generator performances is presented thanks to the calculation of a minimum linear wetting rate based on a fixed contact angle between the ammonia-water solution and the plate. Further work should be carried out to integrate the impact of the operating conditions on the contact angle.

The results of the flooded generator model are validated through experimental data from the literature; and the results of the combined generator model are compared with experimental results presented in *Chapter III*. The Chen model adapted to mixtures and involving the Stephan and Abdelsalam nucleate boiling correlations model shows a good agreement with the measurements: The heat supplied is predicted with less than 15% of error; the ammonia vapor mass flowrate and the ammonia concentration difference of the solution between the inlet and the outlet of the generator are predicted with less than 20% and 25% of error, respectively. The accuracy of the combined generator model performance predictions with the unflooded operating mode is approximately 20% concerning the heat supplied by the HTF, the vapor mass flowrate generated, and the temperature and concentration of the solution at the exit of the generator. It drops to 30% with the partly flooded operating mode due to the difficulty of modeling the boiling of binary mixtures for counter-current flows.

The models developed give useful tools to predict the generators behavior in an  $\text{NH}_3\text{-H}_2\text{O}$  absorption chiller.

Finally, the performances of the flooded generator and of the combined generator are studied through the mass, thermal, and species effectiveness. A parametric study on the inlet operating variables of the generators (HTF and solution temperatures and solution mass flowrate) provides some information on their behaviors. The flooded generator has higher mass and thermal effectiveness ( $\varepsilon_{mass}$  and  $\varepsilon_{th} > 0.6$ ), except for high solution mass flowrates; and it shows a maximum thermal effectiveness for an inlet HTF temperature of  $T_{gen} = 110^\circ\text{C}$ . Concerning the combined generator, the unflooded operating mode presents the best performances. For the mass and thermal effectiveness of both operating modes, the maximum value is obtained at the inlet HTF temperature of  $T_{gen} = 110^\circ\text{C}$ ; and the inlet solution temperature corresponds to a solution superheated of  $+5^\circ\text{C}$  and a solution mass flowrate of  $130 \text{ kg}\cdot\text{h}^{-1}$  that enable wetting of the plates.

The performances of the generators must be investigated through the joint analysis of the different effectiveness. The effectiveness ratio between the thermal and mass effectiveness is useful to compare the generators performances when they work under the same operating conditions. The generators models confirm that the energy performance of the combined generator is better than the flooded generator one.

## 9 References

- Bennett D. L., Chen J.C., (1980), "Forced convective boiling in vertical tubes for saturated pure components and binary mixtures", *Applied International Chemical Journal* 26, 454–461
- Bennett D. L., Davis M. W., Hertzler B. L., (1980), "The suppression of saturated nucleate boiling by forced convective flow", *AIChE Symposium Series* 76, 91–103
- Chen J.C., (1966), "Correlation for boiling heat transfer to saturated fluids in convective flow", *Industrial & Engineering Chemistry Process Design and Development* 5, 322–329
- Chisholm D., (1967), "A theoretical basis for the Lockart-Martinelli correlation for two-phase flow", *International Journal of Heat and Mass Transfer* 10, 1767–1778
- Fernandes C. S., Dias R. P., Maia J. M., (2008), "New plates for different types of plates heat exchangers", *Recent Patents on Mechanical Engineering* 1, 198–205
- Friedel L., (1979), "Improved friction pressure drop correlations for horizontal and vertical two-phase pipe flow", *European two-phase flow group meeting, paper E2, Ispra, Italy*
- Hartley D.E., Murgatroyd W., (1964), "Criteria for the break-up of thin liquid layers flowing isothermally over solid surfaces", *International Journal of Heat and Mass Transfer* 7, 1003–1015
- Inoue T., Kawae N., Monde M., (1998), "Characteristics of heat transfer coefficient during nucleate pool boiling of binary mixtures", *Heat and Mass Transfer* 33, 337–344
- Inoue T., Monde M., (2008), "Prediction of pool boiling heat transfer coefficient in ammonia–water mixtures", *Transactions of the Japan Society of Mechanical Engineers, Part B* 74, 1114–1118
- Jung D. S., Radermacher R., (1993), "Prediction of heat transfer coefficient of various refrigerants during evaporation", *International Journal of Refrigeration* 16, 201–209
- Jung D.S., McLinden M., Radermacher R., Didion D., (1989), "A study of flow boiling heat transfer with refrigerant mixtures", *International Journal of Heat and Mass Transfer* 32, 1751–1764
- Kaern M.R., Modi A., Jensen J.K., Andreasen J.G., Haglind F., (2016), "An assessment of in-tube flow boiling correlations for ammonia–water mixtures and their influence on heat exchanger size", *Applied Thermal Engineering* 93, 623–638
- Lockart R.W., Martinelli R.C., (1949), "Proposed correlation of data for isothermal two-phase, two-component flow in pipes", *Chemical Engineering Progress* 45, 39–48
- Norman W.S., (1960), "Heat transfer to a liquid film on a vertical surface", *Transactions of the Institution of Chemical Engineers* 27, 301–307
- Schlünder EU., (1983), "Heat transfer in nucleate boiling of mixtures", *International Chemical Engineering* 23, 589–599
- Stephan K., Abdelsalam M., (1980), "Heat transfer correlation for natural convection boiling", *International Journal of Heat and Mass Transfer* 23, 73–87
- Triché D. (2016), "Étude numérique et expérimentale des transferts couplés de masse et de chaleur dans l'absorbeur d'une machine à absorption ammoniac-eau", PhD thesis, *Université de Grenoble Alpes*
- Triché D., Bonnot S., Perier-Muzet M., Boudéhenn F., Desmales H., Caney N., (2017), "Experimental and numerical study of a falling film absorber in an ammonia–water absorption chiller", *International Journal of Heat and Mass Transfer* 111, 374–385
- Whalley P. B., (1987), "Boiling condensation and gas-liquid flow", *Oxford Science Publications*
- Zacarias A., Ventas R., Venegas M., Lecuona A., (2010), "Boiling heat transfer and pressure drop of ammonia–lithium nitrate solution in a plate generator", *International Journal of Heat and Mass Transfer* 53, 4768–4779
- Ziegler F., (1999), "Recent Developments and Future Prospects of Sorption Heat Pump Systems," *International Journal of Thermal Sciences* 38, 191–208



## **Part V: Discussion, conclusions, perspectives**

*The fifth part of this manuscript is dedicated to the discussion, conclusions and perspectives of the work. The main achievements of this PhD work are summarized, including the development of the numerical models and the experimental results and observations. Proposals for continuity and expanding the work are suggested.*

### **Reminder of the challenge**

The development of a compact generator, able to produce a high ammonia concentration vapor at low energy cost, is a promising opportunity to improve the performance and compactness of  $\text{NH}_3\text{-H}_2\text{O}$  absorption chillers, as well as to reduce the investment and operating costs.

In the past few years, various technologies of generators, rectifiers, or combined components were modeled and designed. However, these components have limits in terms of compactness, costs, or the quality of ammonia vapor produced. The opportunity to combine a generator and a rectifier in one unique compact falling-film and plate heat exchanger was identified as very promising, as was the development of a numerical model simulating the heat and mass transfer occurring in this type of component, specifically in counter-current flow configuration.

Thus, this PhD study consisted in developing an innovative compact falling-film and plate combined generator designed for an  $\text{NH}_3\text{-H}_2\text{O}$  absorption chiller of 5-kW cooling capacity. The exchanger, involving both production and purification of ammonia vapor, was aimed to produce a sufficiently high ammonia vapor concentration to operate without a rectifier.

### **Specificity of the approach**

First, the literature review presented the absorption chiller operation and performance, and the chosen ammonia–water working pair. The second part of the state of the art focused on a review of the generator and rectifier technologies. A classification of the heat exchanger technologies and vapor generation processes was presented, and the potential offered by the development of an exchanger combining generation and rectification of the ammonia vapor was underlined. A focus was also placed on the distribution system, which is crucial in a falling-film and plate exchanger. The last part of the bibliographic review focused on the heat and mass transfer occurring in an ammonia–water falling-film, on the dynamics of the flows, and on the mechanisms involved during pool boiling. The fluid properties as well as several other phenomena need to be carefully considered such as the film thickness, the wetted area, the surface tension, and the flooding.

The bibliographic work underlined the importance of the ammonia vapor generation in  $\text{NH}_3\text{-H}_2\text{O}$  absorption chillers, gave some leads for the modeling of the new combined generator, showed the importance of the experimental validation, and introduced the main work to follow. Then, the approach was elucidated in four chapters investigating numerically and experimentally the behavior and the performance of the new combined generator designed here and its impact on the performance of the  $\text{NH}_3\text{-H}_2\text{O}$  absorption chiller in which it is integrated.

*Chapter I* described the development of a numerical model characterizing the combined generator. The behavior of the new component was simulated through the modeling of the absorption and desorption processes occurring in a falling-film and plate heat exchanger. The simulations could be operated in co-current or counter-current flow configurations: the counter-current mode (the vapor generated and the HTF compared to the solution) appeared to be the most efficient. The new design, combining adiabatic plates for ammonia purification on top of heated plates for ammonia generation, allowed us to increase the ammonia concentration in the vapor exiting the exchanger. The subcooling of the solution at the combined generator inlet enhanced the rectification process but also had a significant impact on the energy cost of the process; thus, the best compromise needs to be chosen. The vapor ammonia concentration increased with the increase in the ratio of the adiabatic-heated plate; however, depending on the inlet solution subcooling, it increased the investment cost and affected the operating costs. A high aspect ratio reduced the operating costs. This first chapter offered insights into the design of a combined generator meant to be integrated in an  $\text{NH}_3\text{-H}_2\text{O}$  absorption chiller.

Then, *Chapter II* numerically investigated how the combined generator affected the performance of an  $\text{NH}_3\text{-H}_2\text{O}$  absorption chiller designed for air-conditioning. A model simulating the behavior of the absorption chiller was developed and validated on data from the literature for a large range of operating

conditions. The impact of the combined generator on the absorption machine performance was investigated numerically thanks to the definition of three types of effectiveness: the mass and thermal effectiveness predicted the mass flowrate of the vapor produced, and the species effectiveness predicted the vapor ammonia concentration. To this end, correlations involving non-dimensional numbers (an equilibrium factor, a number of transfer unit, and a modified Jakob number) were developed. At the inlet of the combined generator, the variations in the solution mass flowrate and heating source temperature controlled the cooling capacity of the machine while keeping the COP almost constant. As shown in *Chapter I*, the variation in the inlet solution temperature controlled the ammonia concentration in the vapor produced; this can be done thanks to an exchanger implemented at the inlet of the combined generator. However, the vapor purification process in the adiabatic part was good enough to remove the rectifier in the absorption chiller dedicated to air-conditioning without requiring the inlet solution to be subcooled. Implementing the combined generator in the machine enabled us to reduce the number of components in the system and to increase its compactness. Moreover, it improved the performance by an increase in the COP of approximately 15%. This chapter presented numerical results on the behavior of an absorption chiller including the combined generator.

In *Chapter III*, an experimental characterization of the combined generator, and its impact on the NH<sub>3</sub>-H<sub>2</sub>O absorption chiller performance, was presented. Two operating modes of the combined generator were considered: unflooded and partly flooded. The experimental investigation confirmed that the combined generator produced the required amount of vapor with a high ammonia concentration. Its integration in the machine increased cooling capacity, improved the COP, and enhanced the absorption chiller compactness compared to the initial configuration. Investigations on the inlet operating parameters of the absorption chiller were made, leading to the following observations:

- + The combined generator HTF mass flowrate affected the cooling capacity and the COP slightly, which still reached an optimum at  $\dot{m}_{hot} \sim 1600 \text{ kg}\cdot\text{h}^{-1}$ ;
- + The subcooling of the inlet solution enabled an increase in the ammonia concentration of the vapor produced but degraded the performance of the machine. Therefore, the solution subcooling is not recommended;
- + The partial flooding of the combined generator degraded the performance of the machine compared to the unflooded configuration;
- + The influence of the temperatures of the heating, heat rejection, and chilling sources and the influence of the solution mass flowrate on the combined generator performance were evaluated through a design of experiments. The combined generator operation is highly impacted by the solution flowrate and the concentration of the solution. The results were compared with the adapted NTU model, which offered a better description of the combined generator performance.

A model based on the Carnot-COP was then calibrated to describe the evolution of the absorption chiller performance. The model was used to estimate the performance of an air-conditioning machine for office cooling in Chambéry. A low solution mass flowrate (75 kg·h<sup>-1</sup>) made it possible to reduce the energy consumption by approximately 15% but it required a higher heating source temperature. The increase in the solution mass flowrate up to 100 kg·h<sup>-1</sup> degraded the performance but enabled the machine to run with a low heating source temperature (75 °C) and led to the self-regulation of the machine for air-conditioning applications.

In *Chapter IV*, two numerical models were developed to investigate the performance of a flooded plate generator and of the combined generator operating with its two modes. The predictability of the models was verified through experimental data.

- + In the flooded generator, the nucleate boiling heat transfer prevailed compared to the convective boiling one. The pressure drops were found to be negligible. The heat supplied was predicted with less than 15% of error; the ammonia vapor mass flowrate and the solution ammonia concentration difference between the inlet and the outlet of the generator were predicted with less than 20% and 25% of error, respectively. The ammonia concentration of the vapor produced varied from 0.97 to 0.99, still needing to be purified at the generator outlet to reach the desired ammonia concentration.
- + The influence of the wettability of the falling-film plate and of the nucleate boiling occurring in the partly flooded zone was introduced in the combined generator model. The model predicted the performance of the combined generator operating in unflooded mode with less than 20% of error on average. However, the model was less accurate for the partly flooded mode, with errors reaching 30–40% due to

the difficulty to describe the boiling heat transfer of binary mixtures in counter-current flow configuration.

Finally, the performance of the flooded generator and of the combined generator operating with its two modes was studied through their mass, thermal, and species effectiveness for various inlet operating conditions. For each generator at the nominal point, the inlet solution is slightly superheated by +3°C. The flooded generator showed globally higher mass, thermal, and species effectiveness compared to the combined generator. However, its global performance was worse than that of the combined generator, which produced vapor at a lower energy cost. The effectiveness ratio between the thermal and mass effectiveness enabled us to compare the performance of the generators when they worked under the same operating conditions.

### **Improved overview**

- ✦ A numerical model is developed to characterize the heat and mass transfer occurring in a falling-film and plate combined generator, bringing together a heated section where the vapor is generated to an adiabatic section where the vapor is purified.
- ✦ The numerical work improves the models available in the literature by providing a new adaptable and reversible numerical tool. Indeed, the model is able to simulate co-current and counter-current flow configurations, absorption and desorption processes, wetting influence on the transfers, as well as boiling processes that can develop in the flooded section.
- ✦ The description of the performance of heat and mass exchangers through the mass, thermal, and species effectiveness is useful for dynamic absorption machine simulation software, as well as for the comparative analysis of the components.
- ✦ The numerical and experimental work confirms the opportunities offered by the combined generator to improve the performance and compactness of the NH<sub>3</sub>-H<sub>2</sub>O absorption chiller in which it is integrated.

### **Perspectives and expansion**

This numerical and experimental study confirmed that the impact of the refrigerant vapor generation and purification system on the performance of an absorption chiller in which it is integrated is significant. The inlet operating parameters, as well as the geometry of the generation-purification system, are crucial for the machine operation. The results obtained and the observations made through the study have led to some potential areas of improvement for future work.

#### *Design optimization of the combined generator*

In *Chapter I*, the numerical parametric studies based on the operating parameters and on the geometry of the combined generator provided the first indications for the design of the exchanger. Developing a methodology for the design optimization of this component, considering its integration in an absorption chiller for a specific application, would be an interesting work perspective to explore. The objective function should integrate the investment costs, the operating costs, the compactness of the machine, and the component should be able to produce the required amount of vapor, with a sufficient ammonia concentration.

Thanks to this optimization, a second combined generator could be designed, built, and integrated, replacing the combined generator studied in this work. It would allow us to confirm experimentally the efficiency of the optimization method for designing a generation component for NH<sub>3</sub>-H<sub>2</sub>O absorption chillers of small capacity.

In the meantime, since the prototype of the combined generator designed here showed promising results (in terms of machine performance and compactness gains), developing an industrial version of the combined generator is a work angle to focus on.

### *Operating range of the absorption chiller*

A new suggestion concerning expansion of the experimental work would be to operate the absorption chiller in a wider range of operating conditions, in particular regarding the chilling temperature at the evaporator outlet. Indeed, it could be interesting to take advantage of the opportunity of using ammonia as the refrigerant to produce negative cold.

### *Improvement of the absorption chiller model and alternative modeling*

In *Chapter II*, the model describing the absorption chiller performance could be improved thanks to the use of the mass, thermal, and species effectiveness to characterize all the components.

In the model of the absorption chiller developed in *Chapter II*, the accumulators and separators were not simulated. The development of a dynamic model taking into account the filling and emptying of the accumulators and separators is another interesting possibility.

### *Wettability of the plates*

In the combined generator model presented in *Chapter I* and improved in *Chapter IV*, the variation of the wetted area by the introduction of a fixed contact angle between the solution falling-film and the plates led to enhance model predictability. However, the contact angle should not be fixed but dependent on the solution properties that vary along the plates. Including the contact angle variations in the falling-film model would be an interesting perspective in order to develop a more precise model of the heat and mass transfer occurring inside the combined generator and to improve the model predictability.

As there is no literature concerning the evolution of the contact angle of an ammonia–water solution flowing on a metallic plate, a parallel experimental study dealing with this subject could be conducted. Thereby, results could lead to useful correlations for modeling.

Concerning the homogeneity of the solution distribution, it would be interesting to conduct studies on the flow at the atmospheric pressure.

### *Integration of boundary layers*

When the falling film starts flowing on the top of the adiabatic or heated plates; species and thermal boundary layers develop along the film. The development of these boundary layers in both adiabatic and heated sections was not considered in the model.

According to some preliminary simulations performed in the nominal operating conditions:

- + In the adiabatic section, the species boundary layer is still under development when the film reaches the bottom of the plates;
- + In the heated section, the species boundary layer reaches its full development at half of the plate.

A useful work prospect would be to take into account the development of the species and thermal boundary layers in the evolution of the heat and mass transfer coefficients along the falling film in the adiabatic and heated sections to improve the model accuracy.

### *Model of the heat transfer fluid*

In the combined generator, the flow of the HTF is modeled as an ideal counter-current flow while it is a methodical crossflow. A more realistic modeling of the HTF flow would change the heat transfer between the HTF and the plates, and the heat and mass transfer inside the combined generator would be more accurate.



## Part VI: Appendix

*The last part of this manuscript gives further information or details some parts of the study. The first appendix relates to the measurements uncertainties, gives precisions about the sensors used and their calibration. The second appendix details the head losses in the solution and in the vapor phases inside the combined generator, and specifically inside the distribution–rectification component. The third appendix shows the values taken for the design of experiments and gives some information about the data analysis.*



## **Appendix 6.1.    Uncertainties**

There are two main laws of uncertainty propagation:

- + Type A method: the components are evaluated through the statistical distribution of measurements series. The standard errors are experimental.
- + Type B method: the components are evaluated admitting the laws of probability according to previous experimentations or manufacturer information. The standard errors are estimated.

For statistical analysis with the B type method, most of the time, the coverage factor k is:

- + For a rectangular distribution:  $k = \sqrt{3}$  ;
- + For a conventional (*law 01.01.92*) calibration uncertainty:  $k = 2$ .

Illustration of a rectangular distribution of 1.000 values.

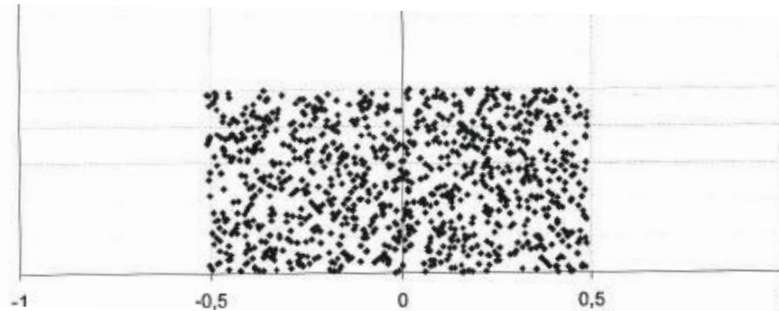


**Figure 7.1.1.** *Distribution values illustration.*

The half-span is  $u = 0.5$  and the standard deviation is  $\varepsilon = 0.287$ .

Then,  $\frac{\text{half-span}}{\text{standard deviation}} = 1.732 = \sqrt{3}$

It demonstrates that if not all the values are known, but only the limit values, the standard deviation can still be estimated considering the half-span divided by  $\sqrt{3}$ .

Model:

$$y = x + C1 + C2 + \dots \quad (5.1.1)$$

- + y: final result with correction ;
- + x: raw score ;
- + C1, C2: corrections.

$$Uc^2(y) = Uc^2(x) + Uc^2(C1) + Uc^2(C2) + \dots \quad (5.1.2)$$

- +  $Uc^2(y)$ : Total variance ;
- +  $Uc^2(x), Uc^2(C1)$ : Variances due to each uncertainty parameter ;
- +  $Uc(y)$ : composed uncertainty ;

$$U = k \cdot Uc(y) \quad (5.1.3)$$

The expanded measurement uncertainty U, uses a coverage factor of  $k = 2$ , which gives a level of confidence of approximately 95 %.

### Calibration

The main values of the calibration are:

- + Reference value:  $X_{\text{ref}}$  ;
- + Read value:  $X_{\text{read}}$  ;
- + Theoretical calculated value:  $X_{\text{th}}$  ;

## Appendix

Then, the following parameters are deduced:

- ✦ Absolute error:  $\varepsilon_{abs} = X_{read} - X_{ref}$  ;
- ✦ Real error:  $\varepsilon_{real} = (X_{read} - X_{ref}) / X_{ref}$  ;
- ✦ Correction:  $C = X_{ref} - X_{read}$  ;
- ✦ Correction coefficient:  $k = X_{ref} / X_{read}$  ;

The calibration uncertainties need also to be considered. For the reference value, the uncertainty depends on the certification of the calibration bench. For the read value, the uncertainty takes into account the stability, the repeatability, the resolution and the accuracy of the system.

### Measurement uncertainties

The measurement uncertainties taken into account are considered for the whole measurement chain, which means they are considered from final sensor until the acquisition system device.

The first list of parameters with their uncertainties are presented for the calculation of the thermal power of the four main components of the absorption cycle: absorber, generator, condenser and evaporator. The rectifier, which is directly linked to the generator and the condenser, is also taken into account.

In order to calculate the thermal power  $P$ , the following parameters need to be considered: the mass flowrate  $\dot{m}$ , the thermal capacity  $C_p$  and 2 temperatures  $T1$  and  $T2$ :  $P = \dot{m} \cdot C_p \cdot (T2 - T1)$

The uncertainties allocated to the measurements are presented in the table below.

Thermal capacity $C_p$ [J.kg <sup>-1</sup> .K <sup>-1</sup> ]		Correlation Temperature inside circuit Variability of $C_p$ due to temperature error	Applicable to the 5 components
Temperatures external circuits [°C]	pt100	Measurement chain calibration Measurement chain drift Acquisition system resolution Stray flux of probe sheath Fluid homogeneity Correction residue	Applicable to the 5 components
Flowrate of external water circuits [kg.h <sup>-1</sup> ]	Coriolis flowmeter	Calibration uncertainty Drift Correction residue Repeatability	Applicable to generator and evaporator
	Acquisition system	Gain error Resolution Non linearity Offset error	

Appendix

Flowrate of external absorber water circuit [m <sup>3</sup> .h <sup>-1</sup> ]	Coriolis flowmeter	Calibration uncertainty Drift Correction residue Repeatability	Applicable to absorber
	Acquisition system	Gain error Resolution Non linearity Offset error	
Flowrate of external rectifier water circuit [m <sup>3</sup> .h <sup>-1</sup> ]	Mass flowrate transmitter	Accuracy of transmitter	Applicable to rectifier
	Acquisition system	Acquisition system accuracy Acquisition system resolution Acquisition system drift	
Flowrate of external condenser water circuit [m <sup>3</sup> .h <sup>-1</sup> ]		Sum of uncertainties $\dot{m}_{cond} = \dot{m}_{M6} - \dot{m}_{abs} - \dot{m}_{rect}$	Applicable to condenser
Water density [kg.m <sup>-3</sup> ]		Correlation  Variability of Cp due to temperature error	Used to calculate flowrate from [m <sup>3</sup> .h <sup>-1</sup> ] to [kg.h <sup>-1</sup> ]
Thermal power [kW]		Sum of uncertainties $P = \dot{m} \cdot Cp \cdot (T2 - T1)$	Applicable to the 5 main components

**Table 7.1.1.** Uncertainties considered for each measurement device about thermal power calculation.

Concerning the measurement process for the mass flowrate of the external circuits, the flowmeter gives a signal value in Ampere. In order to obtain a value in a correct unity, here [kg.h<sup>-1</sup>], an intermediate calculation as to be done. The acquisition system is set between a minimum and a maximum value in [kg.h<sup>-1</sup>], the corresponding signal in [A] is also set, and the slope is deduced. This calculation method allow to obtain directly the mass flowrate value in [kg.h<sup>-1</sup>].

Flowrate rich & poor solutions & refrigerant Density	Coriolis flowmeter	Flowmeter accuracy Drift Repeatability
	Acquisition system AGILENT	Acquisition system accuracy Acquisition system resolution Acquisition system drift
Pressure	Pressure transmitter	Accuracy of the transmitter Long-term stability Repeatability
	Acquisition system AGILENT	Acquisition system accuracy Acquisition system resolution Acquisition system drift Precision class of Shunt resistance Resistance variation depending on temperature

**Table 7.1.2.** Uncertainties considered for the pressure, the flowrates and the densities measurements.

## Appendix 6.2. Liquid and vapor head losses

### 1 Singular pressure losses for the liquid part

#### 1.1 Distribution-rectification system

The metal used for manufacture of the distribution system is INOX. The pipes are new (non-used) and welded, then  $\Delta = 0.04$  mm. Head losses calculations are established according to IDELCIK "Memento des pertes de charge" 1960.

The ammonia-water solution enters the distribution system with the following inlet conditions:

	Ammonia fraction in liquid [-]	Pressure [bar]	Mass flowrate [kg.s <sup>-1</sup> ]	Specific volume in liquid mixture [m <sup>3</sup> .kg <sup>-1</sup> ]	$\gamma$ specific weight [N.m <sup>-3</sup> ]
310K	0.58	12	0.038	0.00150651	6510

Table 7.2.1. Inlet solution conditions for the rectifier.

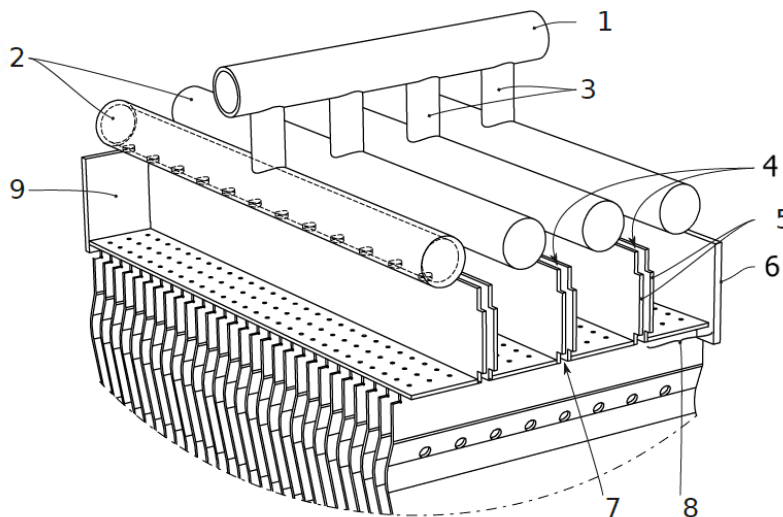


Figure 7.2.1. Schema of the different parts of the distribution-rectification system.

The geometry of the pipes is the following:

Pipe 1 interior diameter [m]	Pipe 3 interior diameter [m]	Pipe 2 interior diameter [m]
0.0103	0.006	0.0103

Table 7.2.2. Geometry of the pipes.

T connection 1  $\rightarrow$  3: Split of the flows with  $F_1 + F_r > F_p$  and  $F_r = F_p$  (p.268)

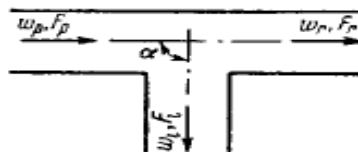


Figure 7.2.2. Schema split of the flows between pipes 1 and 3.

Appendix

	F section area [m <sup>2</sup> ]	w flow speed [m.s <sup>-1</sup> ]	Q Volume flowrate [m <sup>3</sup> .s <sup>-1</sup> ]
p	8.33229.10 <sup>5</sup>	0.687055	5.72474.10 <sup>-5</sup>
r			
l	2.82743.10 <sup>5</sup>	2.0247	

Table 7.2.3. Flow characteristics between pipes 1 and 3.

For the split in the pipe n°3:

$$\zeta_l = \frac{\Delta P_l}{\gamma w_l^2} = \frac{\zeta_{p,l}}{\left(\frac{Q_l F_p}{Q_p F_l}\right)^2} \quad (7.2.1)$$

Where the coefficient  $\zeta_{p,l}$  is determined according to the following graph:

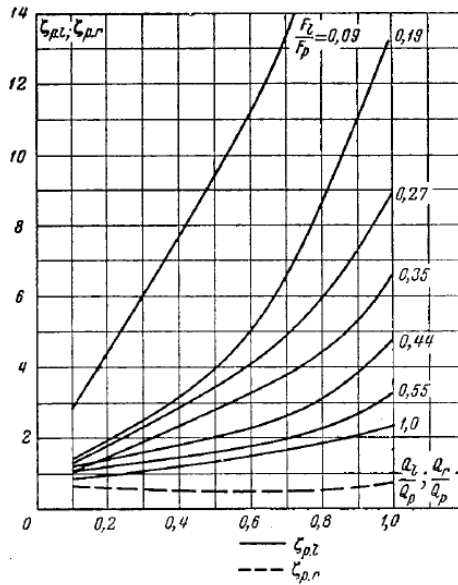


Figure 7.2.3. Graphic for determining head losses coefficients.

$\zeta_{p,l}$	$\zeta_{p,r}$	$\zeta_l$	$\Delta P_l$ [bar]
6.6	0.7	0.76	0.01034

Table 7.2.4. Head losses between pipes 1 and 3.

Symmetrical connection T form, 3 → 2: split of the flows (p.272)

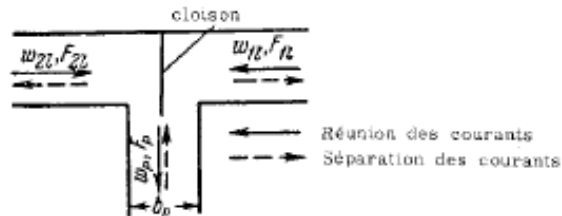


Figure 7.2.4. Schema split of the flows between pipes 3 and 2.

For a split of the flows:

$$\zeta_{p,l} = \frac{\Delta P_{1,l}}{\gamma w_p^2} = 1 + k \cdot \left(\frac{w_l}{w_p}\right)^2 \quad (7.2.2)$$

With  $k = 0,3$  for a welded tube.

Appendix

	F section area [m <sup>2</sup> ]	w flow speed [m/s]	Q Volume flowrate [m <sup>3</sup> /s]	ρ density [kg/m <sup>3</sup> ]
p	2.82743.10 <sup>5</sup>	2.0247		
r	8.33229.10 <sup>5</sup>	0.687055	5.72474.10 <sup>-5</sup>	663.7858
l				

Table 7.2.5. Flow characteristics between pipes 3 and 2.

$\zeta_{p,l}$	$\Delta P_{1,l}$ [bar]
1.0345	0.014076

Table 7.2.6. Head losses between pipes 3 and 2.

Passageway through 2: Side opening of a constant cross section distribution tube

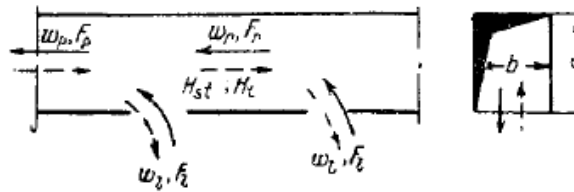


Figure 7.2.5. Schema split of the flows through the holes of 2.

For a split of the flows:

$$\zeta_{p,r} = \frac{\Delta P}{\frac{\rho w_p^2}{2g}} \quad (7.2.3)$$

Where the values of  $\zeta_{pr}$  are determined in the following table, with the pressure inside the tube  $P = 12 \text{ bar}$ , and  $a/b = 1$ .

$\bar{H}_c$	$w_l/w_p$												
	0,6	0,8	1,0	1,2	1,4	1,6	1,8	2,0	2,5	3,0	4,0	5,0	
$a/b = 1,0$													
5	0,14	0,07	0,04	0,02	0,00	—	—	—	—	—	—	—	—
15	—	0,37	0,25	0,20	0,17	0,14	0,12	0,10	0,06	0,03	—	—	—
30	0,59	0,52	0,46	0,42	0,37	0,34	0,31	0,28	0,22	0,18	0,11	0,05	—
50	—	—	0,57	0,52	0,48	0,45	0,42	0,39	0,33	0,29	0,21	0,16	—

Table 7.2.7. Determination of the flow characteristics.

	F section area [m <sup>2</sup> ]	w flow speed [m/s]	Q Volume flowrate [m <sup>3</sup> /s]	ρ density [kg/m <sup>3</sup> ]
P	8.33229.10 <sup>5</sup>	0.687055	0.0000572474	663.7858
l	3.1416.10 <sup>6</sup>	18.2224		

Table 7.2.8. Flow characteristics between pipes 2 and the holes.

$\zeta_{p,r}$	$\Delta P$ [bar]
—	< 1Pa

Table 7.2.9. Head losses of the flows through the holes of 2.

Passageway through 8: Grid of perforated metal sheet, with  $l/D_h > 0.015$

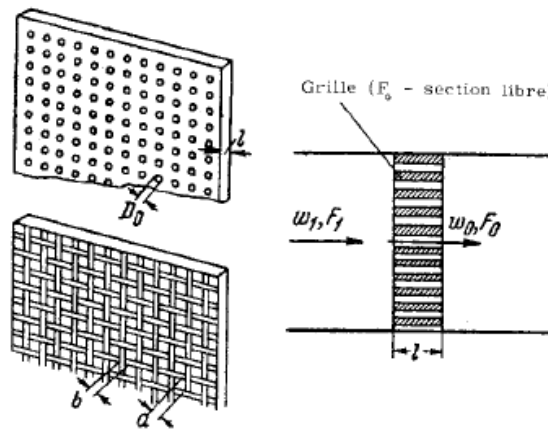


Figure 7.2.6. Schema of the flows through the grid 8.

For a  $Re < 10^5$ :

$$\zeta_{Re} = \frac{\Delta P}{\frac{\gamma w_l^2}{2g}} = \left( \zeta_\varphi + \varepsilon_0^{Re} \cdot \zeta_0 + \lambda \cdot \frac{1}{D_h} \right) \cdot \frac{1}{f^2} \quad (7.2.4)$$

With

$$\zeta_0 = (0,5 + \tau \cdot \sqrt{1-f}) \cdot (1-f) + (1-f)^2 \quad (7.2.5)$$

Hydraulic diameter $d_H$ [m]	Width of the grid $l$ [m]	$\frac{l}{D_h}$	$\tau$ (table p.304)	Re	$\lambda = 64/Re$
0.001	0.0008	0.8	0.42	300	0.2133
$w_l$ flow velocity [m.s <sup>-1</sup> ]	$\rho$ density [kg.m <sup>-3</sup> ]	$\gamma$ specific weight [N.m <sup>-3</sup> ]	$F_p$ Front area [m <sup>2</sup> ]	$F_0$ Free grid area [m <sup>2</sup> ]	
0.0213686	663.7858	6509.5	$2.67904 \cdot 10^{-3}$	$4.39823 \cdot 10^{-5}$	

Table 5.2.10. Characteristics of the flow before the grid 8 and of the grid geometry.

$f = F_0/F_p$	$\zeta_0$	$\zeta_\varphi$ (p.302)	$\varepsilon_0^{Re}$ (p.302)	$\zeta_{Re}$	$\Delta P$ [bar]
0.0164171857	1.8689262996	0.62	0.43	5915.25	0.00896

Table 7.2.11. Head losses of the flow through the grid 8.

Flow between the plates:

In this part, the plates of the rectifier are assumed vertical and straight. According to [1], there are three main film structures, when a condensed film appears along a vertical plate. The thermal transfers through the film are characterized by:

- Laminar smooth film,  $Re_L < 30$ ;
- Laminar film with waves  $30 < Re_L < 1600$ ;
- Turbulent film with waves  $Re_L > 1600$ .

## Appendix

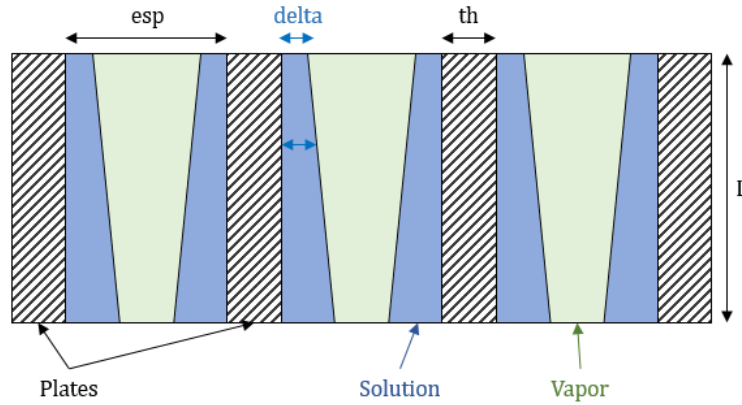


**Figure 7.2.7.** Scheme of the plates, solution film and vapor flow in the rectifier part-Right view.

The liquid head losses  $\Delta P_L$  [Pa] between the plates of the rectifier are determined by:

$$\Delta P_L = \frac{\lambda \cdot \rho_L \cdot U^2 \cdot L}{2 \cdot D_{hL}} \quad (7.2.6)$$

Where  $\rho_L$  is the density of the concentrated ammonia solution [ $\text{kg} \cdot \text{m}^{-3}$ ],  $v_L$  the velocity of the liquid flow [ $\text{m} \cdot \text{s}^{-1}$ ],  $L$  the length of each plate, assuming the plates are straight [m],  $\lambda$  is the head losses coefficient without unity, depending on the Reynolds number of the fluid, and  $D_{hL}$  is the hydraulic diameter of the liquid film [ $\text{m}^2$ ]. The Reynolds number is written as:

$$Re_L = \frac{\rho_L \cdot v_L \cdot D_{hL}}{\mu_L} = \frac{4 \dot{m}_L}{\mu_L \cdot nb \cdot w} \quad (7.2.7)$$

With  $\mu_L$  the viscosity of liquid mixture [ $\text{kg} \cdot \text{m}^{-1} \cdot \text{s}^{-1}$ ],  $B$  the width of the plates [m],  $Nb$  the number of plates, and  $\delta$  the thickness of the film [m], and assuming that the only contact of the liquid with a surface is along the width of the plate:

$$v_L = \frac{\dot{m}_L}{\rho_L \cdot S} \quad \text{and} \quad D_{hL} = \frac{4 \cdot S}{P} = \frac{4 \cdot \delta \cdot w}{w}$$

For the nominal case, the head losses can be determined through the following solution inlet parameters and geometry, and the following variation along the plates:

<b>Width of the plates <math>w</math> [m]</b>	0,09	<b>Thickness of one plate [m]</b>	0.0008
<b>Length of the plates [m]</b>	0.1	<b>Number of plates <math>nb</math></b>	28
<b>Temperature [K]</b>	310-329	<b>Film thickness <math>\delta</math> [m]</b>	$1.28 \cdot 10^{-4} - 1.14 \cdot 10^{-4}$
<b>Ammonia fraction [-]</b>	0.58-0.60	<b>Density of solution <math>\rho_L</math> [<math>\text{kg} \cdot \text{m}^{-3}</math>]</b>	734-723
<b>Viscosity of solution <math>\mu_L</math> [Pa.s]</b>	$4.9 \cdot 10^{-4} - 3.1 \cdot 10^{-4}$	<b>Hydraulic diameter <math>D_{hL}</math></b>	0.0004
<b>Mass flowrate <math>\dot{m}_L</math> [<math>\text{kg} \cdot \text{s}^{-1}</math>]</b>	$3.8 \cdot 10^{-2} - 2.02 \cdot 10^{-2}$	<b>Velocity per plate [<math>\text{m} \cdot \text{s}^{-1}</math>]</b>	0.1605-0.097

**Table 7.2.12.** Characteristics of the solution and plates in the rectifier.

Then, the Reynolds number and the head losses coefficient vary, and the global solution head losses along the plates of the rectifier are:

$Re_L$	$\lambda (64/Re)$	$\Delta P_L$ [bar]
62.5-102	1.02-0.63	0.00474

**Table 7.2.13.** Head losses in the rectifier plates for the solution.

Sum of the solution head losses:

- ✦ Head losses between 1 and 3, one pipe with four junctions:  $\Delta P = 0.04136 \text{ bar}$ ;
- ✦ Head losses between 3 and 2, four pipes for four junctions:  $\Delta P = 0.05630 \text{ bar}$ ;
- ✦ Head losses through pipe 2, four pipes with holes:  $\Delta P \approx 0 \text{ bar}$ ;
- ✦ Head losses through the grid 8:  $\Delta P = 0.00896 \text{ bar}$ ;
- ✦ Head losses along the plates of the rectifier:  $\Delta P = 0.00474 \text{ bar}$ .

The total head losses for the solution in the distribution–rectification system are:

$$\Delta P_L = 0.11136 \text{ bar}$$

## 1.2 Heated plates

In the second part of the combined generator, the plates are not smooth. They are corrugated, as showed in Figure 7.2.9.

The liquid head losses  $\Delta P_L$  between the plates of the generator are calculated in the same way than in the rectifier part, except for the hydraulic diameter  $D_{hL}$ .

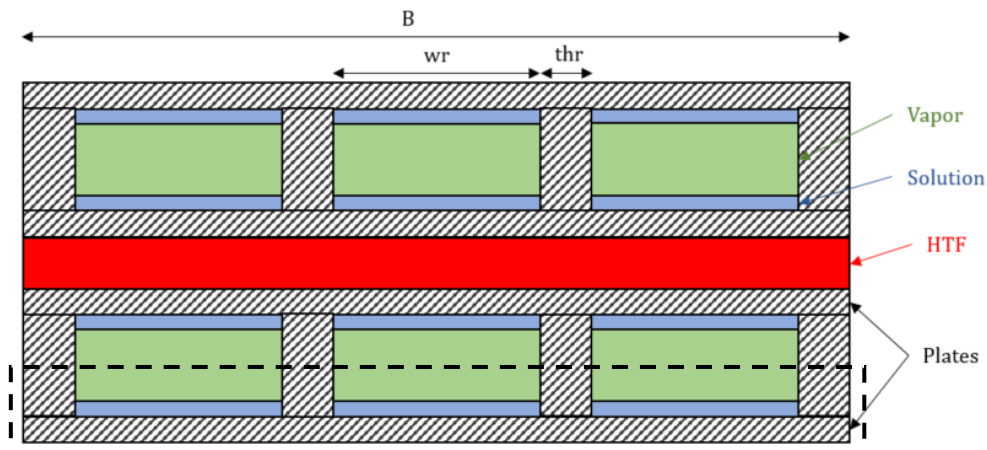


**Figure 7.2.9.** Scheme of the plates, solution film and vapor flow in the generator part—Top view.

Considering that  $w_r$  is the width of the corrugations on one plate [m],  $Nbr$  the number of corrugations, and  $thr$  the thickness of the corrugations [m]:

$$D_{hL} = \left( \frac{4 \cdot \text{delta} \cdot w_r}{(2 \cdot \text{delta} + w_r)} \right) \cdot Nbr \quad (7.2.8)$$

Then,

$$Re_L = \frac{4 \dot{m}_L}{\mu_L \cdot (2 \cdot \text{delta} + w_r)} \quad (7.2.9)$$

If  $Re_L$  is inferior as 1600, then  $\lambda$  is determined by Poiseuille's relation:  $\lambda = 64/Re$ .

## 2 Singular pressure losses for the vapor part

### 2.1 Distribution-rectification system

#### Vapor head losses between the plates

At the exit of the combined generator plates, ammonia vapor is almost pure. The vapor head losses  $\Delta P_V$  [Pa] between the plates of the distributor are determined:

$$\Delta P_V = \frac{\lambda \cdot \rho_V \cdot v^2 \cdot L}{2 \cdot D_h} \quad (7.2.10)$$

With,  $\rho_V$  the density of ammonia vapor [ $\text{kg}\cdot\text{m}^{-3}$ ],  $v$  the velocity of the vapor flow [ $\text{m}\cdot\text{s}^{-1}$ ],  $L$  the length of the plate, assuming the plate is straight [m],  $\lambda$  the head losses coefficient without unity, depending on the Reynolds number of the fluid, and  $D_h$  the hydraulic diameter [m].

Reynolds number is written as:

$$Re_V = \frac{\rho_V \cdot v \cdot D_h}{\mu_V} = \frac{4 \dot{m}_V}{\mu_V \cdot nb \cdot w} \quad (7.2.11)$$

Where,

$$D_{hV} = \frac{4 \cdot S}{P} = \frac{4 \cdot (e - \delta) \cdot w}{w} \quad (7.2.12)$$

With  $w$  the width of the plates [m],  $e$  the space between two plates [m],  $\delta$  the thickness of the solution film [m].

For the nominal case, the head losses can be determined through the following vapor outlet parameters and geometry, and the following variation along the plates:

<b>Width of the plates <math>w</math> [m]</b>	0.09	<b>Thickness of one plate [m]</b>	0.0008
<b>Length of the plates [m]</b>	0.1	<b>Number of plates <math>nb</math></b>	28
<b>Space between two plates <math>e</math> [m]</b>	0.0042	<b>Film thickness <math>\delta</math> [m]</b>	$1.28 \cdot 10^{-4}$ – $1.14 \cdot 10^{-4}$
<b>Temperature [K]</b>	338.5–342		
<b>Ammonia fraction [-]</b>	0.987–0.983	<b>Density of solution <math>\rho_L</math> [<math>\text{kg}\cdot\text{m}^{-3}</math>]</b>	7.94–7.83
<b>Viscosity of solution <math>\mu_L</math> [Pa.s]</b>	$1.17 \cdot 10^{-5}$ – $1.18 \cdot 10^{-5}$	<b>Hydraulic diameter <math>D_{hV}</math></b>	$7.9 \cdot 10^{-3}$
<b>Mass flowrate <math>\dot{m}_L</math> [<math>\text{kg}\cdot\text{s}^{-1}</math>]</b>	$1.7 \cdot 10^{-4}$ – $2.1 \cdot 10^{-4}$	<b>Velocity per plate [<math>\text{m}\cdot\text{s}^{-1}</math>]</b>	$2.1 \cdot 10^{-3}$ – $2.6 \cdot 10^{-3}$

**Table 7.2.14.** Characteristics of the vapor and plates in the rectifier.

Then, the Reynolds number and the head losses coefficient vary, and the global vapor head losses along the plates of the rectifier are:

<b><math>Re_V</math></b>	<b><math>\lambda (64/Re)</math></b>	<b><math>\Delta P_V</math> [bar]</b>
646–788	0.099–0.081	$9 \cdot 10^{-7}$

**Table 7.2.15.** Head losses in the rectifier plates for the vapor.

#### Passageway from the space between two plates to the chimneys 7 through side opening:

When the vapor reaches the top of the plates, it enters by three holes, leading to the evacuation chimneys. There are abrupt narrowing, followed by abrupt widening. The head losses for the ammonia vapor evacuating through the evacuation chimneys are calculated with the following parameters:

Appendix

Number of evacuation chimneys	3	Width of the chimneys [m]	0.002
Length of the chimneys [m]	0.145	High of the chimneys passage [m]	0.02
Width of the plates w [m]	0.09	Thickness of one plate [m]	0.0008
Length of the plates [m]	0.1	Number of plates nb	28
Space between two plates e [m]	0.0042	Film thickness $\delta$ [m]	$1.28 \cdot 10^{-4}$
Temperature [K]	338	Density of solution $\rho_L$ [ $\text{kg} \cdot \text{m}^{-3}$ ]	7.94
Ammonia fraction [-]	0.987	Hydraulic diameter $D_{hV}$	$7.9 \cdot 10^{-3}$
Viscosity of solution $\mu_L$ [Pa.s]	$1.17 \cdot 10^{-5}$	Velocity per plate [ $\text{m} \cdot \text{s}^{-1}$ ]	$2.1 \cdot 10^{-3}$
Mass flowrate $\dot{m}_V$ [ $\text{kg} \cdot \text{s}^{-1}$ ]	$1.7 \cdot 10^{-4}$	Reynolds number (plates)	646
$\gamma$ specific weight [ $\text{N} \cdot \text{m}^{-3}$ ]	77.86		

Table 7.2.16. Characteristics of the vapor and chimneys at the rectifier outlet.

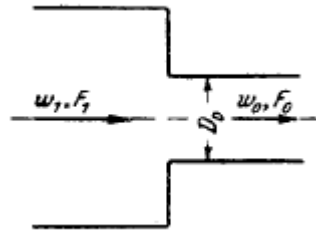


Figure 7.2.10. Schema of the narrowing between the plates and the opening.

For  $10 < \text{Re} < 10^4$ ,

$F_0/F_1$ \ Re	10	20	30	40	50	$10^2$	$2 \cdot 10^2$	$5 \cdot 10^2$	$10^3$	$2 \cdot 10^3$	$4 \cdot 10^3$	$5 \cdot 10^3$	$10^4$	$> 10^4$
0,1	5,00	3,20	2,40	2,00	1,80	1,30	1,04	0,82	0,64	0,50	0,80	0,75	0,50	0,45
0,2	5,00	3,10	2,30	1,84	1,62	1,20	0,95	0,70	0,50	0,40	0,60	0,60	0,40	0,40
0,3	5,00	2,95	2,15	1,70	1,50	1,10	0,85	0,60	0,44	0,30	0,55	0,55	0,35	0,35
0,4	5,00	2,80	2,00	1,60	1,40	1,00	0,78	0,50	0,35	0,25	0,45	0,50	0,30	0,30
0,5	5,00	2,70	1,80	1,46	1,30	0,90	0,65	0,42	0,30	0,20	0,40	0,42	0,25	0,25
0,6	5,00	2,60	1,70	1,35	1,20	0,80	0,56	0,35	0,24	0,15	0,35	0,35	0,20	0,25

Table 7.2.17. Determination of the head losses coefficient.

$$\zeta = \frac{\Delta P}{\frac{\rho w_0^2}{2g}} \quad (7.2.13)$$

For each narrowing, the characteristics are:

	F section area [ $\text{m}^2$ ]	w flow speed [ $\text{m} \cdot \text{s}^{-1}$ ]	Q Volume flowrate [ $\text{m}^3 \cdot \text{s}^{-1}$ ]	$\rho$ density [ $\text{kg} \cdot \text{m}^{-3}$ ]
1	$1.1984 \cdot 10^{-4}$	0.17866	$2.14105 \cdot 10^{-5}$	7.94
0	$8.4 \cdot 10^{-6}$	2.5489		

Table 7.2.18. Flow characteristics between the rectifier plates.

$\zeta$	$\Delta P$ [bar]
0.9	0.0002321

Table 7.2.19. Head losses for narrowing.

Appendix

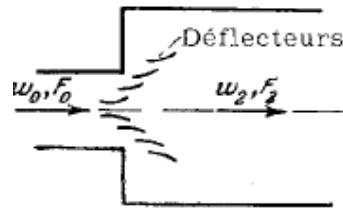


Figure 7.2.11. Schema of the widening between the opening and the chimneys.

For  $10 < Re < 3,5 \cdot 10^3$ :

$F_0/F_2$	Re												
	10	15	20	30	40	50	$10^2$	$2 \cdot 10^2$	$5 \cdot 10^2$	$10^3$	$2 \cdot 10^3$	$3 \cdot 10^3$	$3,5 \cdot 10^3$
0,1	3,10	3,20	3,00	2,40	2,15	1,95	1,70	1,65	1,70	2,00	1,60	1,00	0,81
0,2	3,10	3,20	2,80	2,20	1,85	1,65	1,40	1,30	1,30	1,60	1,25	0,70	0,64
0,3	3,10	3,10	2,60	2,00	1,60	1,40	1,20	1,10	1,10	1,30	0,95	0,60	0,50
0,4	3,10	3,00	2,40	1,80	1,50	1,30	1,10	1,00	0,85	1,05	0,80	0,40	0,36
0,5	3,10	2,80	2,30	1,65	1,35	1,15	0,90	0,75	0,65	0,90	0,65	0,30	0,25
0,6	3,10	2,70	2,15	1,55	1,25	1,05	0,80	0,60	0,40	0,60	0,50	0,20	0,16

Table 7.2.20. Determination of the head losses coefficient.

$$\zeta = \frac{\Delta P}{\gamma w_0^2 / 2g} \quad (7.2.14)$$

For each widening, the characteristics are:

F section area [m <sup>2</sup> ]	w flow speed [m.s <sup>-1</sup> ]	Q Volume flowrate [m <sup>3</sup> .s <sup>-1</sup> ]	$\rho$ density [kg.m <sup>-3</sup> ]
0	$8.4 \cdot 10^{-6}$	2.5489	
2	$1.07 \cdot 10^{-5}$	2	$2.14105 \cdot 10^{-5}$
			7.94

Table 7.2.21. Flow characteristics for the opening in the chimneys.

$\zeta$	$\Delta P$ [bar]
0.1	0.000025792

Table 7.2.22. Head losses for widening.

Head losses between the plates of the chimney 7:

The head losses of the ammonia vapor inside of the chimney are characterized by:

Number of evacuation chimneys	3	Width of the chimneys [m]	0.002
Length of the chimneys [m]	0.145	High of the chimneys passage [m]	0.02
Temperature [K]	338.5		
Ammonia fraction [-]	0.987	Density of solution $\rho_L$ [kg.m <sup>-3</sup> ]	7.94
Viscosity of solution $\mu_L$ [Pa.s]	$1.17 \cdot 10^{-5}$	Hydraulic diameter $D_{hV}$	$7.9 \cdot 10^{-3}$
Mass flowrate $\dot{m}_L$ [kg.s <sup>-1</sup> ]	$1.7 \cdot 10^{-4}$	Velocity per plate [m.s <sup>-1</sup> ]	$2.1 \cdot 10^{-3}$

Table 7.2.23. Characteristics of the vapor in the chimney.

Then, the Reynolds number and the head losses coefficient vary, and the global vapor head losses along the plates of the rectifier are:

$Re_V$	$\lambda (64/Re)$	$\Delta P_V$ [bar]
646	0.099	$3.02 \cdot 10^{-8}$

Table 7.2.24. Head losses in the chimneys.

## Appendix

### Head losses at the outlet of the chimneys 7:

$$\zeta = \frac{\Delta P}{\frac{\gamma w_0^2}{2g}} \quad (7.2.15)$$

For each widening, the characteristics are:

	<b>F section area [m<sup>2</sup>]</b>	<b>w flow speed [m.s<sup>-1</sup>]</b>	<b>Q Volume flowrate [m<sup>3</sup>.s<sup>-1</sup>]</b>	<b>ρ density [kg.m<sup>-3</sup>]</b>
<b>0</b>	1.07.10 <sup>-5</sup>	2	2.14105.10 <sup>-5</sup>	7.94
<b>2</b>	0.0135	0.00158596		

**Table 7.2.25.** Flow characteristics for the outlet of the chimneys.

Using Table 7.2.20 values, the coefficient and the head losses can be determined:

<b>ζ</b>	<b>ΔP [bar]</b>
2	7.6.10 <sup>-8</sup>

**Table 7.2.26.** Head losses for widening at the outlet of the chimneys.

### Head losses at the outlet of the combined generator for the evacuation of vapor:

For the narrowing, the characteristics are:

	<b>F section area [m<sup>2</sup>]</b>	<b>w flow speed [m.s<sup>-1</sup>]</b>	<b>Q Volume flowrate [m<sup>3</sup>.s<sup>-1</sup>]</b>	<b>ρ density [kg.m<sup>-3</sup>]</b>
<b>1</b>	0.0135	0.00158596	2.14105.10 <sup>-5</sup>	7.94
<b>0</b>	8.04.10 <sup>-4</sup>	0.02663		

**Table 7.2.27.** Flow characteristics for the outlet of the chimneys.

Using the table 17, the coefficient and the head losses can be determined:

<b>ζ</b>	<b>ΔP [bar]</b>
1	2.35.10 <sup>-6</sup>

**Table 7.2.28.** Head losses for narrowing at the outlet of the combined generator.

### Sum of the solution head losses:

- ✦ Head losses through the outlet of the desorber:  $\Delta P = 2.35.10^{-6}$  bar;
- ✦ Head losses through the 3 openings at the outlet of the chimneys:  $\Delta P = 2.28.10^{-7}$  bar;
- ✦ Head losses through the 3 chimneys:  $\Delta P = 9.06.10^{-8}$  bar;
- ✦ Head losses through the 28 openings in the chimneys:  $\Delta P = 7.22.10^{-4}$  bar;
- ✦ Head losses through the narrowing before the 3 chimneys:  $\Delta P = 6.963.10^{-4}$  bar;
- ✦ Head losses along the 28 plates of the rectifier:  $\Delta P = 2.52.10^{-5}$  bar;

The total head losses for the vapor in the distribution-rectification system are:

$$\Delta P_V = 1.44.10^{-3} \text{ bar}$$

## 2.2 Heated plates

The vapor head losses  $\Delta P_V$  between the plates of the generator are also determined through the same process. With  $hei$  the space between two plates [m]:

$$D_{hV} = \frac{4 \cdot (hei/2 - \delta) \cdot wr}{(2 \cdot (hei/2 - \delta) + wr)} \cdot Nbr \quad (7.2.16)$$

## Appendix

Then,

$$Re_V = \frac{4 \dot{m}_V}{\mu_V \cdot (2 \cdot (\frac{he^i}{2} - \delta) + wr)} \quad (7.2.17)$$

If  $Re_V$  is inferior as 2300, then  $\lambda$  is determined by Poiseuille's relation:  $\lambda = \frac{64}{Re}$ .

### 2.3 Shearing constraint for the vapor:

According to the part III.2.2 of the state of the art and according to the inlet conditions previously established, the shear strain rate for the solution is:

$$\tau_V = -3,53 \cdot 10^{-18}$$

Thus,  $\tau_L \gg \tau_V$ . This means, the shearing stress of the vapor on the solution flow, between two plates is negligible.

### Appendix 6.3. Design of experiments

Table 7.3.1 presents the matrix of experiments associated to the Doehlert network method with four factors, and its correspondence, calculated thanks to the measurements ranges.

TEST	Doehlert Matrix				Measurements matrix			
	X1	X2	X3	X4	X1	X2	X3	X4
1	0	0	0	0	0.019	-0.036	0.036	0.008
2	1	0	0	0	0.980	-0.042	0.210	-0.002
3	0.5	0.866	0	0	0.446	0.782	0.096	-0.019
4	-0.5	0.866	0	0	-0.518	0.784	0.051	-0.009
5	-1	0	0	0	-0.983	-0.046	0.034	0.016
6	-0.5	-0.866	0	0	-0.515	-0.890	0.034	0.002
7	0.5	-0.866	0	0	0.486	-0.873	0.039	0.072
8	0.5	0.289	0.816	0	0.493	0.293	0.827	0.049
9	-0.5	0.289	0.816	0	-0.517	0.287	0.826	-0.017
10	0	-0.577	0.816	0	0.017	-0.536	0.821	-0.004
11	0.5	-0.289	-0.816	0	0.476	-0.372	-0.681	0.003
12	-0.5	-0.289	-0.816	0	-0.515	-0.371	-0.772	0.010
13	0	0.577	-0.816	0	0.009	0.450	-0.511	-0.011
14	0.5	0.289	0.204	0.791	0.476	0.293	0.246	0.737
15	-0.5	0.289	0.204	0.791	-0.515	0.291	0.239	0.446
16	0	-0.577	0.204	0.791	0.018	-0.536	0.233	0.538
17	0	0	-0.612	0.791	0.015	-0.044	-0.651	0.717
18	0.5	-0.289	-0.204	-0.791	0.414	-0.372	-0.243	-0.814
19	-0.5	-0.289	-0.204	-0.791	-0.517	-0.377	-0.162	-0.831
20	0	0.577	-0.204	-0.791	0.016	0.460	-0.097	-0.813
21	0	0	0.612	-0.791	0.017	-0.038	0.626	-0.787

**Table 7.3.1.** Matrix of experiments for the Doehlert network method and matrix of experiments according to the measurements.

The theoretical values of the inlet variables corresponding to the DOE and the experimental inlet values measured are detailed in Table 7.3.2.

Test	Theoretical inlet values				Measured inlet values			
	$T_{hot}$ [°C]	$T_{cold}$ [°C]	$T_{medium}$ [°C]	$\dot{m}_{RS}$ [kg.h <sup>-1</sup> ]	$T_{hot}$ [°C]	$T_{cold}$ [°C]	$T_{medium}$ [°C]	$\dot{m}_{RS}$ [kg.h <sup>-1</sup> ]
1	95	16	27	110	95.3	15.8	27.2	110.3
2	110	16	27	110	109.7	15.7	28.0	109.9
3	102.5	21	27	110	101.7	20.7	27.5	109.3
4	87.5	21	27	110	87.2	20.7	27.3	109.7
5	80	16	27	110	80.3	15.7	27.2	110.6
6	87.5	11	27	110	87.3	10.7	27.2	110.1
7	102.5	11	27	110	102.3	10.8	27.2	112.5
8	102.5	18	31	110	102.4	17.8	31.1	111.7
9	87.5	18	31	110	87.2	17.7	31.1	109.4
10	95	13	31	110	95.3	12.8	31.1	109.8
11	102.5	14	23	110	102.1	13.8	23.6	110.1
12	87.5	14	23	110	87.3	13.8	23.1	110.3

Test	Theoretical inlet values				Measured inlet values			
	$T_{hot} [^{\circ}C]$	$T_{cold} [^{\circ}C]$	$T_{medium} [^{\circ}C]$	$\dot{m}_{RS} [kg.h^{-1}]$	$T_{hot} [^{\circ}C]$	$T_{cold} [^{\circ}C]$	$T_{medium} [^{\circ}C]$	$\dot{m}_{RS} [kg.h^{-1}]$
13	95	19	23	110	95.1	18.7	24.4	109.6
14	102.5	18	28	137.7	102.1	17.8	28.2	135.8
15	87.5	18	28	137.7	87.3	17.7	28.2	125.6
16	95	13	28	137.7	95.3	12.8	28.2	128.8
17	95	16	24	137.7	95.2	15.7	23.7	135.1
18	102.5	14	26	82.3	101.2	13.8	25.8	81.5
19	87.5	14	26	82.3	87.3	13.7	26.2	80.9
20	95	19	26	82.3	95.2	18.8	26.5	81.5
21	95	16	30	82.3	95.3	15.8	30.1	82.4

Table 7.3.2. Experimental plan.

### Least squares method and polynomial coefficients determination

The method of the least squares is used to find each coefficient of each equation corresponding to the outlet value of the absorption chiller studied. The polynomial equation is written under the form:

$$y_i = b_0 + b_1 \cdot x_{i,1} + b_2 \cdot x_{i,2} + b_3 \cdot x_{i,3} + b_4 \cdot x_{i,4} + b_{11} \cdot x_{i,1}^2 + b_{22} \cdot x_{i,2}^2 + b_{33} \cdot x_{i,3}^2 + b_{44} \cdot x_{i,4}^2 + b_{12} \cdot x_{i,1} \cdot x_{i,2} + b_{13} \cdot x_{i,1} \cdot x_{i,3} + b_{23} \cdot x_{i,2} \cdot x_{i,3} + b_{14} \cdot x_{i,1} \cdot x_{i,4} + b_{24} \cdot x_{i,2} \cdot x_{i,4} + b_{34} \cdot x_{i,3} \cdot x_{i,4} + e_i \quad (7.3.1)$$

Where  $y_i$  is the experimental value observed,  $b_i$  is the coefficient allowing to find the response researched,  $x_{i,j}$  is the value of the inlet parameter for the  $i$ -set of experiment and the  $j$ -inlet variable, and  $e_i$  is the error representing the gap between the experimental value and the calculated value.

Then, the 21 equations, corresponding to the 21 tests led, can be written as:

$$\begin{pmatrix} y_1 \\ \dots \\ y_i \\ \dots \\ y_{21} \end{pmatrix} = \begin{pmatrix} 1 & x_{1,1} & \dots & x_{1,1}^2 & \dots & x_{1,3} \cdot x_{1,4} \\ \dots & \dots & \dots & \dots & \dots & \dots \\ 1 & x_{i,1} & \dots & x_{i,1}^2 & \dots & x_{i,3} \cdot x_{i,4} \\ \dots & \dots & \dots & \dots & \dots & \dots \\ 1 & x_{21,1} & \dots & x_{21,1}^2 & \dots & x_{21,3} \cdot x_{21,4} \end{pmatrix} \cdot \begin{pmatrix} b_0 \\ \dots \\ b_{ij} \\ \dots \\ b_{34} \end{pmatrix} + \begin{pmatrix} e_1 \\ \dots \\ e_i \\ \dots \\ e_{21} \end{pmatrix} \quad (7.3.2)$$

$$(Y) = (X) \cdot (B) + (e) \quad (7.3.3)$$

Where (Y) is the vector of the measured values, (X) is the model matrix, (B) is the estimated coefficients vector and (e) is the residue vector. Then, the calculated values of the absorption performances evaluated can be deduced thanks to:

$$(\hat{Y}) = (X) \cdot (B) \quad (7.3.4)$$

With,

$$(e) = (Y) - (\hat{Y}) \quad (7.3.5)$$

## Appendix

Table 7.3.3 details the polynomial coefficients obtained for each parameter evaluated.

<i>Test</i>	<i>Q<sub>CG</sub> [kW]</i>	<i>m<sub>vap</sub> [kg.h<sup>-1</sup>]</i>	<i>y<sub>vap</sub> [-]</i>
<b>b0</b>	80.26	117.45	1.40
<b>b1</b>	-4.61	-13.03	-1.31E-3
<b>b2</b>	1.35E-1	-7.98E-1	-2.30E-3
<b>b3</b>	15.66	62.89	-1.68E-2
<b>b4</b>	-386.36	-953.69	-7.11E-1
<b>b11</b>	1.68E-2	2.44E-2	1.18E-6
<b>b22</b>	-7.35E-4	-6.94E-3	-2.70E-7
<b>b33</b>	-8.74E-1	-2.76	-2.79E-4
<b>b44</b>	-5.04E-1	-2.28	-1.58E-3
<b>b12</b>	-1.24E-3	1.74E-2	7.90E-6
<b>b13</b>	3.82E-2	1.25E-1	8.23E-5
<b>b23</b>	-2.85E-2	-8.26E-2	-2.79E-5
<b>b14</b>	6.28	16.76	-7.84E-4
<b>b24</b>	6.82E-1	4.18	4.01E-3
<b>b34</b>	11.85	11.74	4.02E-2

**Table 7.3.** Polynomial coefficients corresponding to each parameter evaluated.

### Analysis of Variance

The ANalysis Of VAriance test allows comparing the variances of the values and the residues calculated by the model. The Fisher-Snedecor validation test underlines if the regression is significant, if the equation gives an accurate relation between the factors and the outlet value and can explain the deviations of the calculated values ( $\hat{Y}$ ). It is established thanks to the Mean Squares (MS), the Overall Sum Square (OSS), the regression coefficient  $R^2$  and the Fisher-Snedecor ratio F:

$$MS = \sum_{i=1}^N (y_i - \hat{y}_i)^2 \quad (7.3.6)$$

$$OSS = \sum_{i=1}^N (y_i - \hat{y}_i)^2 + \sum_{i=1}^N (e_i)^2 \quad (7.3.7)$$

$$R^2 = \frac{MS}{TSS} \quad (7.3.8)$$

$$F = \frac{\sum_{i=1}^N (y_i - \hat{y}_i)^2 / (k-1)}{\sum_{i=1}^N (e_i)^2 / (N-1)} \quad (7.3.9)$$

The higher F, the lower the residues. The hypothesis  $H_0$  of the test presumes that “the model cannot describe the variations of the calculated values”. The probability Pr to reject the  $H_0$  hypothesis allows validating the model if the probability is low enough. Table 7.3.4 resumes this test values for the parameters studied

	<b>Sources</b>	<b>Freedom degree</b>	<b>Sum squares</b>	<b>Mean squares</b>	<b>F</b>	<b>Pr &gt; F</b>
<b>Q<sub>des</sub></b>	<i>Model</i>	1	62	62	317.4	<0.0001
	<i>Residues</i>	19	3.74	0.197		
	<i>Total</i>	20	66			
<b>m<sub>vap</sub></b>	<i>Model</i>	1	642	642	193.4	<0.0001
	<i>Residues</i>	19	63.1	3.320		
	<i>Total</i>	20	705			
<b>y<sub>vap</sub></b>	<i>Model</i>	1	2.37E-4	2.37E-4	198.6	<0.0001
	<i>Residues</i>	19	2.27E-5	1.20E-6		
	<i>Total</i>	20	2.60E-4			

**Table 7.4.** Variance analysis for the outlet values of the combined generator.

## **Appendix 6.4. Scientific production**

*During the three years of this PhD, different valuations of the work done were allowed through journal articles publications, conferences papers and presentations, and patent deposits. The list of the scientific production linked to this PhD thesis is presented below.*

---

### ***Articles in Scientific Journals***

Wirtz M., Stutz B., Phan H.T., Boudéhen F.

“Numerical modeling of falling-film plate generator and rectifier designed for NH<sub>3</sub>-H<sub>2</sub>O absorption machines”

*Heat and Mass Transfer* 58, 431–446 (2022)

<https://link.springer.com/article/10.1007%2Fs00231-021-03111-z>

Wirtz M., Stutz B., Phan H.T., Boudéhen F.

“Study of the impact of a combined generator on the performance of an NH<sub>3</sub>-H<sub>2</sub>O absorption machine thanks to the effectiveness method”

*Applied Thermal Engineering*

*(Submitted 2021)*

Wirtz M., Stutz B., Phan H.T., Boudéhen F.

“Experimental study of the impact of a combined generator behavior on NH<sub>3</sub>-H<sub>2</sub>O absorption chiller performance”

*International Journal of Refrigeration*

*(Submitted 2021)*

Wirtz M., Stutz B., Phan H.T., Boudéhen F.

“Characterization and modeling of a flooded generator for small capacity NH<sub>3</sub>-H<sub>2</sub>O absorption chillers.”

*Heat and Mass Transfer*

*(Submitted 2022)*

Wirtz M., Stutz B., Phan H.T., Boudéhen F.

“Combined generator for an NH<sub>3</sub>-H<sub>2</sub>O absorption chiller.”

*International Journal of Heat and Mass Transfer*

*(Submitted 2022)*

---

### ***Conference papers***

Voeltzel N., Phan H.T., Tauveron N., Gonzalez B., Blondel Q., Wirtz M., Boudéhen F.

“Numerical studies of a hybrid cycle for power production and cooling”

*Proceedings of the ISES Solar World Congress 2019 and IEA SHC International Conference on Solar Heating and Cooling for Buildings and Industry 2019*

<https://doi.org/10.18086/swc.2019.55.11>

Wirtz M., Stutz B., Phan H.T., Boudéhen F.

“Numerical modeling of a falling-film plate generator for NH<sub>3</sub>-H<sub>2</sub>O absorption machine”

*Congress of the Société Française de Thermique, Belfort, France, June 2020*

<https://doi.org/10.25855/SFT2020-032>

Phan H.T., Wirtz M., Hergott J., Boudéhenn F.

“Dynamic Simulations of an Absorption Refrigeration System for Automobile Application”  
*Paper 341, Heat Pump Conference, Jeju, Korea, 26 to 29<sup>th</sup> April 2021*

Wirtz M., Stutz B., Phan H.T., Boudéhenn F.

“Numerical modeling and integration of a falling-film plate generator/rectifier in an NH<sub>3</sub>-H<sub>2</sub>O absorption machine prototype”  
*Congress of the Société Française de Thermique, Belfort, France, 1 to 3<sup>rd</sup> June 2021*  
<https://doi.org/10.25855/SFT2021-011>

Wirtz M., Stutz B., Phan H.T., Boudéhenn F.

“Experimentation and modeling of a combined plate generator for NH<sub>3</sub>-H<sub>2</sub>O absorption machine”  
*International Sorption Heat Pump Conference, Berlin, Germany, 22 to 25<sup>th</sup> August 2021*

---

### **Conference posters**

Wirtz M., Stutz B., Phan H.T., Boudéhenn F.

“Optimisation des transferts couplés de masse et de chaleur dans les films tombants du désorbeur d’une machine à absorption”  
*Journée Nationale des Energies Solaires, Annecy, France, 17–19<sup>th</sup> June 2019*

Wirtz M., Stutz B., Phan H.T., Boudéhenn F.

“Modélisation numérique et intégration d’un générateur-rectifieur à plaques et films tombants dans une machine à absorption NH<sub>3</sub>-H<sub>2</sub>O”  
*Journée Nationale des Energies Solaires, Odeillo, France, 25–27<sup>th</sup> August 2021*

---

### **Patent deposits**

Wirtz M., Boudéhenn F., Phan H.T., Stutz B.

“Générateur comprenant une fonction de rectification, une machine à absorption comprenant ledit générateur et un procédé de production de vapeur de fluide frigorigène par ledit générateur”  
*European patent, EP 3 885 672 A1*  
[https://sobjprd.questel.fr/sobj/servlet/get\\_pds/EP3885672A1.pdf?userid=PWW6KXBX&type=0&pdfd=106139727&ekey=1319](https://sobjprd.questel.fr/sobj/servlet/get_pds/EP3885672A1.pdf?userid=PWW6KXBX&type=0&pdfd=106139727&ekey=1319)

Wirtz M., Chandez B., Phan H.T., Stutz B.

“Dispositif de rectification comprenant un rectifieur et un dispositif de distribution, et machine à absorption comprenant ledit dispositif de rectification”  
*European patent, EP 3 885 673 A1*  
[https://sobjprd.questel.fr/sobj/servlet/get\\_pds/EP3885673A1.pdf?userid=PWW6KXBX&type=0&pdfd=106138447&ekey=1310](https://sobjprd.questel.fr/sobj/servlet/get_pds/EP3885673A1.pdf?userid=PWW6KXBX&type=0&pdfd=106138447&ekey=1310)

---

### **Other achievements**

Participation to the “*International Summer school on Renewable energies (IE-ENR)*”  
*University Gaston Berger, Saint-Louis, Senegal, 21 to 30<sup>th</sup> July 2019*

---